Developments in the Application of the Geometrical Theory of Diffraction and Computer Graphics to Aircraft Inter-Antenna Coupling Analysis

Michael Bogusz

A Thesis

in

The Department

of

Electrical and Computer Engineering

Presented in Partial Fulfillment of the Requirements
for the Degree of Master of Engineering at
Concordia University
Montreal, Quebec, Canada

January 1993

Michael Bogusz

ISBN 0-315-84643-7

Canada

ABSTRACT

Developments in the Application of the Geometrical Theory of Diffraction and Computer Graphics to Aircraft Inter-Antenna Coupling Analysis

Michael Bogusz

This thesis examines the need for a systematic methodology for the analysis of aircraft electromagnetic compatibility (EMC) problems. It surveys the available computer aids used in aircraft EMC analysis and establishes the theoretical basis for the complex algorithms which identify and quantify electromagnetic interactions. The thesis presents an overview of one particularly well-established aircraft antenna-to-antenna EMC analysis code, the Aircraft Inter-Antenna Propagation with Graphics (AAPG) Version 07 (V07) software program.

The thesis discusses the specific new algorithms that have been created to compute cone geodesics and their associated path losses, and to graphically portray representations of the physical coupling path. These algorithms are validated against basic principles. Loss computations apply the Uniform Geometrical Theory of Diffraction (UTD) and are subsequently compared to measurement data.

The thesis assesses the increased modelling and analysis capabilities of the newly developed AAPG Version 09 (V09) against those of AAPG V07. Several models of a "real-world" aircraft, namely the Electronics Systems Trainer (EST) Challenger, are generated and are provided as the basis for this preliminary comparative assessment. Issues such as software reliability, algorithm stability, and quality of hardcopy output are also discussed. This comparative study opens several avenues for future research.

ACKNOWLEDGEMENTS

I am obliged and grateful to Dr's Robert Paknys and Miles Upton for their incisive editorial comments which assisted tremendously in getting me to say what I mean and mean what I say.

I would like to thank Dr. Christopher Trueman whose enthusiasm initially sparked my interest in applied electromagnetics and who made me appreciate the subject as more than Greek alphabet soup

I would like to recognize Mr. Milton Pomerantz, my mentor during my time at Paramax Electronics, whose sound advice of "Get the job done!" continues to rattle around in my brain to this day. Thanks again, Milt

I appreciate the moral support and flexibility of my manager and supervisors at Computing Devices Canada, Mr.'s Dave Dean, Joe Daniel, and Tom Howe, and the opportunity they have given me to apply the knowledge and experience gained from my studies at the EMC Laboratory at Concordia University.

I am particularly grateful to my thesis advisor, Dr. Stanley Kubina, whose vast and varied background I have only begun to tap. His patience, reassurance, and financial assistance were invaluable in the perseverance and completion of this undertaking

Finally, to my buddies in the Naval Reserve, the Trail Blazers, the Drift Wood, my sisters and my parents, and all my friends whom I have not yet completely alienated well, I have finally finished, so you can quit bugging me already!

TABLE OF CONTENTS

LIST OF FIGURES

LIST OF TABLES

LIST OF SYMBOLS USED

A	Parameter dependent on Fock parameter used in computation of L_{cs}
$\hat{a}_r$	Unit vector from cone apex along cone surface
$\hat{a}_{r_1}$	Unit vector tangent to the ray OQ_1 which proceeds from cone apex to point Q_1 on cone surface
$\hat{a}'_{r_1}$	Unit vector which has been mapped from the unit vector $\hat{a}_{r_1}$ on cone surface to the developed cone
$\hat{a}_x$	Unit vector in Cartesian x-direction
$\hat{a}_X$	Unit vector in X-direction on developed cone surface
$\hat{a}_y$	Unit vector in Cartesian y-direction
$\hat{a}_Y$	Unit vector in Y-direction on developed cone surface
$\hat{a}_z$	Unit vector in cylinder axial direction, Unit vector in cone axial direction; Unit vector in Cartesian z-direction
(AZ,EL)	Azimuth and elevation angles associated with a vector tangent to the coupling path at a particular point (degrees)
$\hat{a}_\phi$	Unit vector in cylinder circumferential direction, Unit vector in circumferential direction along edge of circular cross-section of cone
$\hat{a}_{\phi_1}$	Unit vector in circumferential direction along edge of circular cross-section of cone at point Q_1
$\hat{a}'_{\phi_1}$	Unit vector which has been mapped from the unit vector $\hat{a}_{\phi_1}$ on cone surface to the developed cone

$\hat{a}_1$	Unit vector tangent to geodesic coupling path Γ on cone surface at point Q_1
$\hat{a}_1'$	Unit vector tangent to geodesic coupling path Γ' on developed cone surface at point Q_1'
$\hat{a}_{\rho_1}$	Unit vector along a ray, ρ_1, which proceeds from cone axis to point Q_1
(BL,WL,FS)	Butt-line, water-line, fuselage-station coordinate system (inches)
B_n	Coefficients for series representation of $V(\xi)$ for ξ large
$\hat{b}$	Unit binormal vector at point Q
$\hat{b}'$	Unit binormal vector at point Q'
$\mathbb{C}$	Complex numbers
CL_R	Insertion losses due to receiver cabling and filters (dB)
CL_X	Insertion losses due to transmitter cabling and filters (dB)
D	Surface ray divergence factor
$D(r_D,\theta_D,\phi_D)$	Intermediate point on geodesic coupling path Γ on cone surface (metres, radians, radians)
$D'(X_D,Y_D)$	Equivalent of point D which has been mapped onto the developed cone surface (metres)
ds'	Differential arc length (metres)
du	Differential of curvilinear coordinate u
dv	Differential of curvilinear coordinate v
$d\eta(Q)$	Width of surface ray strip at point Q (metres)

$d\psi$	Angle between backward tangents to infinitesimally separated surface rays at point Q (radians)
$d\psi_0$	Angle between infinitesimally separated surface rays at point Q' (radians)
e	Parameter in second fundamental form in differential geometry
E	Parameter in first fundamental form in differential geometry
$e^{ik\rho}$	Term describing sinusoidal dependence on distance
$e^{j\omega t}$	Term describing sinusoidal dependence on time
EM	EMI margin, the excess power above the receiver threshold sensitivity detected at the receiver front end (dB)
f	Parameter in second fundamental form in differential geometry
F	Parameter in first fundamental form in differential geometry
f_0	Transmitter fundamental frequency (Hertz); Receiver fundamental frequency (Hertz)
g	Parameter in second fundamental form in differential geometry
G	Parameter in first fundamental form in differential geometry
G_{MB}	Mainbeam gain level above isotropic of an antenna pattern (dBi)
G_R	Receiver antenna gain, relative to an isotropic antenna, in the direction of the EMI coupling path (dBi)
G_{SL}	Mean sidelobe level above isotropic of an antenna pattern (dBi)
G_X	Transmitter antenna gain, relative to an isotropic antenna, in the direction of the EMI coupling path (dBi)
$G_0(ks)$	Free space Green's function (metres^{-1})

$\vec{H}(Q\|Q')$	Asymptotic high frequency magnetic surface field at point Q due to a source current moment at Q' (Amperes/metre)
j	Imaginary unit ($j^2 = -1$)
k	Wave number (metres^{-1})
L_{cs}	Curved-surface diffraction loss factor (dB)
$m(Q)$	Quantity dependent on geodesic radius of curvature at point Q used in computation of L_{cs} (dimensionless)
$m(Q')$	Quantity dependent on geodesic radius of curvature at point Q' used in computation of L_{cs} (dimensionless)
$\vec{M}$	Magnetic current moment (Volt · metre)
n	Index of summation
$\hat{n}$	Unit normal vector at point Q
$\hat{n}'$	Unit normal vector at point Q'
num(·)	Numerator of expression within the parentheses
$O(1/ks)$	Terms in $(1/ks)$ and higher order terms
OQ_i	Straight-line segment between cone apex and point Q_i (metres)
$\overrightarrow{OQ_i'}$	Vector directed from cone apex toward point Q_i' (metres)
P	Power detected at receiver front end (dBm)
P_x	Transmitter output power (dBm)
Q	Location of observed field: Field point
Q'	Location of source field: Source point

Q_c	Point of convergence for backward tangents to infinitesimally separated surface rays at point Q
Q_t	Arbitrary point on cone surface
Q_1	Location of source field; Source point; Start point of geodesic coupling path segment
$Q_1(r_1,\theta_1,\phi_1)$	Start point of geodesic coupling path segment in spherical coordinates (metres, radians, radians)
$Q_1(\rho_1,\phi_1,z_1)$	Start point of geodesic coupling path segment in cylindrical coordinates (metres, radians, metres)
$Q_1'(X_{Q1},Y_{Q1})$	Equivalent of point Q_1 which has been mapped onto the developed cone surface (metres)
$Q_1'Q_2'$	Straight-line segment between points Q_1' and Q_2' (metres)
Q_2	Location of observed field; Field point; End point of geodesic coupling path segment
$Q_2(r_2,\theta_2,\phi_2)$	End point of geodesic coupling path segment in spherical coordinates (metres, radians, radians)
$Q_2(\rho_2,\phi_2,z_2)$	End point of geodesic coupling path segment in cylindrical coordinates (metres, radians, metres)
$Q_2'(X_{Q2},Y_{Q2})$	Equivalent of point Q_2 which has been mapped onto the developed cone surface (metres)
$\overrightarrow{Q_2'Q_1'}$	Vector directed from point Q_1 toward point Q_2 (metres)
r	Distance from cone apex to an arbitrary point on conical spiral geodesic Γ (metres)
$\vec{r}$	Vector that traces out the locus of points which defines the surface of a cone (metres)
$\mathbb{R}$	Real numbers; Real axis

r_D	Distance from cone apex to an point D on cone surface (metres)
r_1	Distance from cone apex to an arbitrary point Q_1 on cone surface (metres)
$\vec{r}'_z$	First order partial derivative of vector $\vec{r}$ with respect to z
$\vec{r}'_{zz}$	Second order partial derivative of vector $\vec{r}$ with respect to z
$\vec{r}'_{z\phi}$	Second order partial derivative of vector $\vec{r}$, first with respect to z, then with respect to ϕ
$\vec{r}'_\phi$	First order partial derivative of vector $\vec{r}$ with respect to ϕ
$\vec{r}'_{\phi z}$	Second order partial derivative of vector $\vec{r}$, first with respect to ϕ, then with respect to z
$\vec{r}'_{\phi\phi}$	Second order partial derivative of vector $\vec{r}$ with respect to ϕ
r_1	Distance from cone apex to point Q_1 on cone surface (metres)
r_2	Distance from cone apex to point Q_2 on cone surface (metres)
s	Distance measured from point Q' to point Q along the geodesic path Γ (metres); Distance measured from point Q_1 to point Q_2 along the geodesic path Γ (metres)
$\{S\}$	Sample space of all possible EMI interactions
s'	Distance measured from point Q' to an arbitrary point along the geodesic path Γ (metres)
$\{S'\}$	Sample space of critical EMI interactions
SF	Shading factor associated with the creeping wave and edge diffraction losses (dB)
S_R	Receiver threshold sensitivity (dBm)

t	Time (seconds): Variable parameter in parametric equations of a conical helix. Variable parameter in parametric equations of a straight line
$\hat{t}$	Unit tangential vector at point Q; Unit tangential vector at point Q_i
$\hat{t}'$	Unit tangential vector at point Q'
TFS	Friis free-space wave-spreading loss (dB)
T_{ij}	EMI interaction between emitter i and receptor j; Element of surface dyadic function $\ddot{T}(Q\|Q')$
T_{ij}^{c}	Critical EMI interaction between emitter i and receptor j
$(\hat{t},\hat{n},\hat{b})$	Orthonormal triad of tangent, normal, and binormal vectors at point Q
$(\hat{t}',\hat{n}',\hat{b}')$	Orthonormal triad of tangent, normal, and binormal vectors at point Q'
$\ddot{T}(Q\|Q')$	Surface dyadic function at point Q due to a source current moment at Q' (Siemens)
$\tilde{T}_{ij}$	Generalized torsion factor (dimensionless)
$U(\xi)$	Soft surface Fock integral (dimensionless)
$\tilde{U}(\xi)$	Generalized soft surface Fock integral (dimensionless)
(u,v)	Curvilinear coordinates on cone surface
$V(\xi)$	Hard surface Fock integral (dimensionless)
$\tilde{V}(\xi)$	Generalized hard surface Fock integral (dimensionless)
$W_2(\tau)$	Fock-type Airy function
$W_2'(\tau)$	Derivative of $W_2(\tau)$ with respect to τ

$X_{D'}$	X-coordinate of point D' on developed cone surface (metres)
$X_{Q1'}$	X-coordinate of point Q_1' on developed cone surface (metres)
$X_{Q2'}$	X-coordinate of point Q_2' on developed cone surface (metres)
(x,y,z)	Left-handed Cartesian coordinate system (metres)
(X,Y)	Cartesian coordinate system on developed cone surface (metres)
(X_{DIR},Y_{DIR})	Components of vector directed from point Q_1' toward point Q_2' on developed cone surface (metres)
$Y_{D'}$	Y-coordinate of point D' on developed cone surface (metres)
$Y_{Q1'}$	Y-coordinate of point Q_1' on developed cone surface (metres)
$Y_{Q2'}$	Y-coordinate of point Q_2' on developed cone surface (metres)
Y_o	Free space admittance (Siemens)
z_1	Distance of point Q_1 from cone apex in the direction along the cone axis (metres)
z_1	Distance of point Q_1 from cone apex in the direction along the cone axis (metres)
z_2	Distance of point Q_2 from cone apex in the direction along the cone axis (metres)
α	Angle between cylindrical spiral geodesic path and cylinder axial direction (radians); Angle between conical spiral geodesic path and unit vector pointing toward cone apex along cone surface (radians)
Γ	Geodesic path; Geodesic path on cone surface
Γ'	Geodesic path on developed cone surface
Γ_{ol}	Mathematical gamma function

η	Constant based on value of parameter A and used in computation of L_{cs}
θ_c	Half-cone angle (radians)
κ	Curvature of a surface (metres^{-1})
λ	Wavelength (metres)
Λ_c	Blending function which smooths the interpolation to the field solution for a canonical cylinder (dimensionless)
Λ_s	Blending function which smooths the interpolation to the field solution for a canonical sphere (dimensionless)
ξ	Fock parameter (dimensionless)
ξ'	Constant based on value of parameter A and used in computation of L_{cs}
ρ	Radius of aircraft surface along which geodesic traverses (metres); Radius of cylinder (metres); Radius of cone (metres)
ρ_g	Geodesic radius of curvature of the geodesic circle at point Q (metres)
ρ_i	Geodesic radius of curvature (metres)
ρ_1	Distance of point Q_1 from cone axis (metres)
ρ_1	Distance of point Q_1 from cone axis (metres)
ρ_2	Distance of point Q_2 from cone axis (metres)
Σ	Smooth perfectly conducting arbitrary convex surface
τ	Term to account for variation in curvature in computation of L_{cs} (dimensionless)

τ_n	Zeros of $W_2'(\tau)$; Coefficients for series representation of $V(\xi)$ for ξ small
ϕ	Angle in circumferential direction along cylinder surface (radians), Angle in circumferential direction along edge of circular cross-section of cone (radians)
ϕ_D	Angular position of point D in circumferential direction along edge of circular cross-section of cone (radians)
ϕ_{OFFSET}	Angular offset between points Q_1 and Q_2 on cone surface (radians)
ϕ'_{OFFSET}	Angular offset between points Q'_1 and Q'_2 on developed cone surface (radians)
$\phi_{Q'Q}$	Angular offset between points Q' and Q on cylinder surface (radians)
ϕ_1	Angular position of point Q_1 in circumferential direction along edge of circular cross-section of cone (radians)
ϕ_2	Angular position of point Q_2 in circumferential direction along edge of circular cross-section of cone (radians)
ω	Radial frequency (radians/second)
Ω_1	Angle between conical spiral geodesic path and unit vector pointing toward cone apex along cone surface at point Q_1 (radians)
Ω_2	Angle between conical spiral geodesic path and unit vector pointing toward cone apex along cone surface at point Q_2 (radians)
	Degrees (angular measure)
"	Inches

LIST OF ABBREVIATIONS USED

AAPG	Antenna Inter-Antenna Propagation with Graphics
AAPG V07	Antenna Inter-Antenna Propagation with Graphics Version 07
AAPG V09	Antenna Inter-Antenna Propagation with Graphics Version 09
AAPG V09A	Antenna Inter-Antenna Propagation with Graphics Version 09A
AAPG V09B	Antenna Inter-Antenna Propagation with Graphics Version 09B
AAPG V09C2	Antenna Inter-Antenna Propagation with Graphics Version 09C2
ADF	Automatic Direction Finding
AISI	Aircraft Instrumentation Subsystem Internal
ALT	Altimeter
ANT	Antenna
AZ	Azimuth angle associated with the vector tangent to the coupling path at a particular point
BL	Butt-line coordinate
CAETS	Computer Aided EMC Test-Planning System
dB	Decibel
dBi	Decibel relative to an isotropic antenna
dBm	Decibel relative to one milliwatt
deg.	Degrees
DEG	Degrees
DF	Direction Finding

DIV	Division
DME	Distance Measuring Equipment
DND	Department of National Defence
DSS	Department of Supply and Services
ECAC	Electromagnetic Compatibility Analysis Center
ECM	Electronic Counter Measures
EGA	Enhanced Graphics Adapter
EL	Elevation angle associated with the vector tangent to the coupling path at a particular point
ELT	Emergency Locator Transmitter
EMC	Electromagnetic Compatibility
EMCCS	Electromagnetic Compatibility Computation System
EMI	Electromagnetic Interference
EMPP	Electromagnetic Propagation Path
ESM	Electronic Support Measures
EST	Electronics Systems Trainer
FS	Fuselage-station coordinate
GDMS	Graphical Data Management System
GEMACS	General Electromagnetics Model for the Analysis of Complex Systems
GHz	Gigahertz
GTD	Geometrical Theory of Diffraction
HARM	Harmonic
HF	High Frequency
IAP	Intrasystem Analysis Program
IDF	Input Data File

IEEE	Institute of Electrical and Electronics Engineers
IFF	Identification Friend or Foe
ILS	Instrument Landing System
in.	Inches
MHz	Megahertz
MSDF	Mass Storage Data File
NATO	North Atlantic Treaty Organization
NAV	Navigation
NEC	Numerical Electromagnetics Code
OMNI	Omnidirectional
PPDP	Propagation Path Display Package
RCVR	Receiver
RX	Receiver
SUBSYS	Subsystem
SVGA	Super VGA
TES	Threat Emitter Simulator
TX	Transmitter
UHF	Ultra High Frequency
USAF	United States Air Force
UTD	Uniform Geometrical Theory of Diffraction
VGA	Virtual Graphics Array
VHF	Very High Frequency
VOR	VHF and Omnidirection and Radio Range
WL	Water-line coordinate
XMTR	Transmitter

2-D	Two-dimensional
3-D	Three-dimensional

CHAPTER 1

INTRODUCTION

1.1 THE NEED FOR ELECTROMAGNETIC COMPATIBILITY ANALYSIS COMPUTER CODES

Weapon systems such as military aircraft have become very sophisticated collections of electronic circuitry with great potential for complications from electromagnetic interference (EMI) [1]. In modern weapon systems, EMI interactions typically number in the thousands and their occurrence and importance are difficult to predict.

The traditional approach to addressing potential EMI problems and realizing system level electromagnetic compatibility has been to invoke a plethora of EMI specifications and standards at all levels of development, including the system, subsystem, and equipment levels. At the system level, MIL-E-6051 [2] is called out and imposes an immense responsibility and obligation on contractors to achieve and prove system level electromagnetic compatibility (EMC).

In spite of their responsibilities, prime contractors or system integrators have tended to downplay, or ignore outright, the system level principles of MIL-E-6051. Their EMC design strategies have often relied too heavily on specifications geared towards individual equipments in the hope that the different subsystems will function compatibly once combined into a complete system. When a proper EMC analysis of a system design is not performed, coupling mechanisms between individual equipments are neglected. One pitfall of such an approach is the high cost of repair and retrofit of equipments found to be electromagnetically incompatible. Another risk is the high cost of unnecessary EMC overdesign of some equipments. A proper EMC analysis may reveal that some

equipments do not require full compliance with equipment level EMI specifications in order to work compatibly in the overall system.

To address the responsibility and obligation of system level EMC, the United States Air Force (USAF) established in the early 1970's the Intrasystem Analysis Program (IAP) [1,3] as a unified, comprehensive, and systematic methodology to be applied to the EMC analysis process over the entire life cycle of a weapon system. The IAP provided a focal point toward which many independent developers of EMC analysis computer codes could direct their efforts. The outgrowth of these efforts was a considerable system level EMC analysis capability. These system level EMC analysis computer codes provided the means of establishing a detailed EMC profile or baseline for the initial design of a complex weapon system. This baseline would then serve as a point of reference for planned system upgrades, modernization programs, or other contingencies, such as the Persian Gulf mission.

The first computer codes associated with the IAP were run on mainframe computers that generated substantial amounts of tabular numerical data. These vast amounts of data tended to overwhelm the analyst and failed to provide a focus on the trends suggested by the data. This drawback was remedied with the advent in the mid-1970's of the Aircraft Inter-Antenna Propagation with Graphics (AAPG) computer code which combined sophisticated electromagnetic coupling algorithms with interactive computer graphics [4,5,6] The AAPG analysis provides detailed electromagnetic interference data which are formatted and organized in poignant fashion for further study by the user. The refinement of the algorithms of this code forms the substantial portion of this thesis.

1.2 SURVEY OF EMC ANALYSIS CODES AND THEIR APPLICATIONS

As noted above, first generation EMC analysis codes required mainframes to run properly. This requirement placed many limitations on the EMC analysis process. Mainframes were limited in availability, processing power, and memory, which in turn limited the size and complexity of data file representations of an EMC problem. Furthermore, any execution of an EMC analysis code that provided useful data required much processing time which was expensive. At that time, interactive graphics were provided by expensive dedicated graphics workstations. Hard copy outputs were provided by expensive dedicated scanning plotters.

State-of-the-art codes, on the other hand, are executed on computing hardware that is widely available and reasonably priced and has superior processing power. For example, a typical system which can run an EMC analysis code consists of a 80386 based microcomputer, a Virtual Graphics Array (VGA) or SuperVGA (SVGA) monitor, with PostScript file or hardcopy laser output. Current efforts for code update and extension include the incorporation of fuzzy logic [7] and expert systems [8] to allow EMC analysis codes to broaden the scope of their analysis capabilities.

The technical literature is rife with references that encompass the advances in the EMC analysis methodology, in numerical electromagnetic techniques associated with the Geometrical Theory of Diffraction (GTD), and in the implementations of the methodology and the techniques into sophisticated EMC analysis computer codes. Spina [1] develops a broad and extensive framework for an EMC analysis methodology. The IEEE Transactions on Electromagnetic Compatibility dedicated a special issue to a survey of numerical electromagnetic codes [9]. Siarkiewicz [10] provides an informational tutorial on the "General Electromagnetic Model for the Analysis of Complex Systems" (GEMACS) computer code developed by the USAF to accomplish a sophisticated analysis of the electromagnetic field phenomena associated with a given avionics system

Burnside et al. [11] and Gerbi and Anrò [12] describe several user-oriented computer codes that employ GTD numerical techniques in order to analyze gain patterns of antennas and EMC coupling phenomena on aircraft surfaces. Li et al. [13] examine an automated procedure which applies GTD techniques to the analysis of shipboard exterior RF communication systems. Hodes and Widmer [14] narrow the focus to a study of the aircraft antenna-to-antenna analysis and graphics display capabilities of AAPG and to the validation of these capabilities against a "real-world" test case.

The above references highlight the established acceptance of EMC analysis codes and afford the rationale for this thesis by recognizing the benefit of maintaining and upgrading those codes and of exploring viable alternative codes.

1.3 THESIS OVERVIEW

This thesis examines the status of current developments in antenna-to-antenna EMC analysis computer codes. It then investigates a number of limitations and errors in antenna-to-antenna coupling algorithms, describes algorithm improvements which were created by the author, and presents the impact of those improvements. The material is presented in a sequence structured to provide a comprehension of the background, the theory, the application, and the current state-of-the-art.

Chapter 2 examines the EMC analysis methodology and its challenges. The concept of EMI margin is introduced as a quantifying factor in determining the severity of an EMI interaction. The EMC analysis methodology, the EMI margin, and modelling considerations are then studied in the context of the Aircraft Inter-Antenna Propagation with Graphics (AAPG) computer code.

Chapter 3 focuses on the theory associated with the curved-surface diffraction loss factor used in the computation of the EMI margin. The presentation lays the framework for the general principles required in the assessment of the algorithm deficiencies in

subsequent chapters. A detailed assessment of the specific implementations of the curved-surface diffraction loss factor is deferred until Chapter 6.

Chapter 4 applies the insight gained from the derivation of the curved-surface diffraction loss factor in Chapter 3 to the examination of the deficient areas of the cone geodesic computational algorithms in AAPG Version 07 (V07). The improvements, test results, and their impact on realistic aircraft EMC problems are outlined.

Chapter 5 builds on the improvements of Chapter 4 by assessing the analogous graphics display algorithms for the cone section. The principle of one to one correspondence between the computed paths and the path which is graphically displayed is discussed. The corresponding improvements, test results, and their impact on realistic aircraft EMC problems are presented.

With the mathematical expressions derived in Chapter 3 and the satisfactory implementation and test results of the AAPG V07 algorithm improvements of Chapters 4 and 5, Chapter 6 moves to the presentation and assessment of current developments in specific implementations of the curved-surface diffraction loss factor by comparison with measurement data. The study of the expanded capabilities of computing curved-surface diffraction loss factor for arbitrarily convex cross-sections in AAPG Version 09 (V09) forms a major portion of this chapter.

Chapter 7 rounds out the theoretical and algorithmic aspects of the previous chapters with a user-directed comparative evaluation of AAPG V07 and V09. The differences in EMI margins and the relative merits of each code in the context of a "real world" test case are explored.

Chapter 8 summarizes the thesis work and highlights suggestions for future investigations in order to increase the reliability and capabilities of EMC analysis codes and to increase the user community's confidence in those tools.

1.4 THESIS' CONTRIBUTION TO THE ONGOING DEVELOPMENT OF EMC ANALYSIS COMPUTER CODES

Much of this thesis is based on continuing development work being performed at the EMC Laboratory at Concordia University under contract to the Department of Supply and Services (DSS) and the Department of National Defence (DND) Canada. As a consequence of that considerable software engineering endeavour, many deficiency reports were prepared to inform the AAPG V07 community of problem areas and limitations of the code [15]. In the majority of instances, new algorithms were designed and implemented in the code. In other instances, old algorithms were improved both in functionality and in code structure. Upon successful completion of testing of algorithm changes, eight formal change notices and new code releases were issued [15] to document the corrections made to address the previously documented deficiencies. Some of this work was presented in a paper given at the Canadian Conference on Electrical and Computer Engineering in the autumn of 1991 [16] and is elaborated further in this thesis.

AAPG V07 is the aircraft antenna-to-antenna EMC analysis code currently in use and it will continue to be used in Canada by DND and its contractors [17-19] for the immediate future. In addition, AAPG V07 is the only version currently being distributed to users in North Atlantic Treaty Organization (NATO) countries. The work of this thesis has substantially improved the AAPG V07 code by removing serious limitations in frequently encountered data sets and antenna pairs.

Parallel developments are proceeding on AAPG V09, the next generation AAPG code, at the Electromagnetic Compatibility Analysis Center (ECAC) in Annapolis, Maryland. This thesis makes some meaningful comparisons between the well-established AAPG V07 and interim releases of AAPG V09 and provides a firm base for further meaningful research.

CHAPTER 2

EMC ANALYSIS METHODOLOGY AND AAPG

2.1 INTRODUCTION

With ongoing technological developments, the number and sophistication of avionic systems on modern aircraft continue to increase the challenge of the EMC analyst's task. By considering an example such as the Electronic Systems Trainer (EST) CL-600 Challenger aircraft, which contains about 20 avionics and sensor systems and 35 antennas in a relatively small airframe, one can get an appreciation of the magnitude of the number of possible interference interactions between emitters and receptors that confront the EMC analyst [17].

This chapter examines the EMC analysis methodology and its challenges - the reduction of the possible number of interference interactions to a manageable size with the assistance of EMC analysis computer codes, and the modelling considerations of typical EMC analysis computer codes such as AAPG, which was introduced in Chapter 1.

2.2 MATHEMATICAL REPRESENTATION OF THE EMC PROBLEM

A visualization of the EMC interaction problem was put forth by Spina [1]. Mathematically, the sample space {S} of all possible interactions T_{ij} between emitters i and receptors j is represented by a massive matrix shown in Figure 2.1. The objective of an EMC analysis computer code is to cull or eliminate those matrix elements T_{ij} which are unlikely to be troublesome so that the original sample space is reduced to a critical minimum {S'}. The code must then quantify each interaction T'_{ij} in the critical sample space for further analysis and evaluation.

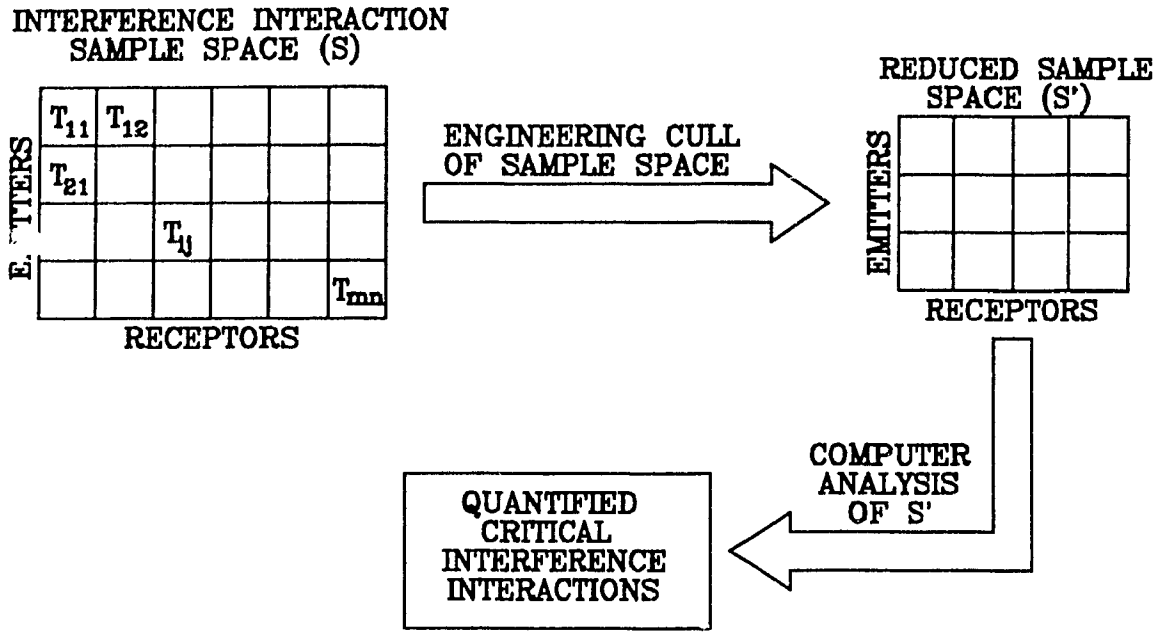

Figure 2.1. EMC analysis methodology of interference interaction sample space reduction [1].

The intrasystem EMC problem is symbolized by unwanted energy coupling from an emitter to a receptor as shown in Figure 2.2. A more accurate EMI interaction representation in Figure 2.3 illustrates that many coupling modes exist between emitter (interference source) antennas, boxes, and wires and the receptor (interference victim) counterparts. Since it is often difficult or impossible to obtain detailed quantified installation information, for example cable runs and box locations, in a timely fashion (if at all), a code such as AAPG restricts itself to the analysis of antenna-to-antenna coupling modes.

2.3 QUANTIFYING EMI INTERACTIONS AND MODELLING CONSIDERATIONS

2.3.1 EMI Margin. To quantify the interaction of the antenna-to-antenna coupling mode, a factor called the "EMI margin" is introduced. The EMI margin associated with a particular interaction is defined simply as the excess power above the receiver threshold sensitivity detected at the receiver front end and is denoted by the

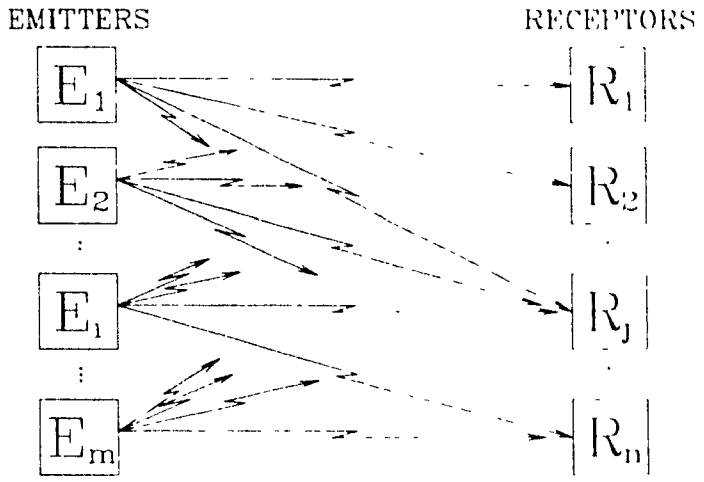

Figure 2.2. Intrasystem EMC problem [1].

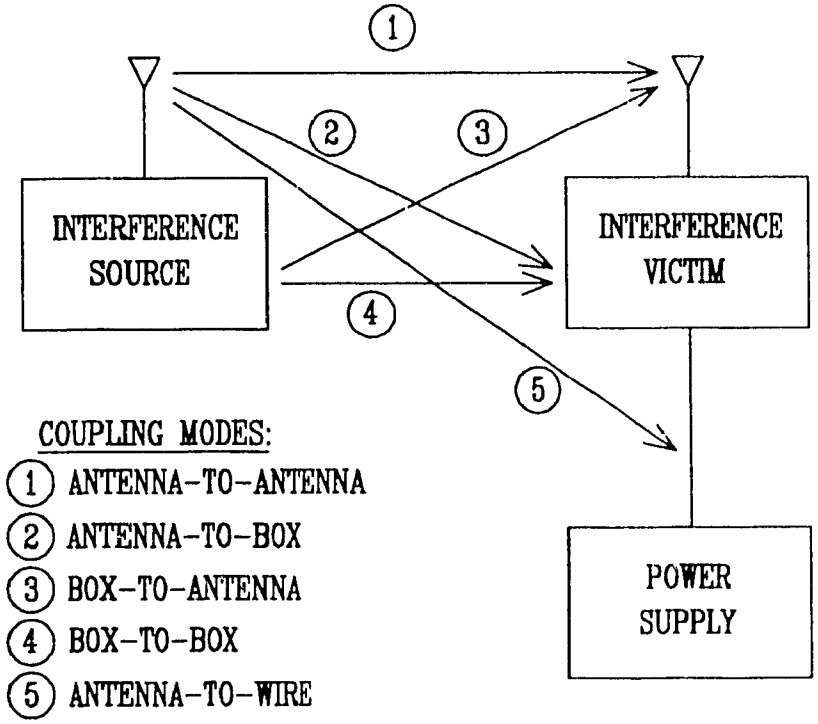

Figure 2.3. EMI coupling modes [20]

symbolic abbreviation "EM". The EMI margin can be represented mathematically, as it is in the AAPG documentation [6], by the equation

$$EM = P - S_R, \tag{2.1}$$

where EM = EMI margin in decibels (dB),

P = Power detected at receiver front end in decibels relative to 1 milliwatt (dBm),

S_R = Receiver threshold sensitivity in dBm.

The parameter P in equation (2.1) is the difference of the power output from transmitter and the losses along the propagation path between the transmitter and the receiver front end, which yields the following more detailed expression for the EMI margin

$$EM = P_X + G_X - (TFS + SF + CL_X + CL_R) - S_R + G_R. \tag{2.2}$$

The terms EM and S_R in equation (2.2) are unchanged from equation (2.1) and P_X is the transmitter output power in dBm. The sum of the terms in parentheses in equation (2.2) represents the total propagation path loss between the transmitter and receiver antennas and is broken down as

TFS = Friis free-space wave-spreading loss in dB [21],

SF = Shading factor associated with the creeping wave and edge diffraction losses in dB,

CL_X = Insertion losses in dB due to transmitter cabling and filters, and

CL_R = Insertion losses in dB due to receiver cabling and filters.

The G_X and G_R terms in equation (2.2) define the transmitter and receiver antenna gains, respectively, in dB relative to an isotropic antenna in the direction of the EMI coupling path.

The transmitter and receiver parameters in equation (2.2) are typically derived from the engineering data associated with the aircraft's avionics. An EMC analysis code then uses these input parameters along with an appropriate model of the airframe in

computing the EMI margins for the critical EMI interactions. The basic modelled parameters are explained in the sections that follow

Good engineering practice allows a safety margin of 3 dB (10 dB for explosives [2]) in equations (2.1) and (2.2) to account for equipment degradation and analysis errors That is to say, appropriate EMC design techniques are used to ensure that the power levels of any unintentional emissions are at least 3 dB below the sensitivity characteristic of any receiver. AAPG allows the user to preset this 3 dB (or any other level) threshold so that any EMI margins computed to be above this threshold are flagged as critical EMI interactions that should be analyzed further

2.3.2 Transmitter Spectrum Model The transmitter fundamental and harmonic spectrum characteristics can be modelled by means of trapezoidal variations with respect to frequency as illustrated in Figure 2.4. The transmitter spectrum model has a constant power level across the operating band and a fall-off of power for out of-band, so called "skirt", frequencies.

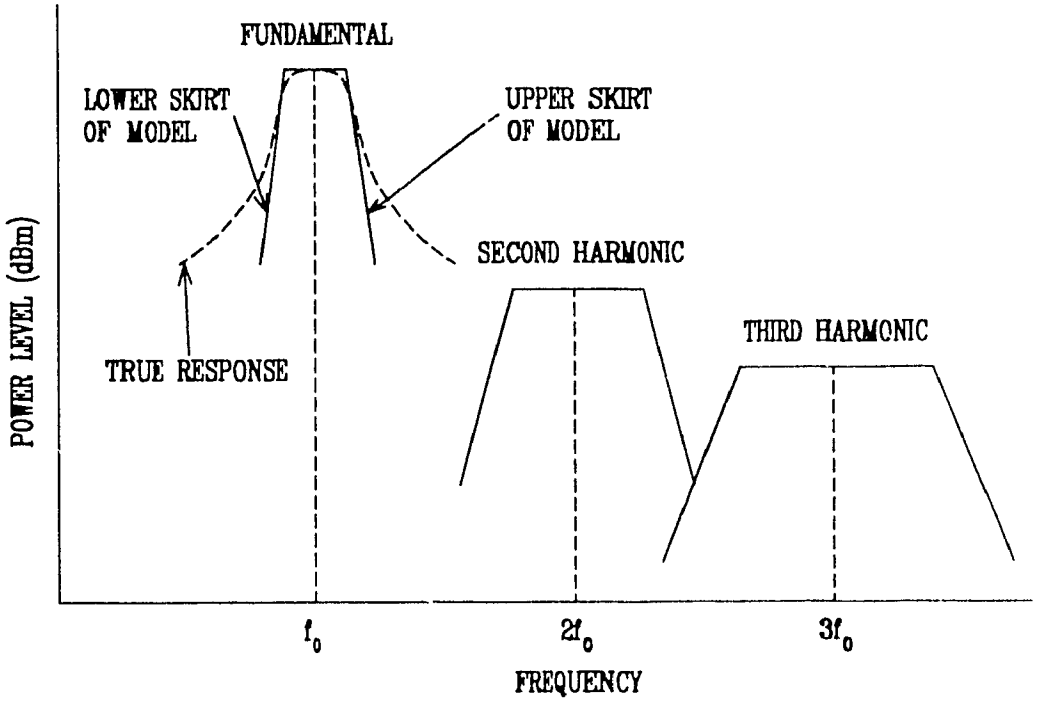

Figure 2.4. Transmitter spectrum model [6]

2.3.3 Receiver Spectrum Model. The receiver spectrum characteristics can be modelled by means of a receiver constant threshold sensitivity level across the operating band and a fall-off of sensitivity for out-of-band skirt frequencies as illustrated in Figure 2.5. Furthermore, known spurious responses can also each be incorporated as part of the receiver model. A user of AAPG, however, must model each spurious response as a separate receiver.

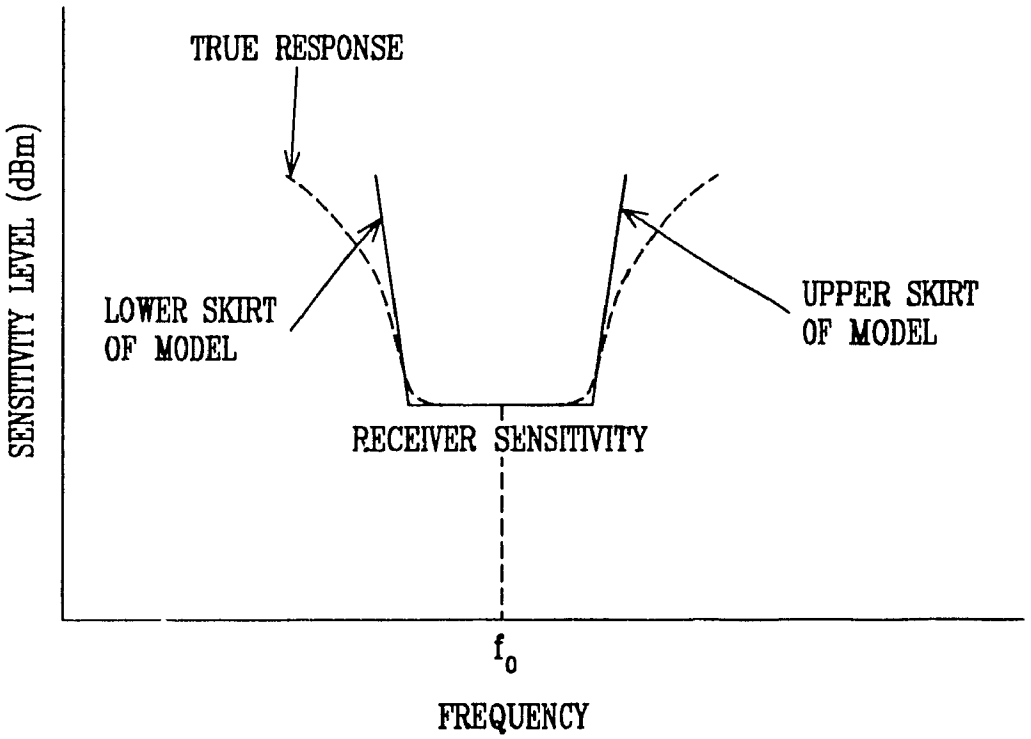

Figure 2.5. Receiver spectrum model [6].

2.3.4 Antenna Gain Pattern Model. To obtain a representative three dimensional directional antenna gain pattern, a cross-sectional cut of the pattern can be taken in two orthogonal planes. A typical algorithm to represent the method of choosing the orthogonal planes from the user input data is explained at length in the AAPG V07 and AA. .i V09 documentation [6,22]. To reduce the complexity of antenna gain pattern modelling, the polarizations of the antennas are often assumed to be oriented in a manner such that the electromagnetic coupling energy is maximized [22].

The simplest means by which an EMC analysis code models the antenna gain pattern in one of the orthogonal planes is a so-called "key-hole" pattern. The mainbeam gain level, G_{MB}, is usually taken as the actual antenna gain at the boresight and is kept constant between a beamwidth defined by the actual 3 dB drop off points, the so called "3 dB beamwidth". Outside the mainbeam, a mean sidelobe level, G_{SL}, is specified. The modelling process is illustrated in Figure 2.6(a) and is implemented in AAPG V07 [6].

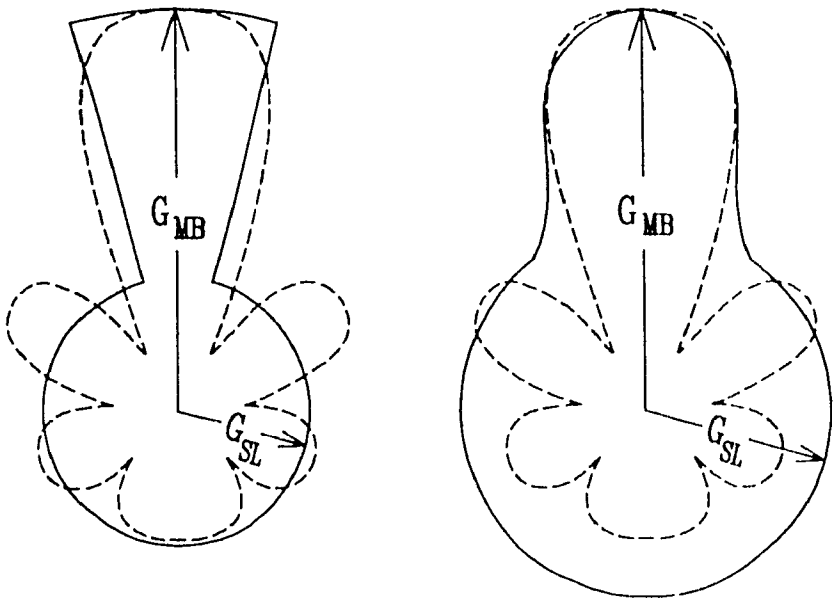

Figure 2.6. Antenna gain pattern model [22]

A more sophisticated method of representing the gain pattern of a directional antenna is to assume a Gaussian fall-off of gain from the antenna boresight. As depicted in Figure 2.6(b), the advantage of this approach is that the modelled antenna pattern is more representative of the mainbeam. The trade-off is the increased computational complexity of the $e^{-\gamma^2/\sigma^2}$ term in the Gaussian expression for the antenna gain, where γ is the angle off the antenna boresight and σ is the angle spanned by the 3 dB beamwidth. This approach is implemented in AAPG V09 [22].

2.3.5 Airframe Models. Modelling the airframe geometry is a classic exercise in engineering compromise. The model should accurately represent the real airframe so that the algorithms which compute the EMI coupling paths and EMI margins yield meaningful results. By the same token, the model should be simple enough so as to minimize algorithm complexity and, ultimately, computer run-times. Furthermore, a reasonably simple model would minimize the total time taken by an analyst in determining airframe model parameters from engineering drawings and in inputting those parameters into an appropriate data file. The practical example studied in Chapter 7 addresses these issues further.

One approach to model a full-scale airframe is to approximate the characteristic features of the airframe geometry by means of simple surfaces as illustrated in Figure 2.7. The fuselage of a fixed wing aircraft is typically modelled by means of a circular cylinder with a cone at the forward end. To accommodate a variety of realistic airframes, the cylinder/cone fuselage can be truncated along the horizontal plane. The wings and stabilizers are modelled by means of four-sided infinitesimally thin flat plates. This approach is implemented in AAPG V07 [6].

The aircraft is described in terms of the manufacturer-specified butt-line (BL), water-line (WL), and fuselage-station (FS) coordinate system. A typical location for the origin of the (BL,WL,FS) coordinate system is illustrated in Figure 2.7.

An increased level of sophistication in modelling the fuselage of the airframe has been introduced by AAPG V09 [22]. The fuselage is modelled by means of a cylinder of arbitrary convex cross-section with a cone at each end of the cylinder. The user specifies a number of points along the cross-section of the airframe. The algorithms in AAPG V09 then compute the coefficients of piece-wise cubic splines which in turn define any point along the cross-section of the airframe. Also, the cones at either end have the same cross-section as the cylinder and can be tilted individually.

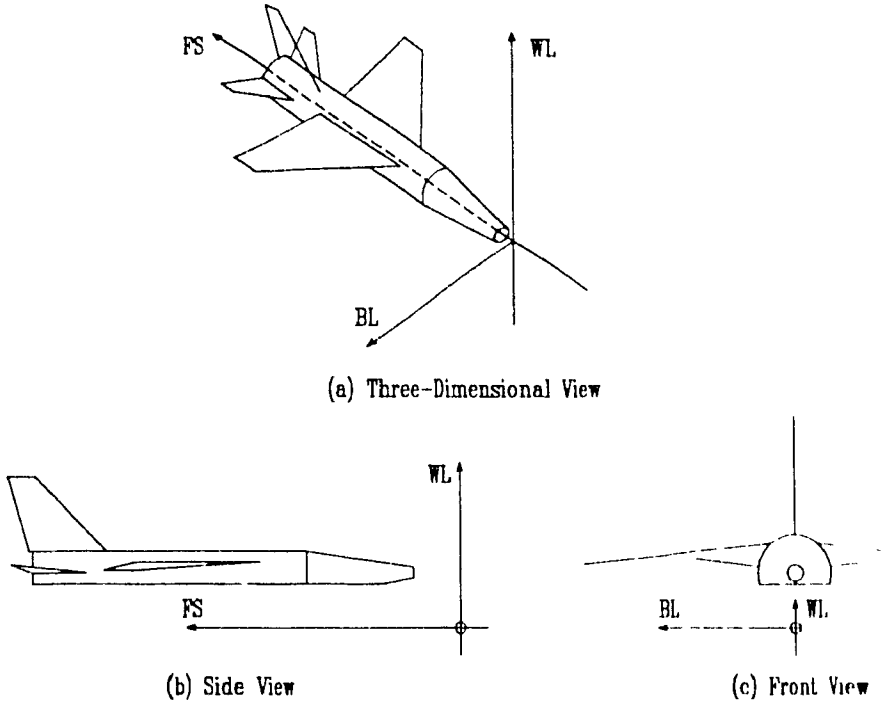

Figure 2.7. Three views of a typical airframe model [6]

As stated earlier, the trade-off of the increased level of modelling sophistication in AAPG V09 is the increased burden on the user in specifying the airframe model parameters as well as an increased complexity required in computing EMI coupling paths and EMI margins.

2.3.6 Typical EMI Coupling Paths. Given that an EMI interaction exists in the frequency domain between a transmitting system and a receiving system on a particular model of an airframe (which is assumed to be perfectly conductive), the correct modelling of the EMI coupling path has a direct bearing on the computation of the EMI margin. Regardless of the airframe model, two types of EMI coupling paths should be considered by an intrasystem EMI computer code: direct coupling paths and paths which are obstructed by the airframe.

Figure 2.8 illustrates, in increasing order of complexity, the types of EMI coupling paths typically computed by an intrasystem EMC analysis code. Figure 2.8(a) illustrates the direct path between two antennas which are obviously in line-of-sight of each other. The EMI margin is computed in accordance with Friis free-space wave-spreading loss formula [21] assuming that the receive antenna is in the far-field of the transmit antenna.

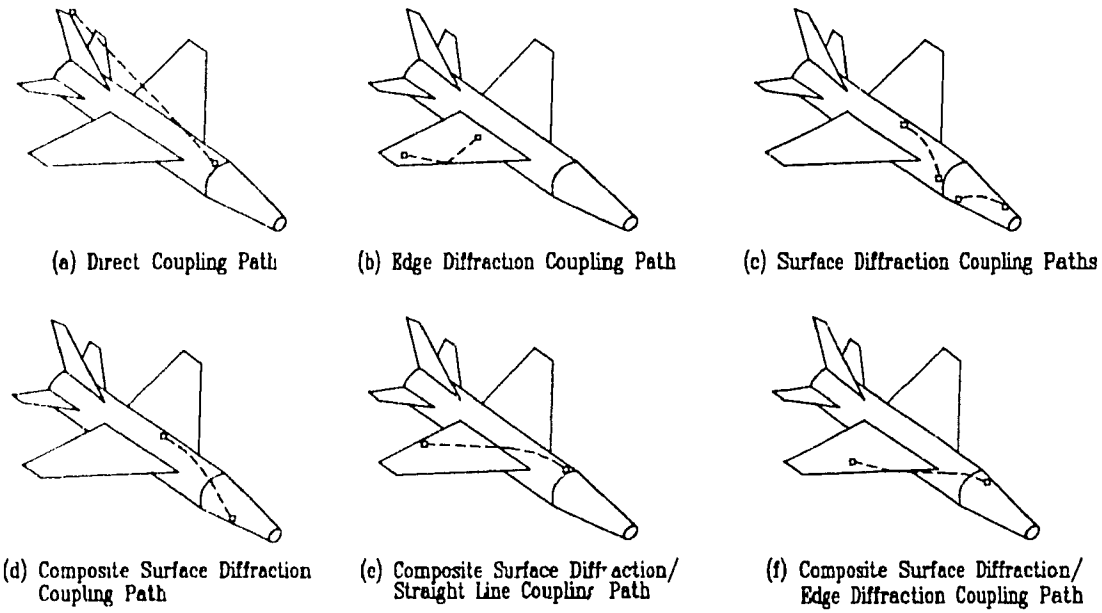

Figure 2.8. Typical EMI coupling paths computed by intrasystem EMC analysis codes.

Figure 2.8(b) shows an elementary edge diffraction coupling path in which the antennas are situated on opposite sides of an aircraft wing. The EMI coupling path proceeds from the transmit antenna to the receive antenna by way of a diffraction point on the forward edge of the aircraft wing. The EMI margin is then computed in accordance with the knife-edge diffraction loss formula [23] assuming that the thickness of the wing edge is electrically small.

Figure 2.8(c) shows two examples of an elementary surface diffraction coupling path in which the antennas are situated on the surface of fuselage and are not in line-of-sight due to the curvature of the fuselage. The EMI coupling path proceeds from the transmit antenna to the receive antenna along a cylindrical spiral on the main body of the fuselage or along a conical spiral on the nose section of the fuselage [24]. The EMI margin is then computed in accordance with the surface diffraction loss formula [25] assuming that the radius of curvature of the fuselage surface is electrically large.

To be of value to the EMC analyst, an intrasystem EMC code should accommodate composite paths and be able to compute the cumulative effects of edge diffraction, surface diffraction, and free-space wave-spreading losses on the EMI margin. Figures 2.8(d) through (f) illustrate various representative composite paths that are typically modelled by AAPG.

2.4 OVERVIEW OF AAPG AS AN EMC ANALYSIS COMPUTER CODE

A practical computer program used for aircraft antenna-to-antenna EMC analysis which incorporates many of the modelling features discussed in section 2.3 is the Aircraft Inter-Antenna Propagation with Graphics, Version 07 (AAPG V07), code. The basic AAPG V07 structure is shown in the functional diagram of Figure 2.9.

The user starts an EMC analysis in AAPG by specifying various aircraft, transmitter, receiver and antenna parameters that were discussed in section 2.3 and then by inputting those parameters to the Input Data File (IDF).

The Electromagnetic Compatibility Computation System (EMCCS) of the AAPG software uses the frequency and harmonic data from the IDF to determine the transmitter/receiver pairs which are frequency coincident and which could produce EMI. The EMCCS then applies sophisticated analytical and geometrical algorithms, which are based on principles from the Uniform Geometrical Theory of Diffraction (UTD), to

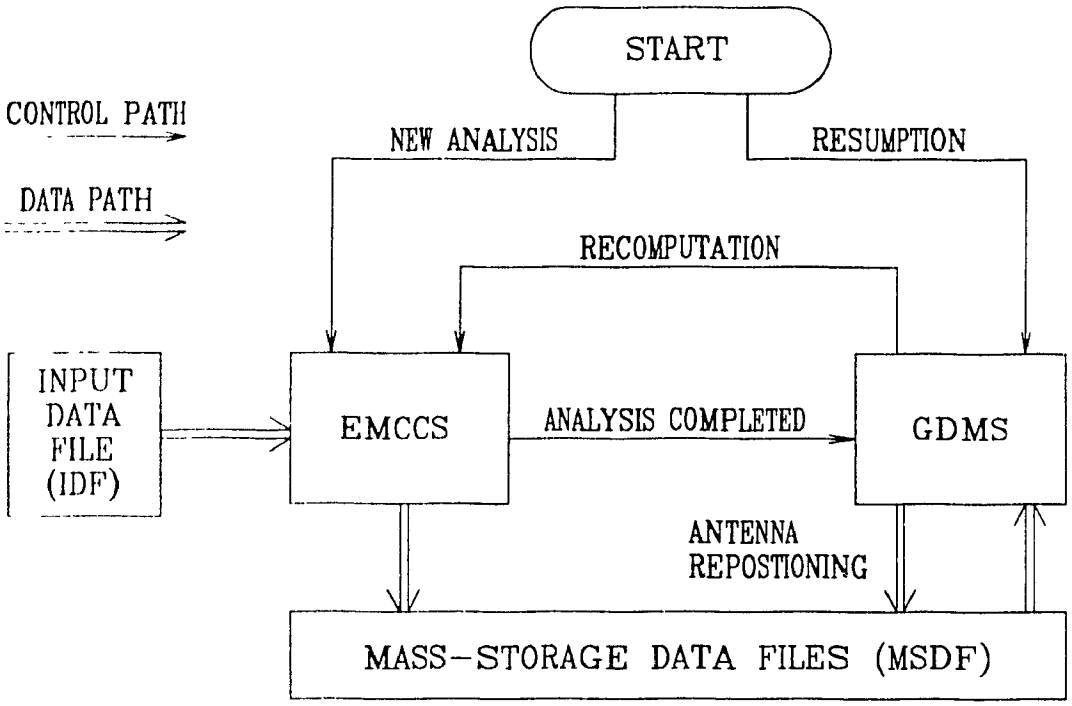

Figure 2.9. Basic AAPG structure [6].

calculate the geodesic coupling paths between the antennas associated with the frequency coincident transmitter/receiver pairs and the coupling losses along the path.

The EMCCS component of AAPG implements the EMC analysis methodology that was described in section 2.2 and was illustrated in Figure 2.1. The EMCCS computes the interference interaction sample space, {S}, from the user-defined IDF using the criterion of frequency coincidence. This sample space {S} is quickly reduced to a critical minimum sample space, {S'}, by flagging those interactions whose EMI margins are greater than some user-specified threshold. Once the EMCCS has completed its computations, control is passed to the GDMS.

The Graphical Data Management System (GDMS) of the AAPG software serves as an intuitive interactive interface between the AAPG program and the user. As illustrated in Figure 2.10, the GDMS is menu-driven and allows the user to pursue a more detailed investigation of each EMI interaction computed by the EMCCS. The top-level

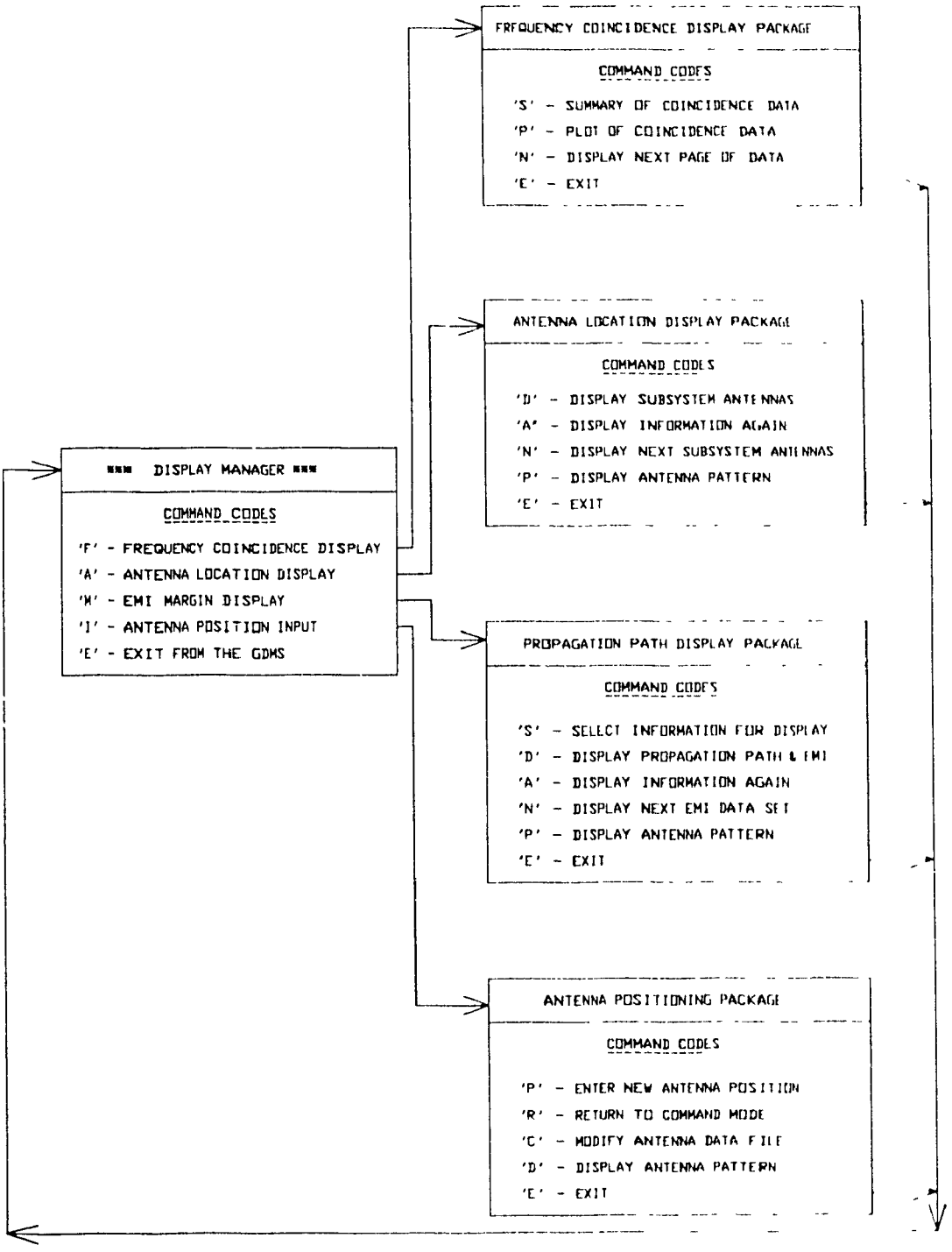

Figure 2.10. AAPG GDMS menu structure [6]

Display Manager menu provides access to four packages whose titles and menu options shed light on their functionality.

Among many of the GDMS's capabilities, the Propagation Path Display Package (PPDP) allows the user to display, in a highly formatted way, numerical results from the EMCCS analysis stored in the Mass-Storage Data Files (MSDF), e.g. the path losses. To complement the numerical display, the PPDP allows the user to examine graphical one-to-one representations of the numerical results, e.g. the modelled EMI coupling path which corresponds to the computed EMI margin. A typical example of such a PPDP display is illustrated in Figure 2.11 and is known as the EMI Margin and Propagation Path Display. All of the GDMS displays are presented in great detail in the AAPG documentation [6,25]

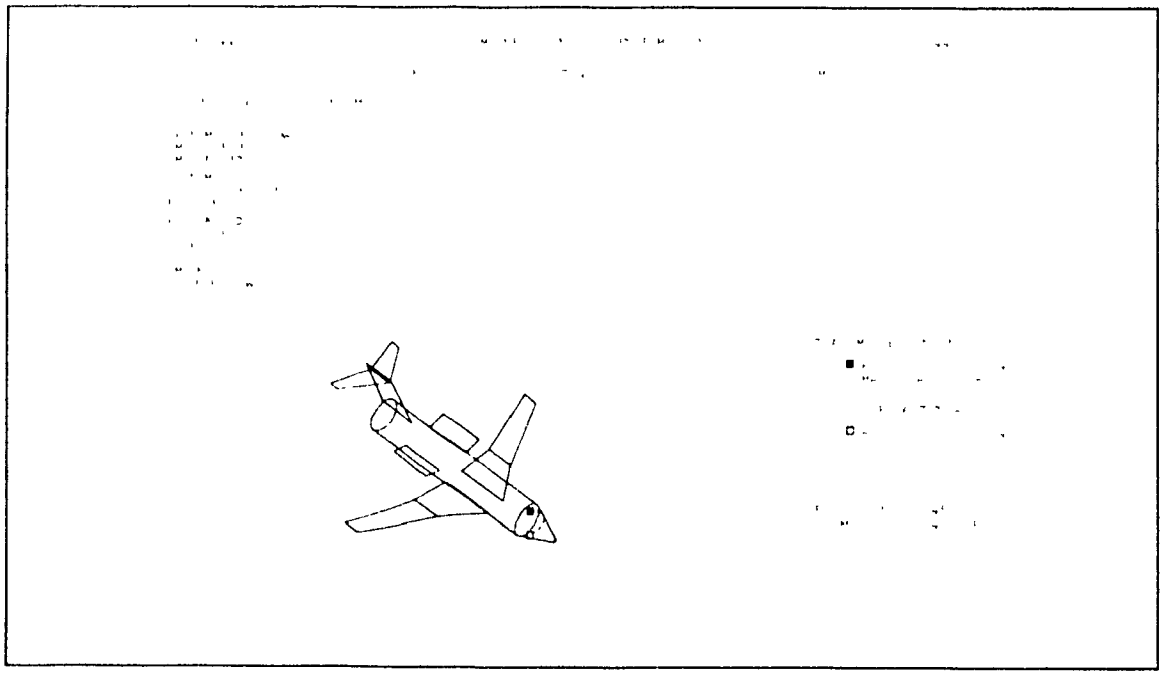

Figure 2.11. Typical EMI Margin and Propagation Path Display [25].

2.5 ASSUMPTIONS, LIMITATIONS, AND PROBLEM AREAS OF AAPG

The AAPG program can be employed to model the geometry of a wide variety of aircraft [22]. Although the AAPG documentation provides some guidelines to assist in modelling an aircraft [22], no established methodology exists in AAPG. In order to obtain meaningful analysis results, the user must employ his ingenuity, his intuition, and his technical understanding of the AAPG algorithms. The user's grasp of the assumptions, the limitations, and the problem areas within the AAPG code is essential. Once the peculiarities of an EMC systems analysis code such as AAPG are understood, the approaches recently suggested by Boston and Bowman [26] can be used to work within the limitations of that code.

2.5.1 Assumptions and Limitations. Before an analyst makes use of an EMC modelling code such as AAPG, he must be aware of the built-in "a priori" assumptions and limitations of that code. The modelling considerations which have been discussed at length in the previous sections are a primary concern of the AAPG user. The AAPG user's and technical manuals [6,25] document many other a priori assumptions and limitations, the details of which are beyond the scope of this thesis.

Concerns of a lesser nature are the general limitations on maximum allowable number of modelled electronics systems, transmitters, receivers, and antennas per input data file [6]. Historically, these limitations were built into the AAPG software in the late 1970's primarily because of the nature of the worst-case aircraft, and to a lesser extent because of the relatively low level of computing power and the high expense of computing resources at that time [1]. In practice, these AAPG limitations have not hindered the EMC analyst in his modelling task.

2.5.2 Problem Areas. A good appreciation of the basic capabilities of an EMC analysis code such as AAPG can be acquired directly through hands on experience

Seasoned users and developers of EMC analysis codes soon acquire an in-depth knowledge of the code's subtleties and of deficiencies that are not immediately obvious to the neophyte.

In keeping with good software engineering practice, the AAPG code developer is obliged to keep the user community informed of known code deficiencies through the issue of deficiency reports. Deficiencies are fixed and software configuration control is maintained through the issue of change notices which document and release code updates.

To illustrate this process, extensive use of the AAPG code and analysis of its algorithms in the EMCCS and GDMS have revealed certain particularly serious deficiencies in the computation and display of geodesics. These deficiencies have been documented [15] for the cases in which the antennas associated with the frequency coincident transmitter/receiver pairs are located on or near the frustrum cone model of the aircraft's nose. The recent improvements to remedy the deficiencies in the EMCCS and GDMS modules of the AAPG code and their impact on realistic aircraft EMC problems have also been documented [15] and are examined further in Chapters 4 and 5.

2.6 FINAL REMARKS

For the moment, the detailed presentations of the deficient areas in the AAPG cone geodesic computation and display algorithms are set aside until Chapters 4 and 5. The next chapter focuses on the theory associated with the curved-surface diffraction loss factor alluded to in the expression for the EMI margin of equation (2.2). The presentation of Chapter 3 lays the framework for the general principles required in the assessment of the cone geodesic algorithm deficiencies in subsequent chapters.

CHAPTER 3

CURVED-SURFACE DIFFRACTION LOSS THEORY

3.1 INTRODUCTION

The relatively simplistic fuselage modelling capability of AAPG, as discussed in Chapter 2, does not detract from the challenge of implementing accurate, yet concisely expressed, algorithms to calculate the curved-surface diffraction loss along the fuselage of an aircraft. In this chapter, the theoretical basis of the curved-surface diffraction loss factor, which was introduced as the creeping wave contribution to the SI parameter in equation (2.2), is examined and developed. The presentation gives an appreciation of the numerical values under many circumstances of EMC analysis.

In addition to the accuracy of the implemented algorithms, software engineering issues such as code maturity and reliability are also motivations for this study. On the one hand, although the theoretical principles behind AAPG V09 are sound, the summary at the end of Chapter 7 reveals some "teething" problems with this new code. On the other hand, although some relatively crude approximations, as compared to AAPG V09, were made in the AAPG V07 implementation of the curved-surface diffraction loss factor, AAPG V07 remains, in all other respects, a reliable tool which has matured through extensive use throughout the military EMC analysis community over the past dozen or so years. Therefore, another objective of this chapter is to develop an expression for the curved-surface diffraction loss factor suitable for incorporation into AAPG V07 without upsetting the code's reliability.

Since the development of the curved-surface diffraction loss factor is involved, this chapter presents only an overview of that development. A brief summary of the development is now appropriate. The presentation starts with the introduction of the UTD

coupling solution for the field on the surface of a smooth perfectly conducting arbitrary convex surface due to an appropriate source configuration. The resulting field expressions give rise to a general curved-surface diffraction loss factor that has been implemented in the AAPG V09 code by using sophisticated numerical integration techniques.

The application of the general curved-surface diffraction loss factor is reviewed by Hasserjian and Ishimaru [27] for the case of the canonical cylinder and by Lee [28,29], Golden et al. [30], and Chan et al. [31] for the case of the canonical cone. These reviews provide the basis for the closed form expressions for the curved-surface diffraction factor associated with coupling paths along cylindrical and conical surfaces. The resultant closed form expressions are as accurate as those in AAPG V09, are simple and easy to implement into a code such as AAPG V07, but are limited in their applicability. In spite of their limited applicability, the closed form expressions serve to enhance the capabilities of the already reliable and mature AAPG V07 code. Implementation details of the curved surface diffraction loss factor algorithms are deferred until Chapter 6.

3.2 SURFACE FIELD DUE TO A SOURCE ON A SMOOTH PERFECTLY CONDUCTING ARBITRARY CONVEX SURFACE

The UTD coupling solution for a smooth perfectly conducting arbitrary convex surface is developed by Pathak and Wang [32] by generalizing the asymptotic solutions for the canonical problems of the sphere and cylinder. The asymptotic nature of the solutions presupposes that the distances considered in the development are much larger than the wavelength of the source field. The explicit expressions they derive are for the asymptotic surface fields due to an infinitesimal electric or magnetic current moment on a perfectly conducting sphere and cylinder.

In this section, starting with the general field expressions for the arbitrary convex surface, the development of the approximate asymptotic field expressions is presented in order to facilitate the implementation of the curved-surface diffraction loss factor in an

EMC analysis code such as AAPG. It should be noted that although the magnetic field due to a magnetic current moment is considered here, the fields due to an electric current moment, as well as the boundary conditions and asymptotic approximations for the electric field, lead to the same curved-surface diffraction loss factor [32]

Consider a magnetic current moment $\vec{M}$ tangential to a smooth perfectly conducting arbitrary convex surface Σ at source point Q' as shown in Figure 3.1. The

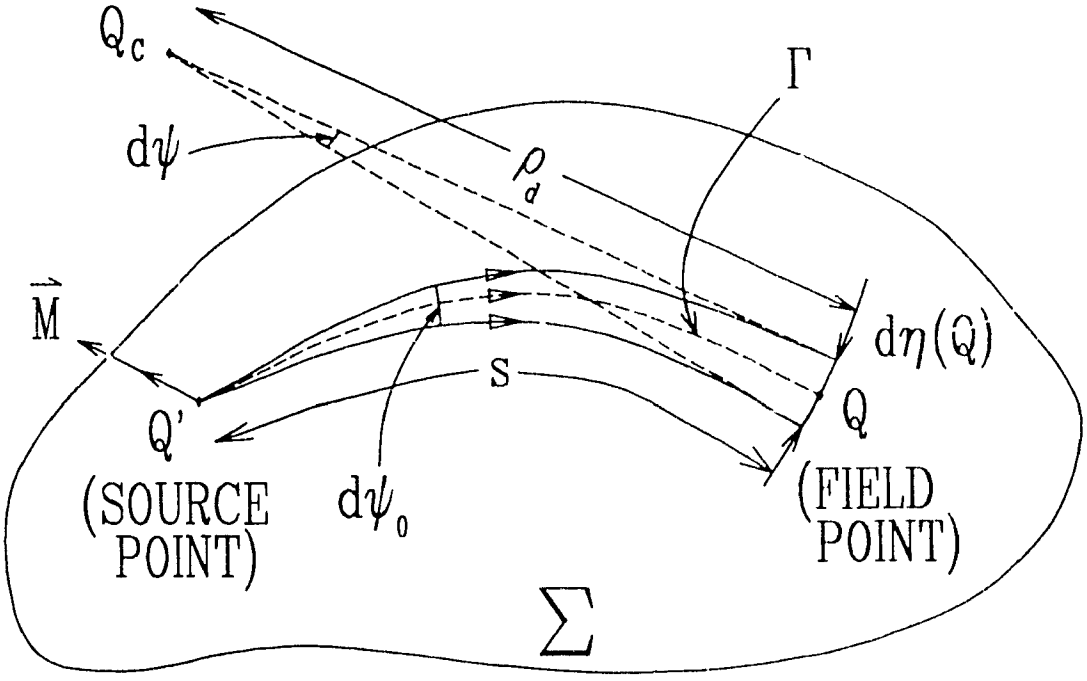

Figure 3.1. Geometry of surface ray strip [32]

symbol $\vec{H}(Q|Q')$ denotes the asymptotic high frequency magnetic surface field at observation point Q, also on surface Σ, due to the source current moment at Q' and may be expressed by the equation

$$\vec{H}(Q,Q') = -\frac{jk}{4\pi}\vec{M}\cdot\ddot{T}(Q|Q')\,D G_0(ks)\,, \tag{3.1}$$

where $\ddot{T}(Q|Q')$ and D are defined below. k is the wave number, s is the length of the geodesic path Γ between Q' and Q, and $G_0(ks)$ is the free space Green's function given by

$$G_0(ks) = \frac{e^{-jks}}{s}, \tag{3.2}$$

with an implied $e^{j\omega t}$ dependence of $\vec{H}(Q|Q')$ on time t. The geodesic path is defined to be the shortest arc between two points on a general surface [24].

The surface ray divergence factor D in (3.1) describes the variation of the surface field resulting from the change in the width of the surface ray strip or tube, which is shown in Figure 3.1, and is given by

$$D = \sqrt{\frac{s\, d\psi_0}{d\eta\,(Q)}} \tag{3.3a}$$

where

$$d\eta\,(Q) = \rho_d\, d\psi\,. \tag{3.3b}$$

The surface dyadic function $\ddot{T}(Q|Q')$ in (3.1) describes the launching of the surface ray field at Q', the variation of the surface ray field between Q' and Q due to surface diffraction, and the attachment of the surface ray field at Q and is given by the equation from reference [32] as

$$\begin{aligned}\ddot{T}(Q|Q') = \quad & T_{11}\,\hat{t}'\hat{t} + T_{12}\,\hat{t}'\hat{n} + T_{13}\,\hat{t}'\hat{b} \\ & + T_{21}\,\hat{n}'\hat{t} + T_{22}\,\hat{n}'\hat{n} + T_{23}\,\hat{n}'\hat{b} \\ & + T_{31}\,\hat{b}'\hat{t} + T_{32}\,\hat{b}'\hat{n} + T_{33}\,\hat{b}'\hat{b}.\end{aligned} \tag{3.4}$$

In (3.4) above, the surface ray-fixed coordinate systems at Q' and Q are expressed in terms of orthogonal triads of unit tangent, normal, and binormal vectors, $(\hat{t}',\hat{n}',\hat{b}')$ for Q' and $(\hat{t},\hat{n},\hat{b})$ for Q as shown in Figure 3.2. The surface dyadic function $\ddot{T}(Q|Q')$ is a tensor quantity in which a term such as $T_{11}\hat{t}'\hat{t}$ denotes a weighting factor of T_{11} contributed by the $\hat{t}'$-component of the magnetic current moment vector, $\vec{M}$, which is located at point Q', to the $\hat{t}$-component of the magnetic field vector $\vec{H}$, which is observed at point Q. It can be shown that some of the terms of $\ddot{T}(Q|Q')$ in (3.4) vanish due to the boundary conditions on the perfectly conducting surface [32].

$$\hat{n}' \cdot \ddot{T}(Q|Q') = 0 \tag{3.5a}$$

and $$\ddot{T}(Q|Q') \cdot \hat{n} = 0 . \tag{3.5b}$$

The dominant behaviour of an element T_{η} in the surface dyadic function in (3.4) may be represented asymptotically as an infinite series, which in turn can be expressed [32] in terms of the Fock integrals $U(\xi)$ and $V(\xi)$.

$$U(\xi) \equiv \frac{\xi^{3/2}\, e^{j\frac{\pi}{4}}}{\sqrt{\pi}} \left[\int_{\infty e^{j2\pi/3}}^{0} d\tau \; \frac{W_2'(\tau)}{W_2(\tau)} \; e^{j\xi\tau} \right] \tag{3.6}$$

and $$V(\xi) \equiv \frac{\xi^{1/2}\, e^{j\frac{\pi}{4}}}{2\sqrt{\pi}} \left[\int_{\infty e^{j2\pi/3}}^{0} d\tau \; \frac{W_2(\tau)}{W_2'(\tau)} \; e^{j\xi\tau} \right]. \tag{3.7}$$

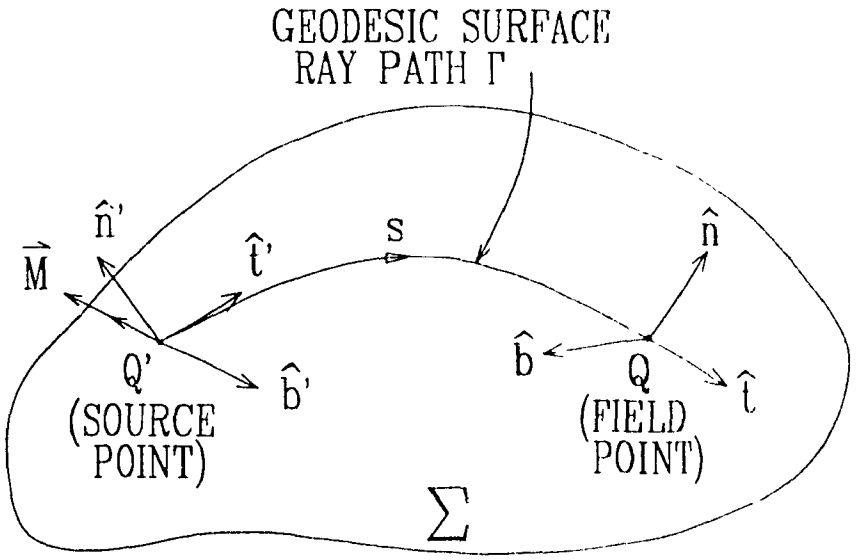

Figure 3.2. Surface ray-fixed coordinate systems [32].

The lower and upper limits of the integral, with respect to the complex ($\mathbb{C}$) variable τ in (3.6) and (3.7) represent an integration contour in the complex plane which goes from ∞ to 0 along the line whose argument is $-2\pi/3$ radians and which continues from 0 to ∞ along the real ($\mathbb{R}$) axis [33]. The function $W_2'(\tau)$ in (3.6) and (3.7) is the derivative of $W_2(\tau)$ with respect to τ, where $W_2(\tau)$ is the Fock-type Airy function [34] defined by the complex integral

$$W_y(\tau) \equiv \frac{1}{\sqrt{\pi}} \left[\int_{e^{-j2\pi/3}\infty} dZ\ e^{\tau Z - Z^3/3} \right]. \tag{3.8}$$

The generalized Fock parameter ξ in (3.6) and (3.7) is a key element in the computation of the curved-surface diffraction loss factor. For an arbitrary convex surface, the Fock parameter is expressed as a path integral from source point Q' to field point Q along the geodesic path Γ with

$$\xi = \int_{\substack{Q' \\ along\ \Gamma}}^{Q} ds' \frac{m(s')}{\rho_g(s')}, \tag{3.9a}$$

where

$$m(s') = \left[\frac{k\rho_g(s')}{2} \right]^{1/3} \tag{3.9b}$$

and $\rho_g(s')$ is the radius of curvature at point s' on the geodesic path Γ. Substituting (3.9b) into (3.9a), the Fock parameter ξ along the path Γ on surface Σ is given by

$$\xi = \left(\frac{k}{2}\right)^{1/3} \int_{\substack{Q' \\ along\ \Gamma}}^{Q} \frac{ds'}{[\rho_g(s')]^{2/3}} . \tag{3.10}$$

Using the simplifying expressions in (3.5), the following explicit expression for the surface magnetic field $\vec{H}(Q|Q')$ in (3.1) is obtained,

$$\begin{aligned} \vec{H}(Q|Q') = & -\frac{jk}{4\pi}\vec{M} \\ & \cdot \left\{ 2Y_0 \left(\hat{b}'\hat{b} \left[\left(1 - \frac{j}{ks}\right) \tilde{V}(\xi) + D^2 \left(\frac{j}{ks}\right)^2 (\Lambda_s \tilde{U}(\xi) + \Lambda_c \tilde{V}(\xi)) \right. \right. \right. \\ & \left. + \tilde{T}_0^2 \frac{j}{ks} (\tilde{U}(\xi) - \tilde{V}(\xi)) \right] \\ & + \hat{t}'\hat{t} \left[D^2 \frac{j}{ks} \tilde{V}(\xi) + \frac{j}{ks} \tilde{U}(\xi) - 2 \left(\frac{j}{ks} \right)^2 (\Lambda_s \tilde{U}(\xi) + \Lambda_c \tilde{V}(\xi)) \right] \\ & \left. \left. + (\hat{t}'\hat{b} + \hat{b}'\hat{t}) \left[\frac{j}{ks} \tilde{T}_0 (\tilde{U}(\xi) - \tilde{V}(\xi)) \right] \right) \right\} DG_0(ks), \end{aligned} \tag{3.11}$$

where Y_0 is the free space admittance. An expression similar to (3.11) is also derived by Lee [28]. The generalized Fock integrals $U(\xi)$ and $V(\xi)$ in (3.11) are given by

$$\tilde{U}(\xi) = \left[\frac{ks}{2\,m(Q')\,m(Q)\,\xi}\right]^{1/2} U(\xi), \tag{3.12a}$$

$$\tilde{V}(\xi) = \left[\frac{ks}{2\,m(Q')\,m(Q)\,\xi}\right]^{1/2} V(\xi), \tag{3.12b}$$

where m(Q') and m(Q) correspond to the parameter in (3.9b) evaluated at the source point Q' and at the field point Q, respectively, and U(ξ) and V(ξ) are defined in (3.6) and (3.7). The Λ_s and Λ_t terms in (3.11) are introduced heuristically to ensure a smooth transition between the canonical cylinder and sphere solutions to terms in $(1/ks)^3$. The generalized torsion factor $\tilde{T}_0$ in (3.11) accounts for the attenuation of the field due to the surface ray torsion, i.e. the measure of the rate at which the coupling ray curve twists out of the plane defined by the tangent and the normal to the curve.

Consider the lowest-order term in the expression for the surface magnetic field $\vec{H}(Q|Q')$ in (3.11) as

$$\vec{H}(Q|Q') = -\frac{jk}{4\pi}\vec{M}\cdot\left\{2Y_0\left(\hat{b}'\hat{b}\left[\tilde{V}(\xi) + O\left(\frac{1}{ks}\right)\right] + O\left(\frac{1}{ks}\right)\right)\right\} D\,G_0(ks), \tag{3.13}$$

where O(1/ks) denotes a polynomial in powers of (1/ks) in which the (1/ks) term is dominant. Ignoring the O(1/ks) and higher order terms and substituting (3.12b) and (3.2) into (3.13), the approximate expression for the surface magnetic field $\vec{H}(Q|Q')$ to be considered for use in AAPG's calculation of the curved-surface diffraction loss factor is obtained from reference [35] as

$$\begin{aligned}\vec{H}(Q|Q') &= (\vec{M}\cdot\hat{b}')\,\tilde{V}(\xi)\,D\left[-\frac{jkY_0}{2\pi}\,G_0(ks)\right]\hat{b} \\ &= (\vec{M}\cdot\hat{b}')\left[\frac{ks}{2m(Q')\,m(Q)\,\xi}\right]^{1/2} V(\xi)\,D\,G(s)\,\hat{b}.\end{aligned} \tag{3.14}$$

where G(s) is defined by

$$G(s) = -\frac{jkY_0}{2\pi} G_0(ks)$$

$$= \frac{k^2 Y_0}{2\pi j} \frac{e^{-jks}}{ks} . \qquad (3.15)$$

3.3 CURVED-SURFACE DIFFRACTION LOSS FACTOR FOR COUPLING PATHS ON A CYLINDER OR CONE OF ARBITRARY CONVEX CROSS-SECTION

To obtain the maximum coupled field from the expression in (3.14), it is necessary to make two assumptions about the polarization of the source current moment $\vec{M}$ at Q' and of an antenna which detects the field at Q: $\vec{M}$ is oriented parallel to binormal vector $\hat{b}'$ at Q' and the antenna detecting the field is polarized parallel to binormal vector $\hat{b}$ at Q (see Figure 3.2). Polarization issues have been studied in much greater detail by Bhattacharyya and Kubina [36].

Further examination of (3.14) determines that the field due to a magnetic current moment on a smooth perfectly conducting arbitrary convex surface can be expressed as the product of the field due to the same source at the same distance on a flat ground plane and an attenuation factor to account for the curvature of the coupling path.

The factor G(s) in (3.14) and (3.15) represents the asymptotic behaviour of the field due to the magnetic current moment as if it were located on a perfectly conducting ground plane. The attenuation factor, in decibels, which accounts for the curved-surface diffraction loss, is then defined from the remaining terms in (3.14) as

$$L_{cs} = 20 \log \left(D \, |V(\xi)| \left[\frac{ks}{2m(Q')m(Q)\xi} \right]^{\frac{1}{2}} \right)$$

$$= 20 \log(|V(\xi)|) + 20 \log \left(\frac{ks}{2m(Q')m(Q)\xi} \right)^{\frac{1}{2}} . \qquad (3.16)$$

Note that since the surfaces modelled by AAPG are developable (see section 5.4), the surface ray divergence factor D equals one (see (3.3)) and is therefore omitted from

(3.16). The Fock integral V(ξ) in (3.7) is a complex quantity that can be represented by the infinite series expressions [27,33,37]

$$V(\xi) = \begin{cases} e^{-j\pi/4}\sqrt{\pi}\ \xi^{1/2} \sum_{n=1}^{\infty} (\tau_n')\ e^{j\xi\tau_n'}, & \text{for } \xi \text{ large.} \quad (3.17a) \\ -\sqrt{\pi} \sum_{n=0}^{\infty} B_n \frac{\left[e^{j\pi/4}\ \xi^{1/2}\right]^n}{\Gamma_{GI}\left(\frac{3n+1}{2}\right)}, & \text{for } \xi \text{ small.} \quad (3.17b) \end{cases}$$

where the coefficients τ_n' are the zeros of $W_2'(\tau)$ (see (3.8)), the coefficients B_n are described by Logan [37], and Γ_{GI} is the mathematical gamma function [34]. Instead of using the cumbersome equations for V(ξ) in (3.17), the 20 log|V(ξ)| term in (3.16) is approximated by a much simpler expression in the AAPG implementation of the curved surface diffraction loss L_{CS}. The expression is given as

$$L_{CS} = -\frac{A}{\eta A + \xi'} + 20 \log\left(\frac{ks}{2m(Q')\, m(Q)\, \xi}\right)^{\frac{1}{2}} \quad (3.18)$$

where

$$A = \sqrt{2}\ \xi^{3/2}, \quad (3.19a)$$

$$\eta = \begin{cases} 0.005478 & \text{for } A < 26 \\ 0.003340 & \text{for } A \geq 26 \end{cases}, \quad (3.19b)$$

and

$$\xi' = \begin{cases} 0.5083 & \text{for } A < 26 \\ 0.5621 & \text{for } A \geq 26 \end{cases}. \quad (3.19c)$$

As plotted in Figure 3.3, there is excellent agreement (to within 1 dB) between the solid curve of 20 log|V(ξ)| and the dashed curve of -A/(η A + ξ') for values of ξ below 16. For values of ξ above 16, the -A/(η A + ξ') approximation predicts a smaller curved-surface shading loss (or larger coupling gain) than 20 log|V(ξ)|. This fact is little cause for concern because the approximation errs on the conservative side in that interference may be predicted when the actual losses may provide enough isolation

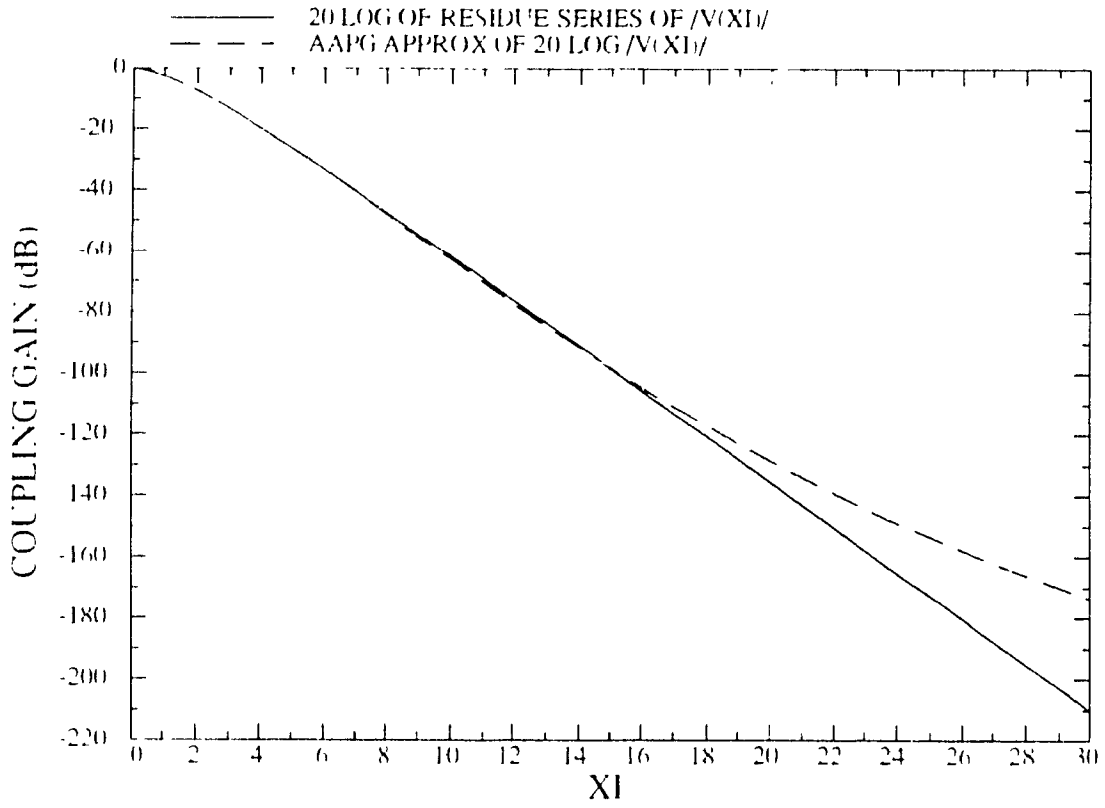

Figure 3.3. Plot of $20 \log|V(\xi)|$ (solid curve) and $-A/(\eta A + \xi')$ (dashed curve) versus ξ (denoted by "XI") [38].

between antennas to ensure compatibility. The reader is referred to the listings found in Appendices A and B for more information about the series computation of $V(\xi)$ from (3.17) used in the generation of Figure 3.3.

3.4 CURVED SURFACE DIFFRACTION LOSS FACTOR FOR COUPLING PATHS ON A RIGHT CIRCULAR CYLINDER

To obtain an efficient AAPG V07 algorithm to compute the curved-surface diffraction loss factor L_{cs} from (3.18) for coupling paths on a right circular cylinder requires that closed form expressions be derived for the Fock parameter ξ and the term in parentheses on the right-hand side of (3.18), which is denoted as

$$\tau = \left(\frac{ks}{2m(Q')\, m(Q)\, \xi} \right)^{\frac{1}{2}} . \tag{3.20}$$

3.4.1 Fock Parameter ξ for Cylindrical Paths. Consider Figure 3.4 in which source point Q' and field point Q on the surface of a right circular cylinder of radius ρ are joined by geodesic path Γ

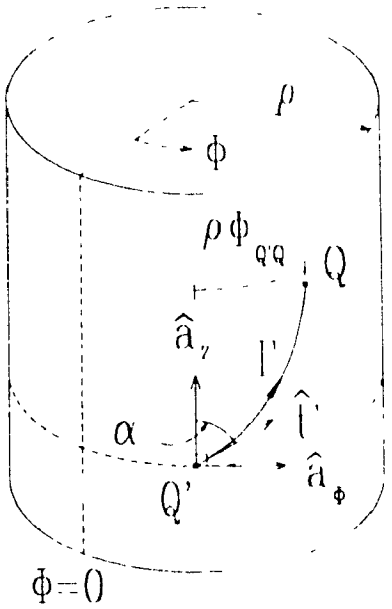

Figure 3.4. Geodesic path Γ on a right circular cylinder [24,32,48]

The Fock parameter ξ along the path Γ on the surface of the cylinder is given by (3.10). The geodesic radius of curvature at point s', $\rho_g(s')$, on a right circular cylinder can be derived from Euler's Theorem in differential geometry [40] to give

$$\rho_g(s') = \frac{\rho}{\sin^2 \alpha} . \tag{3.21}$$

The geometry for this problem is more easily visualized by unrolling (or developing) the cylinder into a rectangular plane as shown in Figure 3.5. Since $\rho_g(s')$ in (3.21) is a constant and

$$\sin \alpha = \frac{\rho \phi_{Q'Q}}{s} , \tag{3.22}$$

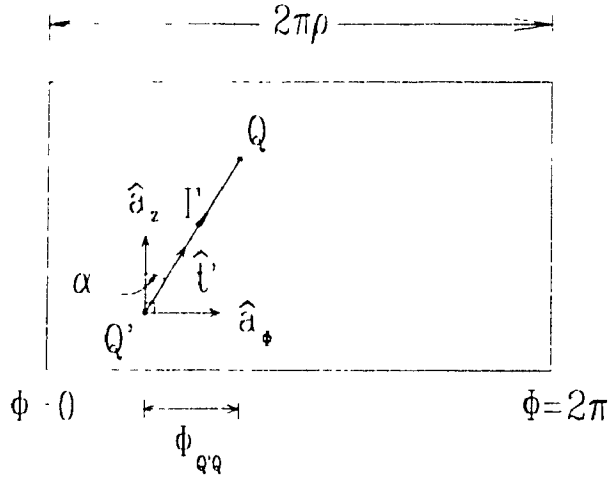

Figure 3.5. Geodesic path Γ on a right circular cylinder developed into a rectangular plane [39].

the integral from Q' (s'=0) to Q (s'=s) along Γ in (3.10) simplifies easily into an expression which depends only on the angular offset $\phi_{Q'Q}$ between Q' and Q, the path length s, and the cylinder radius ρ, giving

$$\xi = \left(\frac{k \rho^2 \phi_{Q'Q}^4}{2 s} \right)^{1/3} . \tag{3.23}$$

In the notation of the above derivation, the parameter A in (3.19a) is calculated in the AAPG documentation [35] directly from the result in (3.23) to be

$$A = \rho \phi_{Q'Q}^2 \left(\frac{k}{s} \right)^{1/2} . \tag{3.24}$$

3.4.2 τ Parameter for Cylindrical Paths. The τ parameter in (3.20) can be shown to be equal to one by the substitution of (3.9b) for m(Q') and m(Q), (3.23) for ξ, (3.21) for $\rho_p(Q')$ and $\rho_p(Q)$, and (3.22) for sin α, and by some algebraic manipulation.

Therefore the curved-surface diffraction loss factor in (3.18) is reduced to an expression for coupling paths on a right circular cylinder of the form

$$L_{CS} = -\frac{A}{\eta A + \xi'} , \tag{3.25}$$

where A was given explicitly in (3.24) and η and ξ' are retained from (3.19b) and

(3.19c).

3.5 CURVED-SURFACE DIFFRACTION LOSS FACTOR FOR COUPLING PATHS ON A RIGHT CIRCULAR CONE

In a manner similar to the previous section, explicit expressions are derived for the Fock parameter ξ and the term τ in (3.20) for coupling paths on a right circular cone [28]. These expressions can then be used in an efficient AAPG V07 algorithm to compute the curved-surface diffraction loss factor $L_{c,s}$ in (3.18).

3.5.1 Fock Parameter ξ for Conical Paths Consider Figure 3.6 in which source point Q_1 and field point Q_2 on the surface of a right circular cone of half cone angle θ_0 are joined by geodesic path Γ.

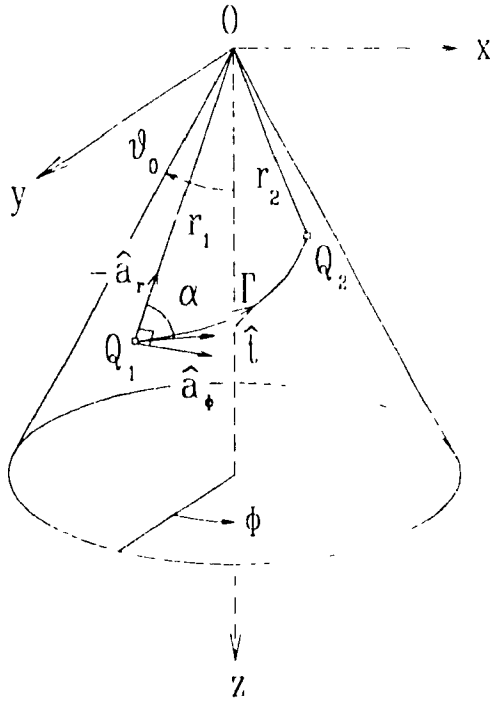

Figure 3.6. Geodesic path Γ on a right circular cone [28]

The Fock parameter ξ along the path Γ on the surface of the cone is given by (3.10) in which Q_1 and Q_2 replace Q' and Q as the limits of integration. The geodesic radius of curvature at point s', $\rho_g(s')$, on a right circular cone is derived in Appendix C

and is found to be

$$\rho_g(s') = \frac{r \tan\theta_0}{\sin^2\alpha} , \tag{3.26}$$

where r, the distance of point s' on path Γ from the cone apex, and α, the angle between r and Γ, vary with position s' on path Γ.

As was the case for the cylinder problem, the geometry is more easily illustrated by developing the cone into a planar pie-slice as shown in Figure 3.7. From the

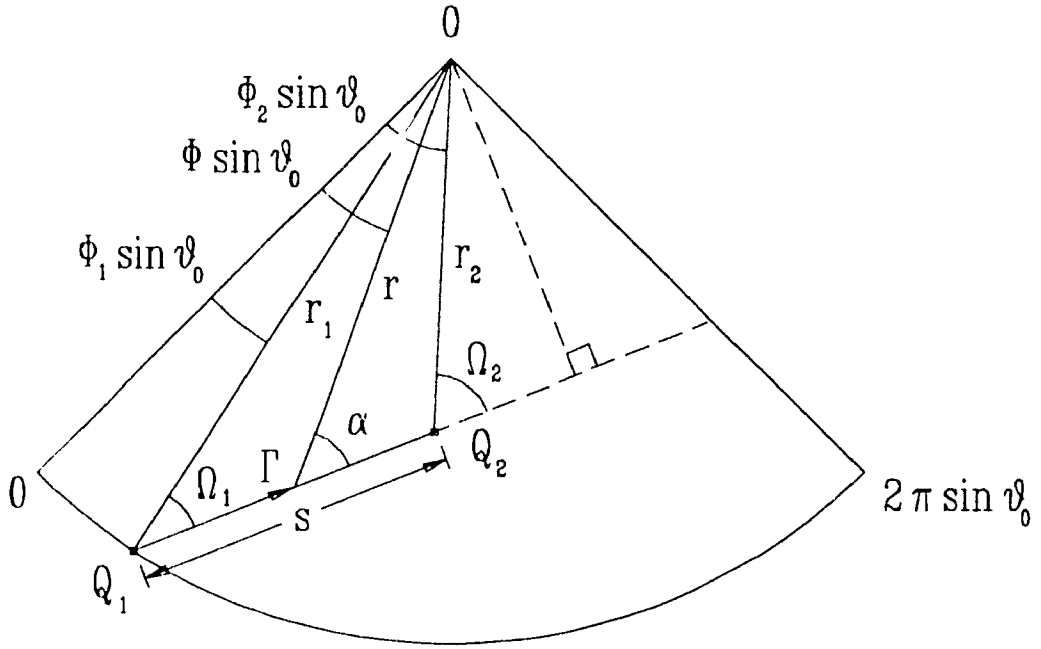

Figure 3.7. Geodesic path Γ on a right circular cone developed into a planar pie-slice [28]

derivation in Appendix C the differential path length ds' in (3.10) is expressed in terms of the differential angle dα as

$$ds' = \frac{r_1 \sin\Omega_1}{\sin^2\alpha}\, d\alpha \tag{3.27}$$

where r_1, Ω_1, and α are shown in Figure 3.7. With the change in the variable of integration, the limits of integration in (3.10) become angles Ω_1 and Ω_2 which are determined from the geometry of Figure 3.7 to be

$$\Omega_1 = \sin^{-1}\left\{\frac{r_2}{s}\sin[(\phi_2 - \phi_1)\sin\theta_0]\right\} \tag{3.28a}$$

and

$$\Omega_2 = \Omega_1 + (\phi_2 - \phi_1)\sin\theta_0 \quad . \tag{3.28b}$$

Also from the geometry of Figure 3.7, it follows that

$$r_1 \sin\Omega_1 = r_2 \sin\Omega_2 = r\sin\alpha \, . \tag{3.29}$$

Substituting (3.26), (3.27), and (3.29) into (3.10), the integral for the Fock parameter, which must be positive for convex surfaces, becomes

$$\begin{aligned}\xi &= \left(\frac{k}{2}\right)^{1/3}\int_{\Omega_1}^{\Omega_2}\left[\frac{r_1\sin\Omega_1\tan\theta_0}{\sin^3\alpha}\right]^{-2/3}\frac{r_1\sin\Omega_1}{\sin^2\alpha}\,d\alpha \\ &= \left(\frac{k}{2}r_1\sin\Omega_1\right)^{1/3}(\cot\theta_0)^{2/3}\,|\Omega_2 - \Omega_1| \quad .\end{aligned} \tag{3.30}$$

Since the angle difference $|\Omega_2-\Omega_1| = |\phi_2-\phi_1|\sin\theta_0$, from (3.28b), the Fock parameter is expressed explicitly by Lee [28] as

$$\xi = \left(\frac{k}{2}r_1\sin\Omega_1\sin\theta_0\right)^{1/3}(\cos\theta_0)^{2/3}\,|\phi_2 - \phi_1| \quad . \tag{3.31}$$

3.5.2 <u>τ Parameter for Conical Paths</u>. Using (3.9b) and (3.26), the parameters $m(Q_1)$ and $m(Q_2)$ (or equivalently, $m(Q')$ and $m(Q)$, respectively) are expressed as

$$m(Q_1) = \left(\frac{k\,r_1\tan\theta_0}{2\sin^2\Omega_1}\right)^{1/3} \tag{3.32a}$$

and

$$m(Q_2) = \left(\frac{k\,r_2\tan\theta_0}{2\sin^2\Omega_2}\right)^{1/3} \, . \tag{3.32b}$$

The substitution of (3.32) into (3.20) and some algebraic manipulation yield the result

$$\tau = \left(\frac{ks}{\xi}\right)^{1/2}(2k^2 r_1 r_2)^{-1/6}(\sin\Omega_1\sin\Omega_2\cot\theta_0)^{1/3} \tag{3.33}$$

in which all of the parameters have been defined in the previous subsection. Equation (3.33) differs slightly from the result in reference [28], which can only be explained as

a typographical error in reference [28].

3.6 FINAL REMARKS

With the insight gained from this chapter's derivation of the curved-surface diffraction loss factor, next chapter's examination and improvement of the deficient areas of AAPG V07 cone geodesic computational algorithms is kept in the proper theoretical perspective.

A detailed assessment of the specific implementations of the curved-surface diffraction loss factor is covered later in Chapter 6 when the introduction to AAPG V09 is more appropriate.

CHAPTER 4

CONE GEODESIC CALCULATION IN AAPG V07

4.1 INTRODUCTION

A practical computer modelling program for aircraft inter-antenna EMC analysis such as AAPG, should be accurate in its modelling and analysis of the electromagnetic interference (EMI) occurring on and near the aircraft. Extensive use and testing of AAPG V07, however, has revealed some specific weaknesses in the algorithms that compute and analyze the geodesics between anteanas located on or near the frustum cone model of the aircraft's nose. Some representative test cases which reveal the weaknesses in the code are shown in Figures 4.1 through 4.5 and have been previously reported by the author and others [15,16]. It can be seen that the algorithms produce non physical paths.

This chapter examines the prominent routines associated with these weaknesses in the AAPG V07 code and describes solutions that were designed to remedy those weaknesses. The improvements, test results, and their impact on realistic aircraft EMC problems are outlined. The complexity of the logic of geodesic path algorithms requires fairly detailed flow-charts throughout this chapter in order to present the thesis contribution in this area. The flow-charts from the former erroneous algorithms are not presented, but the occurrence of the errors are pointed out in the descriptions of the new algorithms.

4.2 CONE GEODESIC CALCULATION ALGORITHM

The module <CONL> performs the calculation of the cone geodesic as illustrated by the top-level flow-chart in Figure 4.6. The module <CONL> determines all of the specific path segments forward of the cylinder/cone interface, i.e. the nose section of the

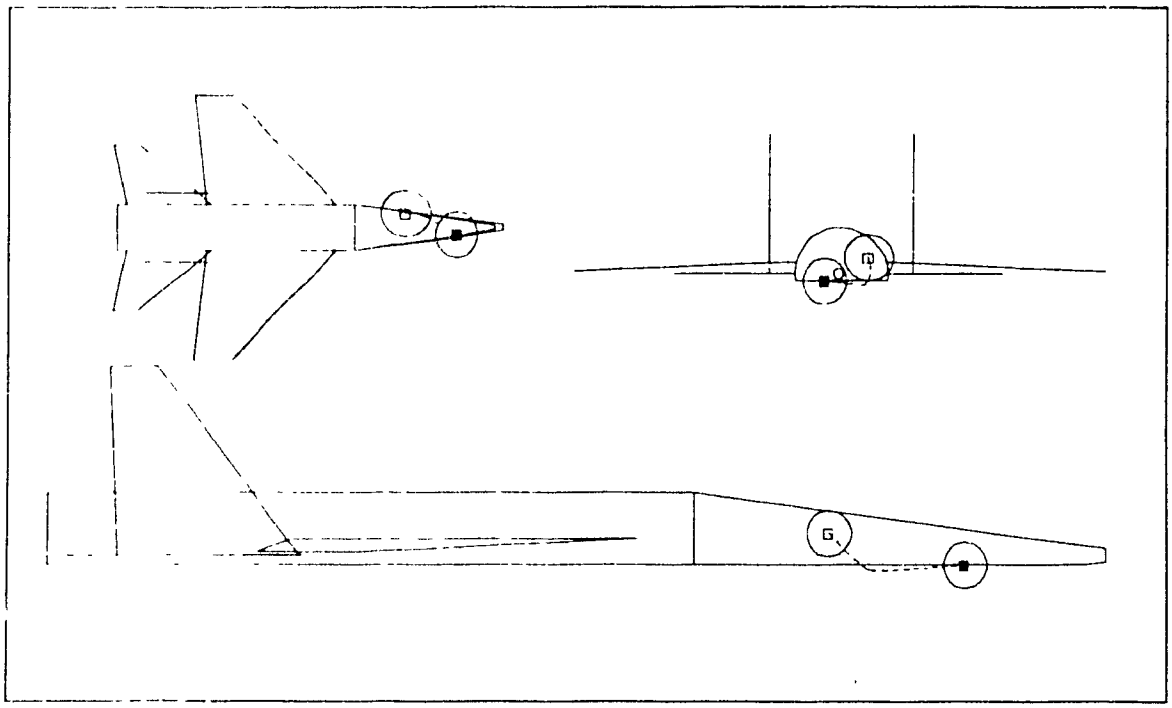

Figure 4.1. AAPG plot showing incorrect cone/flat bottom interface point: frequency = 225 MHz, path length = 2.3 λ, path loss = -32.2 dB [15].

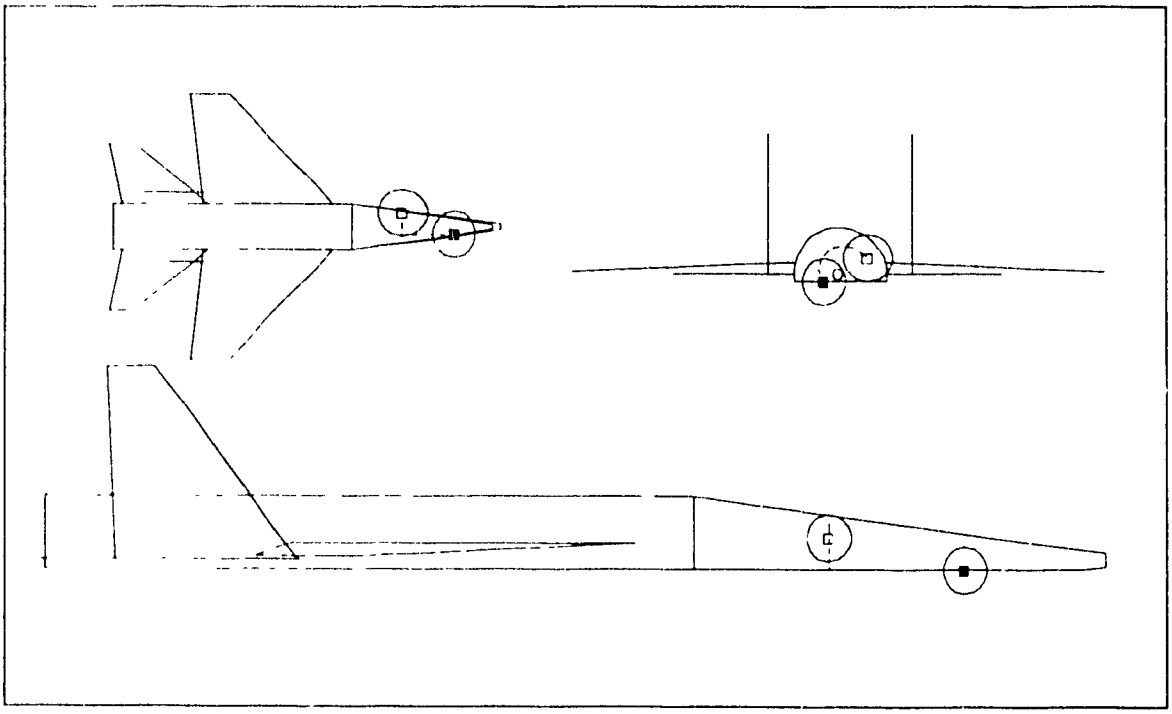

Figure 4.2. AAPG plot showing path penetrating cone fuselage, frequency = 225 MHz, path length = 3.4 λ, path loss = -47.9 dB [15].

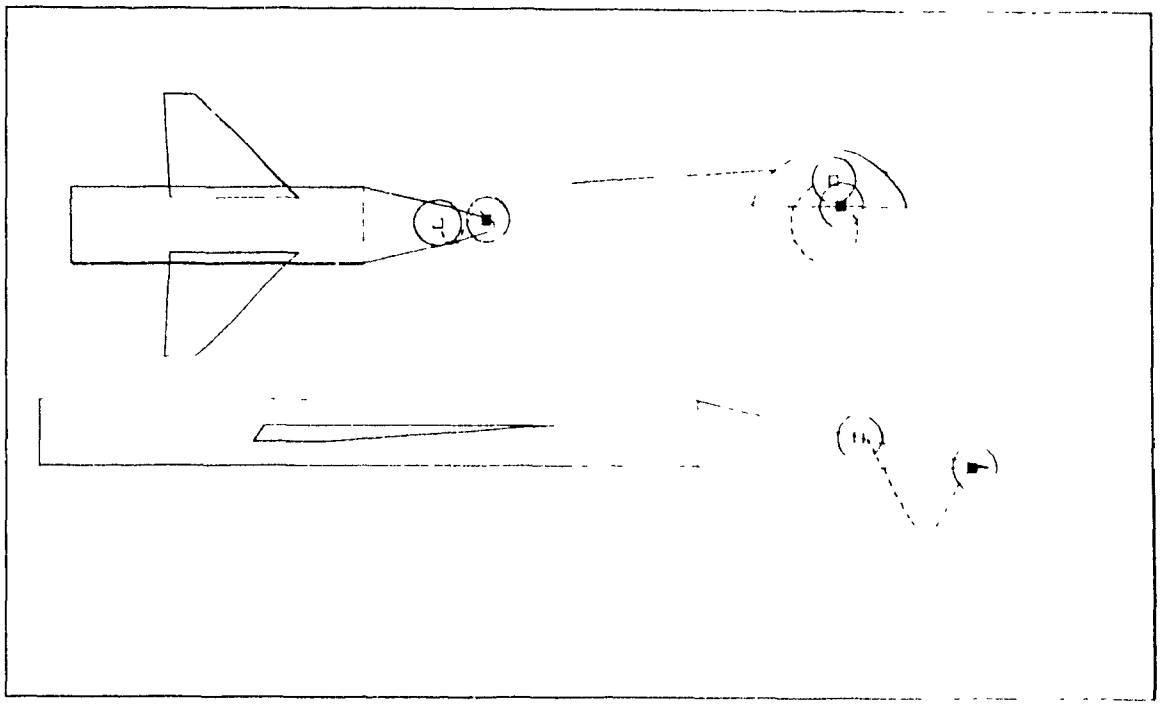

Figure 4.3. AAPG plot showing non-physical path leaving cone surface, frequency 225 MHz, path length = 4.4 λ, path loss = -75.3 dB [15].

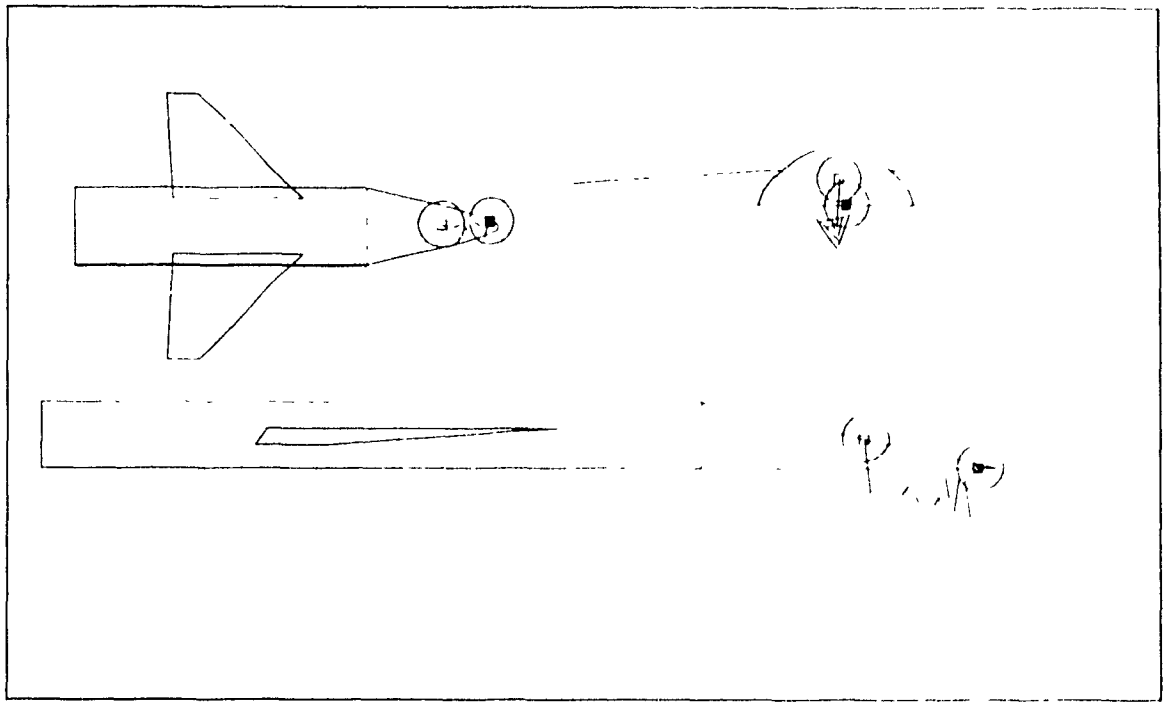

Figure 4.4. AAPG plot showing non-physical path, frequency = 225 MHz, path length = 2.0 λ, path loss = -315.7 dB [15].

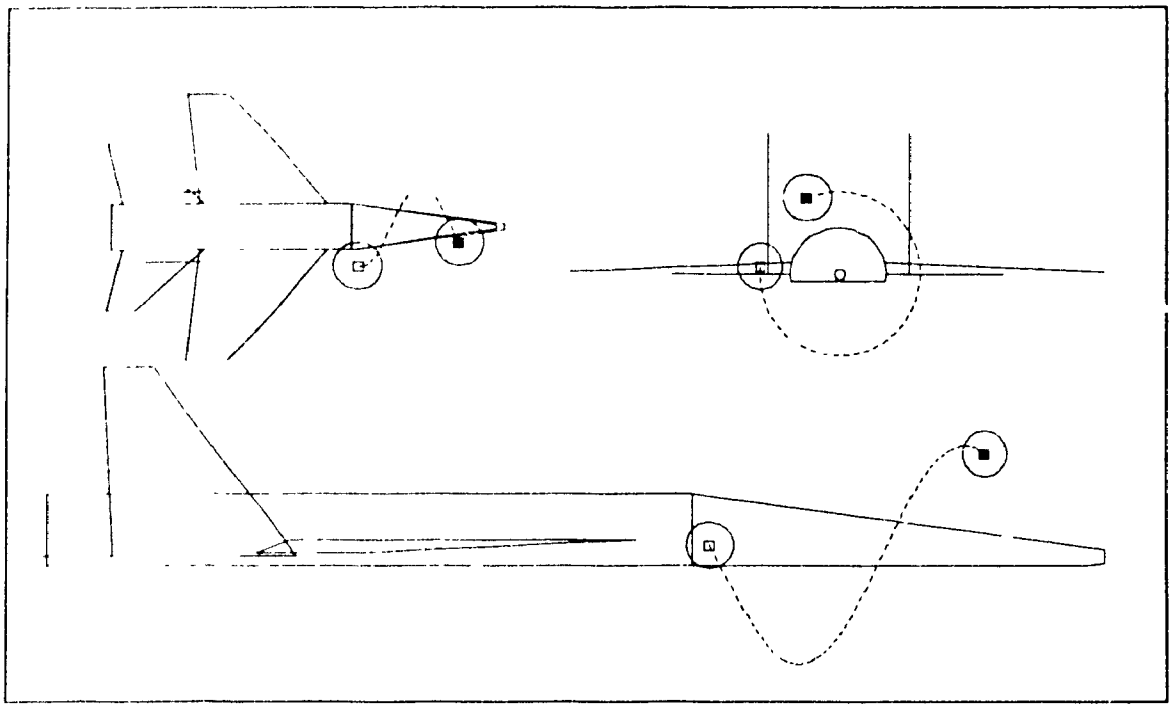

Figure 4.5. AAPG plot showing spiral instead of straight-line path, frequency = 225 MHz, path length = 8.7 λ, path loss = -92.1 dB [15].

aircraft fuselage model.

At the beginning of <CONE>, the routine <APOSTN> is called once for each antenna to set two flags which indicate whether the antenna is located on the fuselage surface and whether the antenna is located below a flat-bottomed fuselage model. (The variety of fuselage model types was described briefly in section 2.3.5 and is explored further in section 4.3.) These flags are used later by other routines called by <CONE> to calculate the geodesic path around the cone section.

When the module <CONE> is first called by its parent routine, it is assumed that at least one of the two antennas is forward of the cylinder/cone interface of the aircraft fuselage model. The purpose of the first branch in <CONE> is then to determine whether both antennas are forward of the cylinder/cone interface. If the test yields a FALSE. result, then only one antenna is located forward of the interface and the other aft, and <CONE> computes the cylinder cone interface point along the coupling path which

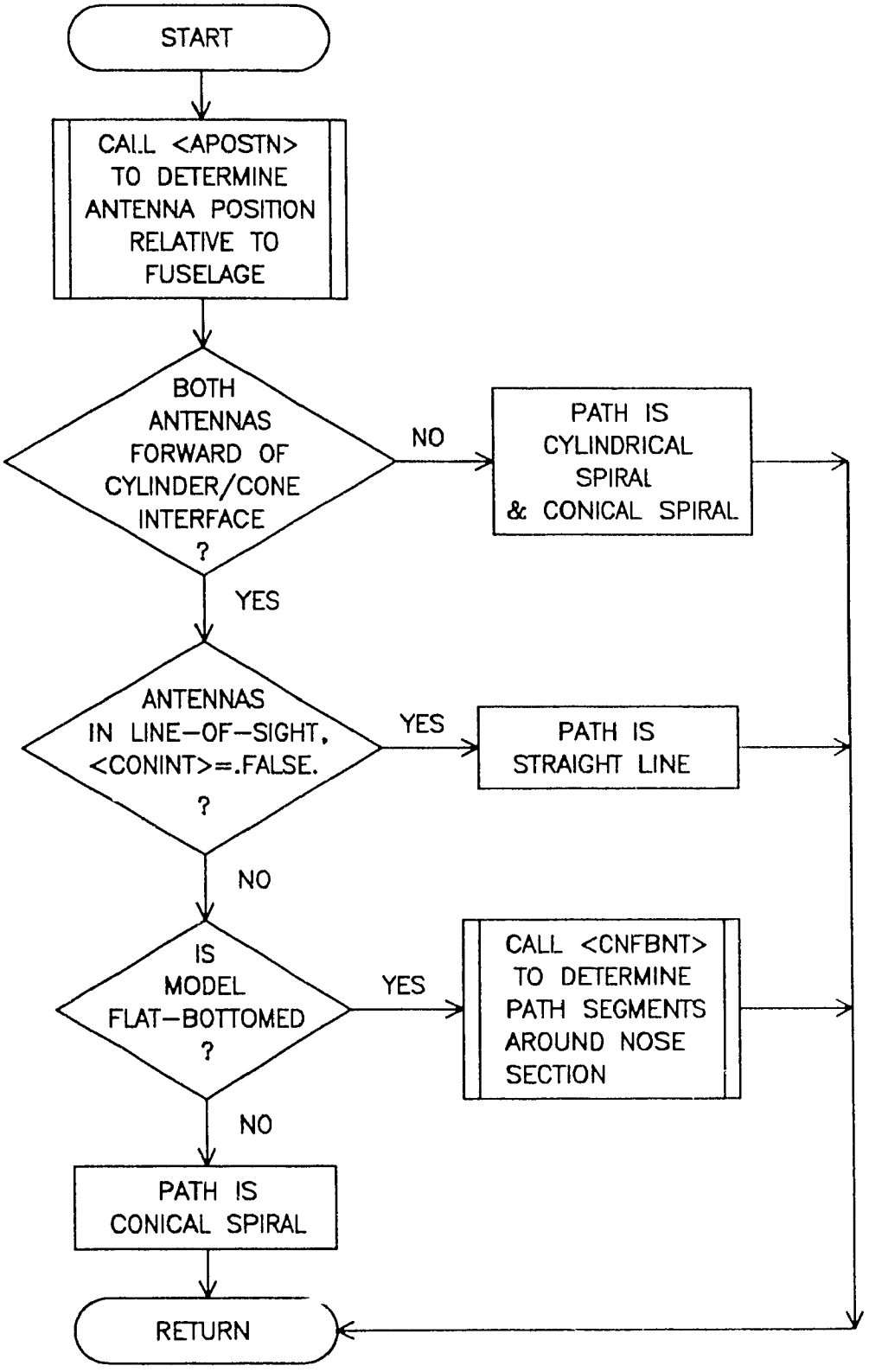

Figure 4.6. Top-level flow-chart of module <CONI>

traverses both the cone and cylinder surfaces. This block of code is described in greater detail in Chapter 5 of Drolet's thesis [39].

If, from the branch above, both antennas are determined to be forward of the cylinder/cone interface, the newly designed function <CONINT> is called to determine whether the straight line path between the antennas intercepts the nose section of the aircraft fuselage. If no interception occurs, the coupling path is simply a straight line between the antennas. If interception occurs, the remainder of the computation assumes that both antennas are located on the nose section surface and that hence a surface coupling path must exist on the nose section.

If the user does not set up his input data file to comply with this last assumption, the path computed by AAPG is erroneous. In other words, this last assumption restricts the EMC analyst to surface coupling cases and ignores the scattering phenomenon in the vicinity of the cone model. Fortunately, as developments are made in the algorithms which compute coupling paths due to scattering [38], the presence of the flags from ·APOSTN· and the modular structure of the code will greatly facilitate the incorporation of those new algorithms. The reader is referred to Chapter 6 of Drolet's thesis [39] which proposes an approach to the computation of the scattering path in the vicinity of a round-bottomed nose cone section of an aircraft fuselage model.

The next step of the module <CONE> is to determine whether the aircraft fuselage model has a flat or round bottom. If the model is flat-bottomed, the module <CNFBNT> is called to compute the various path segments that make up the geodesic on the surface of the flat-bottomed nose cone. If the model is round-bottomed, the coupling path is simply a conical spiral.

The remaining subsections describe the function, deficiencies, modifications, and new designs of the modules which <CONE> uses in order to compute the EMI coupling path around the nose section of the aircraft fuselage model. The descriptions of the

primary EMCCS modules that are presented in this chapter are shown in Table 4.1 and their relationship is illustrated in the tree diagram of Figure 4.7.

Table 4.1. Descriptions of cone geodesic computation modules

Module Name	Description
<CONE>	Top-level module to determine path segments on or near nose section of aircraft model.
<APOSTN>	Determines whether antenna sits on fuselage or in flat bottom region of aircraft model.
<CONINT>	Determines whether straight line path intersects nose section of aircraft model.
<CNFBNT>	Determines coupling path segments on flat-bottomed nose section of aircraft model.
<ITER>	Determines junction points along hyperbolic edge of nose section's flat bottom for path segments in <CNFBNT>.

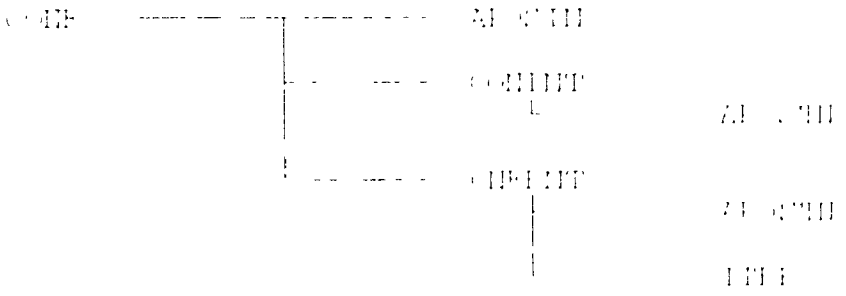

Figure 4.7. Cone geodesic computation modules in EMCCS

4.3 MODULE <APOSTN>

The function of routine <APOSTN> is to set two flags which indicate the position of an antenna relative to the aircraft fuselage: a flag called AONFUS which is returned .TRUE. when the antenna is located on the fuselage surface, and a flag called ANFLT which is returned .TRUE. when the antenna is located below a flat bottomed fuselage model.

The determination of the status of the AONFUS and ANTFLT flags is particularly challenging because of the variety of nose section shapes supported by the AAPG V07 code. The aircraft's nose is modelled by means of a frustum of a right circular cone whose axis of revolution is parallel to the horizontal plane; such models are referred to as "round-bottom" models. The frustum can be truncated along a horizontal plane below or above the axis of revolution, respectively called "flat-bottom" and "sliver" models. Typical round-bottom, flat-bottom and sliver models are illustrated by the orthogonal views of Figure 4.8.

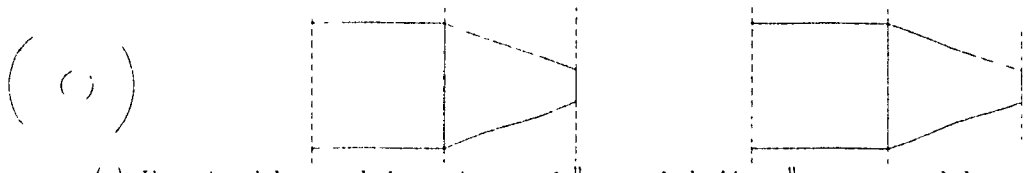

(a) Front, side, and top views of "round-bottom" nose model

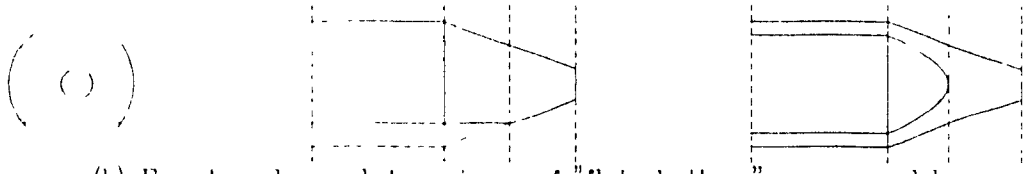

(b) Front, side, and top views of "flat-bottom" nose model.

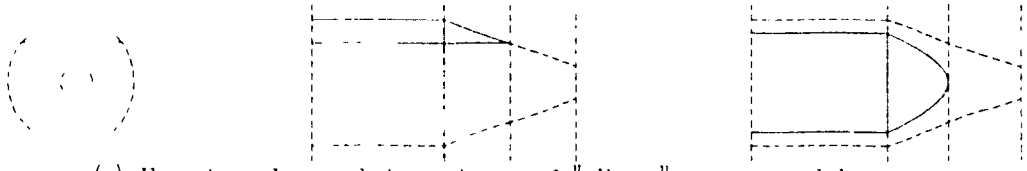

(c) Front, side, and top views of "sliver" nose model

Figure 4.8. Typical round-bottom, flat-bottom, and sliver models in AAPG [16].

The original version of <APOSTN> disregards the nose section shape and immediately sets the AONFUS and ANTFLT flags assuming that the antenna is located aft of the cylinder/cone interface, i.e. in the vicinity of the cylindrical main body section of the aircraft fuselage [6]. The disregard for the nose section shape causes the incorrect results illustrated in Figures 4.9 and 4.10. Figure 4.9 shows how <APOSTN> erroneously

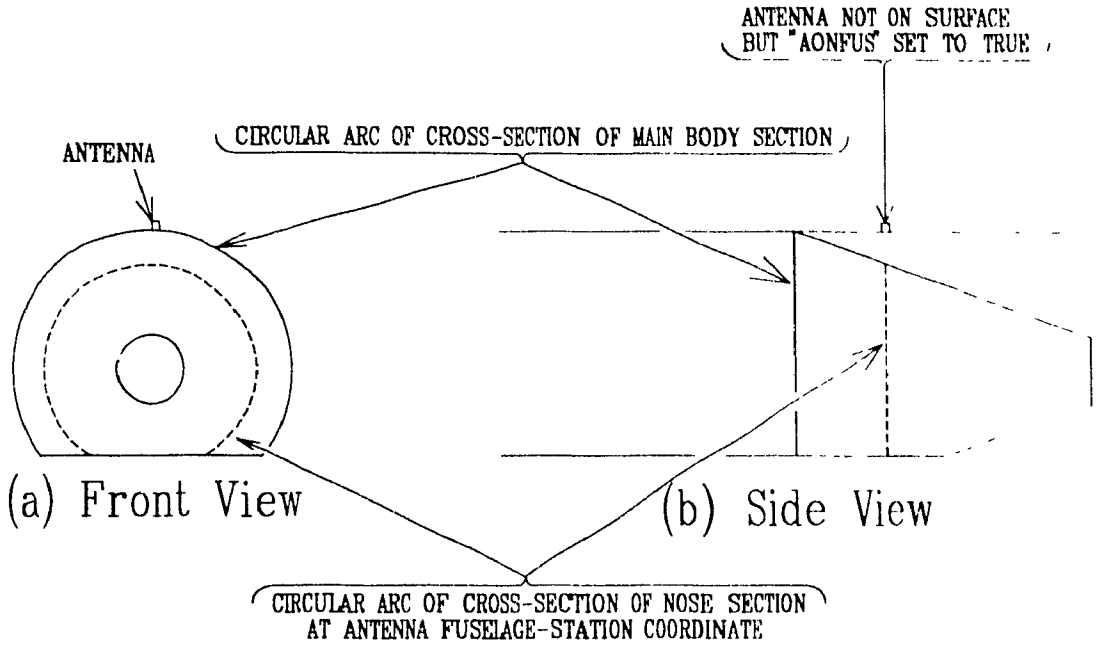

Figure 4.9. Erroneous determination of flag AONFUS by module APOSTN for an antenna located forward of the cylinder/cone interface

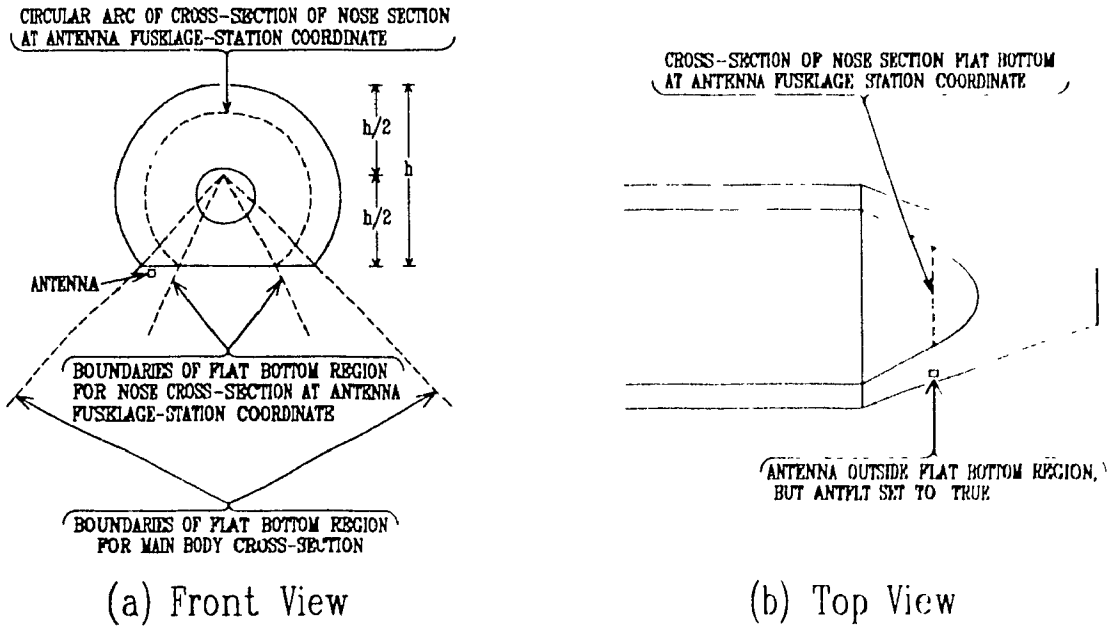

Figure 4.10. Erroneous determination of flag ANTFLT by module APOSTN for an antenna located forward of the cylinder/cone interface [6]

sets AONFUS equal to .TRUE., when in fact the antenna is situated some distance from the cone's surface. Figure 4.10 shows how <APOSTN> sets ANTFLT equal to .TRUE., when in fact the antenna is situated outside the flat bottom region.

The erroneous <APOSTN> algorithm, which is illustrated by the examples of Figures 4.9 and 4.10, was revised and corrected. The flow-chart of the revised version of <APOSTN> is shown in Figure 4.11 and is described below. When <APOSTN> is first called by its parent routine, the new algorithm initializes ANTFLT and AONFUS to .FALSE.. If the antenna is situated forward of the nose section or aft of the cylindrical main body section, the antenna is neither on the fuselage surface nor in the flat bottom region, so <APOSTN> terminates with both of the AONFUS and ANTFLT flags returned as .FALSE..

If <APOSTN> does not terminate, it determines whether the aircraft model has a round or flat bottom. In the case of a round-bottomed model, the flag ANTFLT remains .FALSE. and the program flow jumps forward to the section of code within <APOSTN> that determines the status of the AONFUS flag. In the case of a flat-bottomed or sliver model, the <APOSTN> routine proceeds with the computation of the ANTFLT flag.

In order to determine the status of the ANTFLT for a flat-bottomed or sliver model, <APOSTN> computes the boundaries of the flat bottom region in a transverse BL-WL plane (see section 2.3.5 for definition of aircraft coordinate system) located at the antenna fuselage-station coordinate. These boundaries are shown in Figure 4.10(a). ANTFLT is set to .TRUE. when the antenna is found to be within the boundaries of the flat bottom region.

In order for the AONFUS flag to be returned .TRUE., the antenna must be located within a distance from the fuselage surface equal to 10% of the radius of the BL-WL cross section at the antenna's fuselage-station coordinate. Figure 4.12 shows how

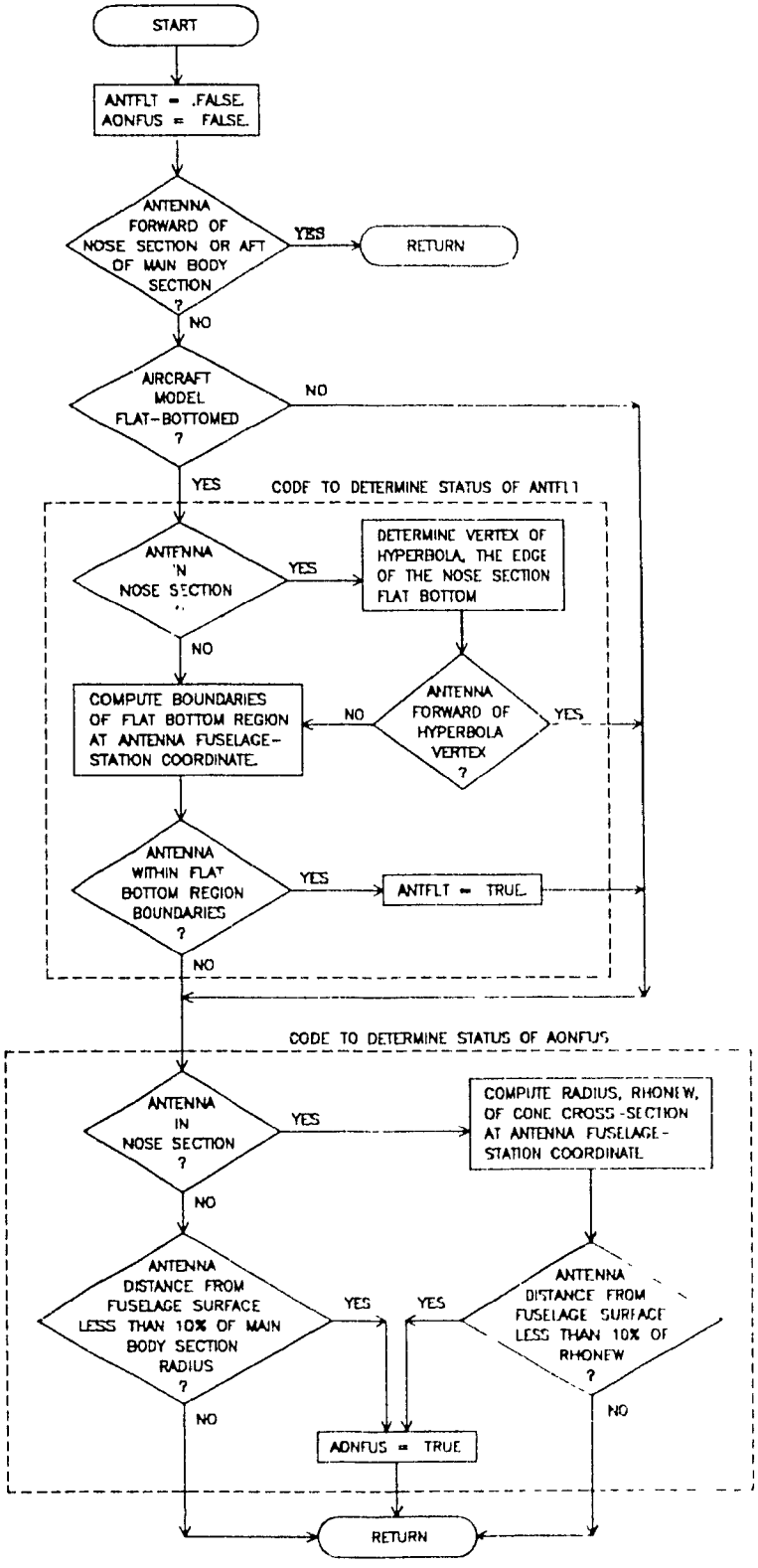

Figure 4.11. Flow-chart of revised module <APOSTN>

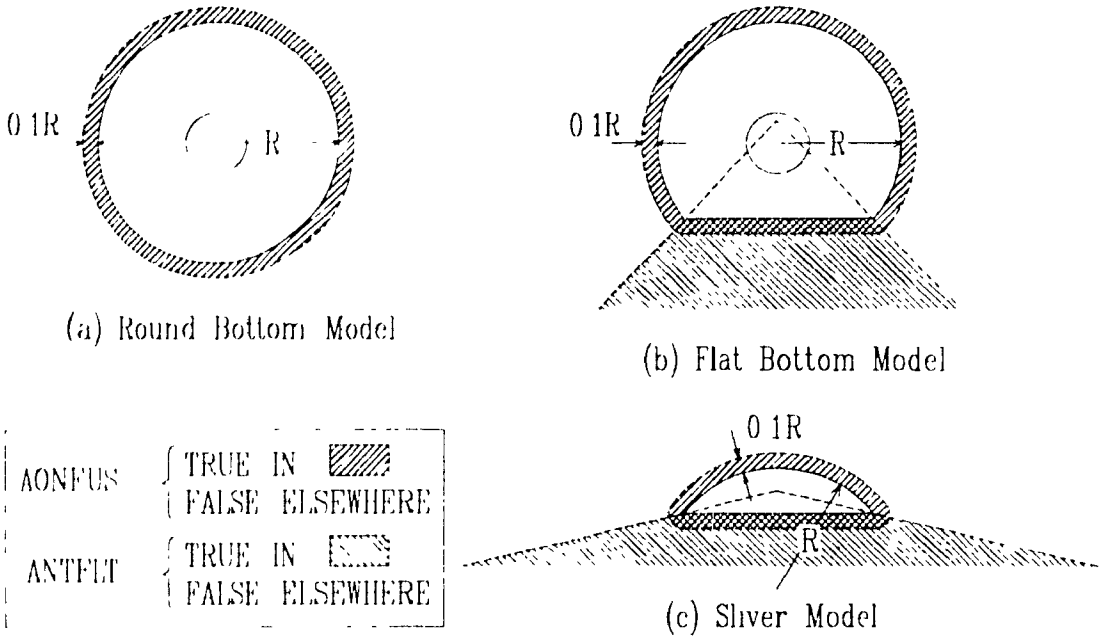

Figure 4.12. Setting of AONFUS and ANTFLT flags in revised module <APOSTN> for different fuselage model cross-sections [6].

<APOSTN> sets the AONFUS and ANTFLT flags for several distinctly shaped nose model cross-sections.

4.4 MODULE <CONINT>

The module <CONINT> is a newly designed LOGICAL function that determines whether the straight line path between two antennas intercepts the cone section of the aircraft fuselage. The function is returned .TRUE. when interception occurs. Chapter 6 of Drolet's thesis [39] originally proposed a similar algorithm, but his version was never formally incorporated into AAPG V07 because testing revealed that his approach does not work. The equations pertinent to the new approach taken in this section as well as some typical test cases are described below.

Consider Figure 4.13 in which two antennas are located at points $Q_1(x_1,y_1,z_1)$ and $Q_2(x_2,y_2,z_2)$ in the presence of a right circular cone. The parametric equations describing the straight line between Q_1 and Q_2 are given by

$$x = x_1 + t \cdot x_{dir} , \tag{4.1a}$$

$$y = y_1 + t \cdot y_{dir} , \tag{4.1b}$$

$$z = z_1 + t \cdot z_{dir} , \tag{4.1c}$$

where

$$x_{dir} = x_2 - x_1 , \tag{4.2a}$$

$$y_{dir} = y_2 - y_1 , \tag{4.2b}$$

$$z_{dir} = z_2 - z_1 . \tag{4.2c}$$

The surface of the right circular cone with half cone angle θ_0, whose axis of rotation is the z-axis and whose apex is located at the origin, is given by the equation

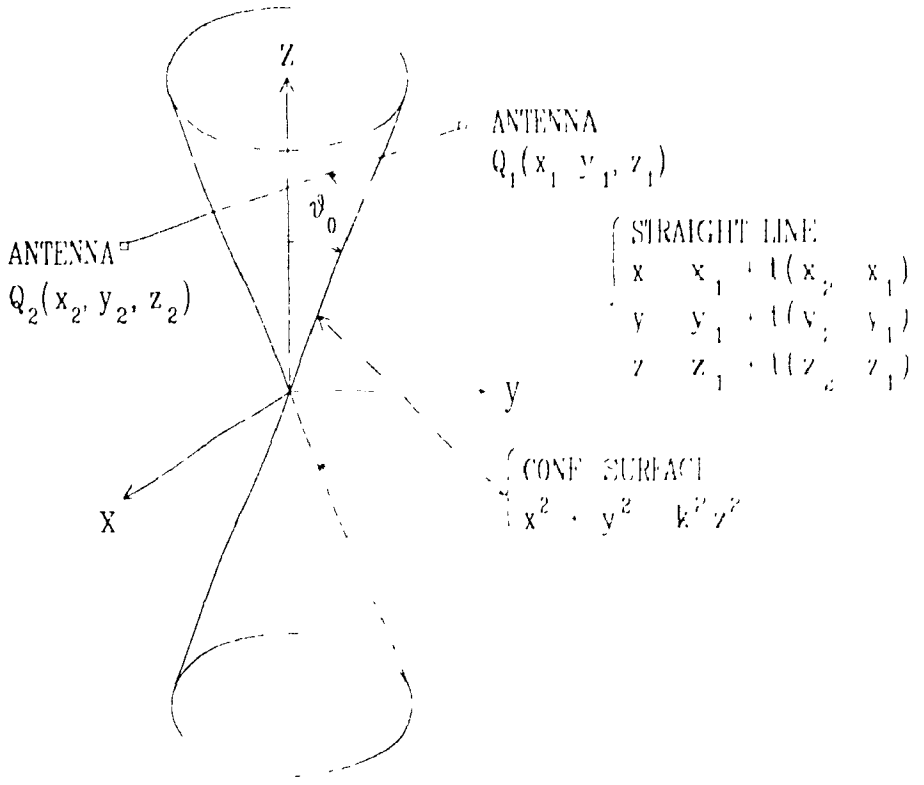

Figure 4.13. Straight line in presence of cone surface

$$x^2 + y^2 = k^2 z^2 \tag{4.3}$$

where

$$k = \tan\theta_0 \ . \tag{4.4}$$

The substitution of (4.1a)-(4.1c) into (4.3) yields a quadratic equation of the form

$$At^2 + Bt + C = 0 \tag{4.5}$$

where

$$A = x_{dir}^2 + y_{dir}^2 - k^2 z_{dir}^2 \tag{4.6a}$$

$$B = 2\left[x_1 x_{dir} + y_1 y_{dir} - k^2 z_1 z_{dir}\right] \tag{4.6b}$$

$$C = x_1^2 + y_1^2 - k^2 z_1^2 \ . \tag{4.6c}$$

The roots of (4.5) are computed by means of the quadratic formula and are examined to determine whether interception of the line with the cone has occurred. Only those roots which are purely real and whose values are between 0 and 1 are considered as candidates for interception. Furthermore, two distinct roots must exist, otherwise the line is tangent to the cone and, for the purposes of AAPG V07, is not considered to intercept the cone. Having satisfied the above conditions, the points associated with the roots must lie on the surface of the aircraft's nose to be valid intersection points. Some typical cases are shown in Figure 4.14.

As a final check, <CONINT> also determines whether interception occurs with the nose flat bottom. The function details of <CONINT> are outlined in the flow-chart of Figure 4.15.

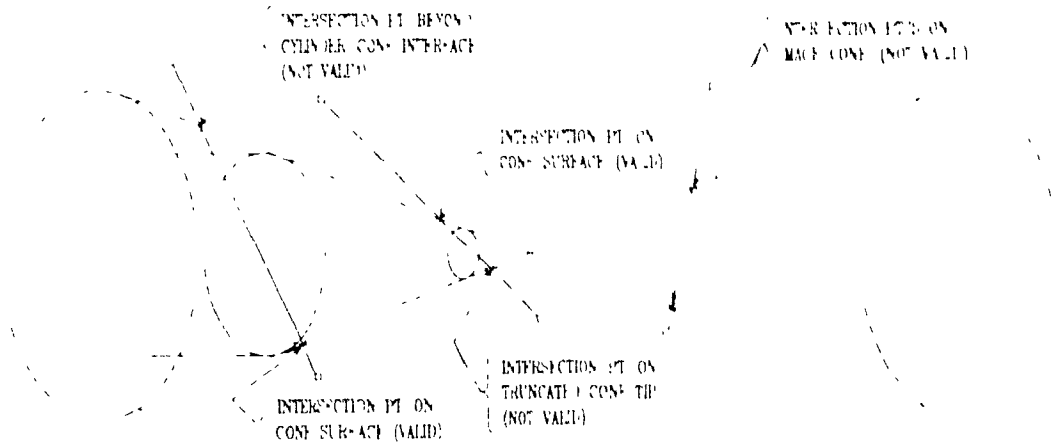

(a) Round bottom model

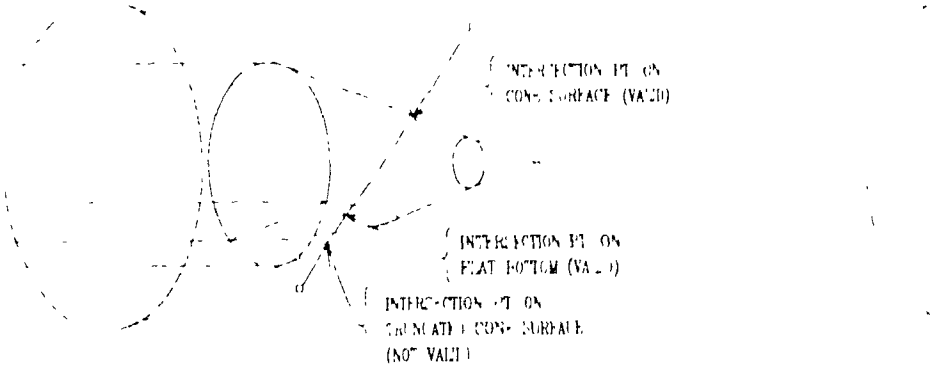

(b) Flat bottom model

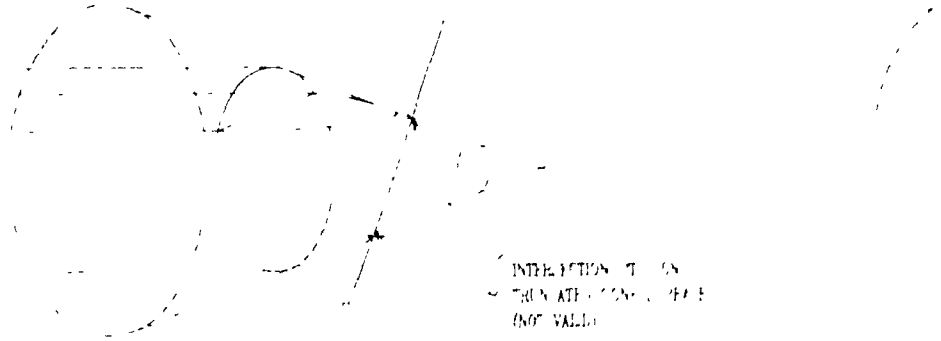

(c) Sliver model

Figure 4.14. Typical intersection points determined by new module CONIC1

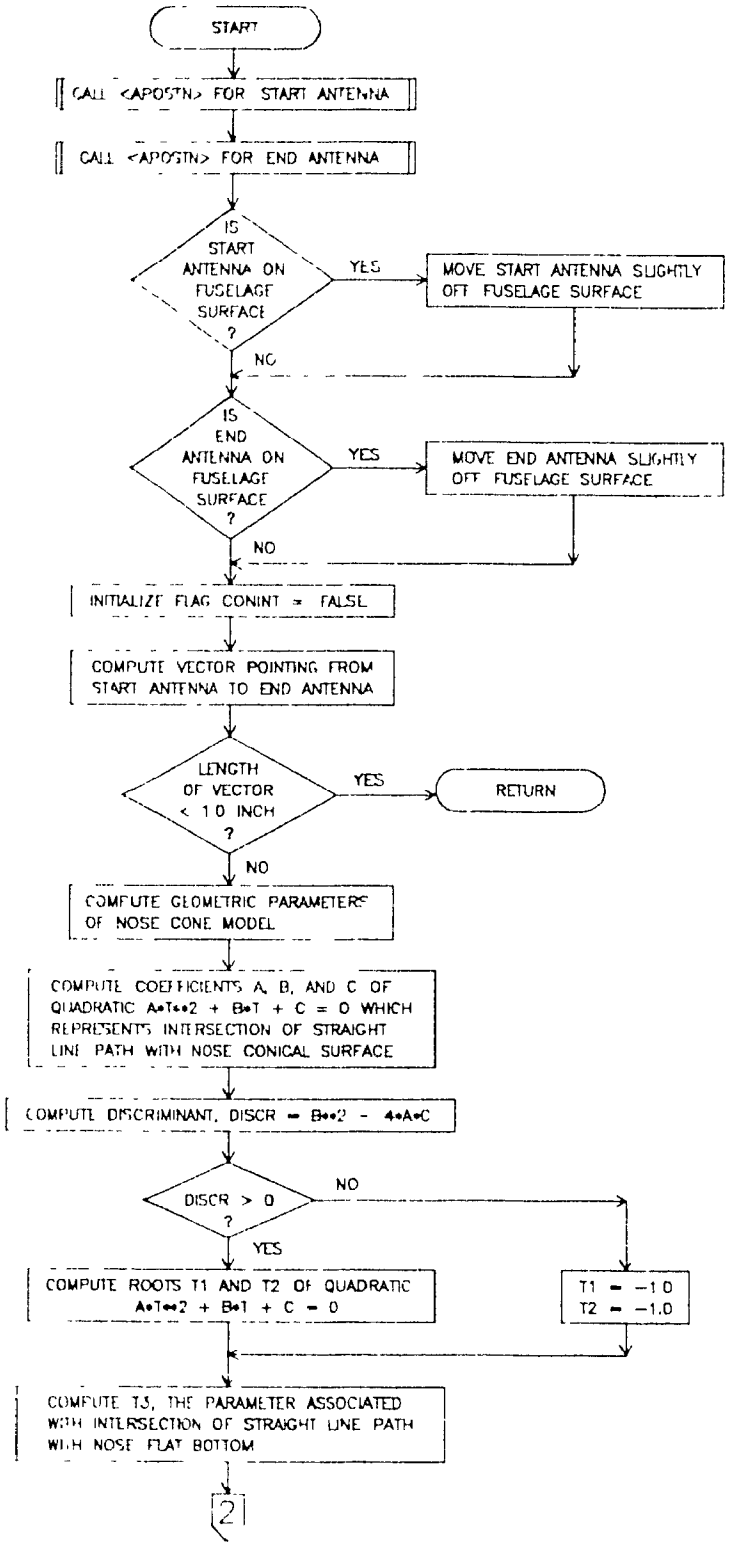

Figure 4.15. Flow chart of new module <CONINT> (Page 1 of 2)

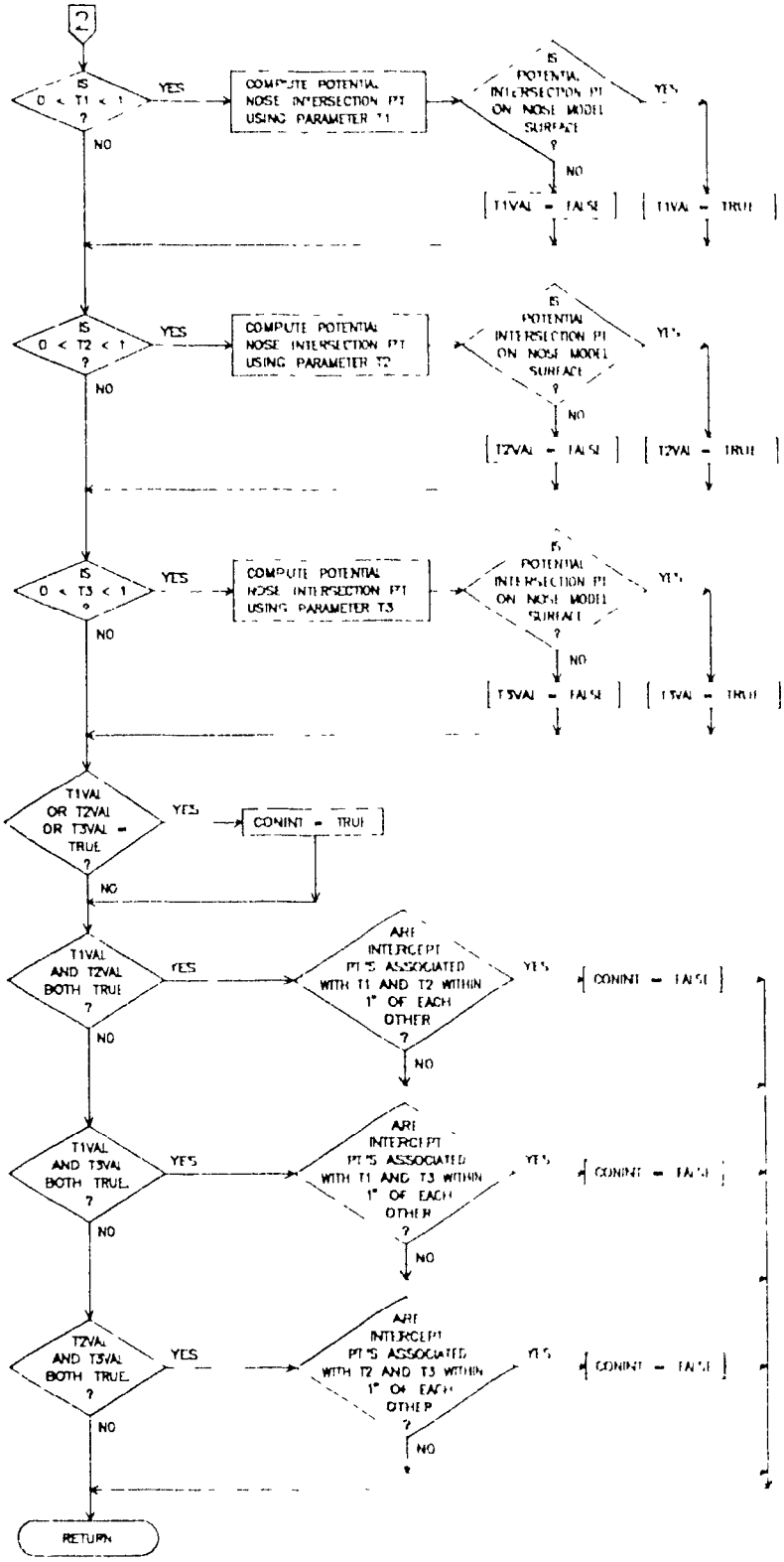

Figure 4.15. Flow-chart of new module - CONINT - (Page 2 of 2)

4.5 MODULES <CNFBNT> AND <ITER>

As described in the AAPG documentation [6], subroutines <CNFBNT> and <ITER> are the key modules used together to determine the nature of the path around the nose section of a flat bottomed aircraft fuselage model. Figure 4.16 illustrates the different types of trajectories along the surface of the "flat-bottom" nose model computed by module <CNFBNT>.

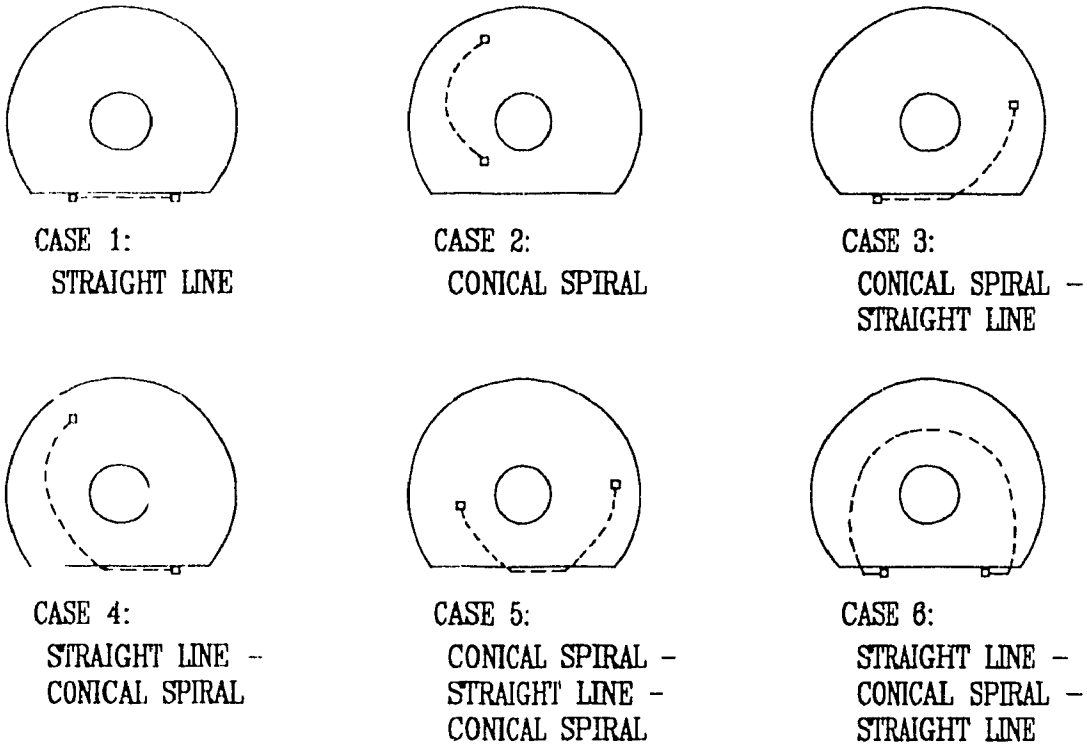

Figure 4.16. Front view of path segments on flat-bottom aircraft nose models as computed by <CNFBNT> [6].

The difficulty in the computation of the coupling paths on the surface of a "flat-bottom" (and "sliver") nose model is the determination of the junction point at which each conical spiral segment meets each straight line segment along the hyperbolic curved edge of the flat bottom in cases 3 through 6 of Figure 4.16. In the deficient version of the code, the module <ITER> is called by <CNFBNT> to compute each junction point in the

path around the cone by means of a numerical search technique in the vicinity of a trial junction point. During testing, it was found that the numerical search technique employed by <ITER> gives inaccurate results and, in some instances, does not converge at all due to the incorrect nose cone modelling of <APOSTN> and the invalid trial junction point used in <ITER>. In other instances, the placement of antennas at or near the cone/flat-bottom intersections causes <ITER> to diverge.

The erroneous <CNFBNT> and <ITER> algorithms were restructured and corrected to address the weaknesses described above. For cases 3 through 6 shown in Figure 4.16, the new version of <CNFBNT> uses a technique of approximating non developable surfaces, namely the geometry of the flat bottomed nose section, by three component developable surfaces. (The concept of developable surfaces is explored in depth in section 5.4.) The approach is similar to one used in finding junction points at the cylinder/flat-bottom intersections. It is important to note here that the cone/flat bottom junction point obtained by this method is not optimal, but is a very good approximation and yields better results than the old version of the code.

Consider the specific instance of case 3 of Figure 4.16. The procedure of finding the junction point is illustrated in Figure 4.17. Module <CNFBNT> first computes the arc length of a circular path from the uppermost antenna to the cone/flat bottom intersection on the port side of the aircraft. This antenna is then 'unwrapped' along this circular path to a new extended butt-line position into the same horizontal plane as the flat bottom.

The new version of subroutine <ITER> is then called to calculate the intersection of the straight line segment joining the antenna on the flat bottom and the new 'unwrapped' point with the hyperbola where the cone meets the flat bottom. One junction point is returned. The approach used in case 4 is analogous to that of case 3 except that the uppermost antenna is unwrapped toward the starboard instead of the port side of the

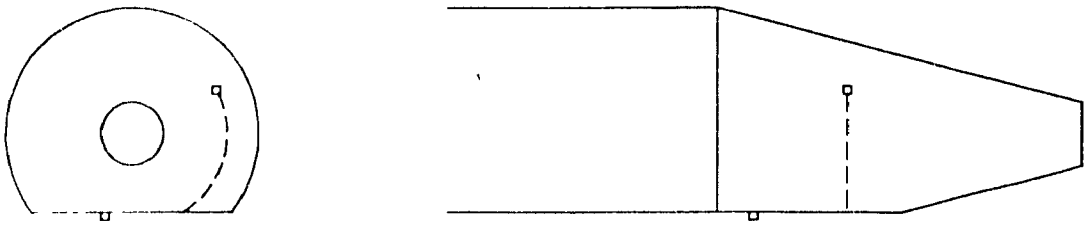

(a) Front and side views of transverse circular arc from antenna on cone to edge of flat bottom.

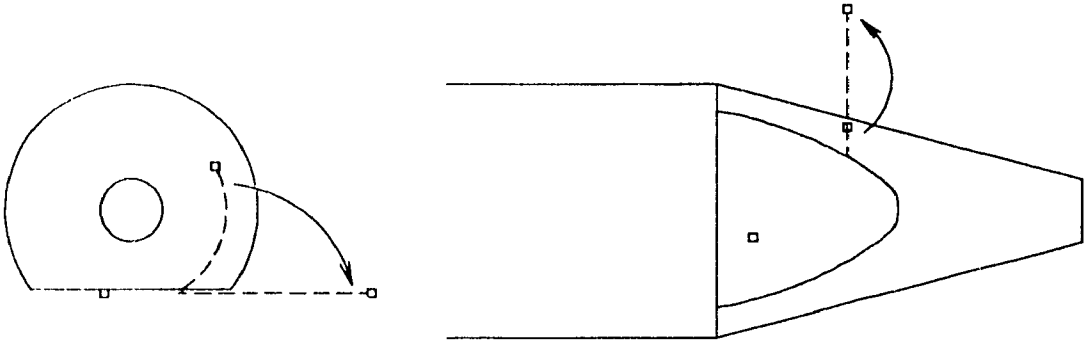

(b) Front and top views of transverse circular arc "unwrapped" into same plane as flat bottom.

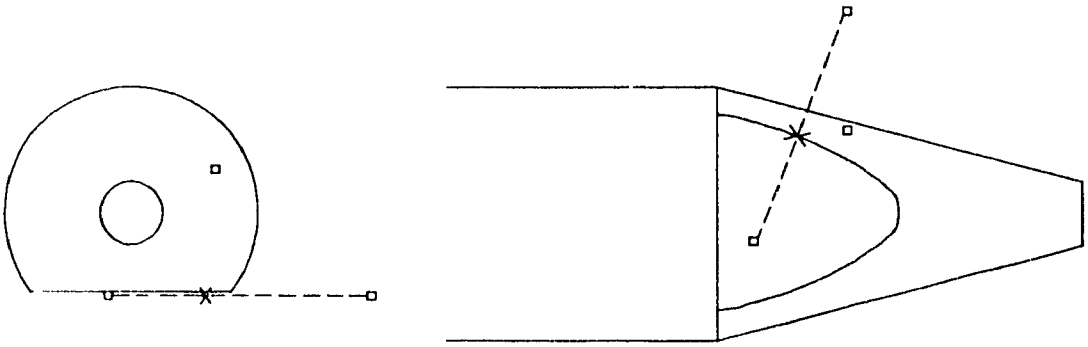

(c) Front and top views of intersection of straight line between "unwrapped" antenna and antenna on flat bottom, and hyperbolic-shaped edge of flat bottom.

Figure 4.17. Conical spiral straight line junction point algorithm [16]

aircraft

For case 5, the new version of <CNFBNT> 'unwraps' both antennas and the new version of <ITER> calculates the intersection of the line connecting the two 'unwrapped' points in the plane of the flat-bottom with the same hyperbola as before, two junction points are returned

For case 6, the version of <CNFBNT> 'unfolds' the antennas each along a constant fuselage-station line away from the aircraft's centroid and toward the nearer cone/flat-bottom intersection to new extended butt line positions in the same horizontal plane as the flat-bottom The new version of <ITER> is called to calculate the intersection of the line connecting the new 'unfolded' points in the plane of the flat bottom with the same hyperbola as before to determine the two required junction points

The changes to <CNFBNT> and <ITER> are noteworthy aside from addressing some deficient test cases. The foremost advantage of the new module <CNFBNT> is that it introduces new flags to indicate whether an antenna (or path point, as the case may be) is close to a cone/flat-bottom junction point. These flags are particularly useful for future expansion of the code for cases in which scattering off the nose section of the aircraft is to be considered

Comparison of the listings of the old and new versions of <ITER> and <CNFBNT> subroutines are summarized in reference [15] The new code's more structured and modular nature allows easier software maintenance and upgrade For example, the new version of module <ITER> reverts to a geometrical analytical approach to get a reasonable cone/flat-bottom junction point, but can be improved by optimizing that point to get the shortest coupling path length The flow charts of the revised modules <CNFBNT> and <ITER> are shown in Figures 4.18 and 4.19

The new algorithms use geometrical analysis to generate shorter coupling paths which usually give higher EMI margin predictions These greater EMI margins allow a

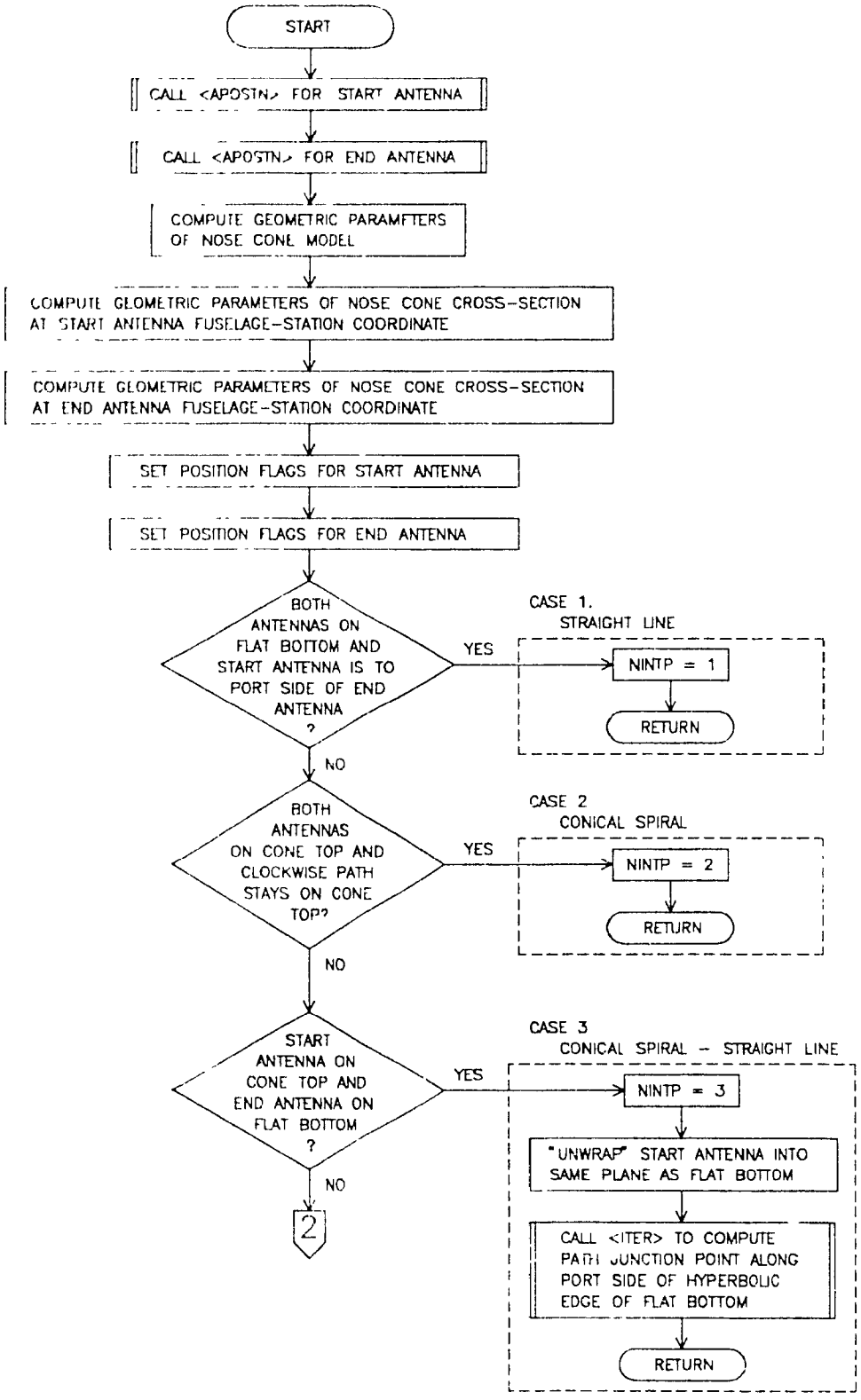

Figure 4.18. Flow-chart of revised module <CNFBNT> (Page 1 of 2).

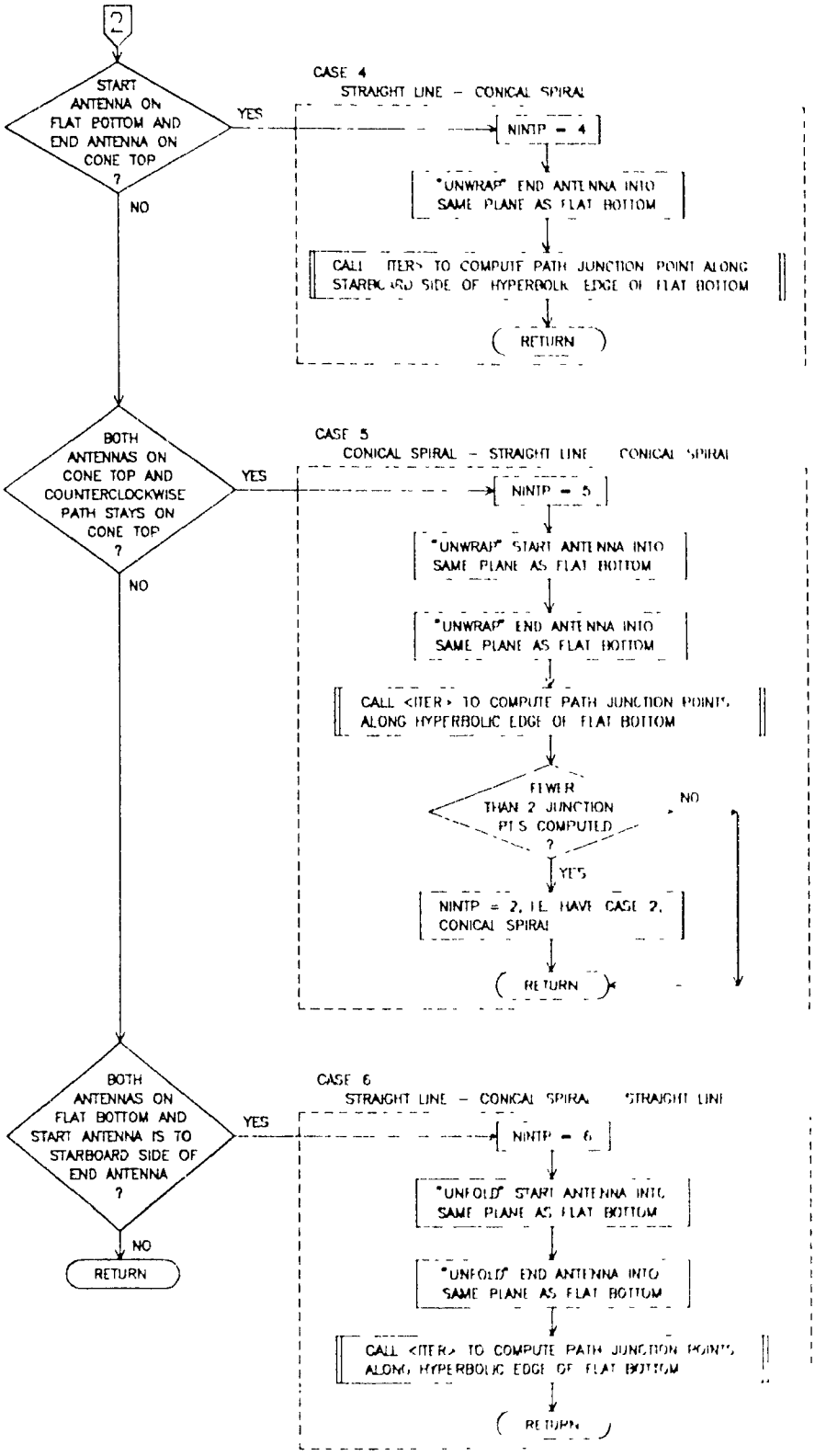

Figure 4.18. Flow chart of revised module <CNFBNT> (Page 2 of 2)

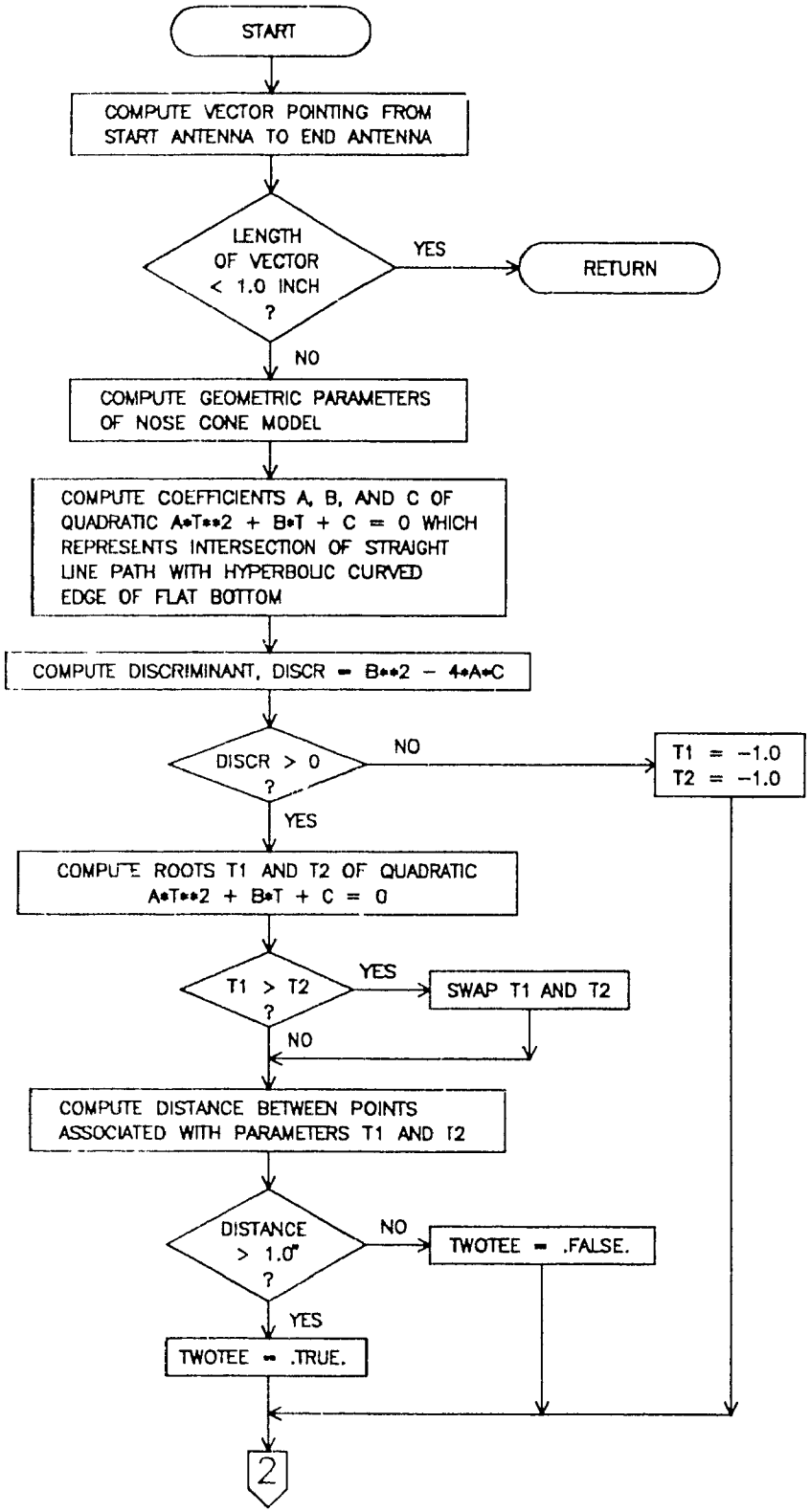

Figure 4.19. Flow chart of revised module <ITER> (Page 1 of 2)

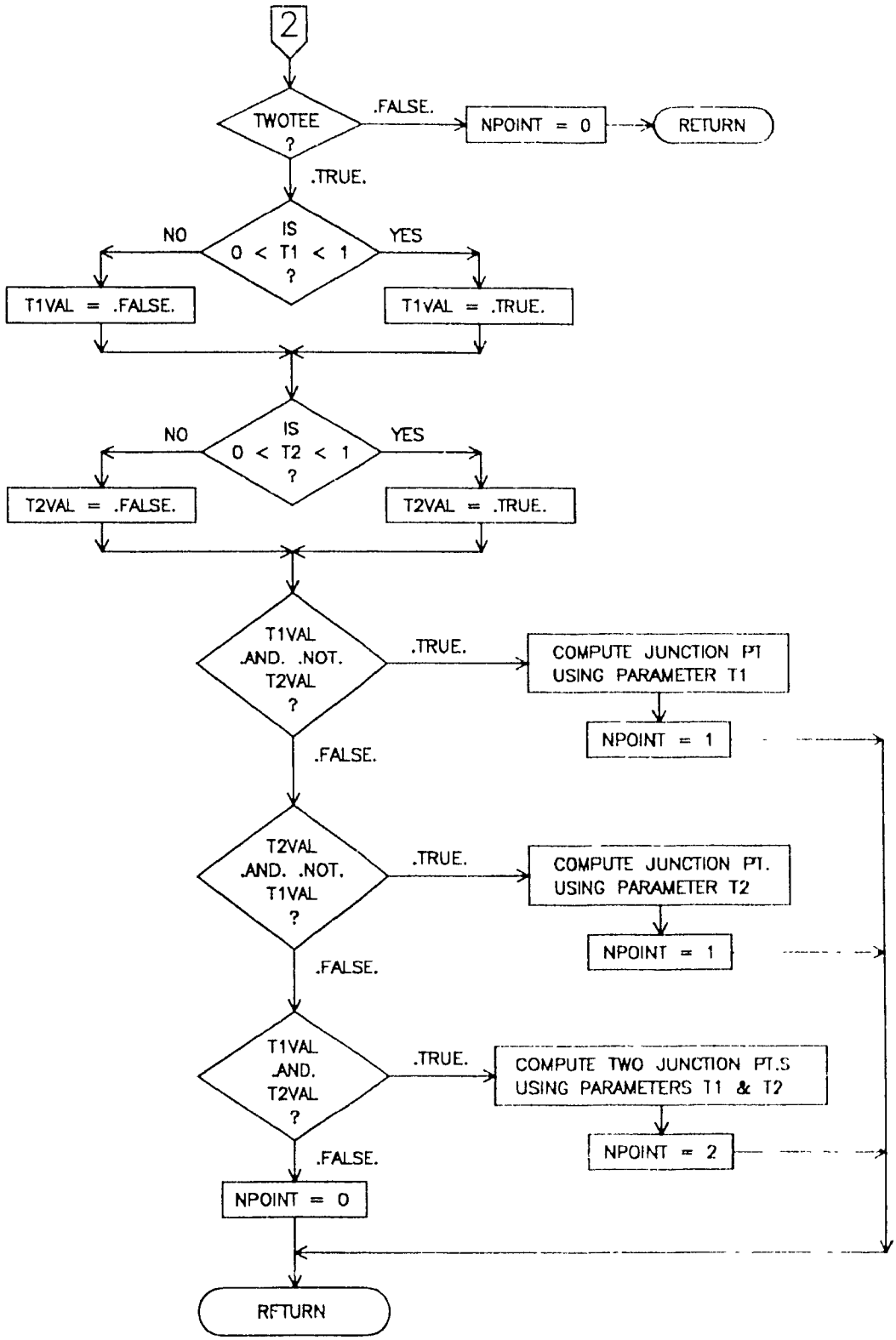

Figure 4.19. Flow-chart of revised module -TTER (Page 2 of 2)

more conservative prediction of the magnitude of the amount of energy being coupled from an emitter to a receptor.

4.6 TEST RESULTS AND FINAL REMARKS

Comparative runs of the improved code on representative test cases have yielded satisfactory results, as shown in Figure 4.20 through 4.24, which correspond to the same test cases previously illustrated in Figures 4.1 through 4.5 respectively. In all cases, the improvements remove a vulnerability in AAPG by eliminating non-physical paths and by computing paths that are intuitively more plausible. The AAPG graphics features make the results all the more striking and serve well in increasing the user's confidence in the code. The revised code produces shorter coupling path lengths and correspondingly lower path loss computations and hence more conservative predictions of EMI margins. In Figures 4.20 and 4.21, the path lengths are reduced by about 10% and the path losses are reduced by a few decibels. In Figures 4.22 and 4.24, the path lengths are halved and the path losses are reduced by approximately 50 dB. In Figure 4.23, the 280 dB decrease in path loss is the most dramatic improvement.

Important applications of these improvements include EMI margin predictions between the large number of antennas of electronic systems located on the nose of a particular aircraft and close formation flying scenarios during refuelling in which an undesirable level of electromagnetic interference from one aircraft to another could have disastrous consequences.

The algorithm changes and improvements described in this chapter make the code more structured and facilitate future code upgrades. The improvements, however, only tell half of the story. Although the computation of the geodesic on the nose section of the airframe is now correct, an analogous assessment of the graphics display algorithms is required so that one-to-one correspondence between the computed and displayed paths

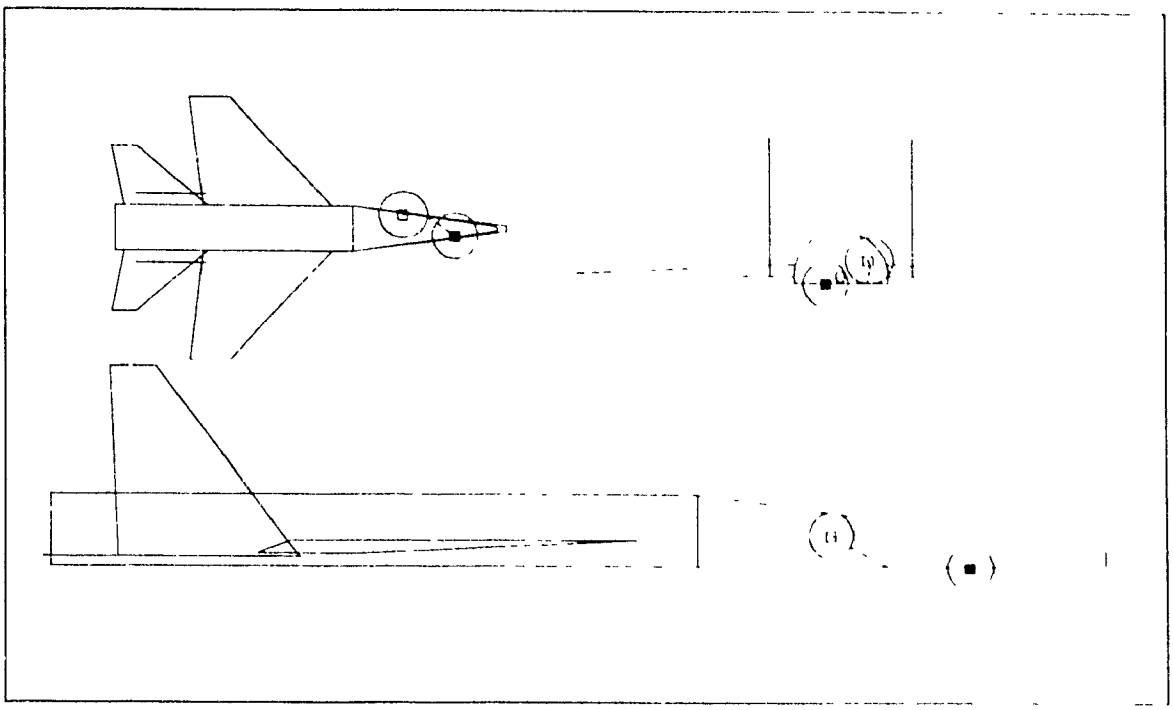

Figure 4.20. AAPG plot showing corrected cone/flat bottom interface point, frequency = 225 MHz, path length = 2.3 λ, path loss = −30.9 dB [15]

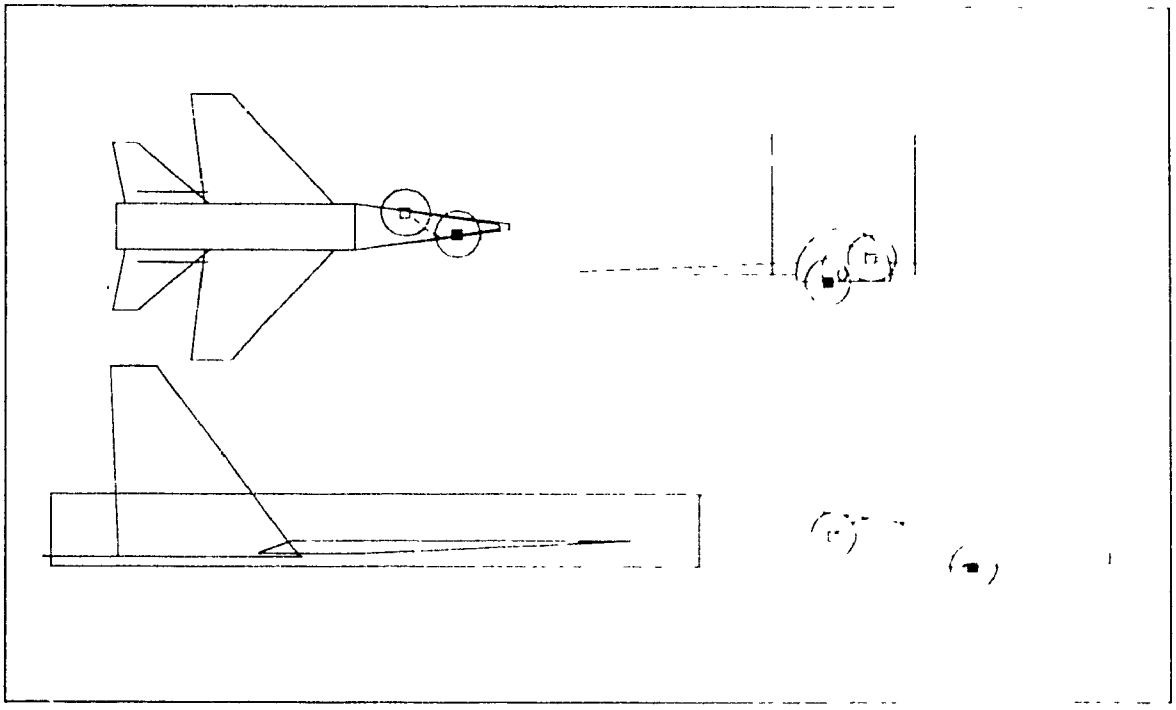

Figure 4.21. AAPG plot showing path no longer penetrating cone fuselage, frequency = 225 MHz, path length = 2.9 λ, path loss = −42.4 dB [15]

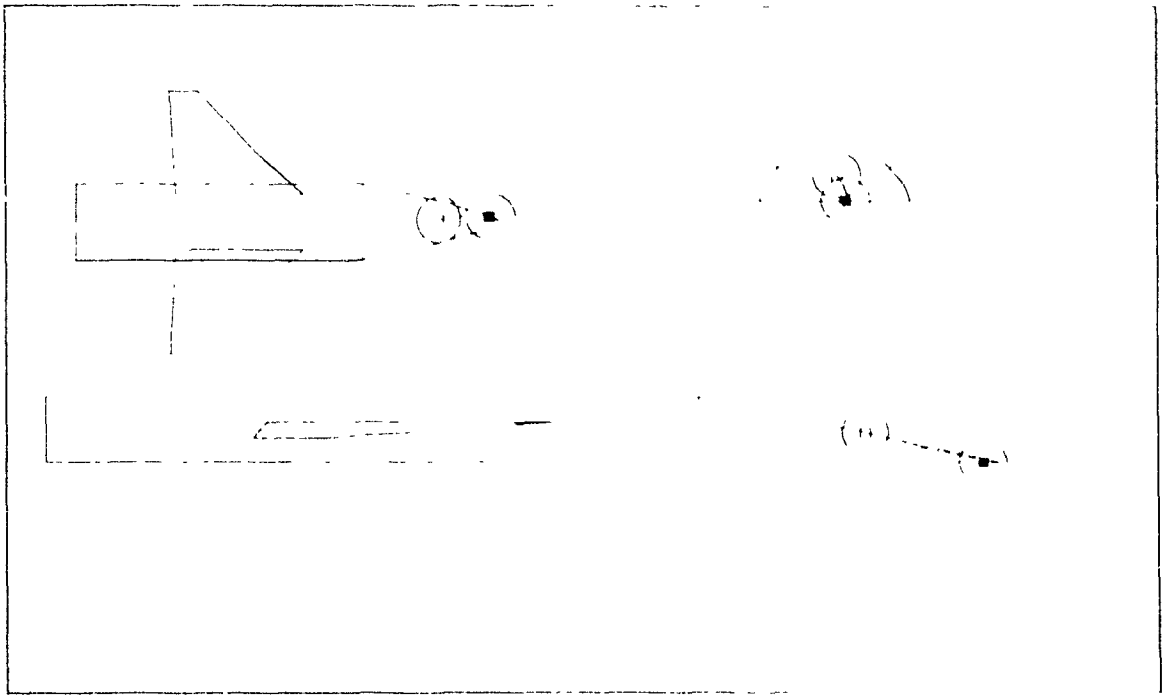

Figure 4.22. AAPG plot showing correct path along cone surface, frequency [illegible] MHz, path length = 2.0 λ, path loss = 28.3 dB [15]

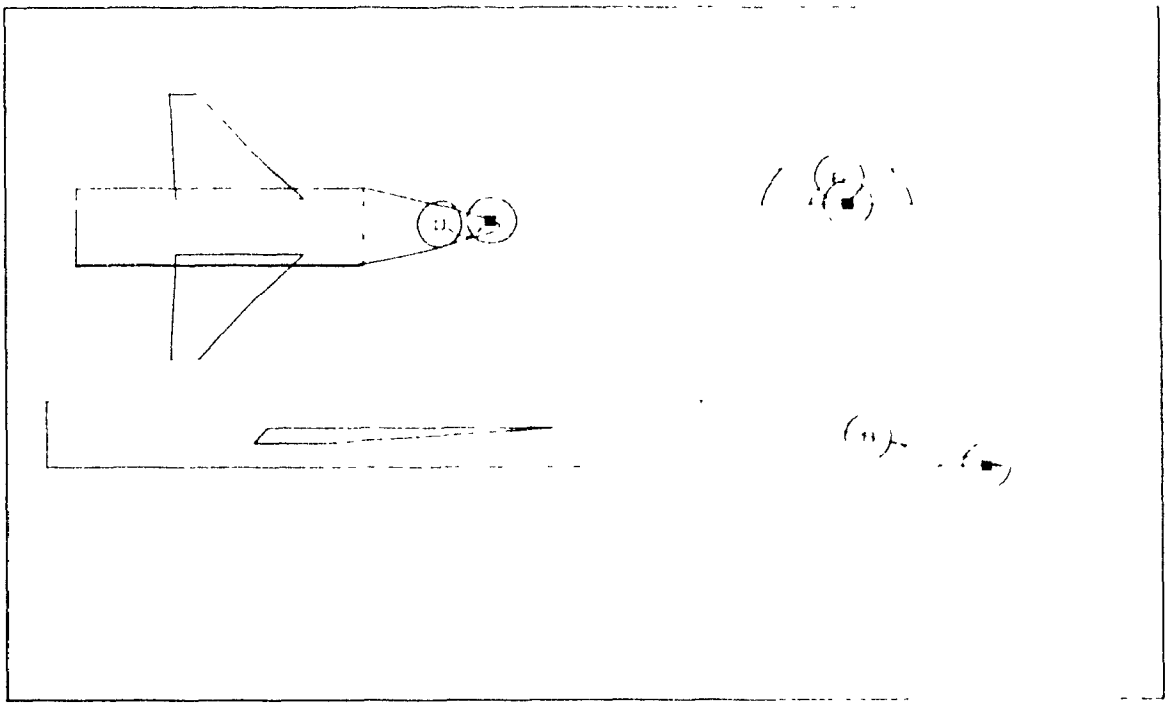

Figure 4.23. AAPG plot showing correct physical path, frequency = 225 MHz, path length = 2.4 λ, path loss = 32.5 dB [15]

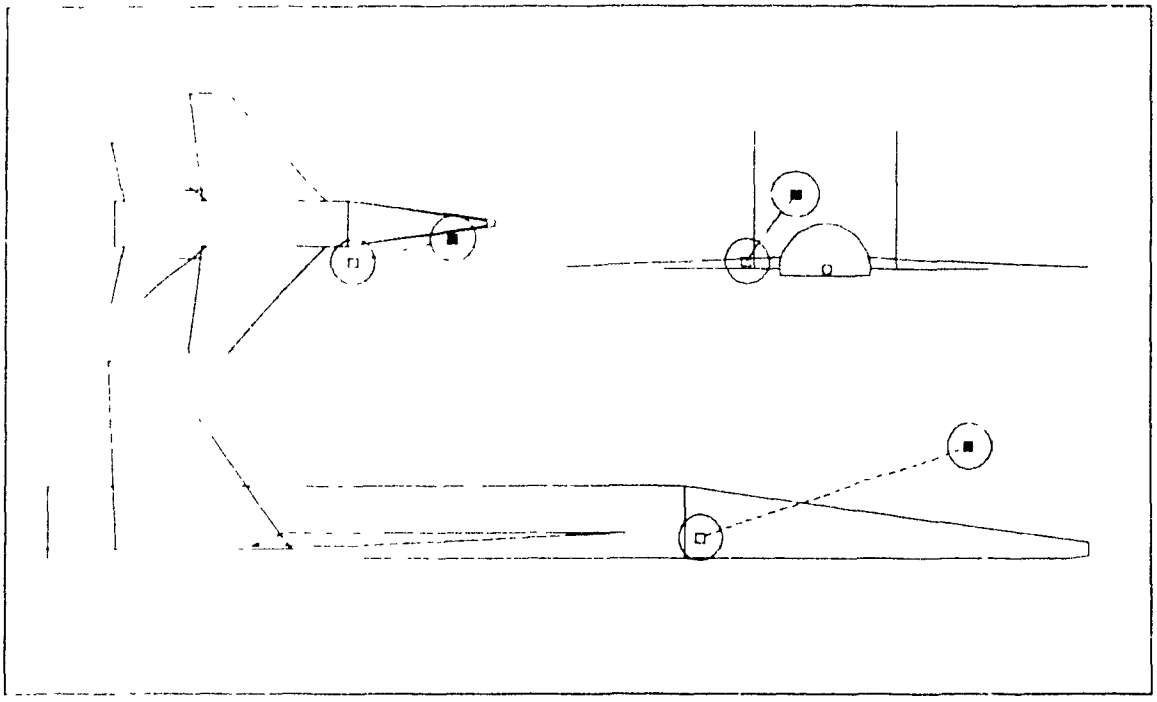

Figure 4.24. AAPG plot showing correct straight-line path, frequency = 225 MHz, path length = 4.1 λ, path loss = -34.2 dB [15].

is maintained. Such an assessment is presented in the next chapter.

CHAPTER 5

CONE GEODESIC DISPLAY IN AAPG V07

5.1 INTRODUCTION

The changes described in Chapter 4 improve and correct the EMCCS algorithms that compute the EMI coupling path on the nose section of the model. Corresponding improvements in the Graphical Data Management System's (GDMS) algorithms that display the calculated geodesics on the aircraft's nose section are necessary in order to maintain the fundamental AAPG principle of one to one correspondence between the calculated trajectory and its graphical representation. This essential principle gives the EMC analyst a natural appreciation of the electromagnetic phenomena be they direct coupling or creeping wave along the perfectly conducting surface of the nose cone model as they occur between the interfering systems. Furthermore, a concise presentation of EMI margin output, in combined numerical-graphical format, is of great assistance to the EMC analyst who would otherwise be overwhelmed by numerical tabulations.

This chapter studies the AAPG V07 routines that display the cone geodesic and describes revisions to those routines that are found to be deficient. The improvements, test results, and their impact on realistic aircraft EMC problems are outlined. Some representative test cases which reveal potential problem areas in the GDMS algorithms are shown in Figures 5.1 through 5.4 and have been reported in references [15,16]. As noted in Chapter 4, the complexity of the algorithms that display the geodesic path requires fairly detailed flow-charts throughout this chapter in order to clearly present this aspect of the thesis' contribution. The flow-charts from the former erroneous algorithms are not presented, but the occurrence of the errors are pointed out in the descriptions of the new algorithms.

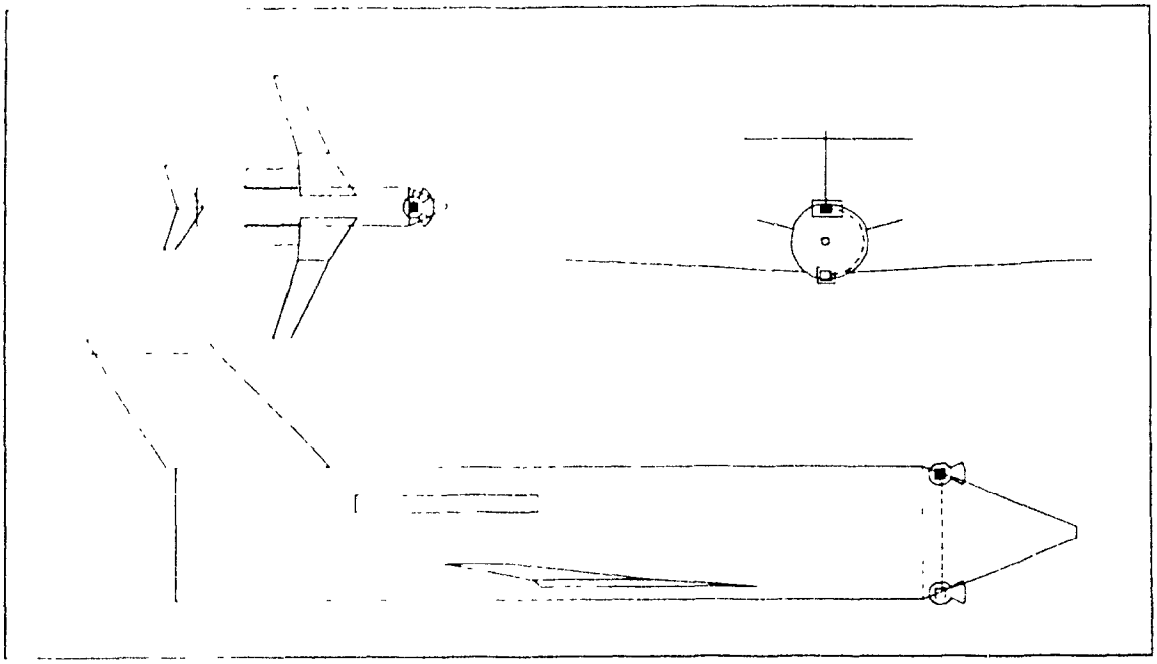

Figure 5.1. AAPG plot showing incorrect display of cone geodesic: frequency = 9.315 GHz, path length = 118 λ, path loss = -164.2 dB: ■(AZ,EL) = (-90.00°,0.00°), □(AZ,EL) = (-90.00°,0.00°) [15]

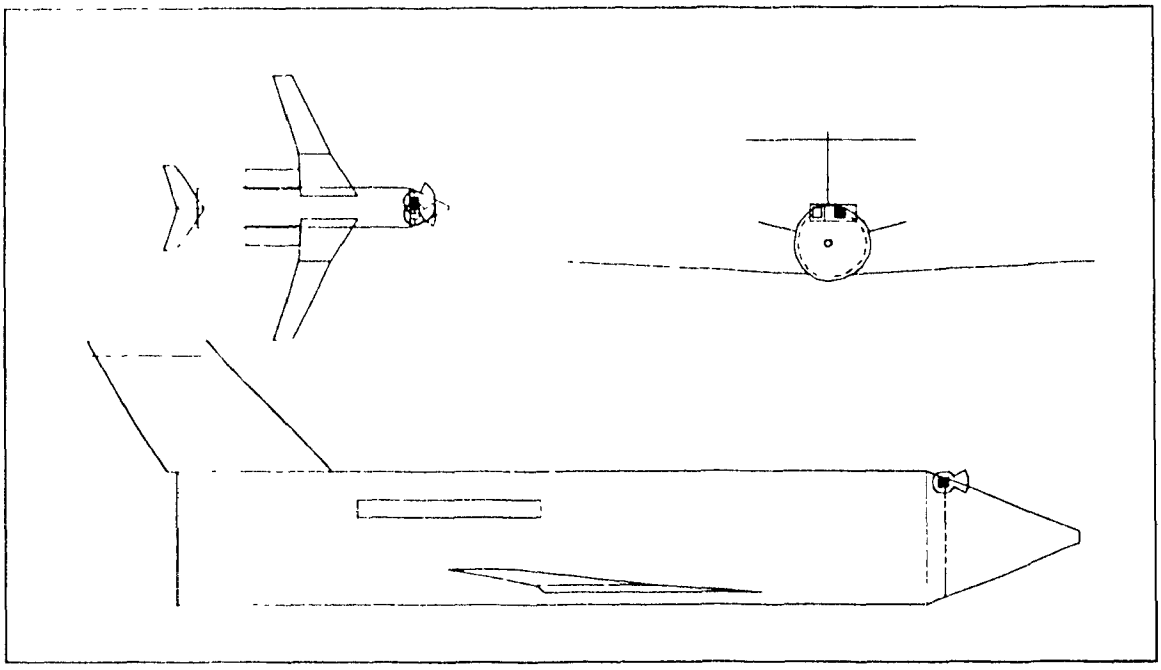

Figure 5.2. AAPG plot showing incorrect display of secondary coupling path on cone: frequency = 9.315 GHz, path length = 208 λ, path loss = -231.6 dB: ■(AZ,EL) = (-90.00°,-19.97°), □(AZ,EL) = (90.00°,-19.97°).

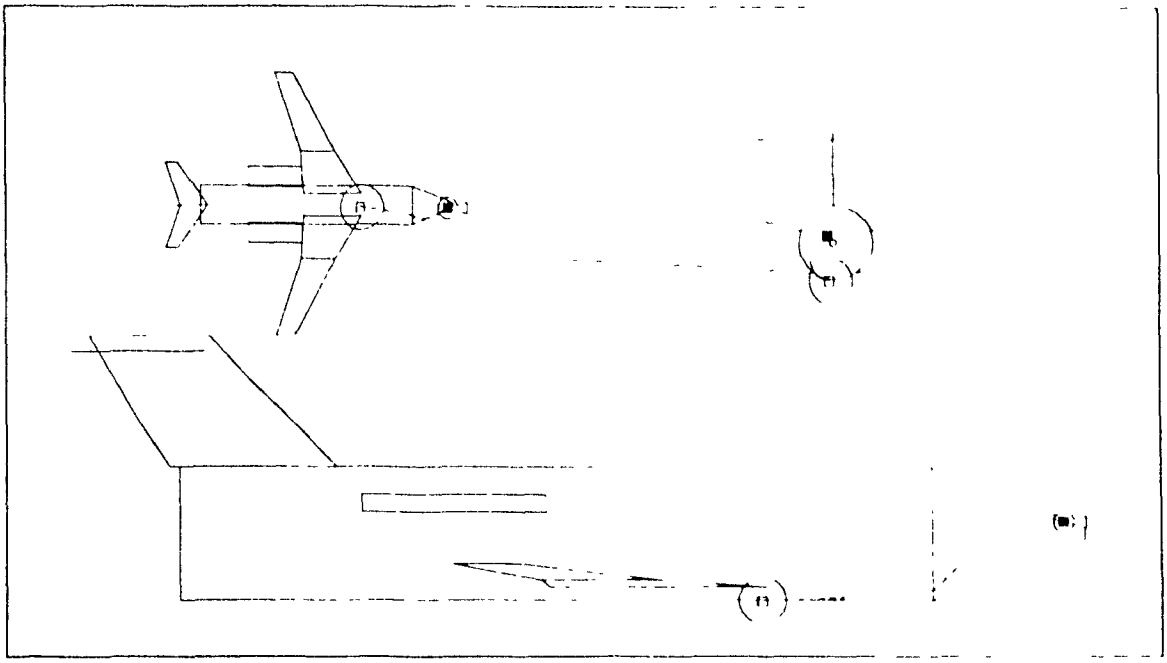

Figure 5.3. AAPG plot showing incorrect display of cone geodesic frequency = 8.000 GHz, path length = 177 λ, path loss = 101.1 dB ■(AZ,EL) = (133.59, -10.48), □(AZ,EL) = (9.52, 0.89)

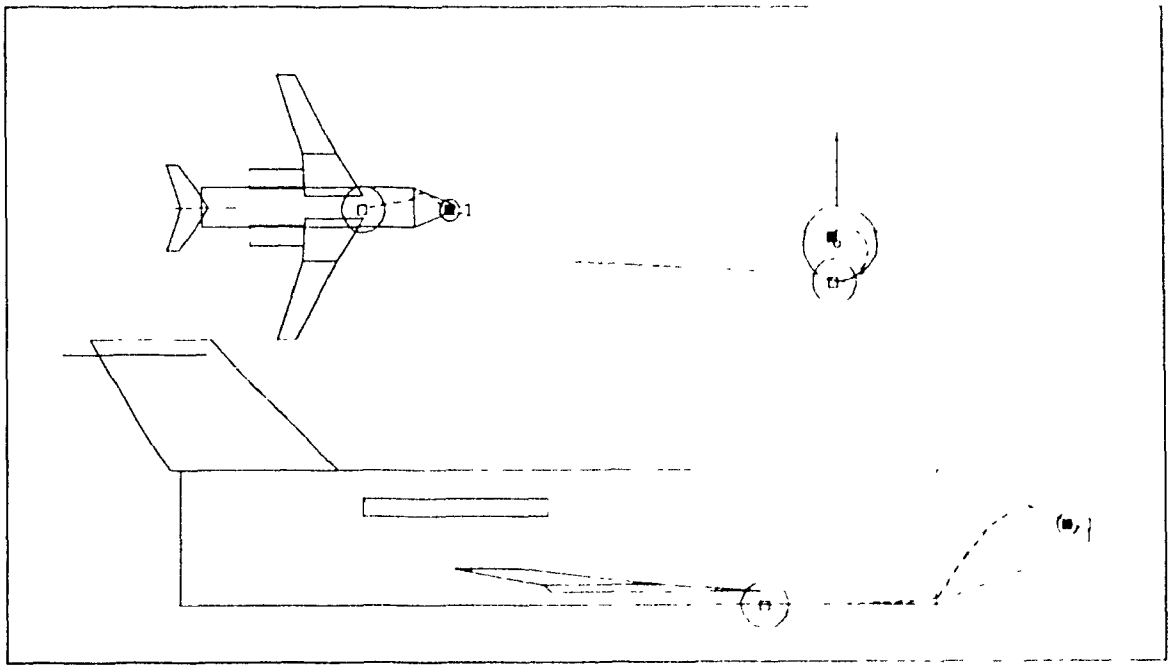

Figure 5.4. AAPG plot showing incorrect display of secondary coupling path on cone frequency = 8.000 GHz, path length = 187 λ, path loss = 140.6 dB ■(AZ,EL) = (-130.99, 40.54), □(AZ,EL) = (11.25, 1.05)

5.2 EMI MARGIN AND PROPAGATION PATH DISPLAY ALGORITHMS IN MODULE <EMIDSP>

Chapter 2 outlines the role of the Graphical Data Management System (GDMS). The GDMS contains the modules of code which handle the various types of graphical displays of the computations associated with the aircraft and interfering electronic subsystems. The routines which manage the EMI Margin and Propagation Path Display are of particular interest because they contain the algorithms that display the aircraft model and the EMI coupling path, such as the cone geodesics. The module <EMIDSP> oversees the key coupling path display tasks. Its logic is illustrated by the top-level flowchart in Figure 5.5 and is described below.

At the beginning of <EMIDSP>, the graphics display screen is cleared and the security classification, if specified in the Input Data File, is written at the top-left and bottom-right corners of the screen. The EMI Margin display header, the aircraft name, and the interfering transmitter and receiver subsystem and antenna names are written to the appropriate areas on the graphics display screen.

The module <DRAWPT> is then called to display the aircraft model and the EMI coupling path. Control is returned to <EMIDSP> which calls the module <PANGLE> (not discussed in this thesis) in order to compute and display the propagation path angles at each antenna. As shown in Figure 2.11, other supporting data are also displayed as part of the EMI Margin and Propagation Path Display such as the aircraft's designation (i.e. "CT-144A"), the names of the interfering transmitter and receiver, and the perspective from which the path is being viewed. The details of these are not essential to this discussion.

It remains to describe the function and deficiencies of, and the modifications to the fundamental modules which <EMIDSP> uses in order to display the EMI coupling path around the nose cone section of the aircraft fuselage model. The descriptions of the

primary GDMS modules that are presented in this chapter are shown in Table 5.1 and their relationship is illustrated in the tree diagram of Figure 5.6.

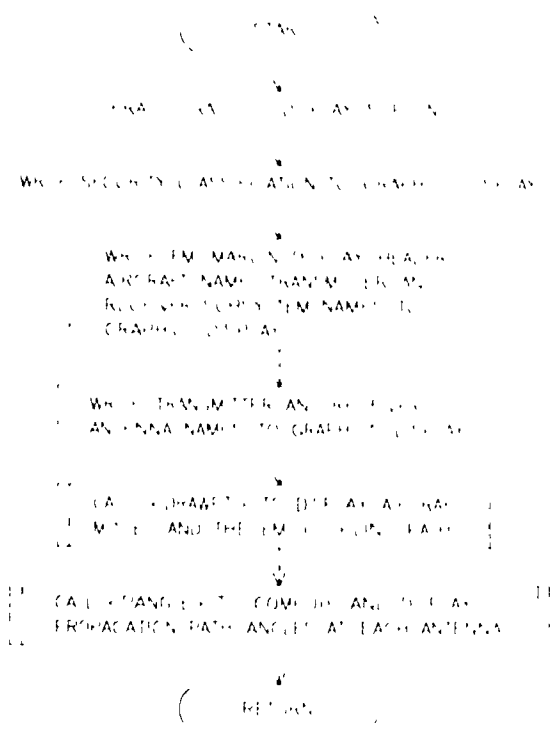

Figure 5.5. Top-level flow chart of module EMIDSP.

Table 5.1. Descriptions of cone geodesic display modules.

Module Name	Description
<EMIDSP>	Top level module to draw graphics portion of EMI Margin and Propagation Path Display.
<DRAWPT>	Draws aircraft model and EMI coupling path
<D3TODC>	Maps point on three-dimensional (3-D) nose cone surface to point on two-dimensional (2-D) developed cone
<DCTOD3>	Maps point on 2-D developed cone to 3-D nose cone surface
<VECDIR>	Determines coupling path direction at a specific point along the path

Figure 5.6. Cone geodesic display modules in GDMS.

5.3 CONE GEODESIC DISPLAY ALGORITHM IN MODULE <DRAWPT>

The function of subroutine <DRAWPT> is to draw the aircraft model and the propagation path which can be displayed for any azimuth and elevation viewing angles requested interactively by the user. The flow-chart of Figure 5.7 illustrates the important aspects of the revised plotting algorithm in <DRAWPT> and is provided to complement the discussion here. The module <DRAWPT> first calls <MODEL> to draw the aircraft model. The remainder of <DRAWPT> deals with the display of the EMI coupling path, and is the main focus of the discussion in this section.

The routine <DRAWPT> retrieves the start and end antenna position information associated with the interfering systems and displays the location and gain pattern relative to the aircraft model. In iterative fashion the routine <DRAWPT> draws each segment of the complete propagation path between the start and end antennas.

For each path segment, the start and end points, $Q_1(\rho_1,\phi_1,z_1)$ and $Q_2(\rho_2,\phi_2,z_2)$, and the path segment type flag indicating either a straight line, cylindrical or conical spiral segment, are retrieved from the appropriate Mass Storage Data Files (MSDF). <DRAWPT> then branches to the block of code pointed to by the path segment type flag. Here the discussion of this process concentrates on the display of conical spiral path

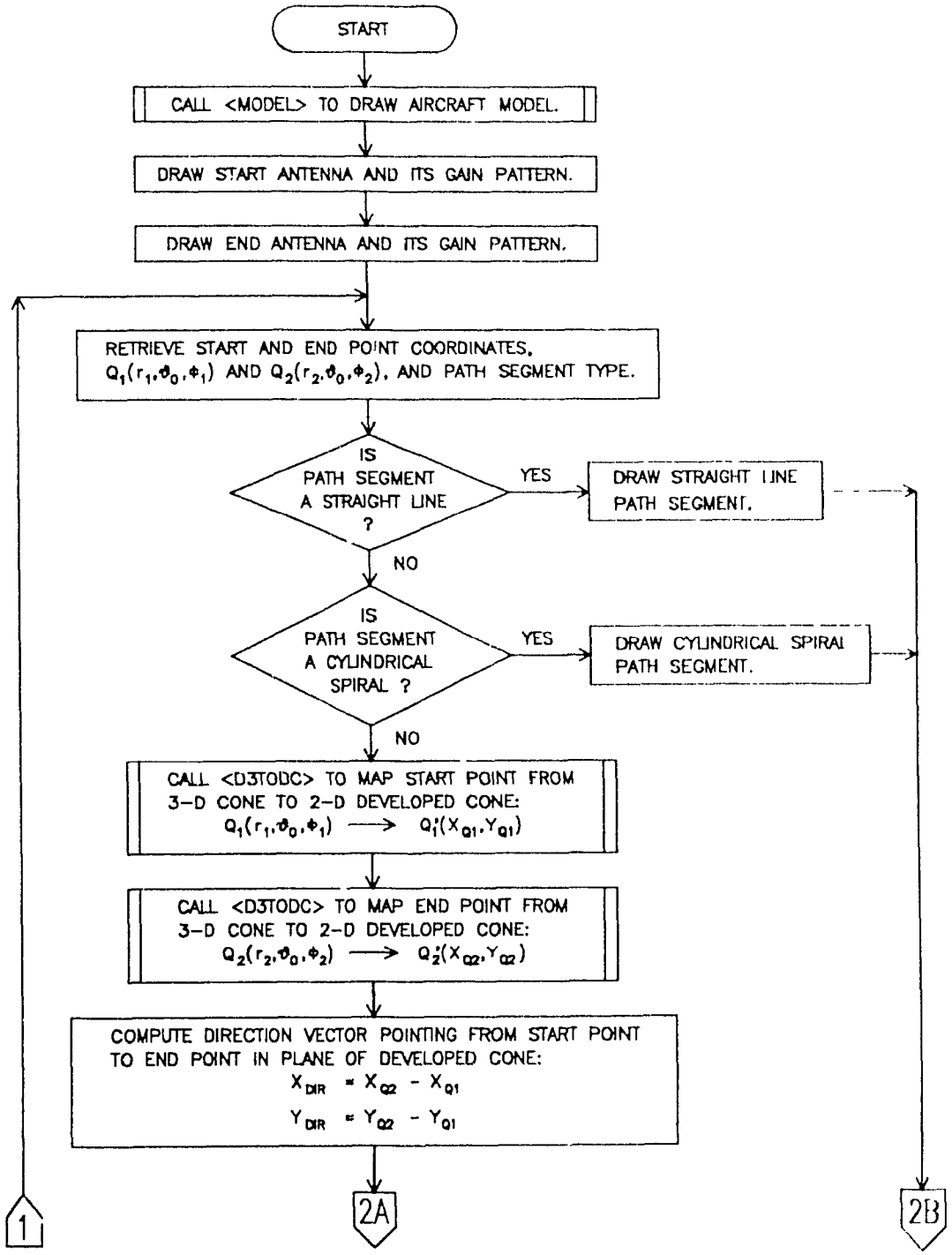

Figure 5.7. Flow-chart of revised module <DRAWPT> (Page 1 of 2)

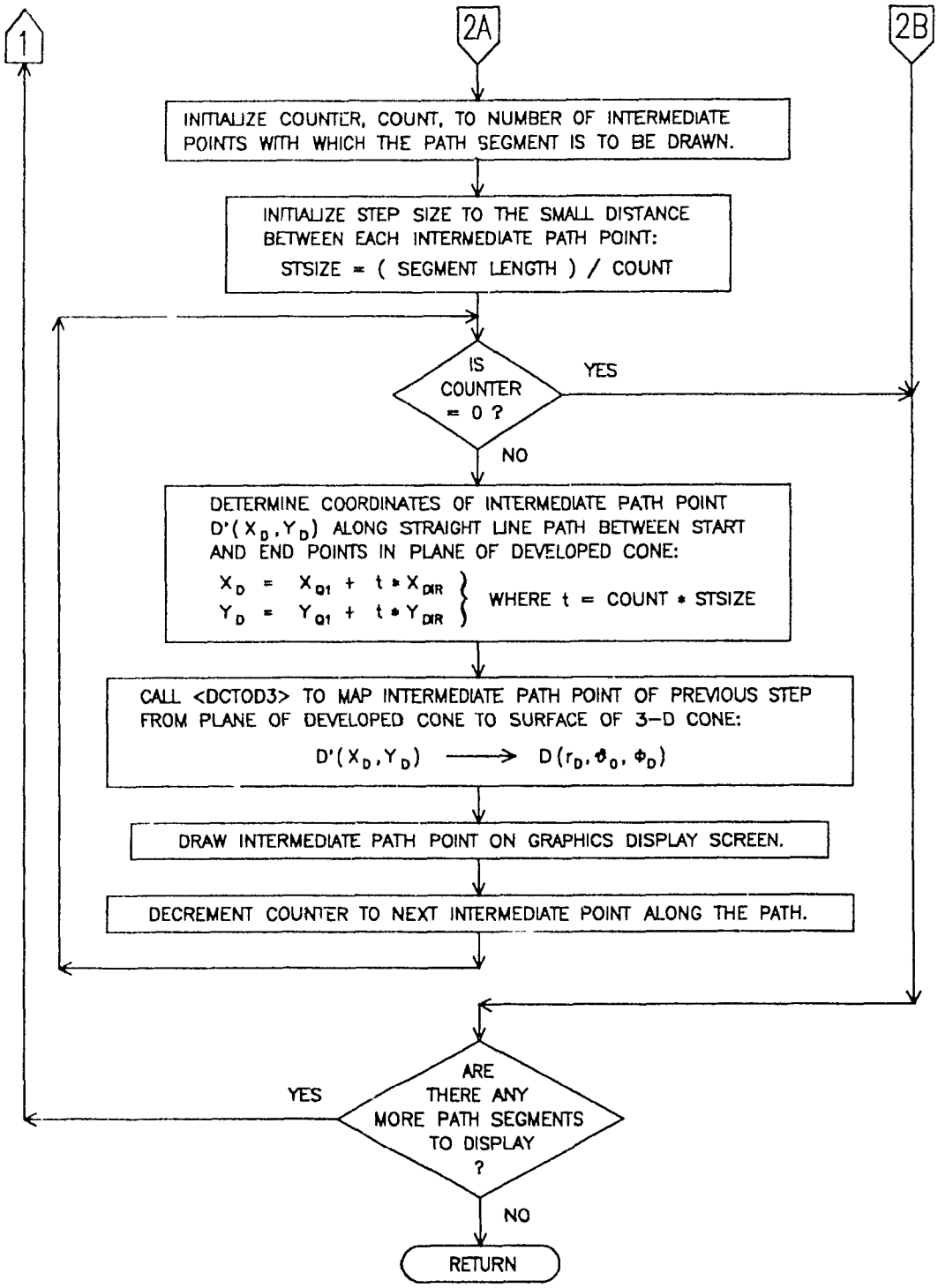

Figure 5.7. Flow-chart of revised module <DRAWPT> (Page 2 of 2).

segments

In the erroneous algorithms of <DRAWPT>, the displayed path is approximated by the parametric equations from reference [25] as

$$\rho = \rho_1 + t(\rho_2 - \rho_1) , \tag{5.1a}$$

$$\phi = \phi_1 + t(\phi_2 - \phi_1) , \tag{5.1b}$$

$$z = z_1 + t(z_2 - z_1) . \tag{5.1c}$$

For example, Figures 5.1 and 5.2 display a semicircular geodesic path on the cone surface for two antennas located at the same fuselage station, $z_1 = z_2$, and on opposite sides of the cone, $|\phi_1 - \phi_2| = \pi$ radians. The approximation of the conical spiral shown in Figures 5.1 and 5.2 is inadequate because the displayed geodesic path should tilt forward slightly to represent the true geodesic path.

The erroneous <DRAWPT> algorithm was revised and corrected. The new algorithms in <DRAWPT> apply the concept of a "developable surface" [24, 10] in which a three-dimensional (3-D) surface is mapped onto a two dimensional (2-D) or planar surface. Based on this principle, the trajectory and length of a conical spiral geodesic between two points on a 3-D cone surface correspond to the trajectory and length of a straight line segment between the mapped points on the equivalent planar "developed" surface which resembles a pie slice. The appropriate mathematical transformations or mappings must be used between points on the 3-D and developed cones as illustrated by Figure 5.8.

The (x,y,z) coordinate system shown in Figure 5.8(a) is shown to be left handed in order to track with the coordinate system used by the AAPG GDMS routines. The points $Q_1(\rho_1,\phi_1,z_1)$ and $Q_2(\rho_2,\phi_2,z_2)$ are represented in spherical coordinates in Figure 5.8(a) as $Q_1(r_1,\theta_0,\phi_1)$ and $Q_2(r_2,\theta_0,\phi_2)$, respectively, where

$$r_i = \frac{z_i}{\cos\theta_0} , \tag{5.2a}$$

$$\rho_i = z_i \tan\theta_0 . \tag{5.2b}$$

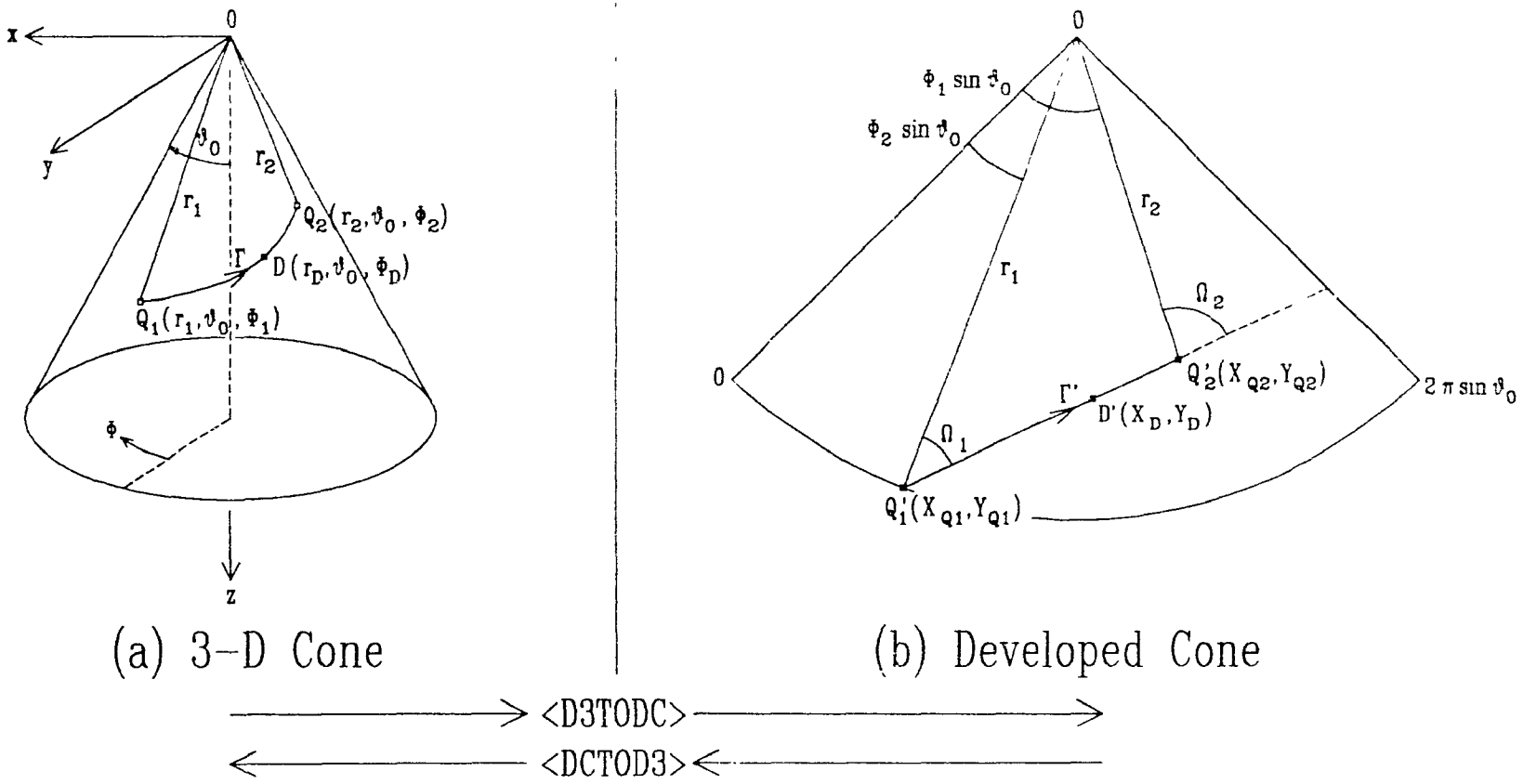

Figure 5.8. Mappings performed by <DCTOD3> and <D3TODC> in module <DRAWPT>

The start and end points of a conical spiral segment on the 3-D cone in Figure 5.8(a) are mapped to the developed cone surface in Figure 5.8(b) by means of the newly designed routine <D3TODC> as follows. Q_1 is mapped to $Q_1'(X_{Q1}, Y_{Q1})$, and Q_2 is mapped to $Q_2'(X_{Q2}, Y_{Q2})$. The parametric equations for the straight line segment between Q_1' and Q_2' are simply

$$X = X_{Q1} + t\,(X_{Q2} - X_{Q1}) \tag{5.3a}$$

$$Y = Y_{Q1} + t\,(Y_{Q2} - Y_{Q1}) \tag{5.3b}$$

where t varies between 0 and 1. As illustrated in the program loop on the second page of the flow-chart of <DRAWPT>, the algorithm proceeds along the straight line path between Q_1' and Q_2' by decrementing the parameter t in equations (5.3) from 1 to 0 in small steps. With each step, the intermediate point $D'(X_D, Y_D)$ on the straight line segment is computed from the parameter t using equations (5.3) and is then mapped from the developed cone to the point $D(r_D, \theta_D, \phi_D)$ on the 3-D cone surface by means of the newly designed routine <DCTOD3>. The point D is then plotted at the appropriate location on the graphics display screen depending on the viewing angle requested by the user.

Once the current path segment is completely plotted, the module <DRAWPT> loops back to repeat the process for each of the remaining path segments until the complete propagation path is drawn. Control is then returned to the calling routine namely, the module <EMIDSP>.

5.4 MAPPING ROUTINES <D3TODC> AND <DCTOD3>

The key to the improvement in the display of conical spiral geodesic paths, which is implemented in the newly created AAPG routines <D3TODC> and <DCTOD3>, is the principle of "developable surfaces". Lee [24] defines a developable surface as one which

> "(a) may be generated by a continuous motion of a straight line (the straight lines on the surface are called <u>generators</u>) and

(b) has the same tangent plane at all points on any given generator."

If a cone is cut along a generator, i.e. any ray originating from the cone apex which runs along the cone surface, it may be opened up or "unwrapped" to become a pie-slice on a plane without stretching or shrinking. A conical spiral becomes a straight line on the developed cone. As depicted in Figure 5.9, a simple and effective method of visualizing this principle is to draw a line segment on a flat sheet of thin cardboard, roll the sheet into a cone and compare the trajectory on the cardboard model with that shown on the AAPG graphics. The resultant developed cone is illustrated in Figure 5.10.

Subroutine <D3TODC> is a new module designed to compute the (X,Y) coordinates of the endpoints of the segment $Q_1'Q_2'$, i.e. the mapped geodesic path Γ', on the developed cone surface. The module <D3TODC> maps the start point $Q_1(\rho_1,\varphi_1,z_1)$ to the point $Q_1'(X_{Q1},Y_{Q1})$ where

$$X_{Q1} = 0 , \tag{5.4a}$$

$$Y_{Q1} = r_1 , \tag{5.4b}$$

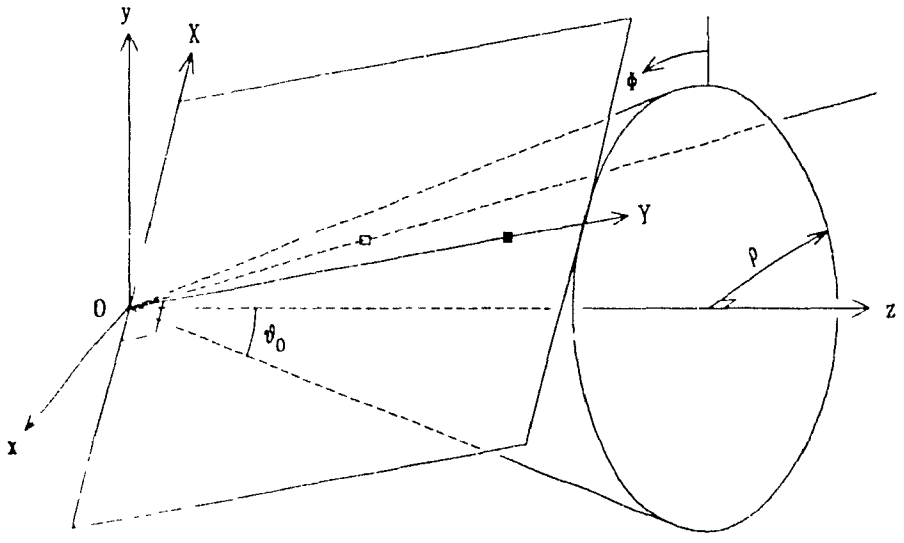

Figure 5.9. Unwrapping function of modules <D3TODC> and <DC1OD3> [39].

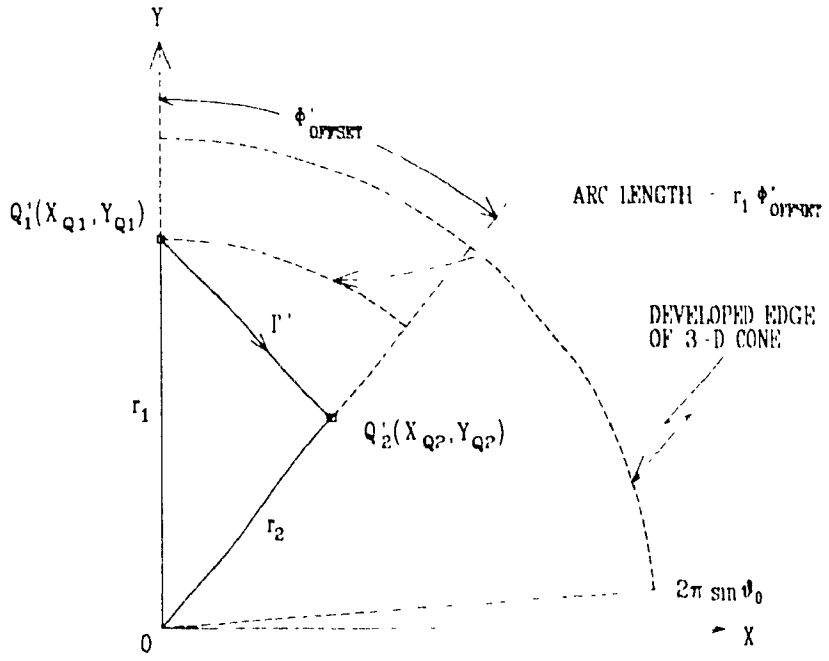

Figure 5.10. Equivalent points $Q'_1(X_{Q1},Y_{Q1})$ and $Q'_2(X_{Q2},Y_{Q2})$ and geodesic path l' on a two dimensional (2-D) pie-slice as mapped by the subroutine <D3TODC>.

and r_1 is computed from equation (5.2a). Figure 5.11 illustrates the offset angle ϕ_{OFFSET} between points Q_1 and Q_2, which can be computed from the position angles ϕ_1 and ϕ_2. Since distances on the surface of the cone are not stretched or shrunken in the process of generating a developed surface, the arc length $\rho_1\phi_{OFFSET}$ from Figure 5.11 equals the arc length $r_1\phi'_{OFFSET}$ from Figure 5.10, i.e

$$r_1 \, \phi'_{OFFSET} \;=\; \rho_1 \, \phi_{OFFSET} \,. \tag{5.5}$$

The module <D3TODC> uses an expression for the angle ϕ'_{OFFSET} in Figure 5.11 in terms of the angle ϕ_{OFFSET} in Figure 5.10 which is derived from equations (5.2a), (5.2b) and (5.5) to be

$$\phi'_{OFFSET} \;=\; \phi_{OFFSET} \sin\vartheta_0 \,. \tag{5.6}$$

The module <D3TODC> maps the end point $Q(\rho_2,\phi_2,z_2)$ to the point $Q(X_{Q2}, Y_{Q2})$ using the equations

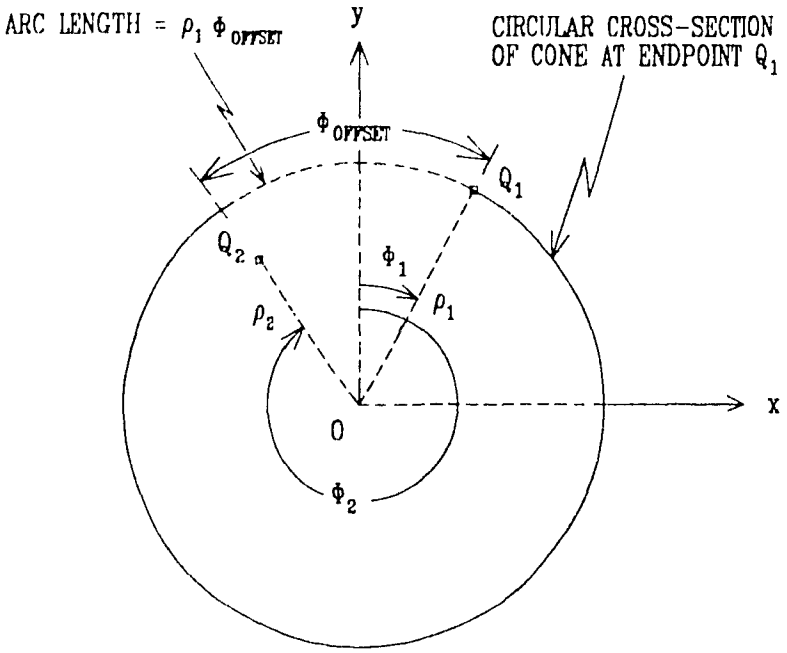

Figure 5.11. View of the cone in Figure 5.8(a) from cone apex.

$$X_{Q2} = r_2 \sin \phi'_{OFFSET}, \tag{5.7a}$$

$$Y_{Q2} = r_2 \cos \phi'_{OFFSET}, \tag{5.7b}$$

where r_2 is computed from equation (5.2a). The flow-chart of Figure 5.12 summarizes the algorithm employed by the routine <D3TODC>.

The routine <DCTOD3> is also a newly designed module. It uses the algorithm described for <D3TODC> in reverse to determine the coordinates of a point on the conical spiral geodesic from the developed cone surface. The flow-chart of Figure 5.13 summarizes the logic of routine <DCTOD3> The flow-chart illustrates how the module <DCTOD3> uses the (X,Y) coordinates of the point on the surface of the developed cone and the parameters of the nose cone model to compute the (ρ,ϕ,z) coordinates on the surface of the 3-D cone

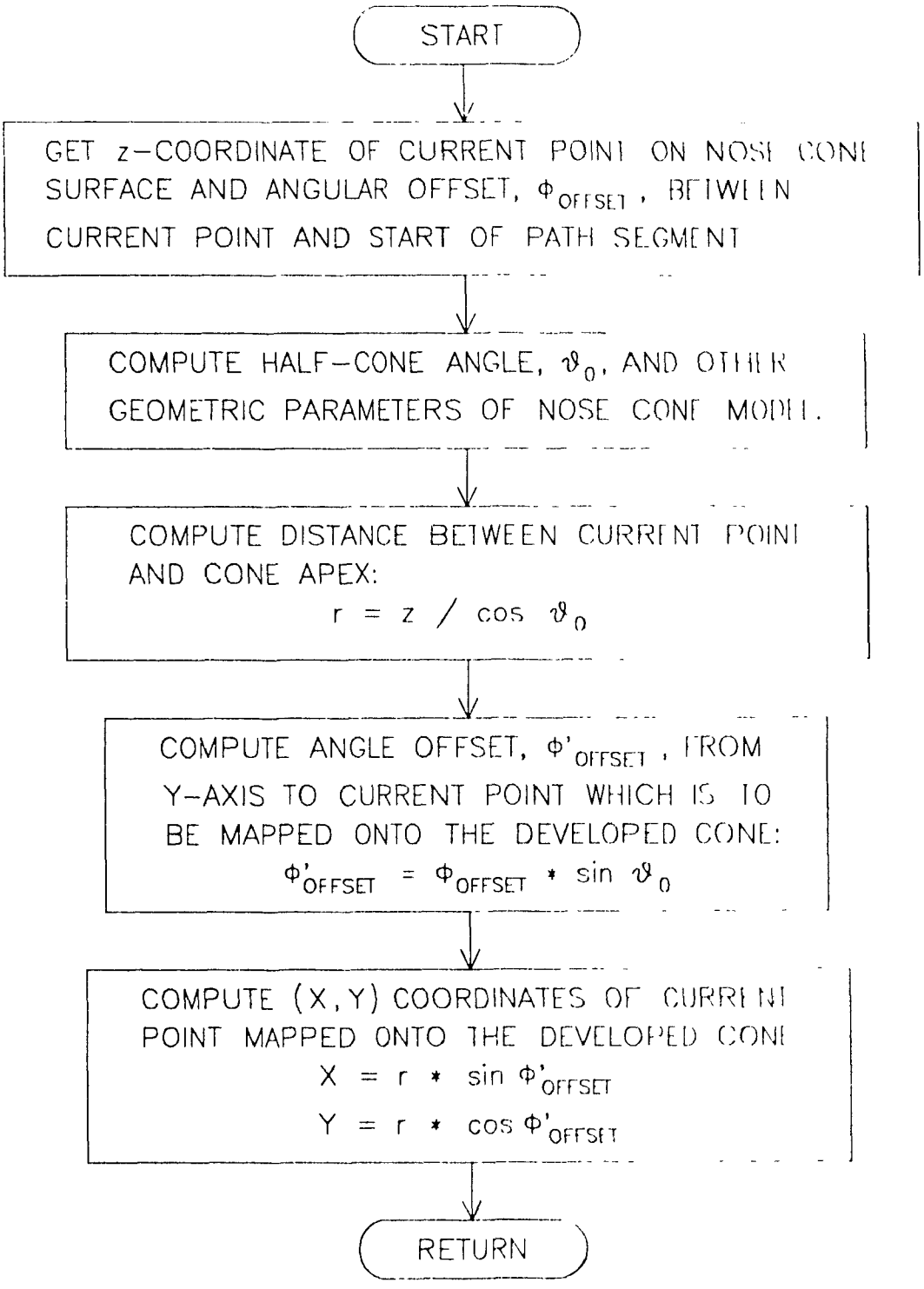

Figure 5.12. Flow-chart of new module "D3TODC".

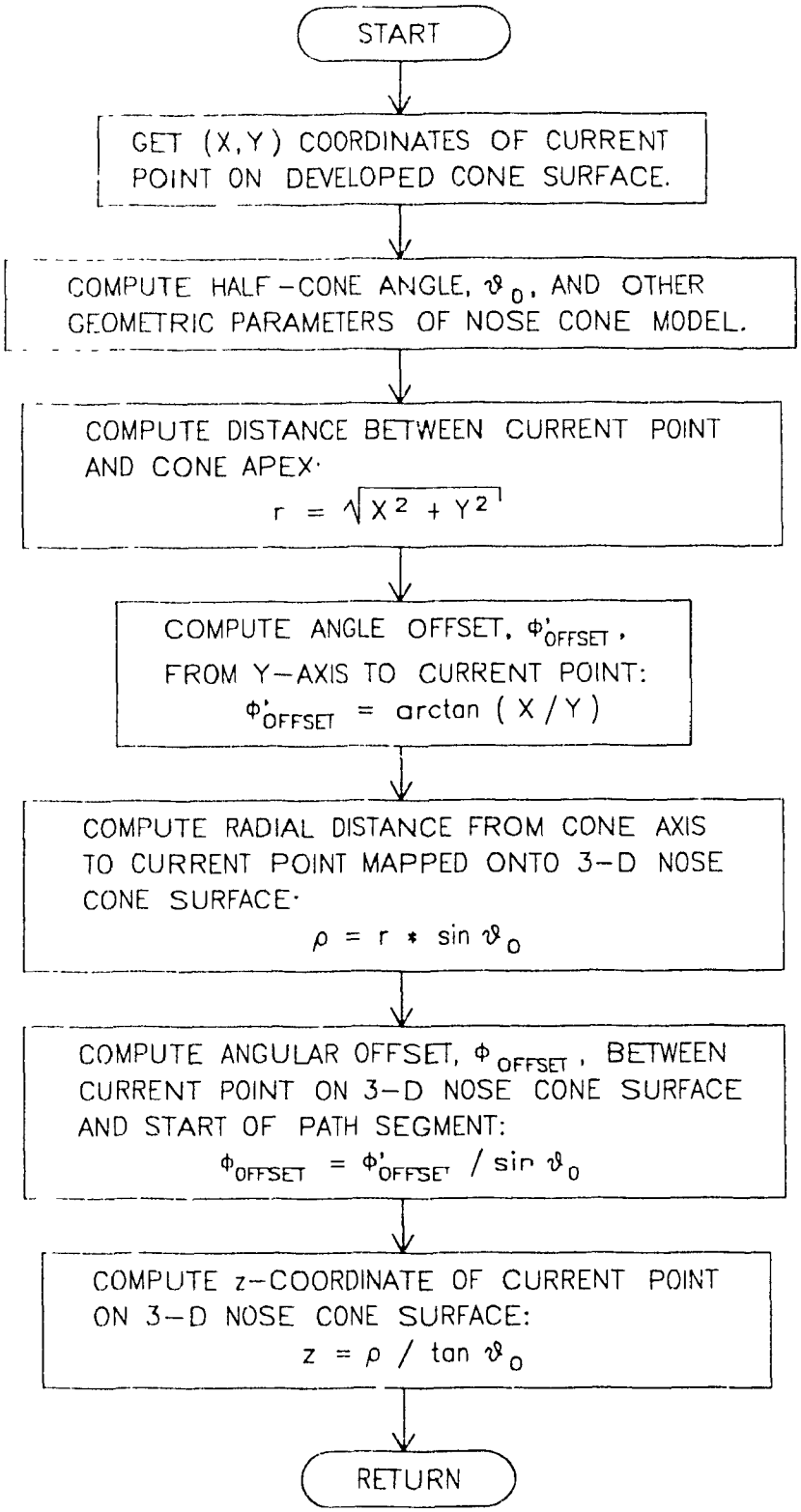

Figure 5.13. Flow-chart of new module <DCTOD3>.

5.5 MODULE <VECDIR>

The improvements implemented in <VECDIR> for a vector tangent to a conical spiral geodesic are important because the vector is used by other routines to compute the azimuth and elevation direction angles taken by the geodesic at a point, Q_1 say, which in turn determine the antenna gain at Q_1 used in the path loss computation. Therefore, more accurate path loss computations are a direct benefit of the improvement in the tangent direction vector. This section provides the mathematical basis for the updated expressions implemented in the subroutine <VECDIR>. The expressions derived in this section supersede those found in the AAPG documentation [25].

Given a geodesic coupling path Γ between endpoints Q_1 and Q_2 in AAPG, the function of the subroutine <VECDIR> is to compute the unit vector, $\hat{a}_1$, tangent to the geodesic path at Q_1 as illustrated in Figure 5.14. The direction of $\hat{a}_1$ in Figure 5.14 is computed as if the geodesic path proceeding from Q_2 to Q_1 were to continue beyond point

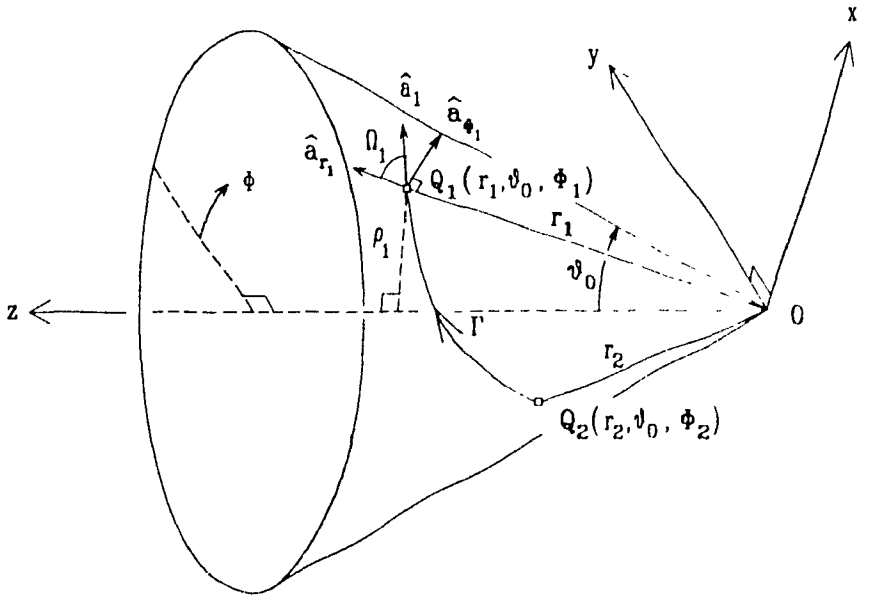

Figure 5.14. Unit vector $\hat{a}_1$ tangent to conical spiral geodesic as computed by AAPG subroutine <VECDIR>.

Q_1. The designations of the points as Q_1 or Q_2 follow from the calling sequence of <VECDIR>, so that the vectors at each end of the geodesic path are computed from separate subroutine calls.

Although Figure 5.14 illustrates the case of a vector tangent to a conical spiral geodesic path, the subroutine <VECDIR> also computes the vector tangent to straight-line and cylindrical spiral geodesic paths. Discussion of the latter two cases is found in the AAPG technical description [25]. This section focuses on the developments for cases in which both endpoints of the geodesic are situated on the conical surface of the aircraft model.

From Figure 5.14, the direction vector $\hat{a}_1$ can be expressed in terms of the orthonormal vectors $\hat{a}_{r_1}$ and $\hat{a}_{\phi_1}$ and the angle Ω_1 as

$$\hat{a}_1 = (\cos \Omega_1)\, \hat{a}_{r_1} + (\sin \Omega_1)\, \hat{a}_{\phi_1}. \tag{5.8}$$

The unit vector $\hat{a}_{r_1}$ is tangent to the cone surface and parallel to a segment drawn from the cone apex to the path endpoint Q_1. The unit vector $\hat{a}_{\phi_1}$ is tangent to the cone surface at a circular cross-section made at the path endpoint Q_1. The angle Ω_1 is measured between the vector $\hat{a}_{r_1}$ and the direction vector $\hat{a}_1$.

Figure 5.15 is a cross-sectional cut of the cone in Figure 5.14 showing the plane which contains the z-axis and the segment OQ_1. The vector $\hat{a}_{r_1}$ is simply

$$\hat{a}_{r_1} = (\cos \theta_0)\, \hat{a}_z + (\sin \theta_0)\, \hat{a}_{\rho_1}. \tag{5.9}$$

Figure 5.16 is a cross-sectional cut of the cone in Figure 5.14 showing the plane which is parallel to the xy-plane and which contains the point Q_1. The vectors $\hat{a}_{\rho_1}$ and $\hat{a}_{\phi_1}$ are then

$$\hat{a}_{\phi_1} = (\cos \phi_1)\, \hat{a}_x + (-\sin \phi_1)\, \hat{a}_y \tag{5.10}$$

$$\hat{a}_{\rho_1} = (\sin \phi_1)\, \hat{a}_x + (\cos \phi_1)\, \hat{a}_y. \tag{5.11}$$

Combining equations (5.8) through (5.11), the direction vector $\hat{a}_1$ can be expressed in terms of the rectangular coordinates as

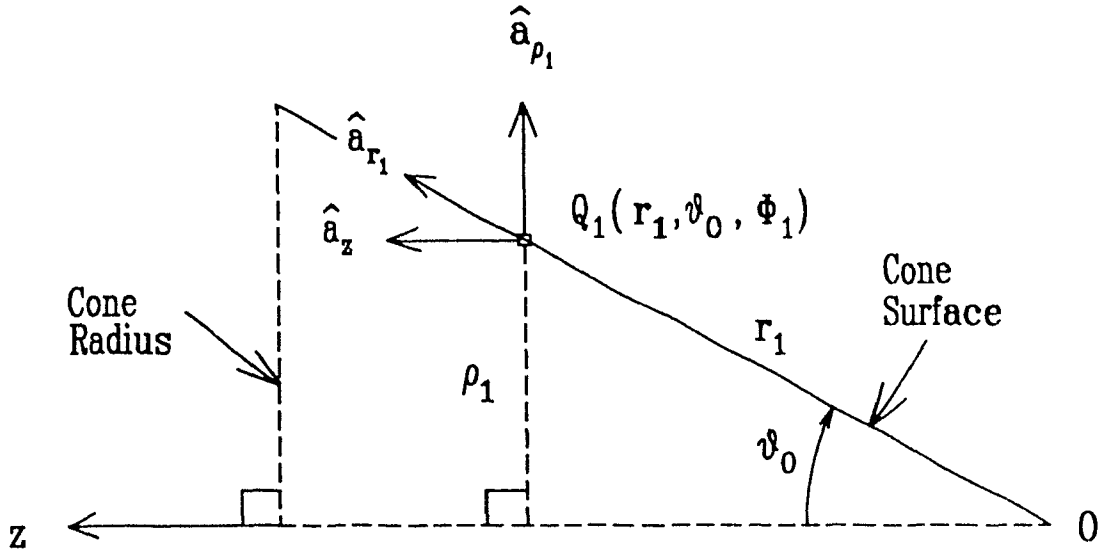

Figure 5.15. Cross-sectional cut of the cone in Figure 5.14 showing the plane which contains the z-axis and the segment OQ_1.

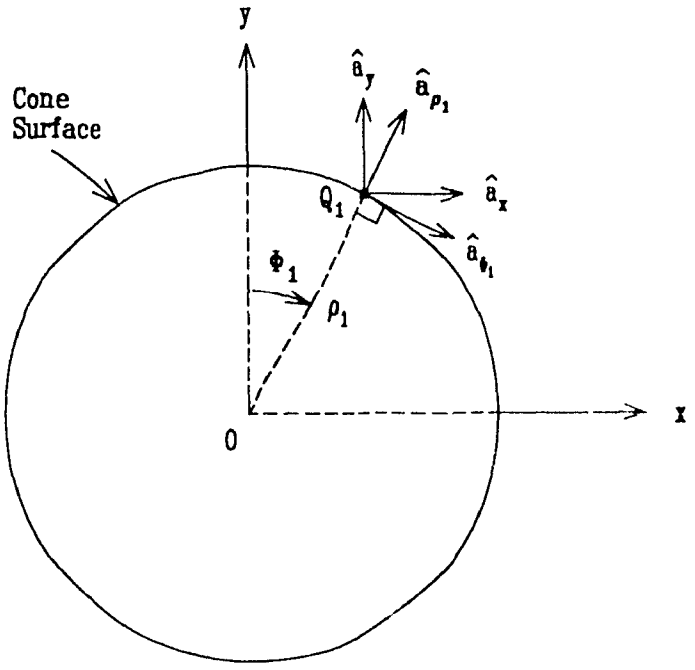

Figure 5.16. Cross-sectional cut of the cone in Figure 5.14 showing the plane which is parallel to the xy-plane and which contains the point Q_1

$$\hat{a}_1 = [(\cos\Omega_1)(\sin\phi_1)(\sin\theta_0) + (\sin\Omega_1)(\cos\phi_1)]\,\hat{a}_x + [(\cos\Omega_1)(\cos\phi_1)(\sin\theta_0) + (\sin\Omega_1)(-\sin\phi_1)]\,\hat{a}_y + (\cos\Omega_1)(\cos\theta_0)\,\hat{a}_z . \quad (5.12)$$

All of the quantities in equation (5.12) are known, except the angle Ω_1. To facilitate the derivation of the expression for the angle Ω_1, the endpoints $Q_1(r_1,\theta_0,\phi_1)$ and $Q_2(r_2,\theta_0,\phi_2)$ of the conical spiral geodesic Γ and the geodesic itself are mapped from the surface of the 3-D cone, as shown in Figure 5.14, to equivalent points, $Q_1'(X_{Q1},Y_{Q1})$ and $Q_2'(X_{Q2},Y_{Q2})$, and the straight-line segment Γ', respectively, on a 2-D pie-slice using the subroutine <D3TODC>, as shown in Figure 5.17. The vector $\hat{a}_1'$ in Figure 5.17 is given by the equation

$$\hat{a}_1' = (\cos\Omega_1)\,\hat{a}_{r_1}' + (\sin\Omega_1)\,\hat{a}_{\phi_1}' . \quad (5.13)$$

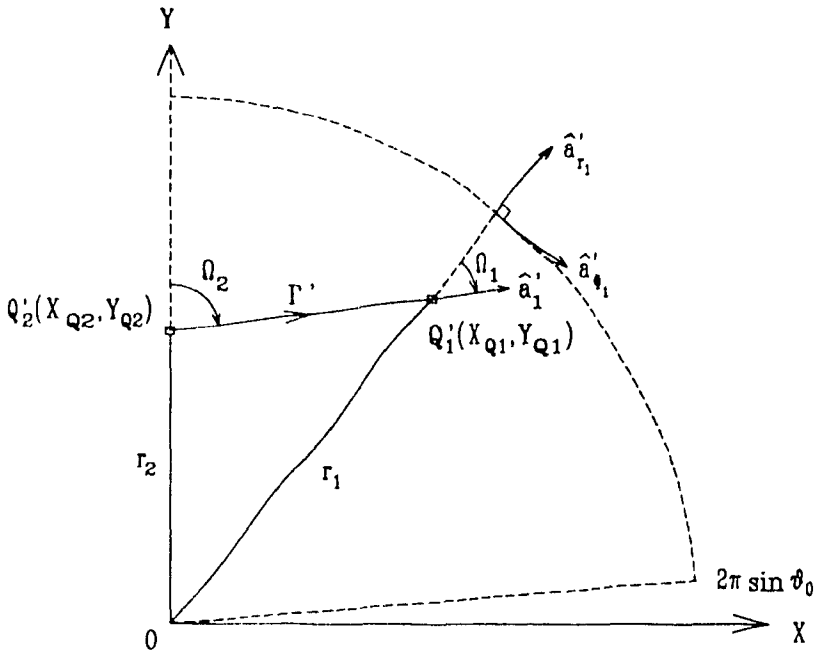

Figure 5.17. Equivalent points $Q_1'(X_{Q1},Y_{Q1})$ and $Q_2'(X_{Q2},Y_{Q2})$ and geodesic path Γ' on a 2-D pie-slice as mapped by the subroutine <D3TODC> within the subroutine <VECDIR>.

From Figure 5.17, the other various vectors and angles on developed cone are also derived. The vector $\overline{Q_2'Q_1'}$, which describes a vector tangent to mapped geodesic 1" at the point Q_1', is given by

$$\overline{Q_2'Q_1'} = (X_{Q1} - X_{Q2})\,\hat{a}_X + (Y_{Q1} - Y_{Q2})\,\hat{a}_Y \,. \tag{5.14}$$

The unit vector $\hat{a}_1'$ is related to the vector $\overline{Q_2'Q_1'}$ by

$$\begin{aligned} \hat{a}_1' &= \frac{\overline{Q_2'Q_1'}}{\left|\overline{Q_2'Q_1'}\right|} \\ &= \frac{(X_{Q1} - X_{Q2})\,\hat{a}_X + (Y_{Q1} - Y_{Q2})\,\hat{a}_Y}{\sqrt{(X_{Q1} - X_{Q2})^2 + (Y_{Q1} - Y_{Q2})^2}} \,. \end{aligned} \tag{5.15}$$

The vector $\overline{OQ_1'}$, a ray which originates at the developed-cone apex and terminates at point Q_1', is given by

$$\overline{OQ_1'} = X_{Q1}\,\hat{a}_X + Y_{Q1}\,\hat{a}_Y \,. \tag{5.16}$$

The unit vector $\hat{a}_{r_1}'$ is related to the vector $\overline{OQ_1'}$ by

$$\begin{aligned} \hat{a}_{r_1}' &= \frac{\overline{OQ_1'}}{\left|\overline{OQ_1'}\right|} \\ &= \frac{X_{Q1}\,\hat{a}_X + Y_{Q1}\,\hat{a}_Y}{\sqrt{X_{Q1}^2 + Y_{Q1}^2}} \,. \end{aligned} \tag{5.17}$$

The cosine of angle Ω_1 is derived from unit vectors $\hat{a}_1'$ and $\hat{a}_{r_1}'$ in equations (5.15) and (5.17), respectively, to be

$$\begin{aligned} \cos\Omega_1 &= \hat{a}_1' \cdot \hat{a}_{r_1}' \\ &= \frac{(X_{Q1} - X_{Q2})\,X_{Q1} + (Y_{Q1} - Y_{Q2})\,Y_{Q1}}{\sqrt{X_{Q1}^2 + Y_{Q1}^2}\,\sqrt{(X_{Q1} - X_{Q2})^2 + (Y_{Q1} - Y_{Q2})^2}} \,. \end{aligned} \tag{5.18}$$

The sine of angle Ω_1 is always positive so it can be computed from the positive square root of the equation

$$\sin\Omega_1 = \sqrt{\left|1 - \cos^2\Omega_1\right|} \,. \tag{5.19}$$

Note that the absolute value of the argument under the square root sign is taken in order prevent run-time errors when rounding errors in equation (5.18) cause the cosine of Ω_1 to be slightly greater than 1.

Therefore equations (5.12), (5.18), and (5.19) fully specify the direction vector $\hat{a}_1$ in terms of known quantities. The flow-chart in Figure 5.18 summarizes the steps in the revised module <VECDIR> which have just been described. Note that the mapping performed by the routine <D3TODC> within the revised module <VECDIR> tracks exactly with the updated approach used by <DRAWPT> in displaying a conical spiral geodesic. The mapping method replaces the closed form expressions for the tangent vector that were previously used by the old version of <VECDIR>. Those closed form expressions for the tangent vector were appropriate since they corresponded exactly to equations (5.1) which were previously used by <DRAWPT> in displaying a conical spiral geodesic. In fact, the closed form expressions for the tangent vector in the old version of <VECDIR> were derived by taking the first order derivative with respect to t of each parametric equation in (5.1) [25].

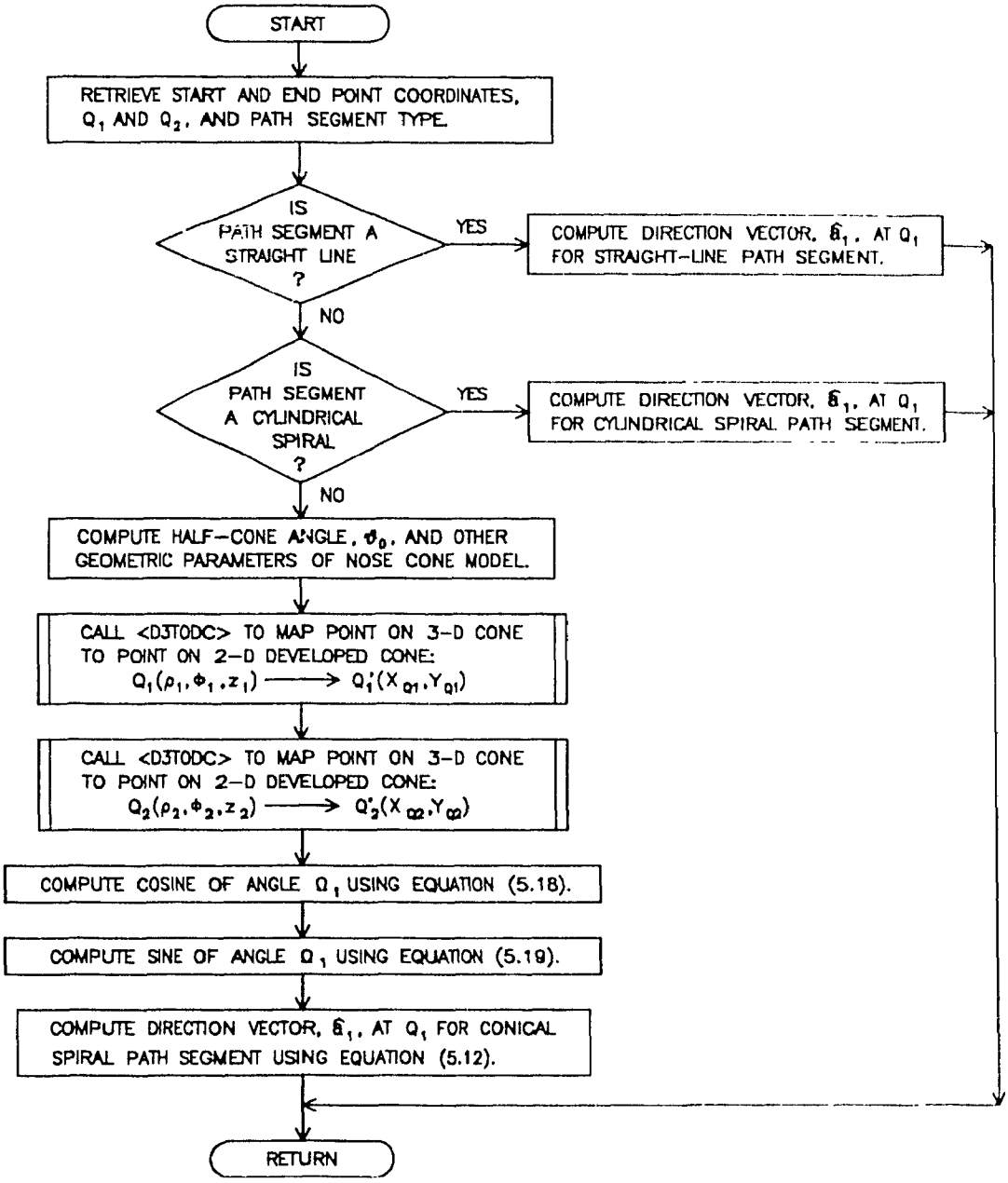

Figure 5.18. Flow-chart of revised module <VECDIR>

5.6 TEST RESULTS AND FINAL REMARKS

Comparative runs of the improved code on representative test cases have yielded satisfactory results, as shown in Figures 5.19 through 5.22, which correspond to the same test cases previously illustrated in Figures 5.1 through 5.4, respectively. The dramatic improvements in the display of cone geodesic path segments restore the fundamental principle of one-to-one correspondence between computed path and displayed path and increase user confidence in the code.

In Figures 5.19 and 5.20, the displayed paths are tilted forward slightly to represent the true geodesic path. In both cases, the revised code produces coupling path lengths that are about 10% shorter, but corresponding path loss computations that are slightly greater than previously computed. The slightly higher path loss values can be explained in terms of the effect of the shorter path length on the parameter A from equation (3.24) and on L_{cs}, the curved surface diffraction loss factor from equation (3.25). A shorter path length, s in equation (3.24), increases the parameter A. The net effect of an increase in A is an increase (in absolute value) of L_{cs} in equation (3.25). A higher curved surface diffraction loss corresponds to a higher path loss value in Figures 5.19 and 5.20.

The change in tangent vectors is best illustrated by comparing the results between Figures 5.1 and 5.19. In Figure 5.1, the trajectory proceeds from the antenna on top of the cone at an azimuth angle of -90.00° and an elevation of 0.00°. In simple terms, the path trajectory at the top antenna is perfectly horizontal and points to the port side of the aircraft. In Figure 5.19, the trajectory computed by the revised code proceeds from the antenna on top of the cone at an azimuth angle of -58.70° and an elevation of -11.64°. In simple terms, the trajectory computed by the revised code at the top antenna is no longer horizontal, but is slightly declined and points slightly forward and to the port side of the aircraft. Thus, in both Figures 5.1 and 5.19, the computed (AZ,EL) angles, which

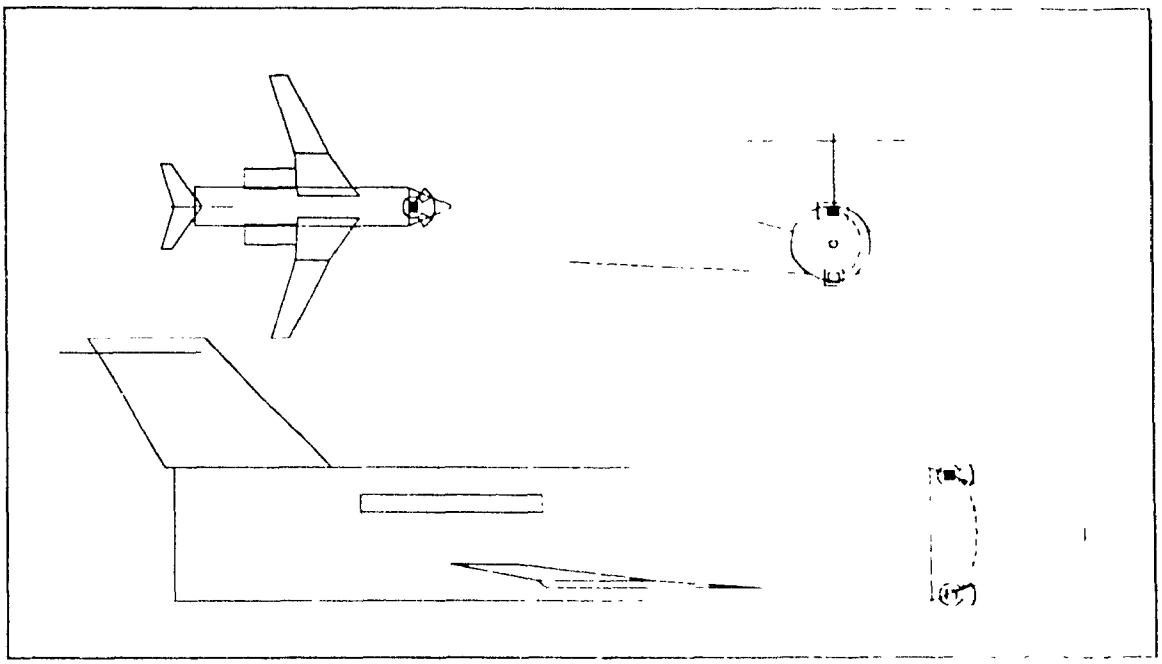

Figure 5.19. AAPG plot showing correct display of cone geodesic, frequency = 9.315 GHz, path length = 110 λ, path loss = 165.9 dB, ■(AZ,EL) = (-58.70°,-11.64°), □(AZ,EL) = (-58.70°,11.64°) [15]

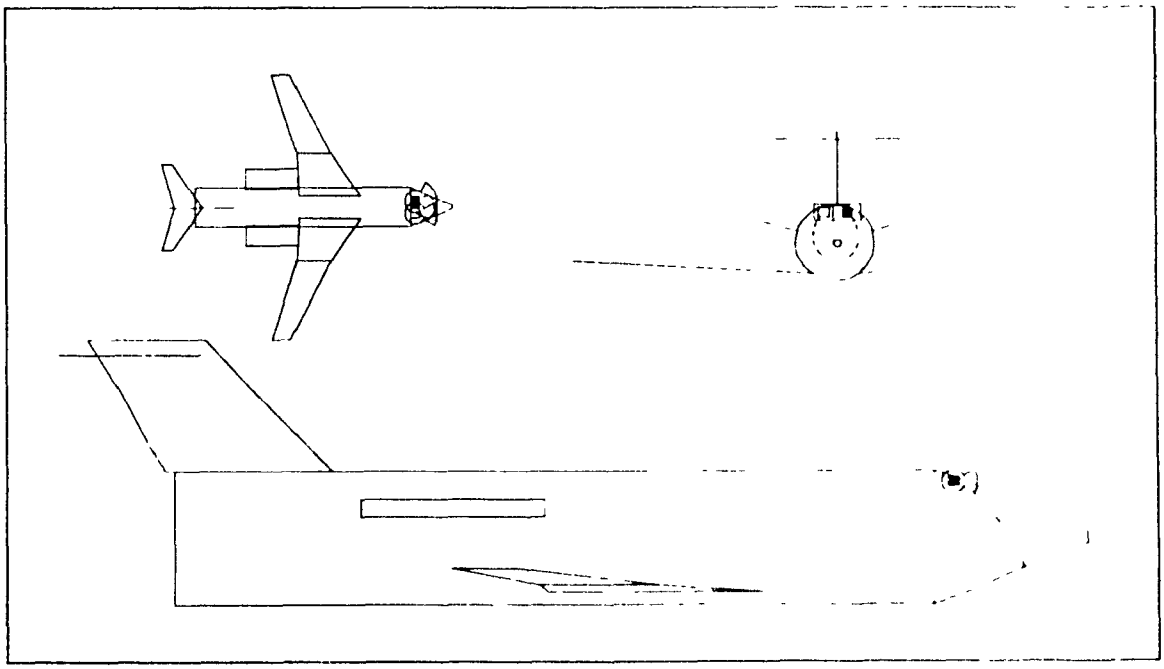

Figure 5.20. AAPG plot showing correct display of secondary coupling path on cone frequency = 9.315 GHz, path length = 173 λ, path loss = 236.8 dB ■(AZ,EL) = (-25.26°,-28.23°), □(AZ,EL) = (25.26°, 28.23°)

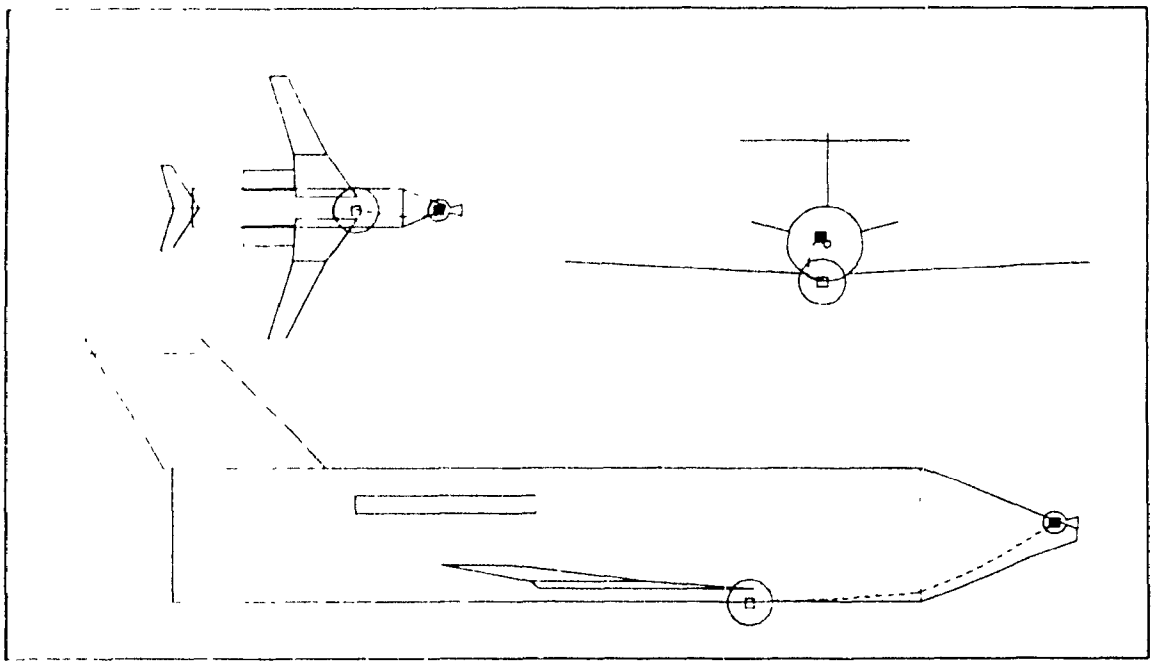

Figure 5.21. AAPG plot showing correct display of cone geodesic: frequency = 8.000 GHz, path length = 177 λ, path loss = -101.1 dB, ■(AZ,EL) = (126.66°,-15.74°), □(AZ,EL) = (9.52°,0.89°) [15].

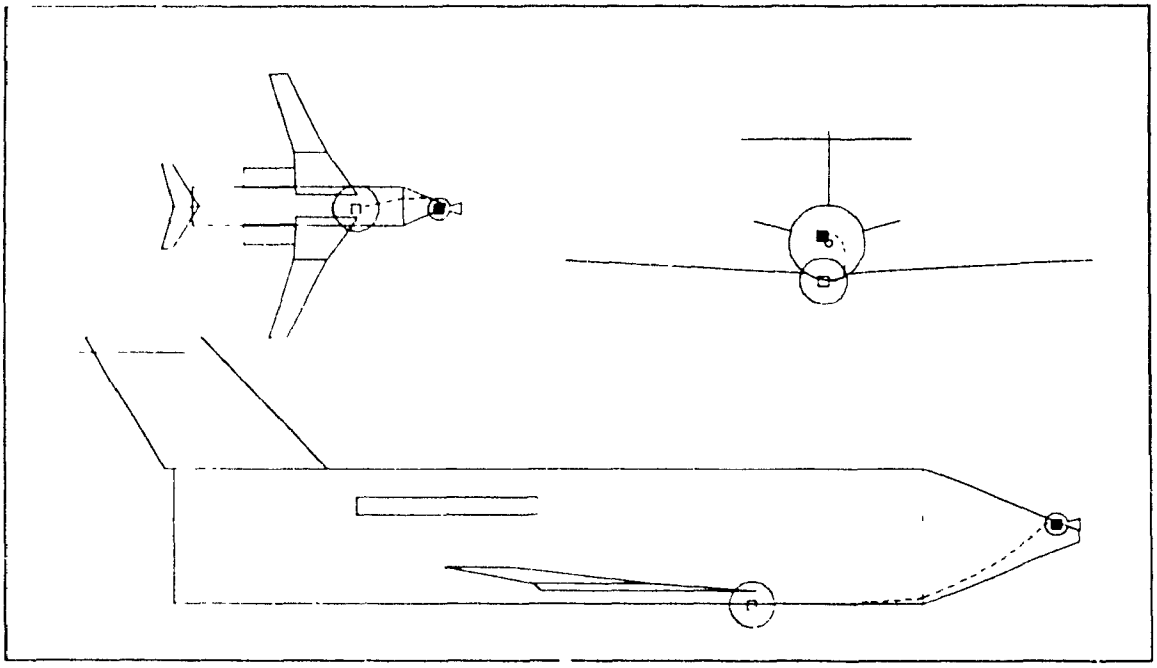

Figure 5.22. AAPG plot showing correct display of secondary coupling path on cone, frequency = 8.000 GHz, path length = 187λ, path loss = -140.6 dB; ■(AZ,EL) = (-98.41°,37.88°) □(AZ,EL) = (-11.25°,-1.05°) [15].

are directly related to the tangent vector computed by SVTCDIRS, match the displayed path trajectory.

The improvement in the display of cone geodesic path segment is particularly opportune in light of the cylinder/cone cross-over point improvement discussed in Chapter 5 of Drolet's thesis [39]. For cases in which the coupling path consists of a cylindrical spiral and a conical spiral, Drolet's algorithm computes the point along the edge of the cylinder/cone interface which minimizes the coupling path length as shown in Figures 5.3 and 5.4. Unfortunately in such cases, the new cylinder/cone cross-over point introduces a "kink" or discontinuity in the slope of the path at the cylinder/cone interfaces. The new cone geodesic display algorithms discussed in this chapter eliminates the "kink" in the composite path as shown in Figures 5.21 and 5.22. Although the latter cases exhibit no change in path length and path loss, a truer physical path is presented and serves to build up the user's experience of associating the trajectory with its corresponding path losses and path length.

With the satisfactory implementation and test results of the AAPG V07 algorithm improvements described here and in the previous chapter, the next chapter moves to the presentation and assessment of current developments in specific software implementations of the curved surface diffraction loss factor. The presentation follows from the mathematical expressions derived in Chapter 3.

CHAPTER 6

AAPG CURVED-SURFACE DIFFRACTION LOSS FACTOR IMPLEMENTATIONS AND TEST CASE RESULTS

6.1 INTRODUCTION

Having introduced the improvements in cone geodesic path computation and display algorithms in Chapters 4 and 5, the presentation of this chapter outlines the software implementations of the curved-surface diffraction loss factor in AAPG V09 and AAPG V07 based on the mathematical expressions derived in Chapter 3. Chapter 6 then examines comparative plots of the curved-surface diffraction loss factor from measurement results in the literature [28-30,41,42] and from computations of AAPG V09 and AAPG V07 on the following geometrical bodies: composite elliptical cylinder, elliptical cylinder, right circular cylinder, and right circular cone. Elliptical and composite elliptical cones were not studied due to the lack of measurement facilities and published measurement results.

6.2 AAPG V09 CURVED-SURFACE DIFFRACTION LOSS FACTOR IMPLEMENTATION

The EMC analyst models the arbitrarily convex cylindrical cross-section of the aircraft fuselage in AAPG V09 by specifying the radial distances from the aircraft's waterline centroid, i.e. its axis of revolution, at specified angles around this axis. AAPG V09 then uses spline interpolation to determine the fuselage cross-section at all points around the waterline centroid. The cone's cross-section has the same shape as that of the cylindrical part of the fuselage and tapers with the slope of the cone which is simply the tangent of the half-cone angle.

This flexibility in fuselage cross-section modelling requires the most general implementation of the Fock parameter of (3.10) as the following numerical integration formula indicates:

$$\xi = \left(\frac{k}{2}\right)^{1/3} \int_{\substack{Q' \\ along\ \Gamma}}^{Q} \frac{ds'}{[\rho_g(s')]^{2/3}}$$

$$\approx \left(\frac{k}{2}\right)^{1/3} \sum_{n=1}^{100} \frac{\Delta s}{[\rho_g(s_n)]^{2/3}} \qquad (6.1)$$

where $\Delta s = s/100$, $s_n = n\Delta s$, and s is the distance between source point Q' and field point Q along the geodesic path Γ. One hundred steps in equation (6.1) seem to have been chosen by the original designers of AAPG V09 as a compromise between enough sample points to reasonably approximate the smoothly varying path integral and too many points to make the expression computationally unmanageable.

The Fock parameter computed by the numerical integration technique in equation (6.1) is used in the expression for the curved-surface diffraction loss given by equation (3.18). Since AAPG V09 can model the arbitrarily convex cross-section of the aircraft fuselage and implements the Fock parameter ξ in the most general way, its calculation of the curved-surface diffraction loss factor agrees very well with measurement results for all four of the cases mentioned in the introduction of this section. The drawback is that the calculations of the summation and the radius of curvature in (6.1) are more computationally intensive than simple closed form expressions.

6.3 AAPG V07 CURVED-SURFACE DIFFRACTION LOSS FACTOR IMPLEMENTATION

In contrast to AAPG V09, AAPG V07 restricts the user to a circular cylinder model of the fuselage cross-section. The shape of the cone's cross section must also be circular and tapers with slope of the cone as specified by the half cone angle. As

mentioned in Chapter 2, AAPG V07 allows the fuselage to be truncated along a horizontal plane, but this capability is ignored here.

Since AAPG V07 is restrictive in its modelling of the aircraft fuselage cross-section, only the right circular cylinder and right circular cone of the four cases mentioned in the introduction of this section are considered. Although AAPG V07 does not have the same flexibility as AAPG V09 in modelling the cross-section of the aircraft fuselage, the closed form expressions of the Fock parameter in (3.23) for the right circular cylinder and in (3.31) for the right circular cone are suitable for implementation into AAPG V07 and are simpler computationally.

In its current configuration, AAPG V07 computes the Fock parameter, in all cases, by means of equation (3.23), which implies that computations of curved-surface diffraction losses on the right circular cone are only approximate. Further inaccuracies are introduced in the computation of the curved-surface diffraction loss because the $20\log(\cdot)$ term in equation (3.18) is not implemented in the current configuration of AAPG V07. This $20\log(\cdot)$ term accounts for losses due nonuniform radii of curvature on the surface of the cone.

The impact of the complete implementation of equations (3.18) and (3.31) in a revised version of AAPG V07 is deferred to section 6.7. The discussion moves to the comparison of measurement results with computed results starting with the most general case of a composite elliptical cylinder.

6.4 CURVED-SURFACE DIFFRACTION LOSS TEST CASES ON THE COMPOSITE ELLIPTICAL CYLINDER

Consider the perfectly conducting composite elliptical cylinder with cross sectional dimensions and holes for mounting monopole antennas numbered and located as illustrated in Figure 6.1 and listed in Table 6.1. Not shown in Figure 6.1 are a second set of holes, also numbered 0 through 7, located at the same relative positions around the cylinder cross-section but at an offset of 96" along the length of the cylinder (z dimension).

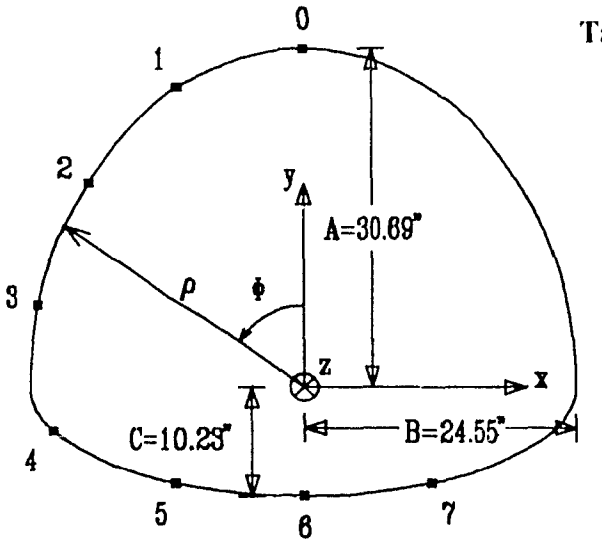

Figure 6.1. Cross-sectional dimensions of and hole locations on the composite elliptical cylinder [42].

Table 6.1. Hole locations on the composite elliptical cylinder

Hole #	ρ (in.)	φ (deg.)
0	30.69	0.00
1	29.49	22.50
2	26.97	46.77
3	24.55	90.00
4	24.55	90.00
5	24.55	135.00
6	19.22	180.00
7	14.96	202.08

Figures 6.2 and 6.3 illustrate the AAPG V09 calculated coupling path and the plots of measured (from reference [42]) and AAPG V09 calculated total coupling gain versus frequency for holes 0 and 3 with 0" z-offset. The measured and calculated curves in Figure 6.3 agree very well, especially in the 2 to 8 GHz frequency range.

Figures 6.4 and 6.5 illustrate the AAPG V09 calculated coupling path and the plots of measured (from reference [42]) and AAPG V09 calculated total coupling gain versus frequency for holes 2 and 5 with 96" z-offset. The measured and calculated curves in Figure 6.5 agree quite well in the 2 to 6 GHz frequency range. A gap in the measured curve between 6 and 8 GHz in Figure 6.5 exists because data was lost during the measurement process [42]. Durham remarks in reference [42] that the measurements above 8 GHz in Figure 6.5 are suspect due to the sensitivity of measurements required near the noise floor as well as to the reflection and diffraction effects from objects in the vicinity of the cylinder. He therefore labelled the portion of the curve above 8 GHz in Figure 6.5 as "NOISE FLOOR" [42].

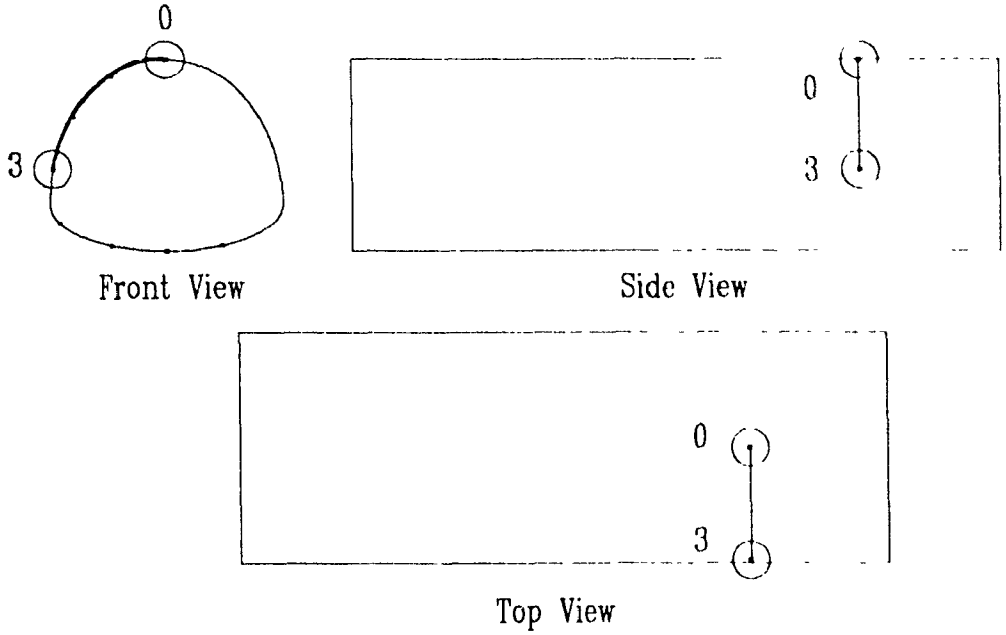

Figure 6.2. Front-, side-, and top-views of coupling path calculated by AAPG V09 for composite elliptical cylinder holes 0 and 3 with 0" z offset

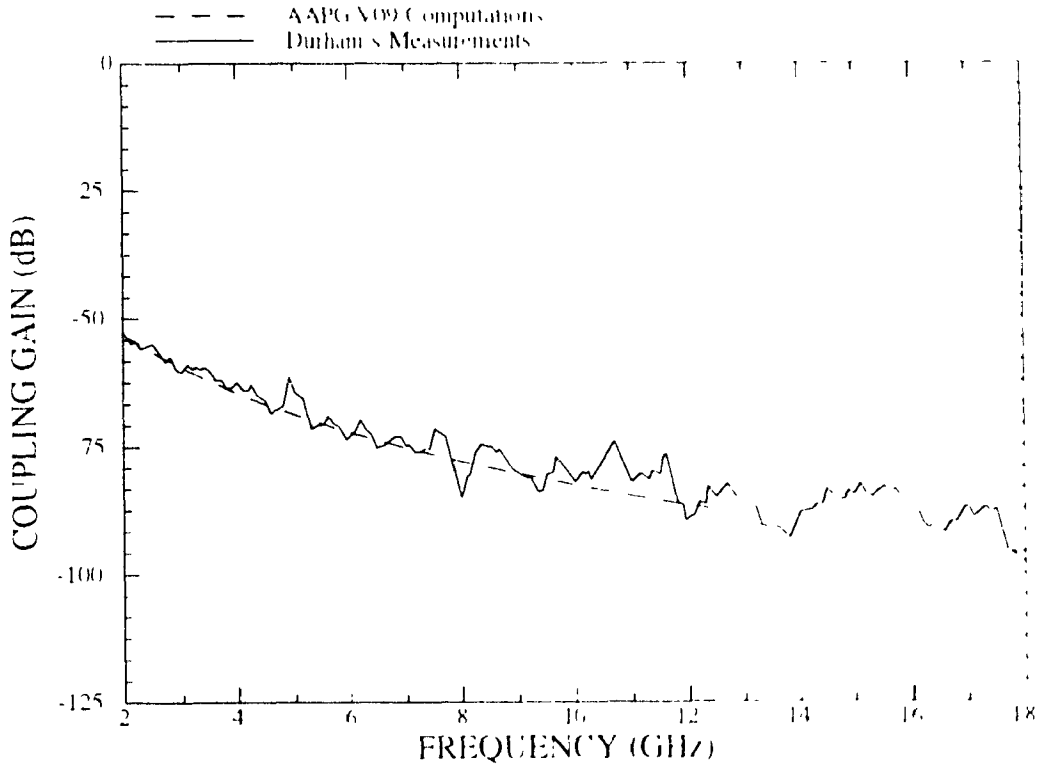

Figure 6.3. Measured and calculated coupling gain versus frequency for composite elliptical cylinder holes 0 and 3 with 0" z-offset [42]

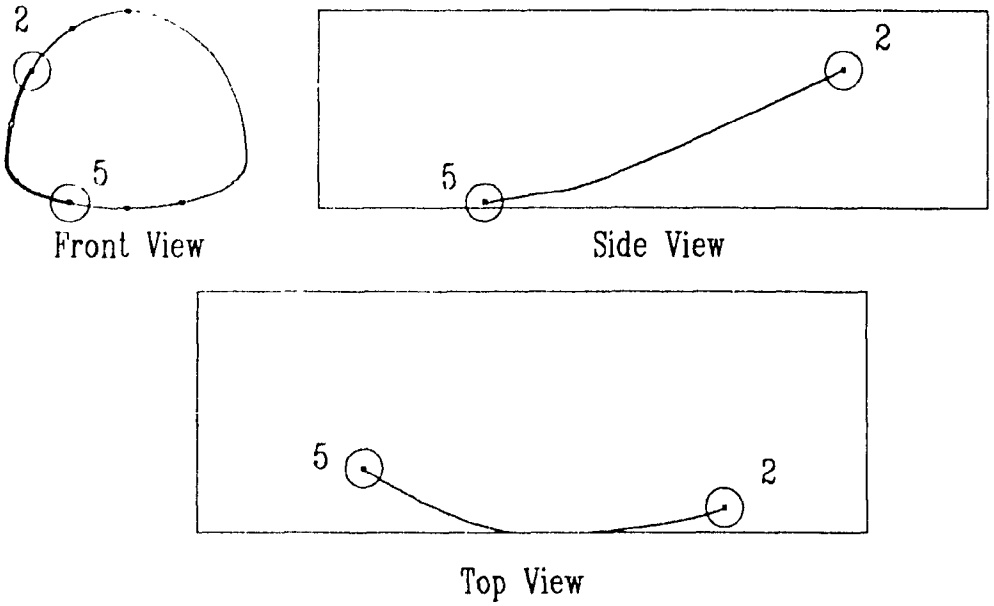

Figure 6.4. Front-, side-, and top-views of coupling path calculated by AAPG V09 for composite elliptical cylinder holes 2 and 5 with 96" z-offset.

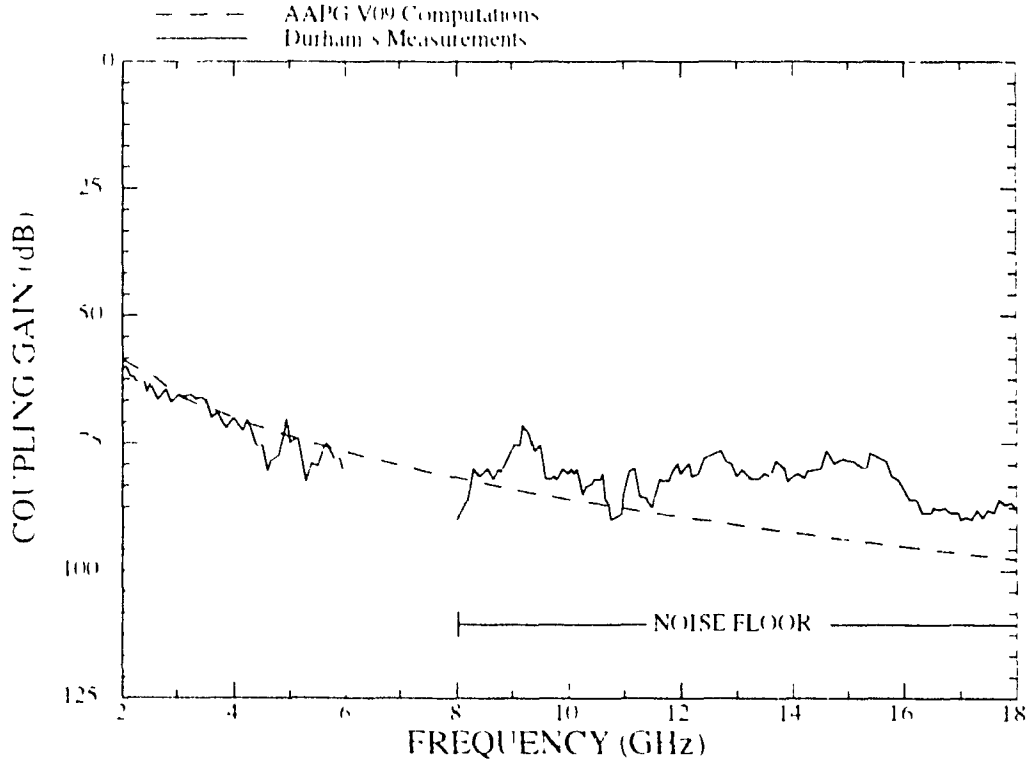

Figure 6.5. Measured and calculated coupling gain versus frequency for composite elliptical cylinder holes 2 and 5 with 96" z-offset [42].

6.5 CURVED-SURFACE DIFFRACTION LOSS TEST CASES ON THE ELLIPTICAL CYLINDER

Consider the perfectly conducting elliptical cylinder with cross sectional dimensions and holes for mounting monopole antennas numbered and located as illustrated in Figure 6.6 and listed in Table 6.2. Not shown in Figure 6.6 are a second set of holes, also numbered 0 through 7, located at the same relative positions around the cylinder cross-section but at a z-offset of 96".

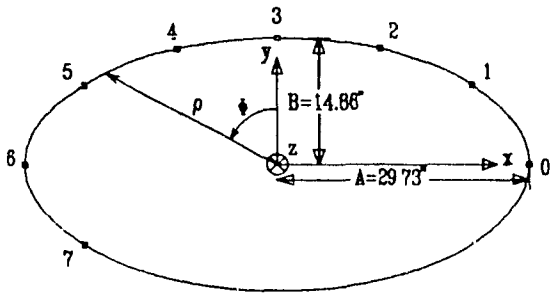

Figure 6.6. Cross-sectional dimensions of and hole locations on the elliptical cylinder [42].

Table 6.2. Hole locations on the elliptical cylinder

Hole #	ρ (in.)	φ (deg.)
0	29.73	90.00
1	24.91	67.96
2	19.09	31.17
3	14.86	0.00
4	19.09	328.83
5	24.91	292.04
6	29.73	270.00
7	24.91	112.96

Figures 6.7 and 6.8 illustrate the AAPG V09 calculated coupling path and the plots of measured (from reference [42]) and AAPG V09 calculated total coupling gain versus frequency for holes 5 and 7 with 0" z-offset. The measured and calculated curves in Figure 6.8 agree very well in the 2 to 12 GHz frequency range. The measurements above 12 GHz in Figure 6.8 are suspect for the same reasons mentioned in section 6.4 and are therefore labelled as "NOISE FLOOR".

Figures 6.9 and 6.10 illustrate the AAPG V09 calculated coupling path and the plots of measured (from reference [42]) and AAPG V09 calculated total coupling gain versus frequency for holes 0 and 4 with 96" z-offset. The measured and calculated curves in Figure 6.10 agree very well across the entire measurement band.

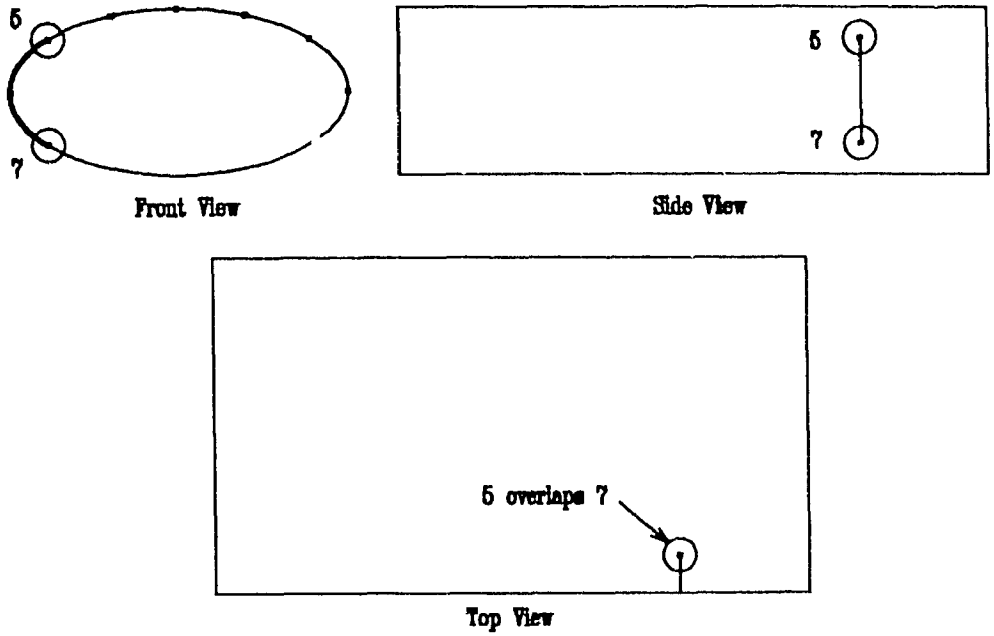

Figure 6.7. Front-, side-, and top-views of coupling path calculated by AAPG V09 for elliptical cylinder holes 5 and 7 with 0" z-offset

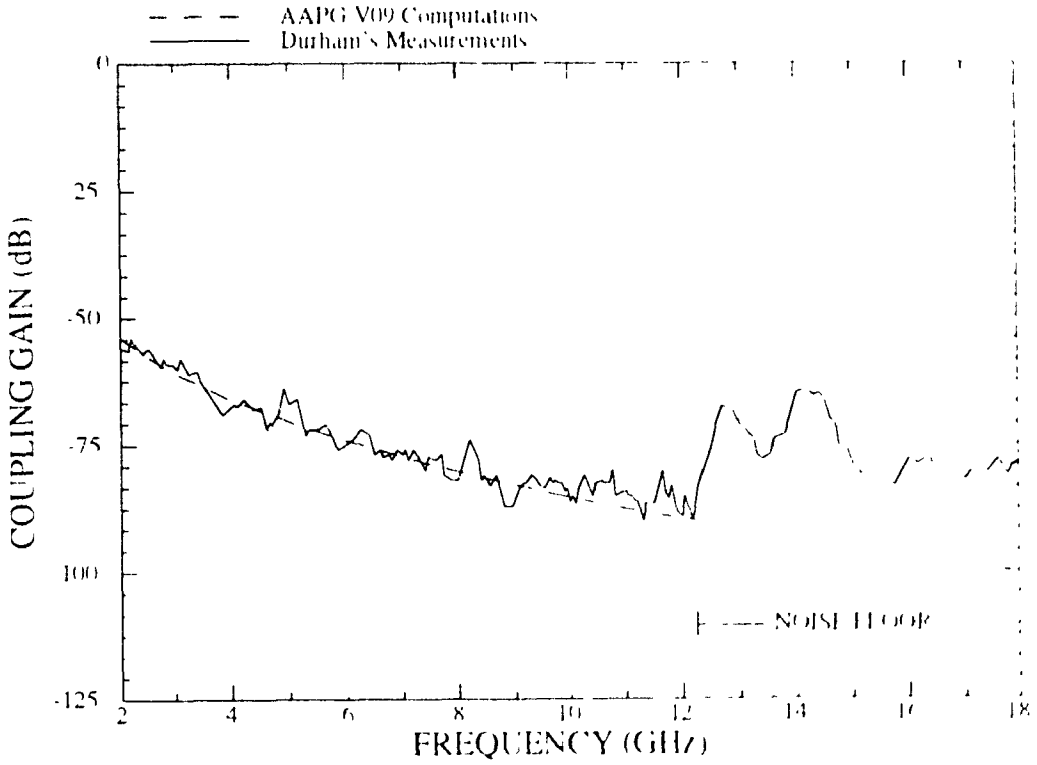

Figure 6.8. Measured and calculated coupling gain versus frequency for elliptical cylinder holes 5 and 7 with 0" z-offset [42]

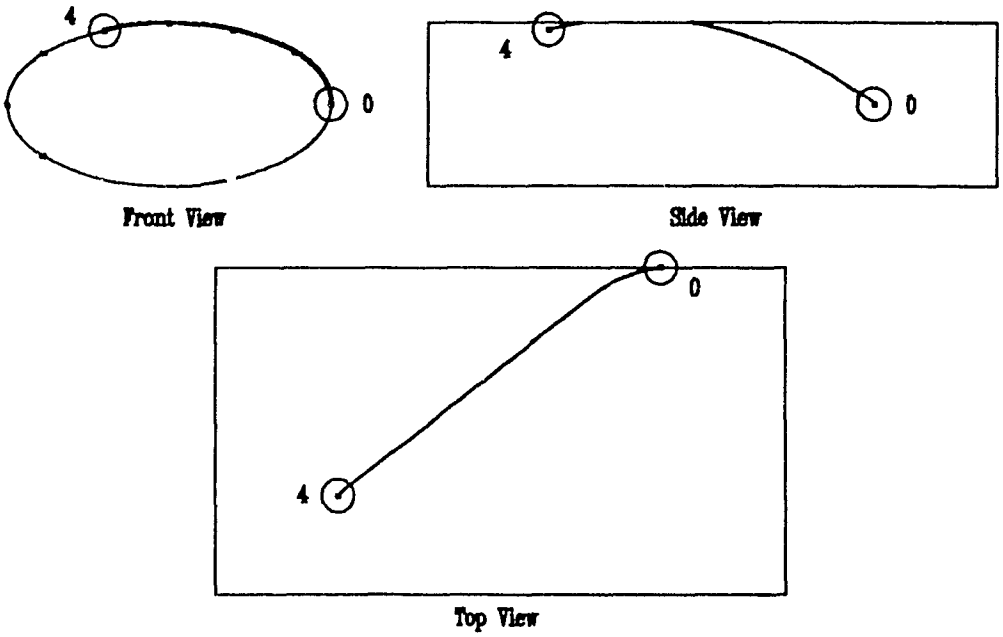

Figure 6.9. Front-, side-, and top-views of coupling path calculated by AAPG V09 for elliptical cylinder holes 0 and 4 with 96" z-offset.

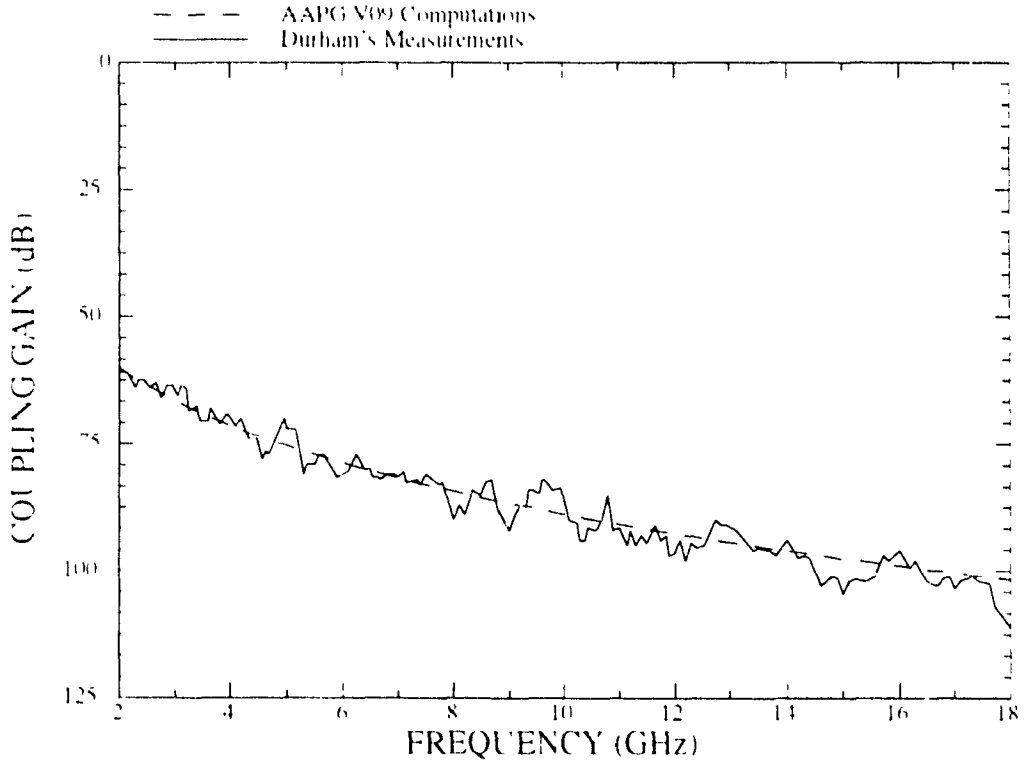

Figure 6.10. Measured and calculated coupling gain versus frequency for elliptical cylinder holes 0 and 4 with 96" z-offset [42].

6.6 CURVED-SURFACE DIFFRACTION LOSS TEST CASES ON THE RIGHT CIRCULAR CYLINDER

Consider the perfectly conducting right circular cylinder with cross-sectional dimensions and holes for mounting monopole antennas numbered and located as illustrated in Figure 6.11 and listed in Table 6.3. Not shown in Figure 6.11 are a second set of holes, also numbered 0 through 7, located at the same relative positions around the cylinder cross-section but at a z-offset of 96".

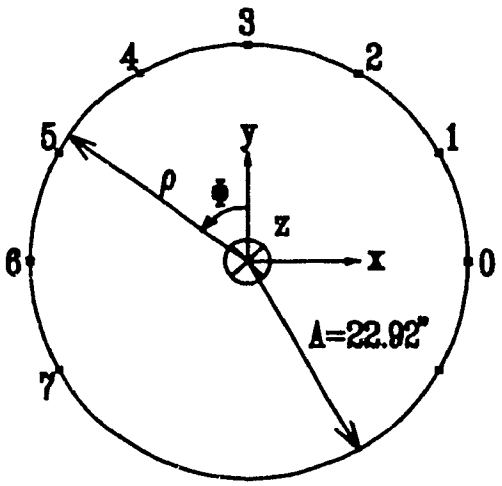

Figure 6.11. Cross-sectional dimensions of and hole locations on the right circular cylinder [42].

Table 6.3. Hole locations on the right circular cylinder

Hole #	ρ (inch)	φ (degrees)
0	9.0	90.00
1	9.0	67.50
2	9.0	45.00
3	9.0	22.50
4	9.0	0.00
5	9.0	337.50
6	9.0	315.00
7	9.0	292.50

Figures 6.12 and 6.13 illustrate the AAPG V07 and V09 calculated coupling path and the plots of measured (from reference [42]) and AAPG V07 and V09 calculated total coupling gain versus frequency for the holes 0 and 2 with 0" z offset. The measured and calculated curves in Figure 6.13 are in excellent agreement across the entire measurement band.

Figures 6.14 and 6.15 illustrate the AAPG V07 and V09 calculated coupling path and the plots of measured (from reference [42]) and calculated total coupling gain versus frequency for the holes 0 and 4 with 96" z-offset. The measured and calculated curves in Figure 6.15 agree quite well in the 2 to 8 GHz frequency range. The measurements above 8 GHz in Figure 6.15 are suspect for the same reasons mentioned in sections 6.4 and 6.5 and are therefore labelled as "NOISE FLOOR".

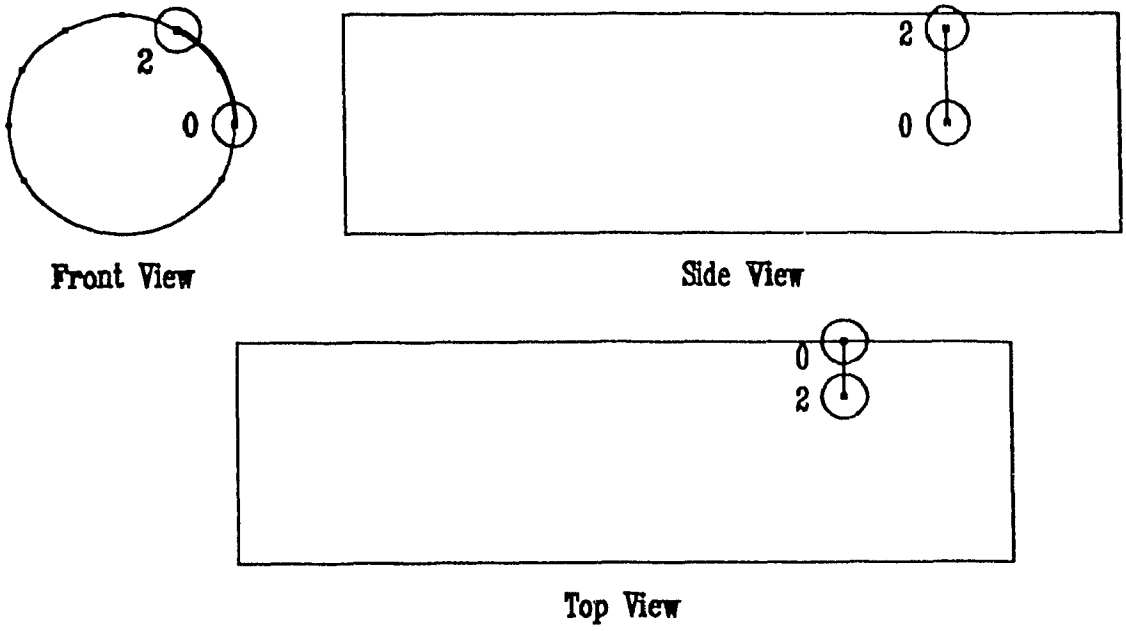

Figure 6.12. Front-, side-, and top-views of coupling path calculated by AAPG V07 and V09 for right circular cylinder holes 0 and 2 with 0" z offset

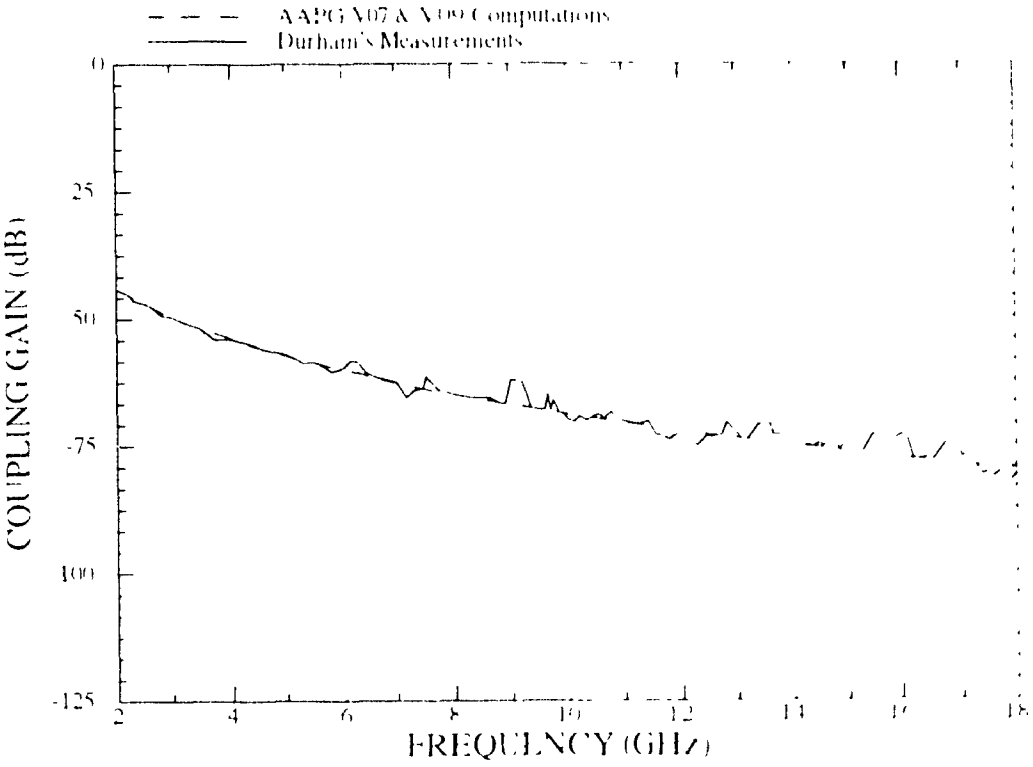

Figure 6.13. Measured and calculated coupling gain versus frequency for right circular cylinder holes 0 and 2 with 0" z-offset [42]

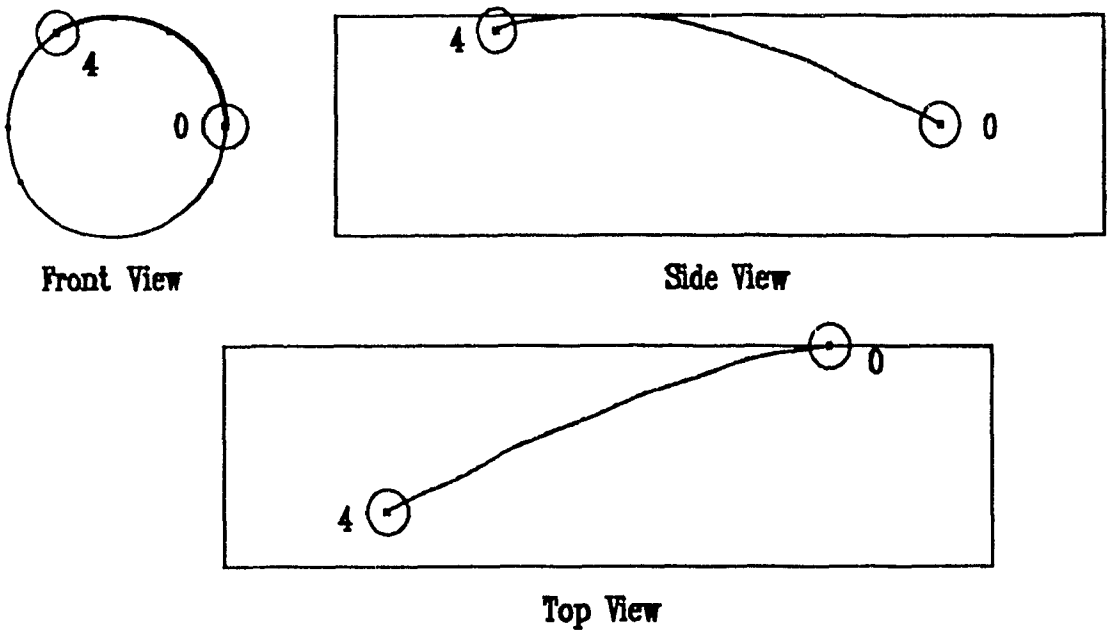

Figure 6.14. Front-, side-, and top-views of coupling path calculated by AAPG V07 and V09 for right circular cylinder holes 0 and 4 with 96" z-offset

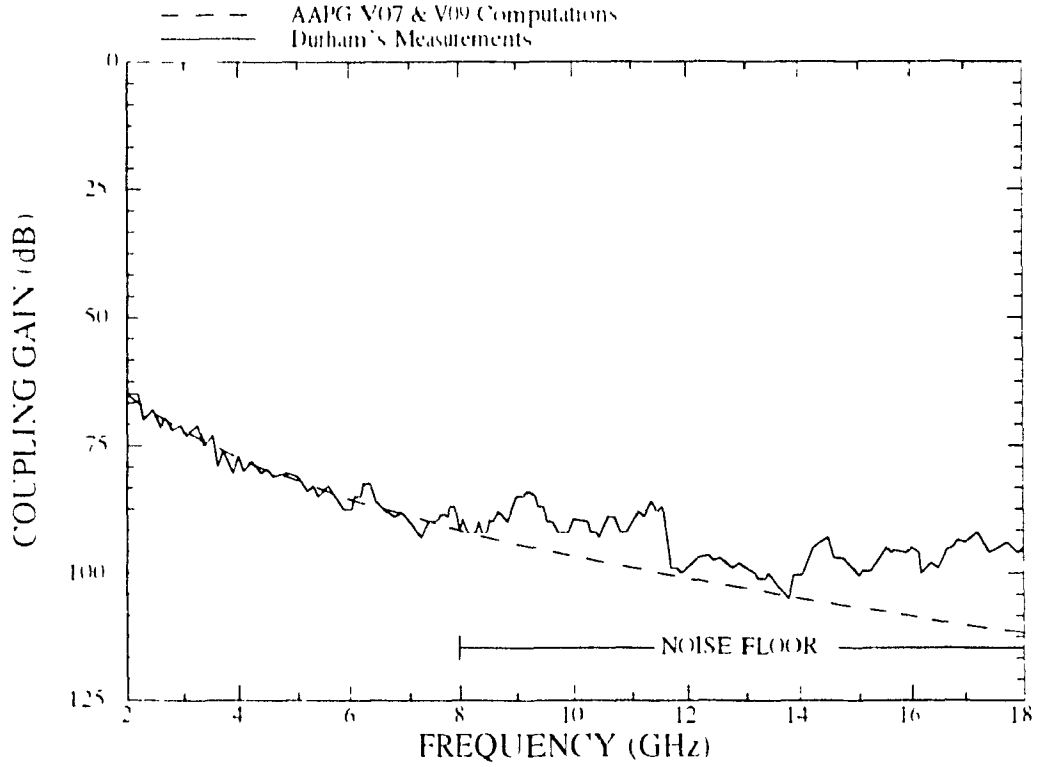

Figure 6.15. Measured and calculated coupling gain versus frequency for right circular cylinder holes 0 and 4 with 96" z-offset [42].

6.7 CURVED-SURFACE DIFFRACTION LOSS TEST CASES ON THE RIGHT CIRCULAR CONE

In this section, the AAPG V07 and V09 curved-surface diffraction loss formulations for the perfectly conducting right circular cone are first compared and then the best formulation is compared with measurement data from the literature.

Figure 6.16 illustrates a test case on a perfectly conducting right circular cone in which AAPG V07 and V09 calculate the coupling path between antenna SOURCE, located at a z-offset of 52.5" from the cone apex, and antenna FIELD, located at a z offset of 122.5" and an angular offset of 116.6 degrees from antenna SOURCE. The cone in Figure 6.16 has a half-cone angle of 27.2 degrees.

Figure 6.17 illustrates the plot of the total coupling gains versus frequency for the coupling path in Figure 6.16. Table 6.4 summarizes the differences between the formulations associated with the curves entitled, "AAPG V09", "AAPG V07 (Present)", and "AAPG V07 (Revised)" in Figure 6.17. The AAPG V09 and AAPG V07 (Revised) curves in Figure 6.17 are identical across the tested frequency band. The lower coupling gain calculation shown in the AAPG V07 (Present) curve of Figure 6.17 is a concern to the EMC analyst because compatibility may be predicted when the actual losses may not provide enough isolation between antennas to ensure compatibility. Therefore the implementation of the formulations associated with the AAPG V07 (Revised) curve is highly recommended.

The AAPG V09 and the AAPG V07 (Revised) curved-surface diffraction loss formulations are now compared with measurement data from reference [30]. Figure 6.18 illustrates a test case on a perfectly conducting right circular cone taken from reference [30] in which AAPG V07 and V09 calculate the coupling path between antenna SOURCE, located at a distance of 17.9" along the cone surface from the cone apex, and antenna FIELD, also located at a distance of 17.9" from the cone apex and an angular

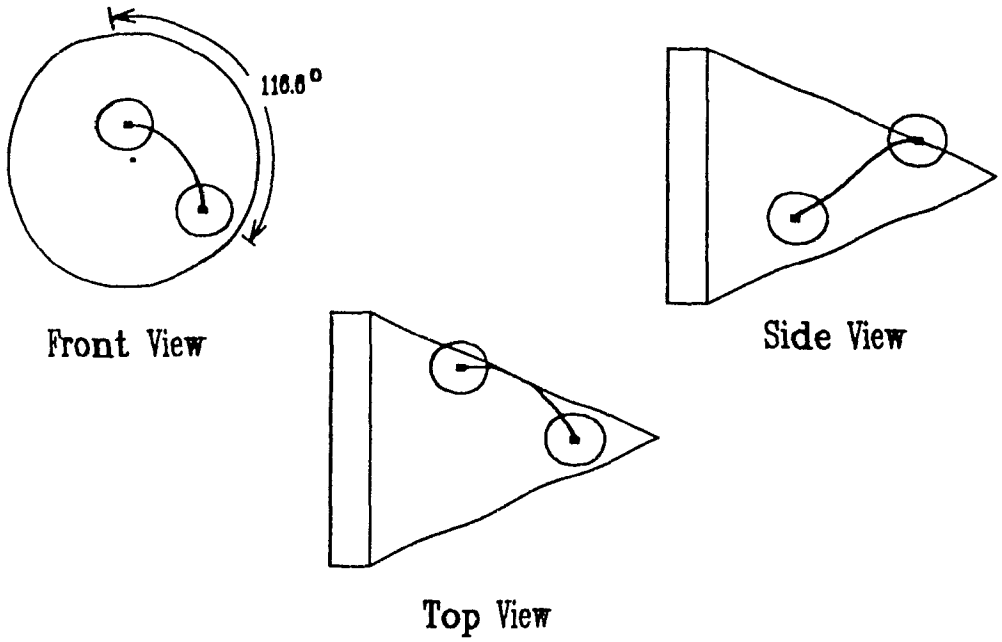

Figure 6.16. Front-, side-, and top-views of coupling path calculated by AAPG V07 and V09 for the right circular cone.

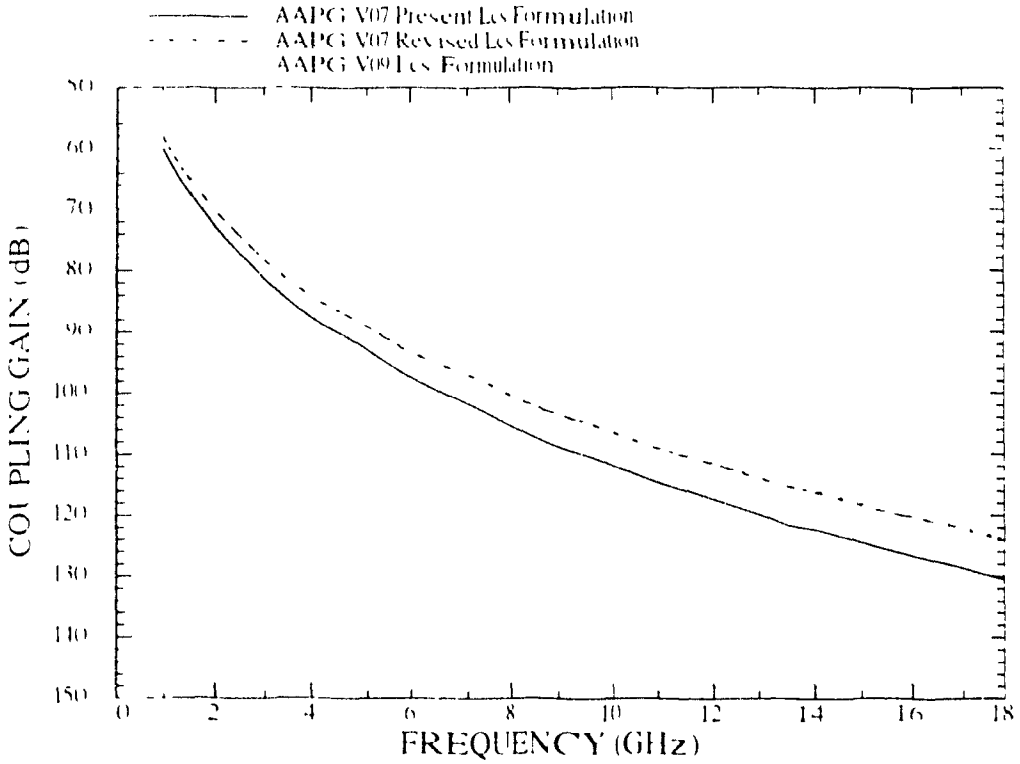

Figure 6.17. Calculated coupling gain versus frequency for right circular cone case illustrated in Figure 6.16 using formulations of Table 6.4.

Table 6.4. AAPG L_{cs} and ξ formulations used in coupling gain calculations of Figure 6.17.

Curve	Equation for L_{cs}	Computation of ξ	Remarks
AAPG V09	(3.18)	(6.1)	- Complex, computationally intensive expressions - Yields surface diffraction losses which are comparable to measurement results - Expressions applicable to any arbitrarily convex surface
AAPG V07 (Present)	(3.25)	(3.23)	- Simple, closed form expressions - Yields surface diffraction losses which are lower than measurement results and results from AAPG V09 and AAPG V07 (Revised) - Expressions applicable only to right circular cylinder - For the case of a cone, ρ_p (3.23) is approximated by the square root of ρ_1 times ρ.
AAPG V07 (Revised)	(3.18)	(3.31)	- Simple, closed form expressions - Yields surface diffraction losses which are comparable to measurement results - Expressions applicable to right circular cylinder and cone

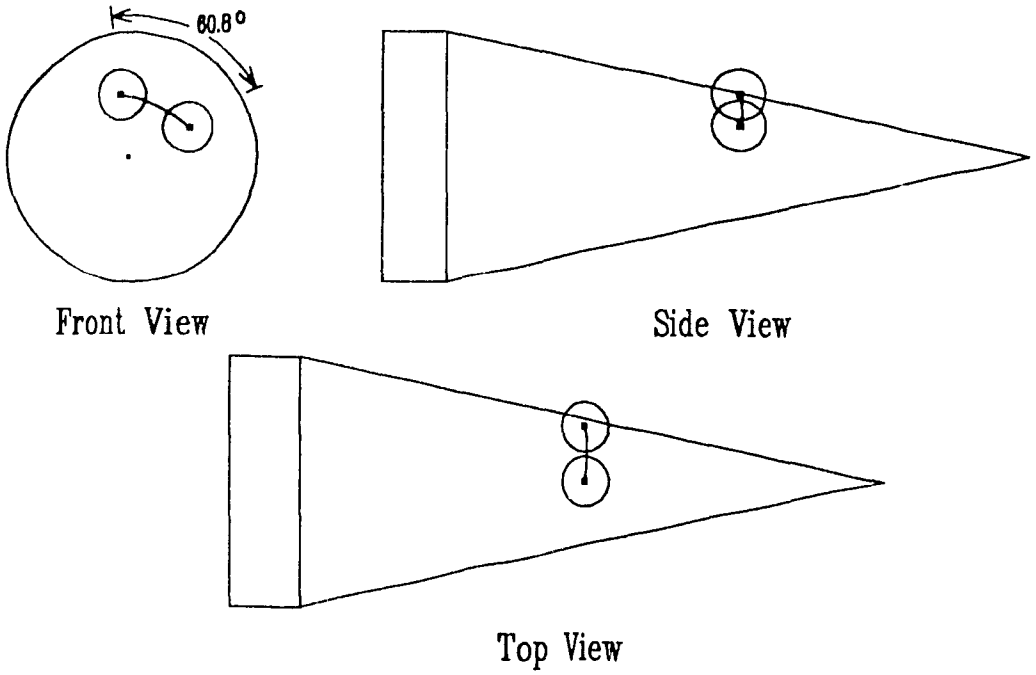

Figure 6.18. Front-, side-, and top-views of coupling path calculated by AAPG V07 and V09 for the right circular cone test case from reference [30].

offset of 60.8 degrees from antenna SOURCE. The cone in Figure 6.18 has a half-cone angle of 12.2 degrees.

Figure 6.19 illustrates the plot of the total measured coupling gain from reference [30] and the total coupling gain computed by AAPG V09 and AAPG V07 (Revised) versus frequency for the coupling path in Figure 6.18. The AAPG V09 and AAPG V07 (Revised) curves in Figure 6.19 are again identical across the tested frequency band but indicate a lower coupling gain calculation, albeit only a 1 dB discrepancy, compared to the measurement data taken by Golden et al. [30]. The discrepancy is exaggerated in Figure 6.19 due to the scale chosen for the vertical axis. The slight oscillatory nature of the curve in Golden's paper [30] indicates that the total coupled field is made up of component fields adding in and out of phase. One possible contribution, in addition to the direct coupled field, suggested by Golden et al. [30] is the field diffracted from the tip of the cone.

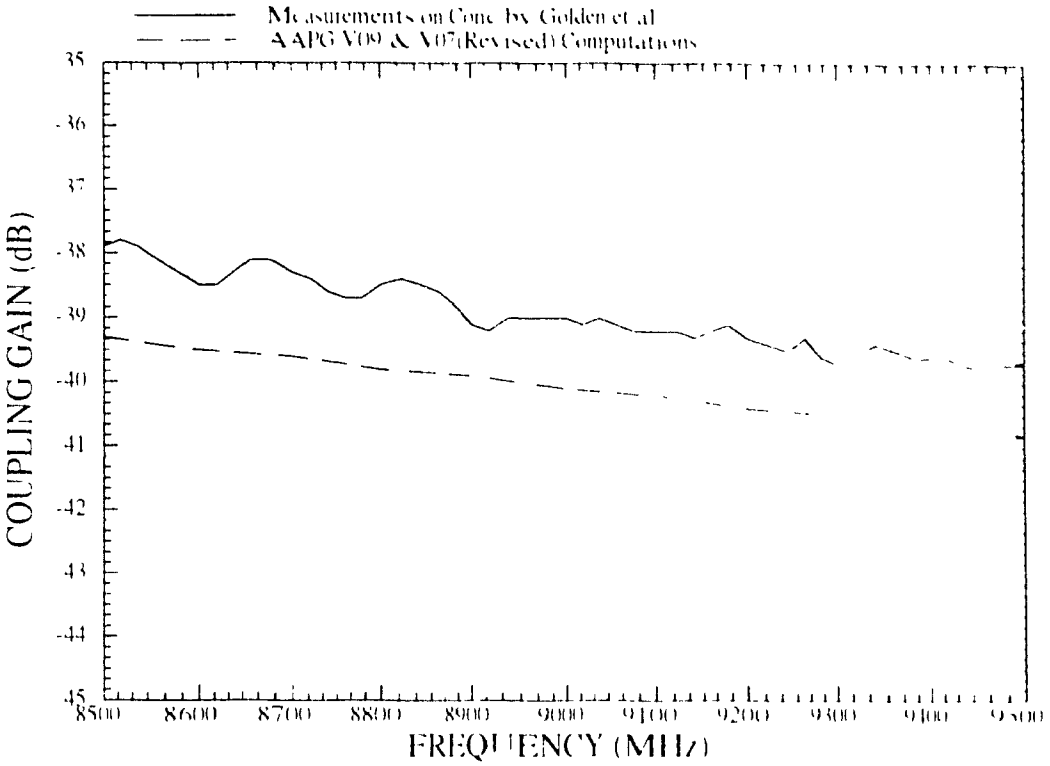

Figure 6.19. AAPG V09 and AAPG V07 (Revised) calculated coupling gain versus frequency for right circular cone test case of Figure 6.18 [30]

6.8 FINAL REMARKS

Some final remarks are in order regarding a similar study done in Chapter 8 of Drolet's thesis [39]. The EMI margin results published in Drolet's thesis [39] are incorrect because his implementation of the curved-surface diffraction loss factor L_{α_s} of (3.18) uses the Fock parameter formulation of (3.31) calculated for a right circular cone only in the calculation of the τ (or rather 20 log τ) term of (3.20). This approach only contributes a few decibels to the total loss in the L_{α_s} expression of (3.18). The formulation of (3.31) was not included, however, in the calculation of A from (3.19a) in the $-A/(\eta A + \xi')$ loss term, which represents the predominant portion of the loss in the L_{α_s} expression of (3.18). Furthermore, Drolet used the expression for τ straight out of Lee's paper [28] which was shown to be erroneous in subsection 3.5.2.

Finally, Drolet erroneously uses a plot from Lee's paper [28], which itself originated in Golden's paper [30], in an attempt to validate his AAPG implementation of the curved surface diffraction loss formulation for a right circular cone. While the plot from Lee's paper [28] clearly validates the mutual coupling formulation in Golden's paper [30], Golden explains that the large peaks and valleys in that plot are the result of interference between the direct coupled and tip diffracted fields. Since, in this context, AAPG considers only the contribution of the direct coupled field, Drolet's use of the plot from Lee's paper [28] is inappropriate for comparison purposes.

Having evaluated specific implementations of the curved-surface diffraction loss term in this chapter, a user-directed technical assessment of AAPG Versions 07 and 09 in Chapter 7 will give a more general appreciation of the relative merits of these two state-of-the art EMC analysis codes.

CHAPTER 7

USER-DIRECTED COMPARATIVE EVALUATION OF AAPG VERSIONS 07 AND 09

7.1 INTRODUCTION

In Chapter 2, the discussion alluded to some of the more complex modelling representations implemented in AAPG V09 as compared to AAPG V07, including the use of nose and aft tail cones. In Chapter 6, the surface diffraction loss algorithms were validated for AAPG V07 and AAPG V09. For the sake of completeness, this chapter briefly examines the difference in EMI margins for the two codes and the relative merits of each code in the context of a "real-world" test case, namely the EST CL 600 Challenger aircraft, which is illustrated in Figure 7.1. This latter aircraft lends itself to a two-cone model representation and has sufficient complexity for a meaningful analysis to be made. The configuration used is that proposed by Lockheed Canada [17] for the Electronic Systems Trainer role in Canada.

7.2 SIDE-BY-SIDE COMPARISON OF SURFACE DIFFRACTION COUPLING PATHS FOR AAPG V07 AND V09

7.2.1 Airframe Model Generation. The initial task in this evaluation is to generate a reasonable approximation to the Challenger airframe. The approach in this section is first to revisit the AAPG V07 model used by Lockheed Canada [17] and then to duplicate that model as closely as possible within the constraints of AAPG V09. In section 7.3 a more elaborate model is examined.

The fuselage of the Challenger lends itself well to being modelled in AAPG V07. The fuselage cross-section is circular so that the model can be made to be essentially an exact representation of the main body of the airframe. The Challenger nose section is

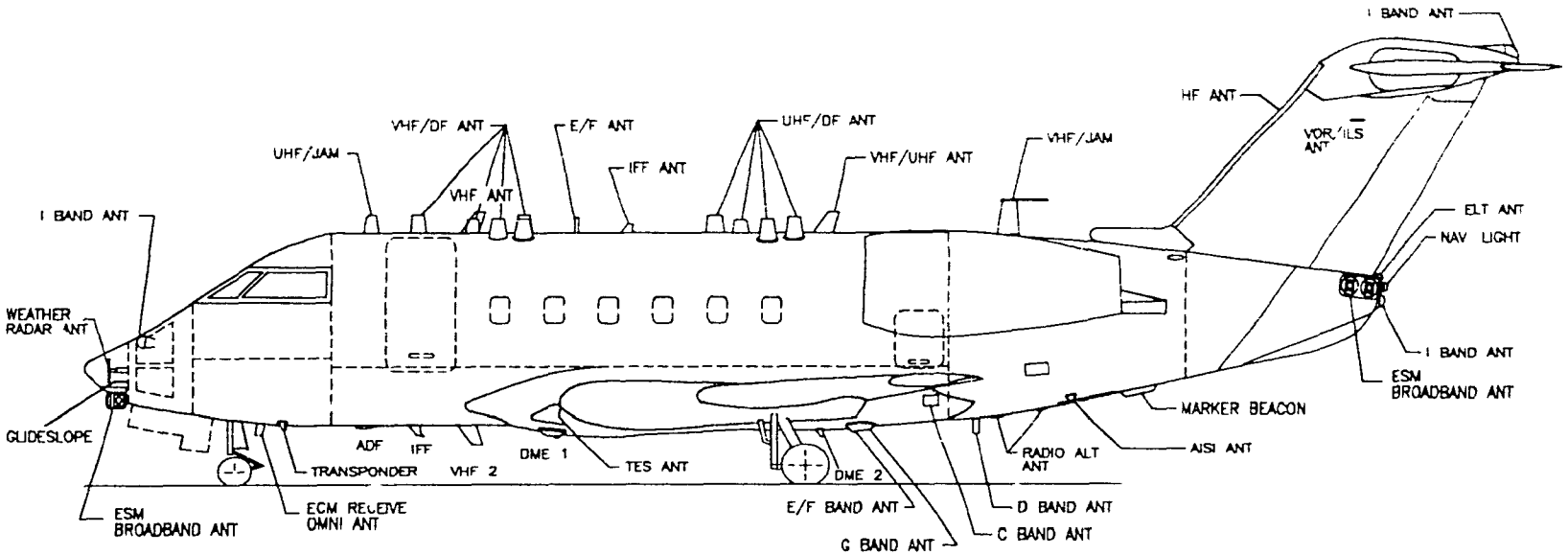

Figure 7.1. Side-view of EST CL-600 Challenger system antenna layout [17].

tilted considerably below the centroid and some engineering compromise is required in determining the forward cone model. Figure 7.2 shows the outline of the AAPG V07 model superimposed over the outline of the actual Challenger airframe.

The AAPG V09 model of the Challenger follows in a straight forward manner from the AAPG V07 model. The AAPG V07 and AAPG V09 models are virtually identical except that AAPG V09 also requires that a tail cone section be specified. An EMC analyst's first inclination is to specify a very short tail cone section in the AAPG V09 model so that the AAPG V09 model matches as closely as possible the AAPG V07 model. Such a model allows a "baseline" comparison to be made with coupling paths being essentially identical, but with different shading loss computations being used.

However, unlike AAPG V07, AAPG V09 imposes the additional constraint that the fuselage station of all of the antennas be positioned between the forward and aft bulkheads of the aircraft model [22]. In the case of the Challenger, this constraint is an issue due to the I-band receive antenna, which is situated on the aft edge of the vertical stabilizer, and the Omega navigation system antenna, which is situated on the right tip of the aft stabilizer. Both of these antennas are located aft of the aft bulkhead of the fuselage.

Figure 7.3 illustrates the compromise approach in addressing the AAPG V09 constraint for the Challenger aircraft. In order to allow all of the transmitters, receivers and antennas to be modelled within one input data file in AAPG V09, one solution is to artificially extend the length of the tail cone. The trade-off is that the AAPG V09 user must then exercise caution in this analysis when dealing with any data pertaining to coupling paths that traverse the artificial tail cone. For the sake of the comparative evaluation of AAPG V07 and AAPG V09 in this section, those paths are ignored.

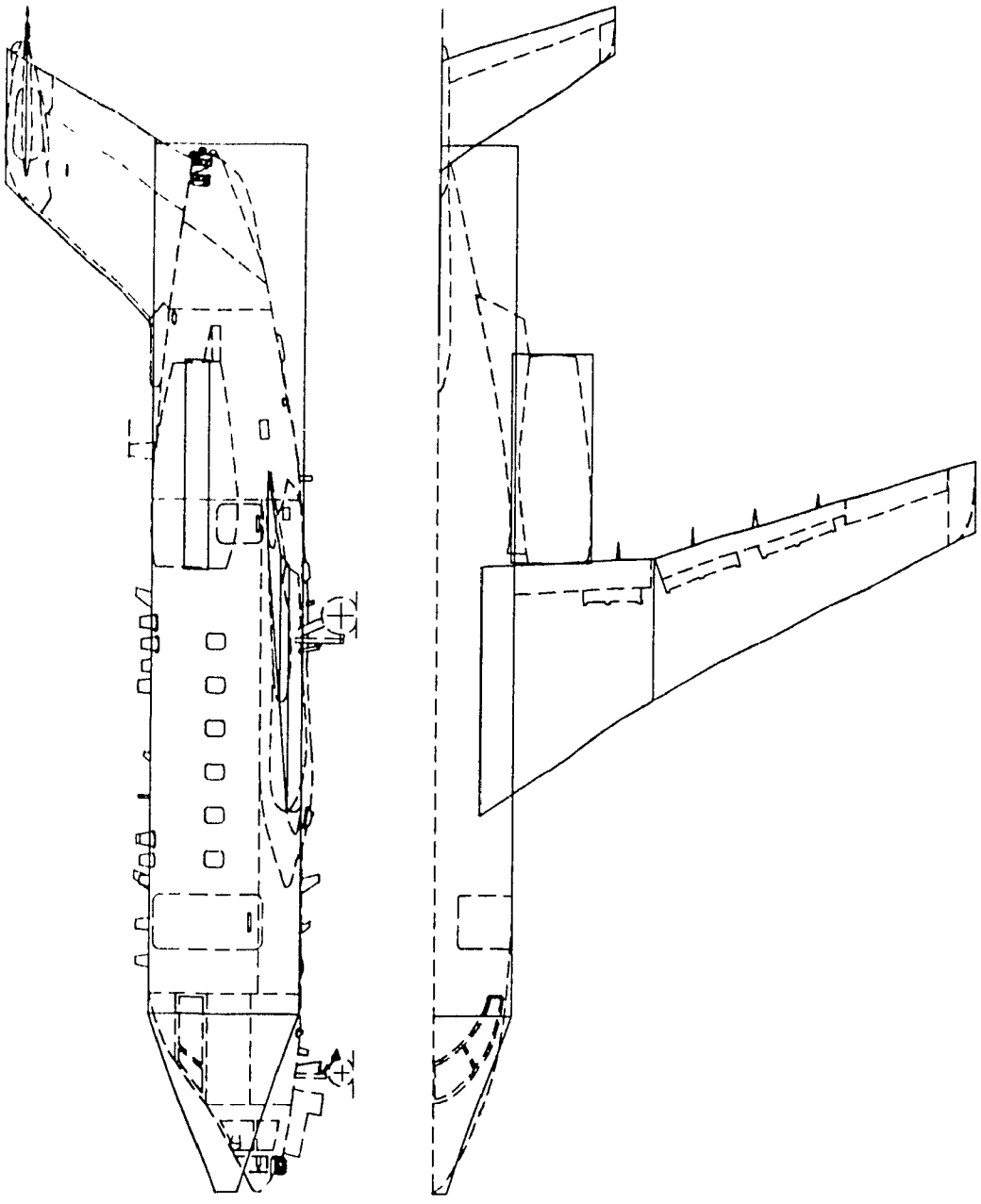

Figure 7.2. AAPG V07 model of the EST CL-600 Challenger airframe.

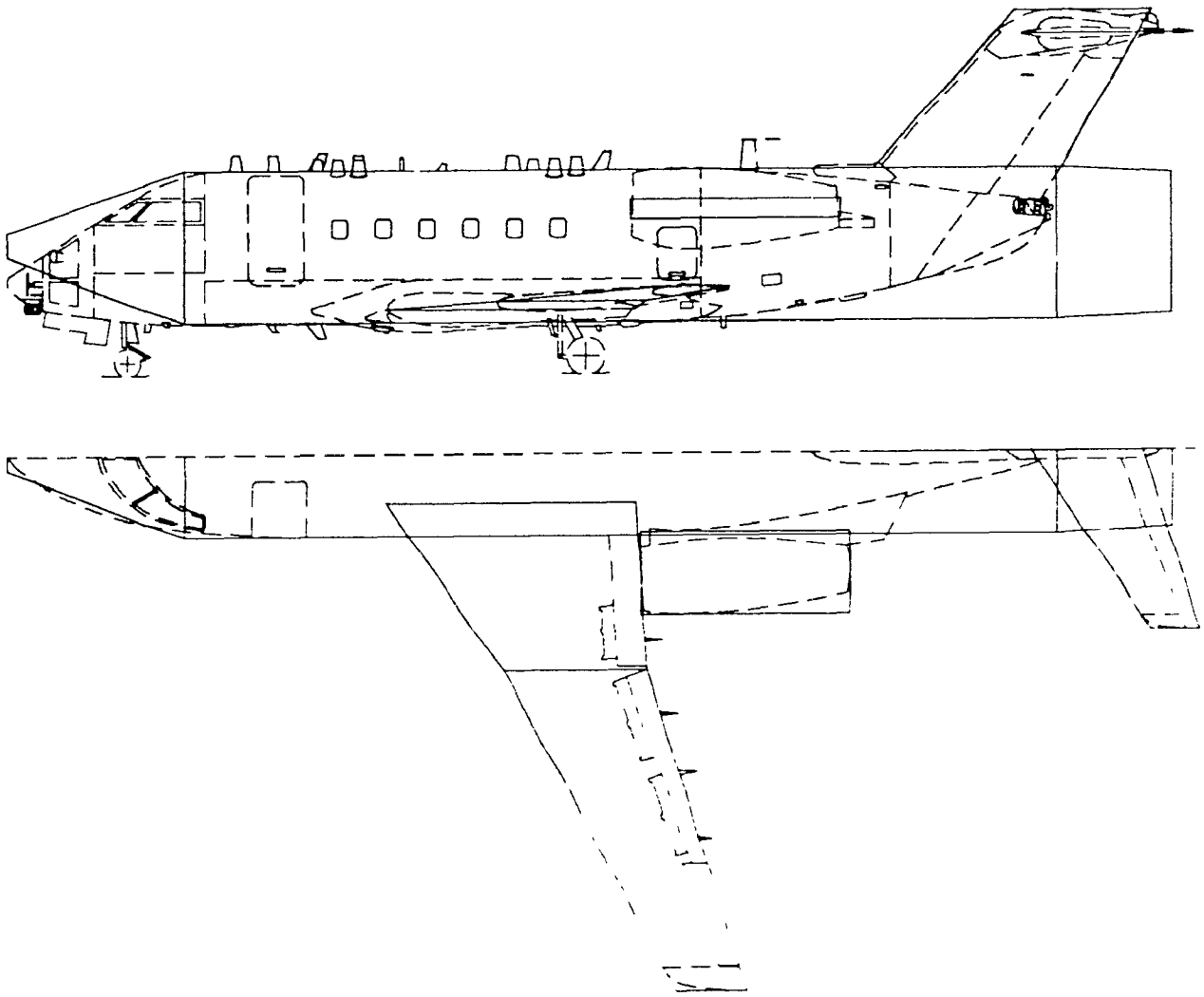

Figure 7.3. AAPG View Simple model of the EST CL-601 Challenger airframe

7.2.2 Surface Diffraction Coupling Paths. The analyses performed by AAPG V07 and by AAPG V09 on their respective FST CL-600 Challenger input data files, which model over 40 transmitter and receiver responses and over 30 antenna systems, yield over 800 coupling paths. This section examines a representative composite cone/cylinder surface diffraction coupling path and compares the results generated by AAPG V07, which are illustrated in Figures 7.4 and 7.5, with the results generated by AAPG V09, which are illustrated in Figure 7.6.

The runs of AAPG V07 and of AAPG V09 on the models discussed in the previous sections yield similar results in many respects. From the casual inspection of the graphical display, the EMI energy traverses a path which is similar in both instances. The energy is transmitted from the I-band transmit antenna (represented by the "■" symbol) located on the forward cone along a conical spiral, transitions to a cylindrical spiral as it moves aft, and arrives at the ESM antenna (represented by the "□" symbol) located on the left side at the aft extreme of the aircraft. An examination of the data associated with the smooth trajectory, with the focus concentrated on the data for harmonic number 1 at a frequency of 8.000 GHz, substantiates the similarity between the two coupling paths. The path lengths are virtually identical at 463 or 464 wavelengths. The "transmission loss" component, which is path length dependent, of the EMI margin is computed to be -75.3 dB in both cases. Furthermore, the AAPG V09 computations of the AZ and EL angles taken by the coupling path at the receive antenna are within 2 degrees of those computed by AAPG V07. In the worse case, those angles at the transmit antenna differ by only 10 degrees from one version's computation to the next. The similarity in path angles lead to computed antenna gains that are also comparable, but the discussion of their relevance is deferred until section 7.4.

The fundamental difference between the results computed by AAPG V07 and those computed by AAPG V09 is the surface shading loss factor. This loss term is computed to be 6 dB lower in AAPG V07 for this test case. This discrepancy can be

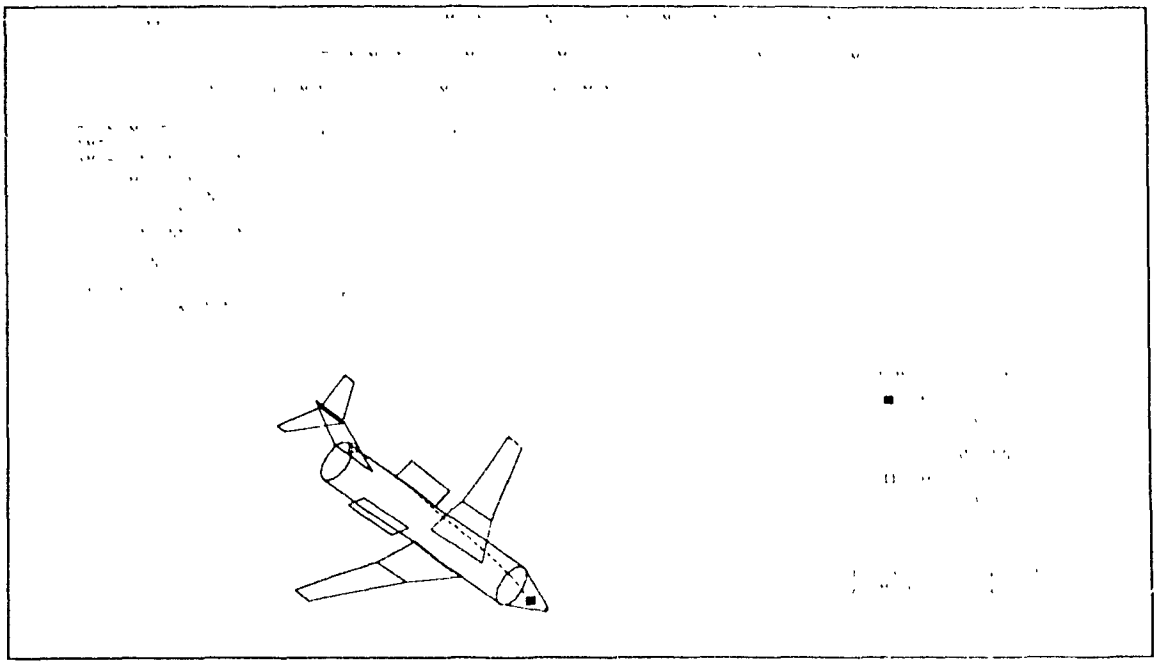

Figure 7.4. EMPP Display of surface diffraction coupling path computed by AAPG V07.

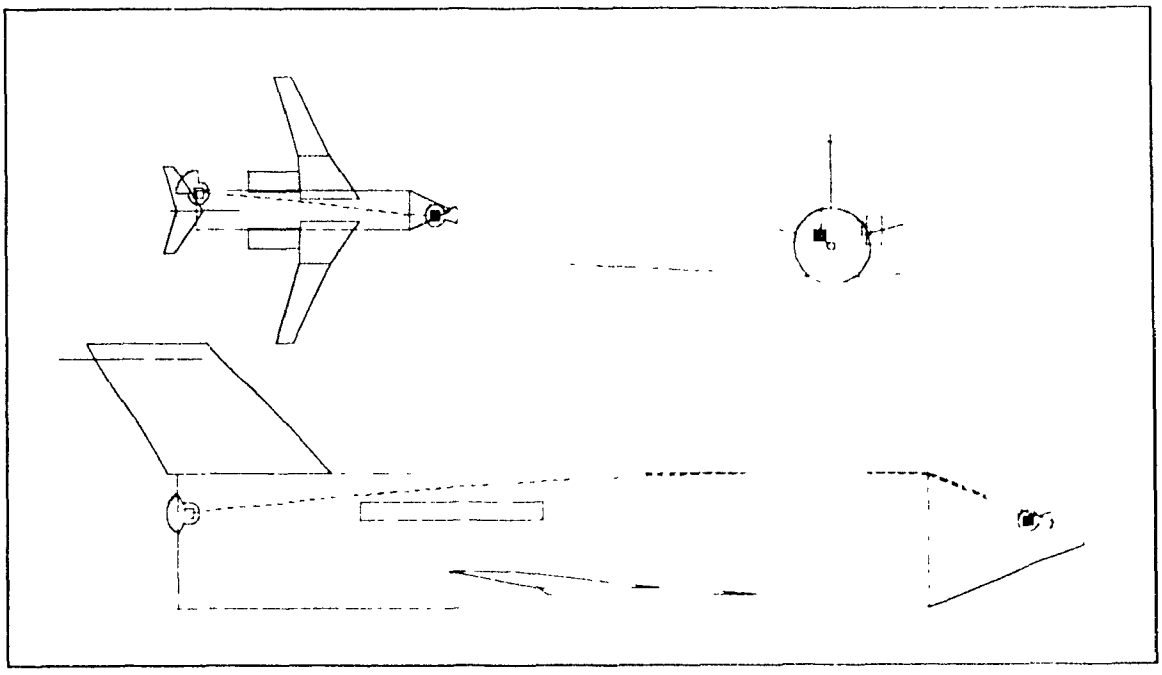

Figure 7.5. Orthogonal views of surface diffraction coupling path computed by AAPG V07.

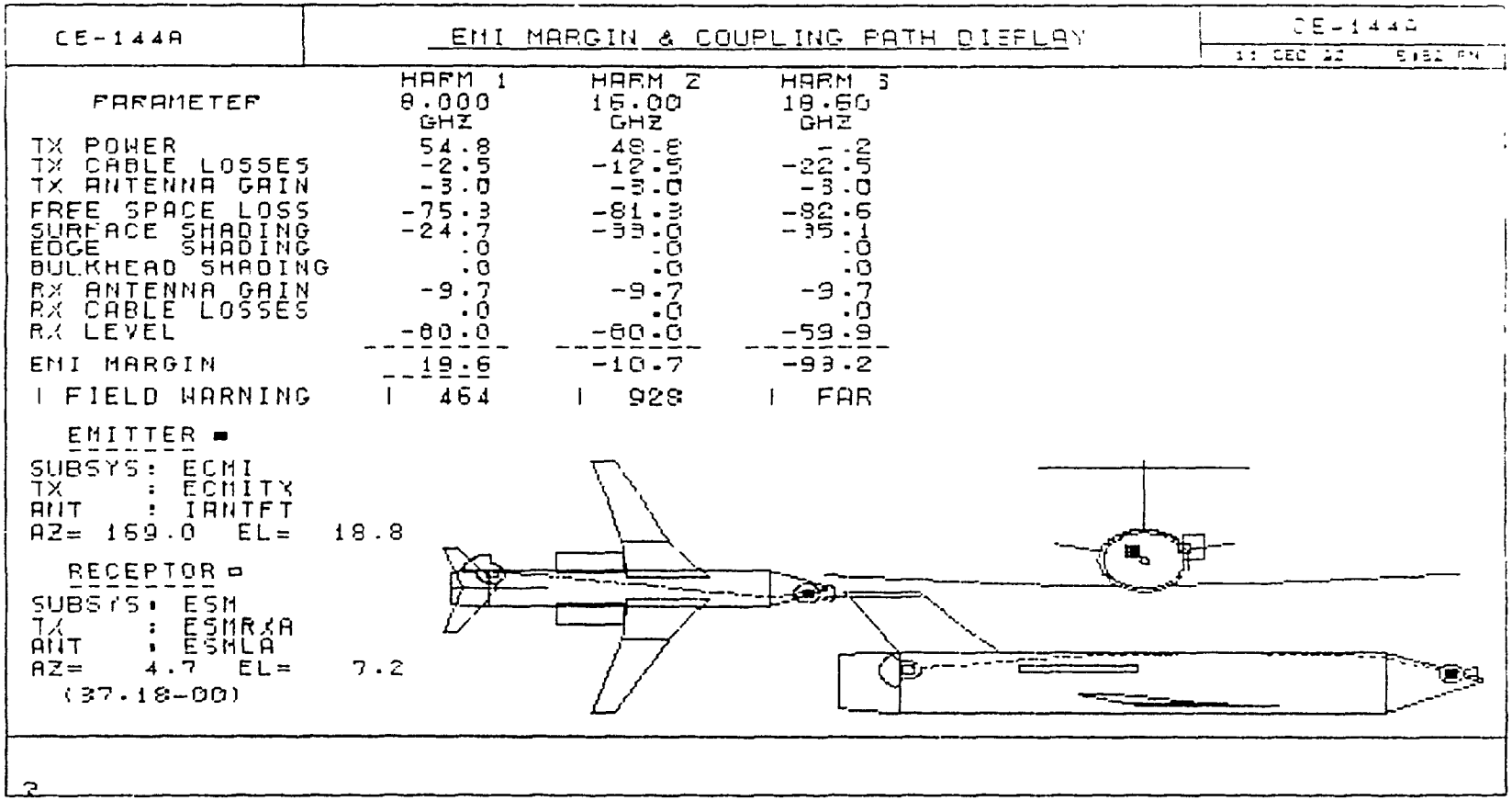

Figure 7.6. EMPP Display of surface diffraction coupling path computed by AAPG V09 on simple model.

attributed to the omission of the second term in equation (3.18), which describes the surface shading loss factor in the EMI margin calculation. The second term accounts for the higher losses on the cone surface due the cone's variation in radius of curvature and was not implemented in the version of the AAPG V07 that was executed. A similar cone study, whose results were discussed in Chapter 6 and plotted in Figure 6.17, further supports this reasoning by showing about the same 6 dB discrepancy at 8 GHz between the "AAPG V07 Present L_{cs} Formulation" curve and the "AAPG V09 L_{cs} Formulation" curve.

7.3 EFFECTS OF AAPG V09 TAIL CONE ON SURFACE DIFFRACTION LOSSES

7.3.1 Model Refinement. The generation of a model of the EST Challenger aircraft with a realistic tail section is the relatively simple process of refining the model created in section 7.2.1.

Once again, the top-view and side-view cross sections of the EST Challenger airframe of Figure 7.1 are considered. The top-view shows a tail section that is symmetrical about the centre line of the aircraft. For simplicity of model generation, a cone of best-fit is superimposed onto the top-view of the tail section. Then, the same tail cone section is viewed from the side to determine the extent of the discrepancy between the model and the actual airframe. Although a discrepancy is evident between the model and actual airframe, the non-tilted cone model is satisfactory for the purposes of this preliminary investigation. The result of this process is illustrated in Figure 7.7.

The choice of a tail cone section that follows the envelope of the top view cross section instead of the envelope of the side-view cross-section gives a smaller tail cone model which has several implications. One implication is that the stabilizers in the vicinity of the tail cone have to be adjusted. The bottom edge of the vertical stabilizer must be extended downwards to meet the surface of the tail cone. The inner edge of the small fins that represent the engine pylons and engine pods must be extended inwards, to

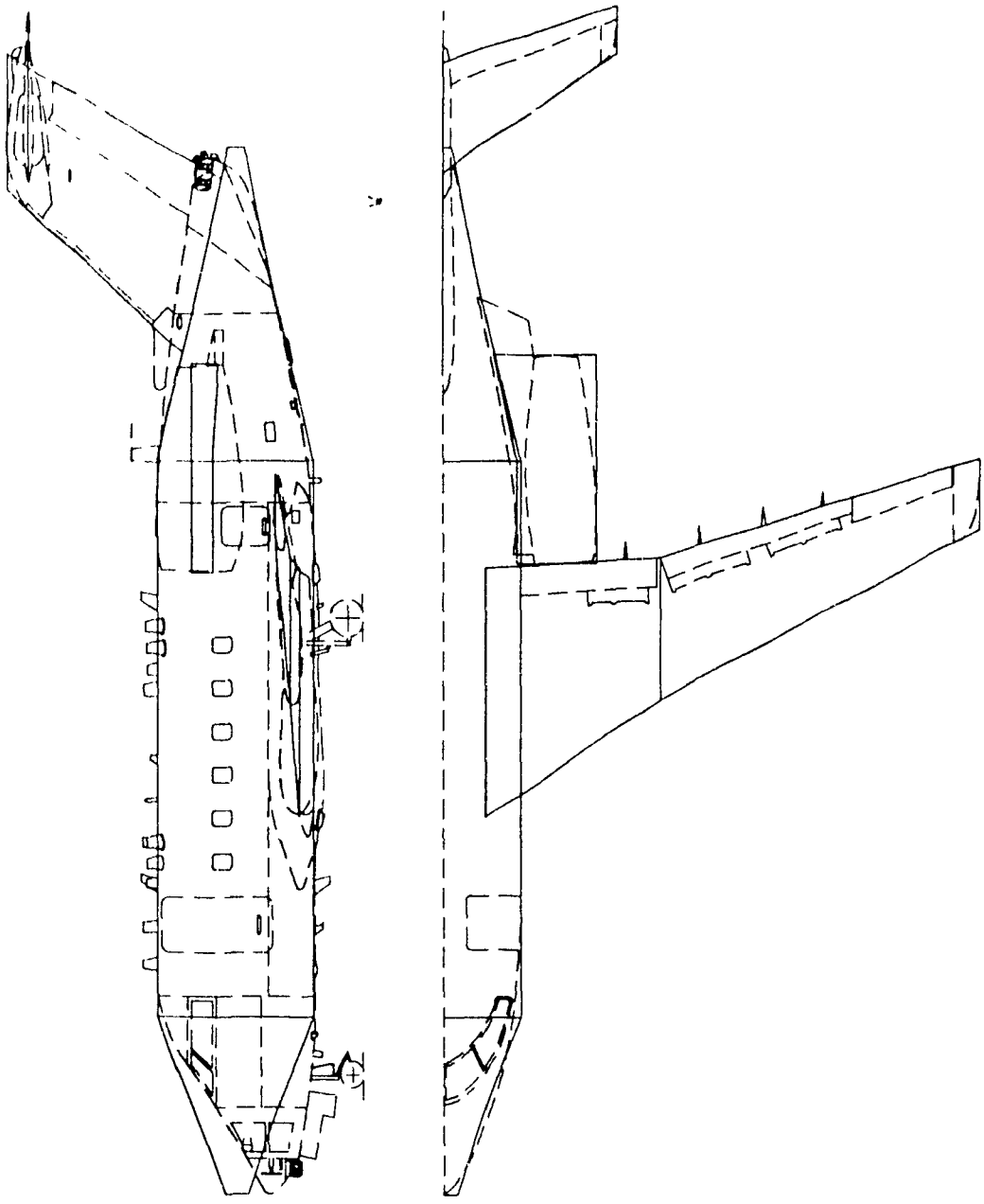

Figure 7.7. AAPG V09 complex model of the EST CL-600 Challenger airframe.

meet the surface of the cone.

The choice of tail cone model has an impact on the positioning of the antennas. The antennas that were located on the surface of the aft end of the cylinder in the previous model are adjusted so that they are located at the same relative position on the surface of the new tail cone model. The I-band antenna discussed in section 7.2.1 is not considered in this model because it violates the AAPG V09 tail cone positioning constraint (also discussed in section 7.2.1) and because this study is concerned primarily with surface diffraction coupling cases. The entire Omega navigation transmitter/receiver system can be ignored because the AAPG V07 and AAPG V09 analyses of section 7.2.2 determined that no frequency coincidence occurred with any other onboard avionics systems. For future consideration, a potential work-around solution in either case would be to re-locate each antenna to a position just slightly forward of the aft bulkhead and to account for that position change in the path length and EMI margin computations.

The choice of a smaller tail cone model has an impact on the computation of the EMI margin values. This choice is more conservative as the coupling paths are expected to be shorter over a smaller tail cone model. It is important to recall from earlier chapters that shorter coupling paths generally yield higher EMI margins.

Clearly, the tail cone section could be refined further by having the cone tilted upwards. However, to simplify the comparative analysis of similar coupling paths, the tail cone is not tilted. Tilted cone sections, both aft and forward, would be a first level of model refinement.

From the scale engineering drawings, it is observed that the tapering of the tail cone is not as severe in the side-view cross-section as it is in the top view cross section. One would then suspect that the cross-section the tail section is elliptical instead of circular. To get an assessment of the effect of an elliptical cross section on the EMI margins, a completely new model of the fuselage would have to be created because AAPG V09 requires that cross-sections of nose and tail cones have the same shape as that

of the fuselage section. An even further refinement would be to have a tail section which is both tilted and elliptical in cross-section.

All of these more complex refinements are interesting explorations that should be considered for future study.

7.3.2 Surface Diffraction Coupling Paths. The repercussions of the model refinement discussed in the previous section are examined in the context of the various aspects of the EMI margin computation. The representative composite cone/cylinder surface diffraction coupling path of section 7.2.2 is revisited and the former results are compared with those generated by AAPG V09 on the complex two cone model, which is illustrated in Figure 7.8.

The runs of AAPG V09 on the simple model of Figure 7.5 and of AAPG V09 on the complex model of Figure 7.7 yield significantly different results, as one might expect. From the casual inspection of the graphical display shown in Figure 7.8, the EMI energy traverses a path which is considerably more complicated than in the preceding instances. The energy is transmitted from the I-band transmit antenna located on the forward cone along a conical spiral, transitions to a cylindrical spiral as it moves aft along the top of the cylindrical section, transitions back to a conical spiral on the tail cone, and arrives at the ESM antenna located on the left side at the aft extreme of the aircraft tail cone. It is important to note that the coupling path is shown to penetrate the vertical stabilizer along the top of the tail cone. One would expect the true path to diffract off the forward edge of the vertical stabilizer and hence have a lower EMI margin due to an additional edge shading (diffraction) loss. Unfortunately, AAPG V09 is not currently capable of considering diffraction from wings or stabilizers that extend along the fuselage into regions where the fuselage is modelled by the cones [22].

Surprisingly, in spite of the differences in the path trajectory, the path length of 464 wavelengths computed at a frequency of 8 GHz for the complex model case is

PARAMETER	HARMONIC NO 1 8.000 GHZ	HARMONIC NO 2 16.00 GHZ	HARMONIC NO 3 18.60 GHZ
TRANSMITTER POWER	54.8	48.8	-.2
XMTR CABLE LOSSES	-2.5	-12.5	-22.5
XMTR ANTENNA GAIN	-3.0	-3.0	-3.0
FREE SPACE LOSS	-75.3	-81.3	-82.6
SURFACE SHADING	-6.0	-11.1	-12.4
EDGE SHADING	.0	.0	.0
BULKHEAD SHADING	.0	.0	.0
RCVR ANTENNA GAIN	-9.3	-9.3	-9.3
RCVR CABLE LOSSES	.0	.0	.0
RCVR LEVEL	-80.0	-80.0	-59.9
EMI MARGIN	38.6 \ 464	11.5 \ 928	-70.2 \ FAR
\ FIELD WARNING	------	------	

EMITTER ■

SUBSYSTEM : ECMI
TRANSMITTER : ECMITX
ANTENNA : IANTFT

AZ = 171.5 EL = 20.6

RECEPTOR □

SUBSYSTEM : ESM
RECEIVER : ESMRXA
ANTENNA : ESMLA

AZ = -.3 EL = 20.9

(33.18-00)

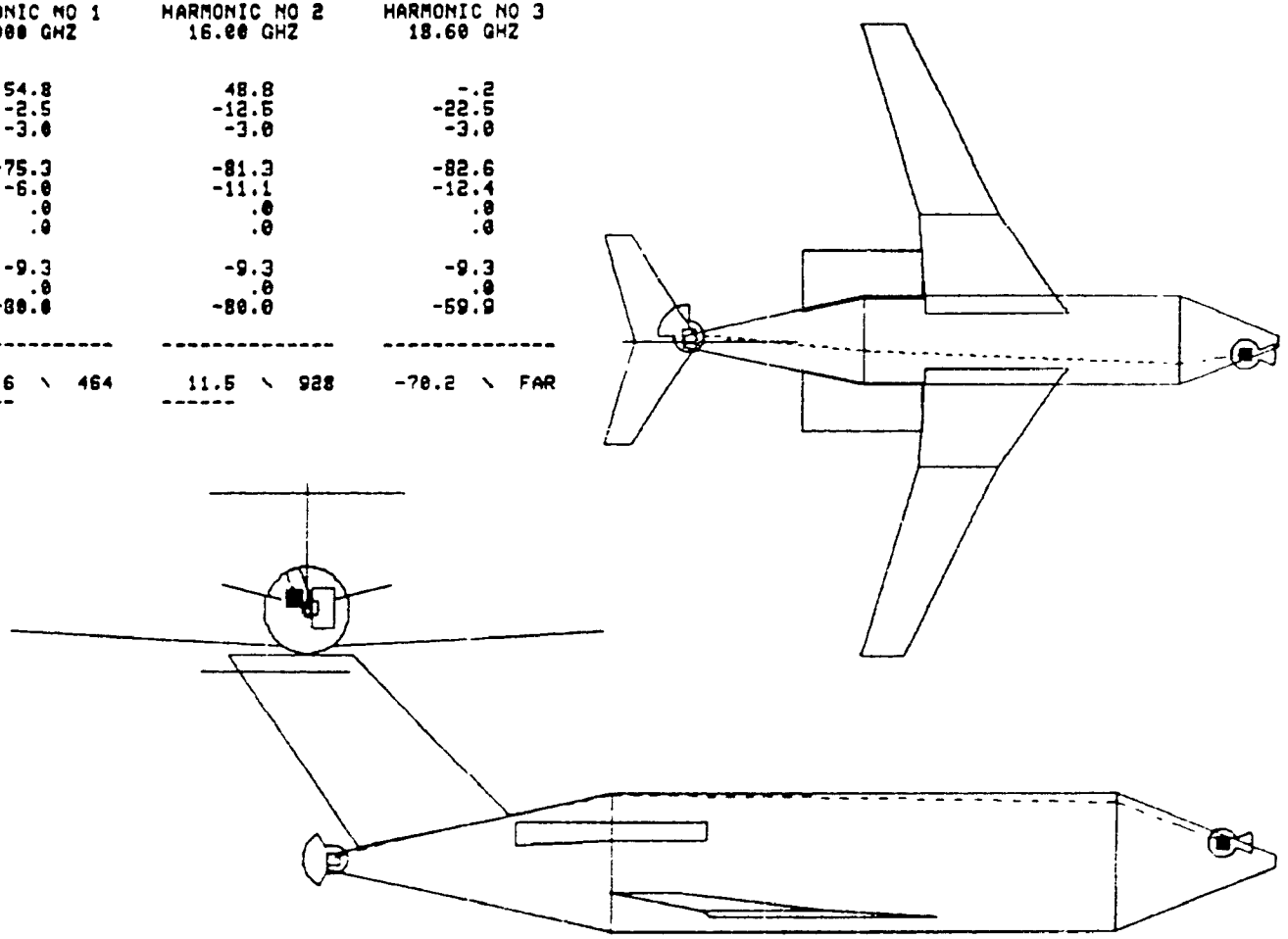

Figure 7.8. EMPP Display of surface diffraction coupling path computed by AAPG V09 on complex model.

identical to the path length computed for the simple model. It follows that the path length dependent transmission loss component of the EMI margin is computed to be -75.3 dB, unchanged from the previous two cases. Further similarities are evident: the AAPG V09 computations of the AZ and EL angles taken by the coupling path at the transmit antenna on the complex model are within 2 degrees of those computed by AAPG V09 on the simple model. In the worse case, those angles at the transmit antenna differ by only 13 degrees from the AAPG V09 computation on the simple model to computation on the complex model. As expected, the similarity in path angles lead to computed antenna gains that are also comparable.

The fundamental difference between the previously computed results and the results computed by AAPG V09 on the complex model is the surface shading loss factor. This loss term is computed to be 18.7 dB lower on the sample path for the AAPG V09 complex model. This discrepancy can be attributed to the shape of the model, not to any inherent differences in the surface shading loss algorithm. The shape, size, and positioning of the nose and tail cones relative to the antenna locations on the complex model are such that the rate of change of angular position of the coupling path is more gradual on the complex model, and hence the surface shading loss is not as severe.

7.4 SIDE-BY-SIDE COMPARISON OF ANTENNA PATTERNS FOR AAPG V07 AND V09

In section 2.3.4, the antenna gain pattern models were discussed in terms of the key hole approximation implemented in AAPG V07 and the Gaussian lobe approximation implemented in AAPG V09. The gain is computed based on the path angles taken by the coupling path at each antenna. In the case of the key-hole approximation of AAPG V07, the gain drops off sharply between the mainbeam and the sidelobe/backlobe, which is reasonable for narrower beam antennas. By contrast in the case of the Gaussian lobe approximation of AAPG V09, the gain drops off gradually and continuously between the

mainbeam and the sidelobe/backlobe, which is appropriate for wider beam antennas.

Regarding the antennas associated with the sample coupling paths studied in the earlier sections, the AAPG V07 gain patterns are illustrated in Figures 7.9 and 7.10 and the respective AAPG V09 gain patterns are illustrated in Figures 7.11 and 7.12. Since the EMI energy is transmitted from the backlobe of the I-band antenna and is received into the backlobe of the ESM antenna, the antenna gains computed in the three cases are within 0.7 dB of each other. Therefore, for this particular choice of coupling path, there is little benefit in the added complexity of the AAPG V09 Gaussian lobe approximation.

In some cases, the AAPG V09 gain pattern model may overestimate the actual antenna gains which lead to computations of higher EMI margins. In such instances, interference may be predicted when compatibility actually exists. The drawback of such a situation would be the time and cost inconvenience to the system integrator of implementing and testing additional, but unnecessary, design measures to ensure system EMC. On the other hand, the AAPG V07 gain pattern model may underestimate the actual antenna gains which lead to computations of lower EMI margins. In such instances, compatibility may be predicted when interference actually occurs. The consequences of a false prediction of EMC range from user annoyance and the loss of system performance to the loss of the aircraft and the loss of life [2]. Clearly, AAPG V09 errs on the side of conservatism, but its computation of antenna gains may be more appropriate in many cases.

A remark on the peculiarities of the AAPG V07 and AAPG V09 antenna pattern diagrams shown in Figures 7.9 through 7.12 is relevant at this point. The information in AAPG V07 antenna pattern plots of Figures 7.9 and 7.10 is somewhat lacking in clarity. For example, the dotted circle representing the 0 dB reference level differs only slightly from the other scale circles. Also, the key hole pattern transition from the sidelobe level to the mainbeam level is not drawn. On the other hand, the information in AAPG V09 antenna pattern plots of Figures 7.11 and 7.12 is displayed clearly and concisely. The

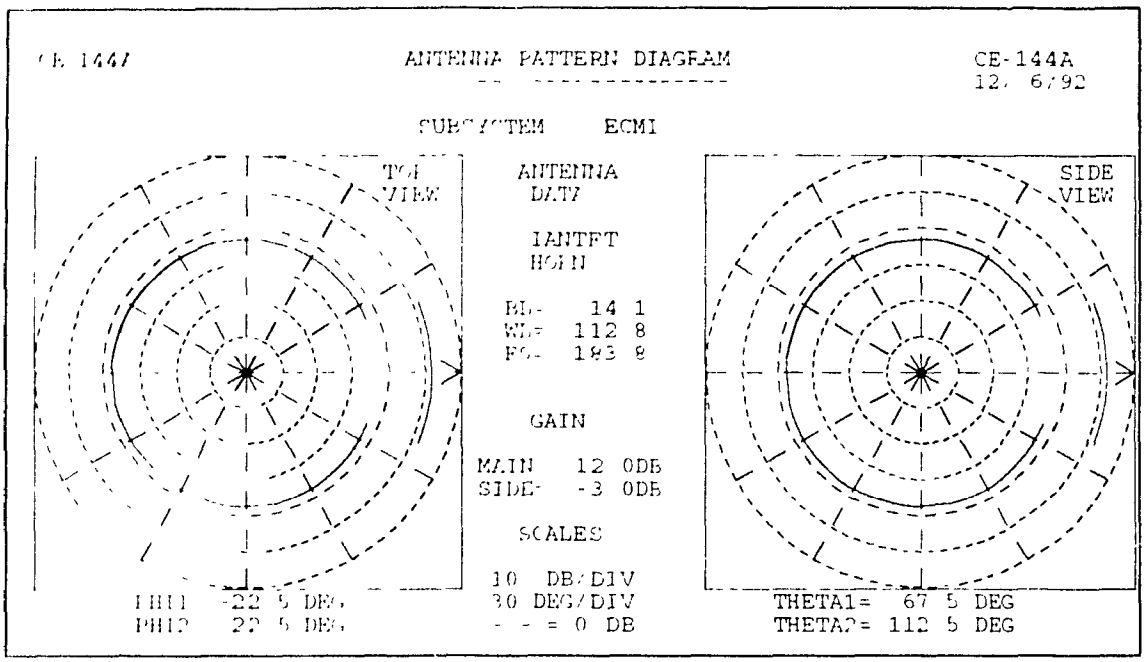

Figure 7.9. AAPG V07 display of gain pattern for transmit antenna in test case of Figures 7.4 and 7.5.

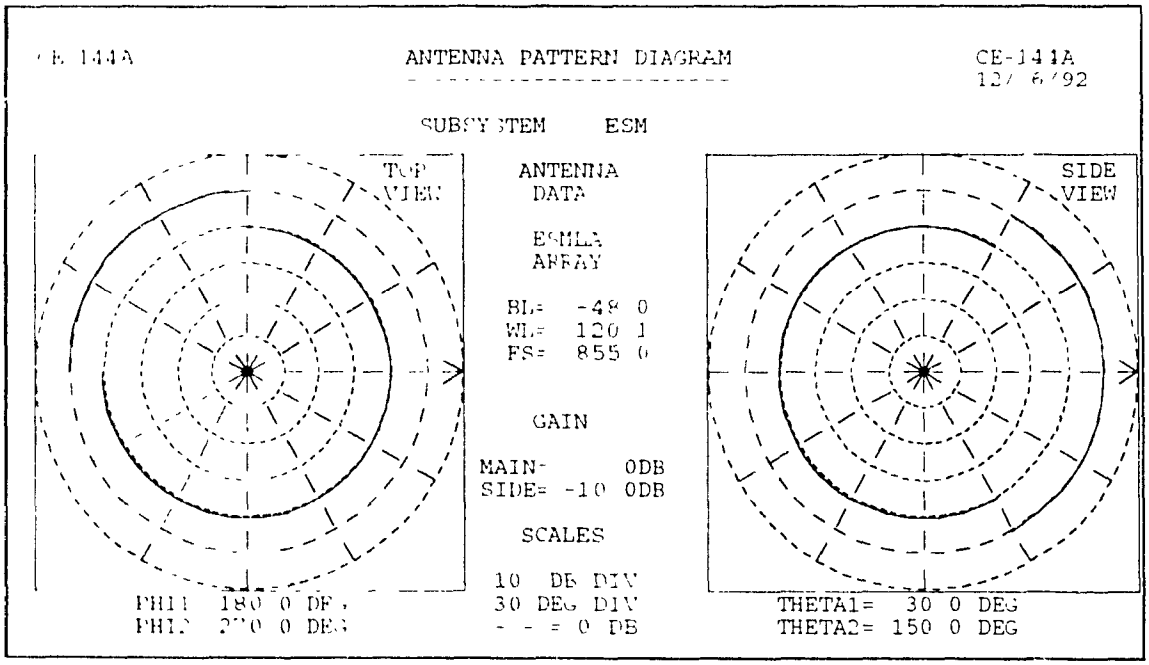

Figure 7.10. AAPG V07 display of gain pattern for receive antenna in test case of Figures 7.4 and 7.5.

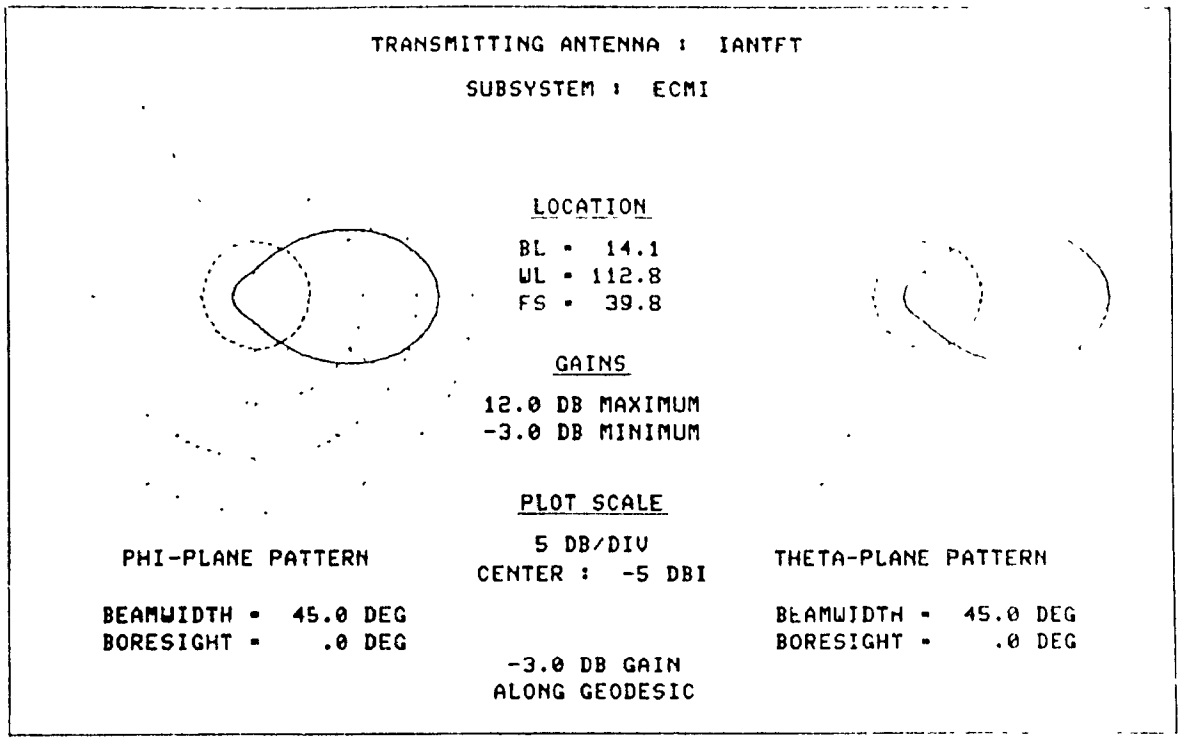

Figure 7.11. AAPG V09 display of gain pattern for transmit antenna in test case of Figure 7.6 and in test case of Figure 7.8.

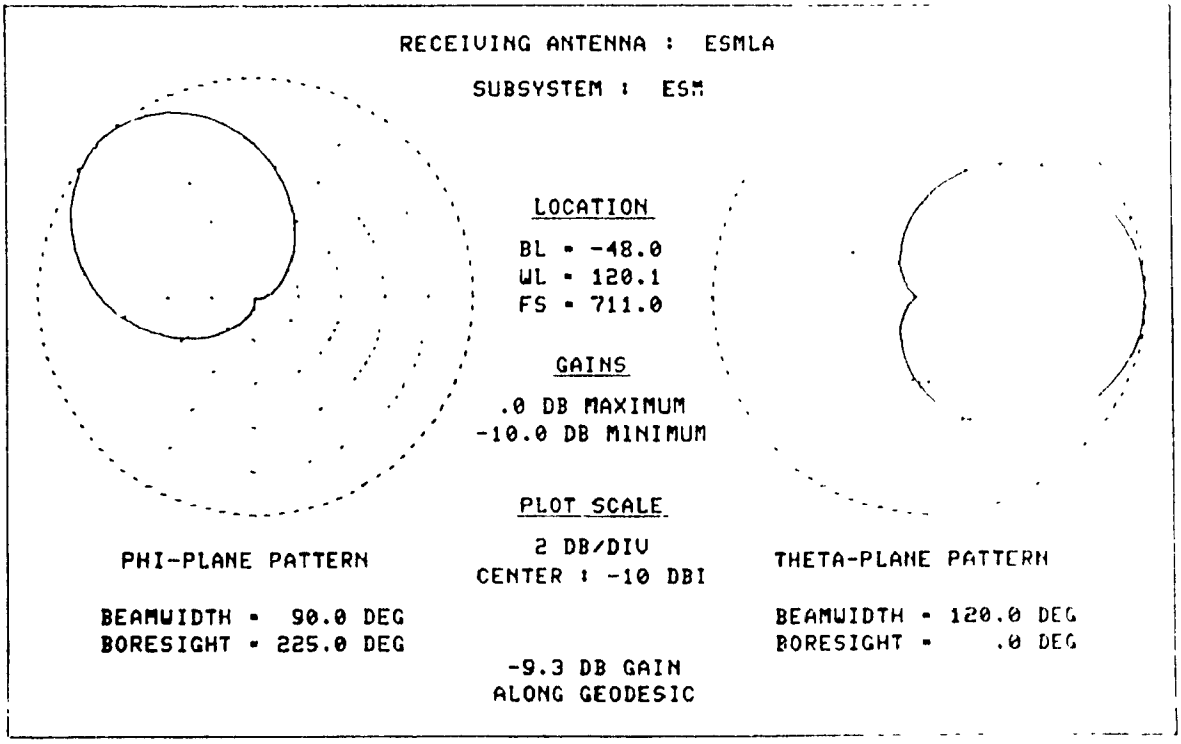

Figure 7.12. AAPG V09 display of gain pattern for receive antenna in test case of Figure 7.6 and in test case of Figure 7.8

reference level value is clearly indicated as the centre of the AAPG V09 antenna pattern plot and the gain pattern is drawn in its entirety. In addition, a useful reminder of the gain along the geodesic is provided at the bottom of the AAPG V09 antenna gain plot.

7.5 FINAL REMARKS

The work of this chapter allowed the addressing of several important issues in EMI analysis code development and application: geometric considerations in model development, repercussions in shading loss values based on consequent geodesic path differences, and the trade-offs in model complexity. These issues are summarized in Table 7.1. This thesis could not explore these issues completely, but exposed these aspects for further systematic exploration.

A general remark on the quality of the AAPG output is in order. Current configurations of AAPG V07 produce PostScript file output that are professional in appearance and easy to manipulate for documentation purposes as evidenced by Figures 7.4 and 7.5. The various configurations of AAPG V09 however produce only hard-copy output. The manipulation of output for documentation purposes is more awkward with the involved process of photocopying/photoreduction, and cutting and pasting. Moreover, the AAPG V09 output varies considerably in quality. The dot matrix screen bitmap dump shown in Figure 7.6 is poor in resolution and is distorted due to the assymmetrical aspect ratio of the screen. The Tektronix hard-copy unit output shown in Figure 7.8 is more professional in appearance, but caution had to be exercised in photocopying the plot to ensure that none of the numerical values were obscured.

It is crucial to point out that, through the course of this study, several difficulties were encountered with three particular variants of AAPG V09 available at the EMC Laboratory at Concordia University, whereas all of the variants of AAPG V07 ran trouble free. All AAPG V09 variants were provided by the Electromagnetic Compatibility Analysis Center (ECAC) in Annapolis, Maryland and were run on a

Table 7.1. Summary of AAPG sample coupling paths on 3 EST Challenger models.

	AAPG V07 model	AAPG V09 simple model	AAPG V09 complex model
Aircraft model features	- Nose cone only - All systems modelled - Figure 7.2	- Artificially extended tail cone - All systems modelled - Figure 7.3	- Realistic nose and tail cones - Antennas aft of aft bulkhead ignored - Figure 7.7
Coupling Path Description	- Conical/cylindrical spiral - Figures 7.4 and 7.5	- Conical/cylindrical spirals - Figure 7.6	- Conical/cylindrical/conical spirals - Diffraction at forward edge of vertical stabilizer - Figure 7.8
Path Length at 8 GHz	463 λ	464 λ	464 λ
Path angles at xmit ant.	AZ = 179.00°, EL = 27.62	AZ = 169.0°, EL = 18.8°	AZ = 171.5 , EL = 20.6°
Path angles at rcv ant.	AZ = 2.99°, EL = 6.32°	AZ = 4.7 , EL = 7.2°	AZ = -0.3 , EL = 20.9
EMI margin	25.2 dB	19.6 dB	38.6 dB
Surface shading factor	-18.7 dB	-24.7 dB	-6.0 dB
Transmit antenna gain	-3.0 dB	-3.0 dB	-3.0 dB
Receive antenna gain	-10.0 dB	-9.7 dB	-9.3 dB
Gain pattern model	Key-hole approximation	Gaussian approximation	Gaussian approximation
Output medium	- PostScript file - Tektronix hard copy	- Dot matrix screen bitmap dump	- Tektronix hard copy
Display hardware	- VGA - Tektronix graphics display	- EGA	- Tektronix graphics display

80386 based microcomputer. The most recent version, AAPG V09C2, was run on the input data files for the models shown in Figures 7.3 and 7.7, and in both instances caused the computer to "hang". The next most recent version, AAPG V09B, was run on the same input data files and generated reasonable numerical output. AAPG V09B however produces poor quality hard copy output so AAPG V09A, which has Tektronix hard copy output capability, was used. AAPG V09A was run on those input data files, but only yielded correct results for the complex model.

It became obvious that many inherent problems of algorithm stability exist in AAPG V09 and that more verification of this complex code is necessary before general release to the AAPG V07 user community. The data sets and results produced for this comparative study provide a good starting point for such a verification.

CHAPTER 8

CONCLUSIONS

8.1 SUMMARY OF THESIS AND CONTRIBUTIONS

This thesis examined the need for a systematic methodology for the analysis of aircraft EMC problems. It surveyed the evolution and the current availability of computer aids used in aircraft EMC analysis and established the theoretical basis for the complex algorithms which identify and quantify electromagnetic interactions. This thesis then presented a series of important new algorithms and graphics routines for the AAPG V07 EMC analysis code and provided a comprehensive assessment of associated code features and their practical relevance. This thesis explored the enhanced features and undocumented limitations of AAPG V09, a next generation EMC analysis code, by means of an example of an existing Canadian military aircraft in a comparative analysis with AAPG V07. This material was presented in a framework which was intended to describe the requirement for this work and to indicate the state of the art of this type of specialized technical analysis.

Chapter 2 examined the EMC analysis methodology and its challenges. The concept of EMI margin was introduced as a quantifying factor in determining the criticality of an EMI interaction. The EMC analysis methodology, the EMI margin and modelling considerations were then studied in the context of aircraft antenna to antenna coupling problems. The Aircraft Inter-Antenna Propagation with Graphics (AAPG) computer code was introduced as a software tool for analyzing aircraft antenna to antenna coupling problems.

The theory associated with the curved surface diffraction loss factor used in the computation of the EMI margin was the focus of Chapter 3. The derivation of a few

elegant expressions associated with the curved-surface diffraction loss factor was examined. One such key expression for the Fock parameter, which plays a crucial role in the computation of the curved-surface diffraction loss factor, was studied in the context of two versions of the AAPG code.

Chapter 4 addressed the deficient areas of the cone geodesic computational algorithms in AAPG V07. The new enhancements to the code, the test results, and their impact on realistic aircraft EMC problems were outlined. The observed improvements ensure that the computation of the EMI margin for coupling paths on the cone surface are more accurate.

Chapter 5 assessed the corresponding graphics display algorithms for the cone section. The essential principle of one-to-one correspondence between the computed paths and the path which is graphically displayed was emphasized and restored. The corresponding improvements were validated by the test results on realistic aircraft EMC problems. The improvements ensure that the displayed coupling path is a truer representation of the physical path.

Chapter 6 compared current developments in specific software implementations of the curved surface diffraction loss factor with measurement data from the technical literature. The study substantiated the expanded capabilities of the curved-surface diffraction loss factor for arbitrarily convex cross-sections implemented in AAPG V09. The expressions derived in Chapter 3 for the curved-surface diffraction loss factor and Fock parameter were implemented in an interim upgraded version of AAPG V07, so-called "AAPG V07 (Revised)". The re[illegible] of AAPG V07 (Revised) on test cases on a right circular cone compared favourably with measurement data ar[illegible] AAPG V09. The chapter concluded by pointing out that previously proposed implementations of the curved surface diffraction loss factor and Fock parameter were incorrect.

Chapter 7 rounded out the theoretical and algorithmic aspects of the previous chapters with a user-directed comparative evaluation of AAPG V07 and V09. The differences in EMI margins and the relative merits of each code were explored in the context of the EST Challenger aircraft currently in use by the Canadian Forces. The investigation revealed that although the modelling capabilities of AAPG V07 are perhaps not as sophisticated as those of AAPG V09, the limitations and deficiencies of AAPG V07 are well-known and well-documented. Many inherent problems of algorithm stability were found to exist in AAPG V09, which have not been previously documented.

8.2 RECOMMENDATIONS FOR FUTURE WORK

The thesis has contributed significantly to the increase in the reliability and the capabilities of AAPG V07, a widely used EMC analysis tool. This contribution should lead to the user community's increased confidence in that instrument. The thesis has also documented some of the previously unreported capabilities, limitations, and deficiencies of AAPG V09. As a consequence of this thesis, several avenues for future research and code enhancement are now available.

The deficient areas of the cone geodesic computational algorithms in AAPG V07 were addressed in Chapter 4. The improvements to the code included algorithm changes as well as code structuring to facilitate software maintenance and upgrade. A potential AAPG V07 upgrade in which such features of the code could be advantageous is the optimization of the cone/flat-bottom junction point computed by the module ITER.

Chapter 6 reconciled the proposed AAPG V07 enhanced implementation of the curved-surface diffraction loss factor and Fock parameter with measurement data. These expressions were implemented only in an interim upgraded version of AAPG V07. This implementation must now be formalized by means of rigorous, formal testing with numerous data sets in the EMC Laboratory at Concordia University. The software

engineering of complex codes such as this requires that the AAPG V07 user community be informed of the code's problem areas and improvements and that proper software configuration control be maintained via deficiency reports and change notices.

The preliminary user-directed comparative evaluation of AAPG V07 and V09 in Chapter 7 revealed many inherent problems of algorithm stability in AAPG V09. A more methodical verification of this complex code, documentation of its deficient areas, and code improvements or strategies for circumventing those deficiencies are necessary before general release to the AAPG V07 community. The data sets and results produced for this thesis provide a good starting point for such a verification, which would complement very well the ongoing efforts at the Electromagnetic Compatibility Analysis Center (ECAC) in Annapolis, Maryland.

Development work continues at the EMC Laboratory at Concordia University on the Computer Aided EMC Test-Planning System (CAETS), a computer analysis code which models the fundamental, intermediate, and image frequency interactions of transmitters and receivers. The CAETS analysis provides tabular and graphical output for the following types of frequency coincidence [43,44]: harmonic frequency coincidence, image frequency coincidence, intermediate frequency coincidence, and local oscillator frequency coincidence. A practical investigation is recommended in which the feasibility of data interaction between AAPG and CAETS and of how such an interaction could be implemented would be assessed.

The EMC Laboratory at Concordia University has developed much expertise in the use of the Numerical Electromagnetics Code [45] and ancillary software tools to analyze radiation patterns and antenna-to-antenna coupling problems by means of wire grid models of aircraft and their antennas. Due to the limitations on the number of wire elements in a particular aircraft model, NEC is restricted to a practical frequency range of 1 to 30 MHz. On the other hand, AAPG is limited to analyses above approximately

150 MHz due to the high frequency approximation used in the curved-surface diffraction loss factor expression [6]. The enhancement of AAPG by means of a hybrid of method of moments and UTD techniques as suggested by Davidson and Thiele [46], the linkage with other modelling methods as suggested by Hubing [47], and perhaps the exploitation of GEMACS as described by Starkiewicz [10] would circumvent AAPG's low frequency limitation.

Regardless, AAPG V07 is the aircraft antenna-to-antenna EMC analysis code currently in use and it will continue to be used in Canada by DND and its contractors, and in NATO countries for the immediate future. Continued efforts to maintain and upgrade AAPG V07, and aircraft EMC analysis tools in general, will surely be well received by that community.

References

[1] Spina, John F., "The EMC Concept for Weapon Systems," AGARD Lecture Series No. 116, Electromagnetic Compatibility, AGARD-LS-116, Lecture No. 1, August 1981

[2] Military Specification Electromagnetic Compatibility Requirements, System, MIL-E-6051D including Notice 1, 26 February 1988.

[3] LaMontagne, Capt Richard R., "Intrasystem Analysis Program," IEEE International Symposium on Electromagnetic Compatibility, Washington, DC, July 13-15, 1976, p 244-245.

[4] Vuille, M., Kubina, S.J., and Widmer, H., "Interactive Graphics for EMC Analysis," IEEE International Symposium on Electromagnetic Compatibility, Atlanta, GA, June 20-22, 1978, pp. 316-319.

[5] Kubina, Stanley J., "Computer Graphic Aids to Weapon Systems EMC Analysis," AGARD Lecture Series No. 116, Electromagnetic Compatibility, AGARD-LS-116, Lecture No 5, August 1981.

[6] Widmer, Hans P., and Klocko, William R., A Guide to Using the AAPG Program (Version 07), Consulting Report ECAC-CR-87-024, DoD ECAC, Annapolis, MD, July 1987.

[7] LoVetri, Joe, and Henneker, William H., "Fuzzy Logic Implementation of an Electromagnetic Interactions Modelling Tool," IEEE International Symposium on Electromagnetic Compatibility, Anaheim, CA, August 17-21, 1992, pp. 127-130.

[8] Drozd, Andrew L., "Overview of Present EMC Analysis/Prediction Tools and Future Thrusts Directed at Developing AI/Expert Systems," IEEE International Symposium on Electromagnetic Compatibility, Anaheim, CA, August 17-21, 1992, pp 528-529.

[9] Larrat, Andrew, "Guest Editorial - Introduction to the Issue," IEEE Transactions on Electromagnetic Compatibility, Vol EMC-22, No. 4, Part I of II, November 1980, pp. 217-218.

[10] Starkiewicz, Kenneth, "GEMACS - An Executive Summary," IEEE International Symposium on Electromagnetic Compatibility, Boston, MA, August 20-22, 1985, pp 75-81.

[11] Burnside, W.D., Rudduck, R.C., and Marhefka, R.J., "Summary of GTD Computer Codes Developed at Ohio State University," IEEE Transactions on Electromagnetic Compatibility, Vol. EMC-22, No. 4, Part I of II, pp 238-243.

[12] Gerbi, G., and Amò, C., "ACAP: Antenna Coupling Analysis Program," 4th Symposium and Technical Exhibition on Electromagnetic Compatibility, Zurich, March 10-12, 1981, pp. 481-486.

[13] Li, Shing Ted, Logan, James C., and Rockway, John W., "Automated Procedure for Shipboard Exterior Communication RF System Design," IEEE Transactions on Electromagnetic Compatibility, Vol. EMC-22, No. 4, Part I of II, November 1980, pp. 219-223.

[14] Hodes, Harry H., and Widmer, Hans P., "The Solution of 'Real World' Aircraft EMC Problems Using the AAPG Computer Program," Proceedings of the IEEE National Aerospace and Electronics Conference - NAECON 1982, Vol. 1, Dayton, OH, May 18-20, 1982, pp. 11-18.

[15] Bogusz, M. and Kubina, S.J., AAPG V07 Auxiliary Manual - Code Changes through Version V07J, Technical Note TN-EMC 92-09, EMC Laboratory, Concordia University, Montreal, QC, 23 December 1992.

[16] Bogusz, M., and Kubina, S.J., "Improvements in Antenna Coupling Path Algorithms of Aircraft EMC Analysis," Proceedings of Canadian Conference on Electrical and Computer Engineering, Quebec City, QC, September 1991, pp. 10.1.1-10.1.4.

[17] EST Systems Project Phase I Preliminary EST Challenger Design Antenna Placement Study, Lockheed Canada Inc., Document No. 1000973, July 1990. (Prepared under Contract W8475-7-KG01/01-BF for the Department of National Defence)

[18] Analysis of a CH-124A Sea King Helicopter Electromagnetic Compatibility, Vol II, Aircraft Inter-Antenna Propagation with Graphics, I.M.P. Group Limited, Engineering Report No. CH124A/R210, 8 February 1989.

[19] Report on AAPG Electromagnetic Compatibility Analysis for the CP121 Tracker, Vol. 2, I.M.P. Group Limited, Engineering Report No. CP121/R180, 27 February 1989.

[20] Skolnik, Merrill L., Radar Handbook, McGraw-Hill Book Company, New York, 1970.

[21] Friis, Harald T., "A Note on a Simple Transmission Formula," Proceedings of the IRE, Vol. 34, No. 5, May 1946, pp. 254-256.

[22] Hussar, Paul E., and Klocko, W.R., User's Manual for the Aircraft Inter-Antenna Propagation with Graphics (AAPG) Computer Program, User's Manual ECAC-UM-90-048, DoD ECAC, Annapolis, MD, August 1990.

[23] Kouyoumjian, Robert G., and Pathak, Prabhakar H., "A Uniform Geometrical Theory of Diffraction for an Edge in a Perfectly Conducting Surface," Proceedings of the IEEE, Vol. 62, November 1974, pp. 1448-1461.

[24] Lee, S.W., Differential Geometry for GTD Applications, Electromagnetics Laboratory Technical Report UILU-ENG-77-2264, University of Illinois at Urbana-Champaign, Urbana, IL, October 1977.

[25] Widmer, Hans P., Klocko, William R., and Hussar, Paul E., A Technical Description of the AAPG Program (Version 07), Consulting Report ECAC CR-87-031, DoD ECAC, Annapolis, MD, July 1987.

[26] Boston, Dean R., and Bowman, Terry G., "Working Within the Limitations of System Analysis Software," IEEE International Symposium on Electromagnetic Compatibility, Anaheim, CA, August 17-21, 1992, pp.35-37.

[27] Hasserjian, G., and Ishimaru, A., "Excitation of a Conducting Cylindrical Surface of a Large Radius of Curvature," IRE Transactions on Antennas and Propagation, Vol. AP-10, May 1962, pp. 264-273.

[28] Lee, S.W., "Mutual Admittance of Slots on a Cone: Solution by Ray Technique," IEEE Transactions on Antennas and Propagation, Vol. AP-26, No. 6, November 1978, pp. 768-773.

[29] Lee, S.W., "A Review of GTD Calculation of Mutual Admittance of Slots Conformal Array," Electromagnetics, Vol. 2, No. 2, April-June 1982, pp. 85-127.

[30] Golden, Kurt E., Stewart, Gordon E., and Pridmore-Brown, David C., "Approximation Techniques for the Mutual Admittance of Slot Antennas on Metallic Cones," IEEE Transactions on Antennas and Propagation, Vol. AP-22, No. 1, January 1974, pp. 43-48.

[31] Chan, Kuan-Kui, Felsen, Leopold B., Hessel, Alexander, and Shmoys, J., "Creeping Waves on a Perfectly Conducting Cone," IEEE Transactions on Antennas and Propagation, Vol. AP-25, No. 5, September 1977, pp. 661-670.

[32] Pathak, P.H., and Wang, N., "Ray Analysis of Mutual Coupling Between Antennas on a Convex Surface," IEEE Transactions on Antennas and Propagation, Vol. AP-29, No. 6, November 1981, pp. 911-922.

[33] Lee, S.W., and Safavi-Naini, S., "Approximately Asymptotic Solution of Surface Field due to a Magnetic Dipole on a Cylinder," IEEE Transactions on Antennas and Propagation, Vol. AP-26, No. 4, July 1978, pp. 593-597.

[34] Abramowitz, M., and Stegun, I.A., ed., Handbook of Mathematical Functions, Dover Publications, Inc., New York, 1972.

[35] Klocko, W., Masters, P., and Campbell, B., A Technical Description of the Aircraft Inter Antenna Propagation with Graphics (AAPG) Computer Program, Handbook ECAC HDBK-90-083, DoD ECAC, Annapolis, MD, April 1990.

[36] Bhattacharyya, Asoke K., and Kubina, Stanley J., "Cross-Polarization Components in Inter-Antenna Coupling Calculations," IEEE International Symposium on Electromagnetic Compatibility, San Diego, CA, September 16-18, 1986, pp. 184-187.

[37] Logan, Nelson A., General Research in Diffraction Theory, vol 1, LMSD 288087, Missiles and Space Div., Lockheed Aircraft Corp., Sunnyvale, CA, December 1959.

[38] Chatterjee, Debobroto, Evaluation of a Class of Creeping Wave Formulations with Applications to Practical Modeling of Aircraft Antenna EMI Coupling Problems, Master of Applied Science Thesis, Concordia University, Montreal, QC, March 1992.

[39] Drolet, Marc J.L., Advances in PATH LOSS Algorithms in the Antenna to Antenna Propagation with Graphics (AAPG) EMC Analysis Program, Master of Engineering Thesis, Concordia University, Montreal, QC, August 1989.

[40] Struik, Dirk J., Lectures on Classical Differential Geometry, 2nd ed., reprint, Dover Publications, Inc., New York, 1988, originally published by Addison-Wesley Publishing Company, Reading, MA, 1961.

[41] Durham, Timothy E., "Analysis and Measurement of EMI Coupling of Aircraft Mounted Antennas at SHF/EHF," IEEE International Symposium on Electromagnetic Compatibility, Atlanta, GA, August 25-27, 1987, pp. 420-427.

[42] Durham, T.E., SHF/EHF Antenna-to-Antenna EMI Coupling, Vol. I, Harris Corporation, Government Aerospace Systems Division, Report 0890H/SHF 001, August 1987. (Prepared under Contract F30602-85-C-0114 for Rome Air Development Center, Air Force System Command, Griffiss Air Force Base, NY.)

[43] Christopoulous, C. and Kubina, S. CAFTS Version 5.0 Version Description, Technical Note TN-EMC-92-02, EMC Laboratory, Concordia University, Montreal, QC, 22 May 1992.

[44] Christopoulous, C., Advances in Frequency-Coincidence Algorithms for EMC Testing, Master of Applied Science Thesis, Concordia University, Montreal, QC, December 1991.

[45] Burke, G.J. and Poggio, A.J., Numerical Electromagnetic Code (NEC) Method of Moments, Technical Document 116, Naval Ocean Systems Center, July 1977.

[46] Davidson, Steven A., and Thiele, Gary A., "A Hybrid Method of Moments GTD Technique for Computing Electromagnetic Coupling between Two Monopole Antennas on a Large Cylindrical Surface," 4th Symposium and Technical Exhibition on Electromagnetic Compatibility, Zurich, March 10-12, 1981, pp. 277-282.

[47] Hubing, Todd H., "A Survey of Numerical Electromagnetic Modeling Techniques," Interference Technology Engineers' Master (ITEM) Update 1991, Robar Industries Inc., West Conshohocken, PA, 1991.

APPENDIX A

LISTING OF FUNCTION <FOCKV>

```
C     ------------------------------------------------------------
C
C     FUNCTION FOCKV    VERSION 1, REVISION 0, 22 MAY 1991
C     MICHAEL BOGUSZ
C     REFERENCE    A  GDU GTD COURSE NOTES, VOL  1, PP  AP-36 TO AP-39,
C                  B  LOGAN, NELSON A , "GENERAL RESEARCH IN DIFFRACTION
C                     THEORY VOLUME 1", REPORT LMSD 288087, DECEMBER
C                     1959,
C                  C  LEE, S W , AND SAFAVI-NAINI, S., "APPROXIMATE
C                     ASYMPTOTIC SOLUTION OF SURFACE FIELD DUE TO A
C                     MAGNETIC DIPOLE,"  IEEE TRANS. ON ANT  & PROP ,
C                     VOL  AP 26, NO. 4, JULY 1978;
C                  D. ABRAMOWITZ, M., AND STEGUN, I A , ED , HANDBOOK OF
C                     MATHEMATICAL FUNCTIONS, DOVER PUBLICATIONS, INC.,
C                     NEW YORK, 197.
C
C     IMPLEMENTATION NOTES
C     1   RESIDUE SERIES REPRESENTATION
C         A   THE EXPRESSION FOR V(XI) IN REF  A PP. AP-35 TO AP-36 WAS
C             IMPLEMENTED
C         B   THE VALUES FOR THE MAGNITUDE OF TAU_N PRIMED WERE
C             TAKEN FROM THE BETA(S) COLUMN OF TABLE 4 OF REF. B
C         C.  AN ATTEMPT TO  IMPLEMENT THE EXPRESSION IN REF  B P  6-13
C             WAS UNSUCCESSFUL BECAUSE THE (1/BETA(S)) TERM IS MISSING
C             THE -PI/3 PHASE SHIFT.
C         D   THE REPRESENTATION USES 20 TERMS IN ITS SERIES EXPRESSION.
C         E   THE REPRESENTATION IS EMPLOYED WHEN XI > OR = 0 6.
C
C     2   SMALL ARGUMENT SERIES REPRESENTATION.
C         A   THE EXPRESSION FOR V(XI) IN REF  B P. 9-2 WAS IMPLEMENTED
C             EXCEPT THE EXPONENTIAL TERMS USED HERE HAVE THEIR SIGNS
C             INVERTED  THE RESULT IS THAT THE IMPLEMENTED GENERAL
C             EXPRESSION CORRESPONDS TO THE SIMPLIFIED TERMS SHOWN IN
C             REF 'S A AND C
C         B   THE FIFTH USES ONLY 10 TERMS, ALTHOUGH 20 COEFFICIENTS
C             ARE AVAILABLE
C         C   THE REPRESENTATION IS EMPLOYED WHEN XI < 0 6.
C
C     3   VERIFICATION
C         A   THE IMPLEMENTED EXPRESSIONS WERE VERIFIED TO BE CORRECT
C             IN MAGNITUDE AND PHASE BY CHECKING AGAINST THE PLOT IN
C             REF  A P  AP 3
C
C     ------------------------------------------------------------
```

```
C
      FUNCTION FOCKV( XI )
C
C-------------------------- - -----  -
C
C     FUNCTION TO CALCULATE THE GENERALIZED HARD FOCK FUNCTION V(XI)
C
C     INPUT PARAMETER
C          XI.  FOCK PARAMETER
C
C     OUTPUT PARAMETER
C          FOCKV:  HARD FOCK FUNCTION
C
C---------------------------    -- --
C
C     COMMON BLOCKS AND VARIABLE SPECIFICATION
C
      DOUBLE COMPLEX   FOCKV, SUM, TPH, J, TAUPK
      DOUBLE PRECISION XI, TMG(20), B(20), PI, RTPI, GAMMA
C
C
C     COEFFICIENTS OF RESIDUE SERIES REPRESENTATION OF V(XI)
C     (BETA(S) COLUMN OF TABLE 4 OF REF. B)
C
      DATA TMG / 1.01879297164747,   3.24819758217984,
     &           4.82009921117874,   6.16340735563949,
     &           7.37217725504777,   8.48848673401972,
     &           9.5354490524335S, 10.52766039695774 ,
     &          11.475056633480? , 12.38478837184[illegible] ,
     &          13.262218961665? , 14.1115019704630 ,
     &          14.935937196720S , 15.738201373692S ,
     &          16.520503825433[illegible] , 17.28469505021[illegible] ,
     &          18.032344622504[illegible] , 18.76479843766[illegible] ,
     &          19.483221656567? , 20.18[illegible]15094634 /
C
C     COEFFICIENTS OF SMALL ARGUMENT SERIES REPRESENTATION OF V(XI)
C     (B(N) COLUMN OF TABLE 7 OF REF. B)
C
      DATA B   / -1.0          , 0.25         ,
     &           -0.21875      , 0.328125     ,
     &           -0.71435546[illegible] , [illegible].07128906[illegible] ,
     &           -7.55723571   , 33.32006[illegible] ,
     &           -172.342419   , 1022.806406 ,
     &           -6847.767     , 51038.51     ,
     &           -4.190135D+05, 3.756370D+06,
     &           -3.650733D+07, 3.823077D+08,
     &           -4.291192D+09, 5.139460D+10,
     &           -6.541785D+11, 8.818285D+12 /
C
C     PI AND SQRT( PI ) TO 15 SIGNIFICANT DIGITS (REF. [illegible]
C
      DATA PI / 3.14159265358979 /, RTPI / 1.77245385090552 /
```

```
C
C     ------------------------------------------------------------------
C
C     FOR XI < 0.6, USE SMALL ARGUMENT SERIES REPRESENTATION OF V(XI)
C     OTHERWISE, USE THE RESIDUE SERIES REPRESENTATION OF V(XI)
C
      SUM    ( 0.0, 0.0 )
      J      ( 0.0, 1.0 )

C
C     *** SMALL ARGUMENT SERIES REPRESENTATION ***
C
      IF( XI .LT. 0.6 ) THEN
          DO 100 N=0, 9
              SUM = SUM +
     &              ( CDEXP( J * PI / 4.0 ) * DSQRT( XI**3 ) )
     &                  ** N * B(N+1) / GAMMA( 3*N + 1, 2 )
  100     CONTINUE
          FOCFV = SUM * RTPI
C
C
C     *** RESIDUE SERIES REPRESENTATION ***
C
      ELSE
          TPH = DCMPLX( 1.0, -DSQRT(3.0) ) / 2.0
          DO 200 N=1, 20
              TAUPR = TPH * TMG(N)
              SUM = SUM + CDEXP( -J * TAUPR * XI ) / TAUPR
  200     CONTINUE
          FOCFV = SUM * RTPI * DSQRT( XI ) * CDEXP( -J * PI / 4.0 )
      ENDIF
C
C     ------------------------------------------------------------------
C
      RETURN
      END
```

APPENDIX B

LISTING OF FUNCTION <GAMMA>

```
C-----------------  -  -----
C
C      FUNCTION  GAMMA :  VERSION  1,  FE  I  I  ,  ,  F
C      MICHAEL  FOGUEL
C      REFERENCES:  A.  ABRAMOWITZ AND  TEGUN  I  ,
C                   B.  ABRAMOWITZ AND  TEGUN  I
C
C      THI   FUNCTION  I   REQUIRED FOR  U E WITH FUNCTION  I  I
C
C-----------------  -  --- -- - -
C
C      FUNCTION GAMMA  (NUM, NDEN)
C
C-----------------  ---------  -   -
C
C      FUNCTION TO CALCULATE THE MATHEMATICAL GAMMA FUNCTION
C      IT  ARGUMENT I  AN INTEGER OR AN HALF-INTEGER  .
C
C      INPUT PARAMETER .
C           NNUM:  NUMERATOR OF ARGUMENT T  GAMMA FUNCTION
C           NDEN:  DENOMINATOR OF ARGUMENT T  GAMMA FUNCTION
C
C      OUTPUT PARAMETER
C           GAMMA:  VALUE OF GAMMA FUNCTION
C
C-------------------------------
C
C      COMMON BLOCKS AND VARIABLE  EFINITIONS.
C
       DOUBLE PRECISION GAMMA, PI, ETA
C
C      PI AND SQRT( PI ) T  15 SIGNIFICANT DIGIT
C
       DATA PI   / 3.14159265358979 , ETA  / 1.77245385090552 /
C
C---------- ----------  -  ----     --
C
       GAMMA = 1.0
       N = NNUM  NDEN
C
C      WHEN  I  A POSITIVE INTEGER, GAMMA IS  ,  ,  ,  ,  ,  /
C      (REF  A, EQ  6.1.1 )
C
       IF  MOD(N,2).EQ. 0  THEN
```

APPENDIX C

GEOMETRY OF A RIGHT CIRCULAR CONE

C.1 RADIUS OF CURVATURE DERIVATION

Consider the surface of a right circular cone of half cone angle θ_0 shown in Figure 3.6 and reproduced below in Figure C.1

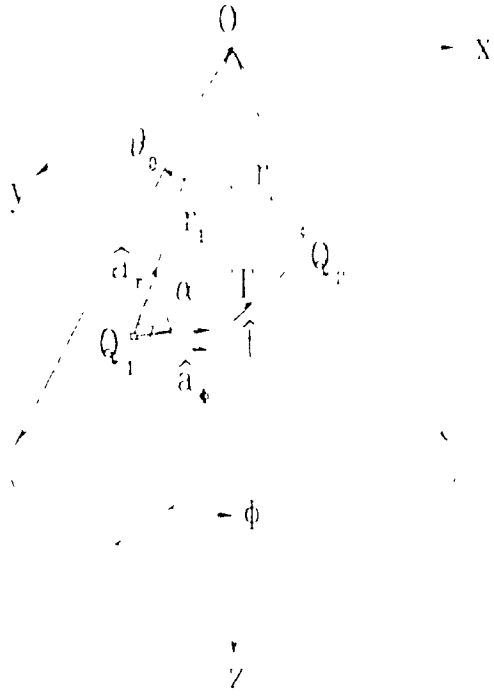

Figure C.1. Geodesic path Γ on a right circular cone [28]

The surface of the cone in Figure C.1 is the locus of points traced out by the tip of a vector $\vec{r}$ defined by

$$\vec{r} = (z \tan\theta_0 \cos\phi)\,\hat{a}_x + (z \tan\theta_0 \sin\phi)\,\hat{a}_y + z\,\hat{a}_z ,$$

or more compactly

$$\vec{r} = (z \tan\theta_0 \cos\phi,\ z \tan\theta_0 \sin\phi,\ z), \qquad (C.1)$$

where $(\hat{a}_x, \hat{a}_y, \hat{a}_z)$ are unit vectors in the direction of increasing Cartesian coordinates (x,y,z), (ρ,ϕ,z) are the cylindrical coordinates, and (r,θ,ϕ) are the spherical coordinates.

The cone's surface in (C.1) is a representation in terms of curvilinear coordinates (u,v), in which (u,v) are identified with (ϕ,z), of the form

$$\vec{r}(u,v) = (x(u,v), y(u,v), z(u,v)) \quad . \tag{C.2}$$

The representation in (C.2) greatly facilitates the derivation of the cone's radius of curvature which can be expressed in terms of the first and second order partial derivatives of $\vec{r}$ with respect to ϕ and z. These derivatives are

$$\vec{r}_\phi = \left(\frac{\partial x}{\partial \phi}, \frac{\partial y}{\partial \phi}, \frac{\partial z}{\partial \phi}\right)$$
$$= (-z \tan\theta_0 \sin\phi,\ z \tan\theta_0 \cos\phi,\ 0), \tag{C.3}$$

$$\vec{r}_z = \left(\frac{\partial x}{\partial z}, \frac{\partial y}{\partial z}, \frac{\partial z}{\partial z}\right)$$
$$= (\tan\theta_0 \cos\phi,\ \tan\theta_0 \sin\phi,\ 1), \tag{C.4}$$

$$\vec{r}_{\phi\phi} = \left(\frac{\partial^2 x}{\partial \phi^2}, \frac{\partial^2 y}{\partial \phi^2}, \frac{\partial^2 z}{\partial \phi^2}\right)$$
$$= (-z \tan\theta_0 \cos\phi,\ -z \tan\theta_0 \sin\phi,\ 0), \tag{C.5}$$

$$\vec{r}_{zz} = \left(\frac{\partial^2 x}{\partial z^2}, \frac{\partial^2 y}{\partial z^2}, \frac{\partial^2 z}{\partial z^2}\right)$$
$$= (0,\ 0,\ 0), \tag{C.6}$$

$$\vec{r}_{\phi z} = \left(\frac{\partial^2 x}{\partial \phi \partial z}, \frac{\partial^2 y}{\partial \phi \partial z}, \frac{\partial^2 z}{\partial \phi \partial z}\right)$$
$$= (-\tan\theta_0 \sin\phi,\ \tan\theta_0 \cos\phi,\ 0), \tag{C.7}$$

and

$$\vec{r}_{z\phi} = \left(\frac{\partial^2 x}{\partial z \partial \phi}, \frac{\partial^2 y}{\partial z \partial \phi}, \frac{\partial^2 z}{\partial z \partial \phi} \right)$$
$$= (-\tan\theta_0 \sin\phi, \tan\theta_0 \cos\phi, 0)$$
$$= \vec{r}_{\phi z}, \tag{C.8}$$

The parameters in the first fundamental form in differential geometry are found to be [24,40]

$$E = \vec{r}_\phi \cdot \vec{r}_\phi$$
$$= z^2 \tan^2\theta_0 \sin^2\phi + z^2 \tan^2\theta_0 \cos^2\phi$$
$$= z^2 \tan^2\theta_0, \tag{C.9}$$

$$F = \vec{r}_\phi \cdot \vec{r}_z$$
$$= -z \tan^2\theta_0 \sin\phi \cos\phi + z \tan^2\theta_0 \cos\phi \sin\phi$$
$$= 0, \tag{C.10}$$

and

$$G = \vec{r}_z \cdot \vec{r}_z$$
$$= \tan^2\theta_0 \cos^2\phi + \tan^2\theta_0 \sin^2\phi + 1$$
$$= \sec^2\theta_0. \tag{C.11}$$

The parameters in the second fundamental form in differential geometry are defined as [24,40]

$$e = \frac{\vec{r}_{\phi\phi} \cdot (\vec{r}_\phi \times \vec{r}_z)}{\sqrt{EG - F^2}}, \tag{C.12}$$

$$f = \frac{\vec{r}_{\phi z} \cdot (\vec{r}_\phi \times \vec{r}_z)}{\sqrt{EG - F^2}}, \tag{C.13}$$

and

$$g = \frac{\vec{r}_{zz} \cdot (\vec{r}_\phi \times \vec{r}_z)}{\sqrt{EG - F^2}}. \tag{C.14}$$

The terms $\sqrt{EG - F^2}$ and $(\vec{r}_\phi \times \vec{r}_z)$ are common to (C.12), (C.13), and (C.14) and, in the case of a cone are found to be

$$\sqrt{EG - F^2} = \sqrt{z^2 \tan^2\theta_0 \sec^2\theta_0}$$
$$= z \tan\theta_0 \sec\theta_0 \qquad \text{(C.15)}$$

and

$$(\vec{r}_\phi \times \vec{r}_z) = \begin{vmatrix} \hat{a}_x & \hat{a}_y & \hat{a}_z \\ -z\tan\theta_0 \sin\phi & z\tan\theta_0 \cos\phi & 0 \\ \tan\theta_0 \cos\phi & \tan\theta_0 \sin\phi & 1 \end{vmatrix}$$

$$= (z\tan\theta_0 \cos\phi,\ z\tan\theta_0 \sin\phi,\ -z\tan^2\theta_0) \,. \qquad \text{(C.16)}$$

The numerators of e, f, and g in (C.12)-(C.14) are derived below, where num(·) denotes the numerator of the appropriate parameter, as

$$num(e) = \vec{r}_{\phi\phi} \cdot (\vec{r}_\phi \times \vec{r}_z)$$
$$= -z^2 \tan^2\theta_0 \cos^2\phi - z^2 \tan^2\theta_0 \sin^2\phi$$
$$= -z^2 \tan^2\theta_0 \,, \qquad \text{(C.17)}$$

$$num(f) = \vec{r}_\phi \cdot (\vec{r}_\phi \times \vec{r}_z)$$
$$= -z^2 \tan^2\theta_0 \sin\phi\cos\phi - z^2 \tan^2\theta_0 \sin\phi\cos\phi$$
$$= 0 \,, \qquad \text{(C.18)}$$

and

$$num(g) = \vec{r}_{zz} \cdot (\vec{r}_\phi \times \vec{r}_z)$$
$$= 0 \qquad \text{(C.19)}$$

Substituting (C.15) and (C.17)-(C.19) into (C.12)-(C.14), the parameters in the second fundamental form in differential geometry for the cone are found to be

$$e = -z\sin\theta_0, \tag{C.20}$$

$$f = 0, \tag{C.21}$$

and

$$g = 0. \tag{C.22}$$

Euler's Theorem in differential geometry expresses the curvature for a surface in terms of the parameters from the first and second fundamental forms as

$$\kappa = \frac{e}{E}\sin^2\alpha + \frac{g}{G}\cos^2\alpha, \tag{C.23}$$

where α is the angle a trajectory on the surface makes with a u constant line of curvature. As is shown in Chapter 3 and in Figure C.1 for the case of the cone α is the angle the geodesic makes with a ϕ=constant line of curvature, i.e. a straight line that extends from the apex along the surface of the cone. Substituting (C.9), (C.11), (C.20), and (C.22) into (C.23), the curvature of a path on the surface of a cone is then

$$\kappa = \frac{\sin\theta_0}{z\tan^2\theta_0}\sin^2\alpha$$

$$= \frac{-\cos\theta_0}{z\tan\theta_0}\sin^2\alpha. \tag{C.24}$$

The radius of curvature for a cone geodesic, ρ_g, is simply the reciprocal of the curvature in (C.24) and, for the purposes of the calculations in Chapter 3, is a positive quantity given by

$$\rho_g = \frac{1}{|\kappa|} = \frac{z\tan\theta_0}{\cos\theta_0\sin^2\alpha}. \tag{C.25}$$

Since r is the distance from the cone apex along the cone surface, then

$$z = r\cos\theta_0 \tag{C.26}$$

and the radius of curvature for a cone geodesic becomes

$$\rho_g = \frac{r\tan\theta_0}{\sin\alpha} \ . \tag{C.27}$$

C.2 DIFFERENTIAL ARC LENGTH DERIVATION

The first fundamental form, which was alluded to in the previous section, represents the square of the differential arc length ds^2 along a curve on a surface and is expressed in terms of the curvilinear coordinates (u,v) as

$$I = (ds)^2 = E(du)^2 + 2F\,du\,dv + G(dv)^2 \ . \tag{C.28}$$

Using (C.9)-(C.11), the square of the differential arc length along a curve on the cone surface in terms of the cone curvilinear coordinates (ϕ,z) is

$$(ds)^2 = z^2\tan^2\theta_0(d\phi)^2 + \sec^2\theta_0(dz)^2 \ . \tag{C.29}$$

Consider the cone of Figure C.1 developed into a plane surface as shown in Figure 3.7 and now reproduced in Figure C.2. From the geometry in Figure C.2, the angle α is

$$\alpha = \Omega_1 + (\phi - \phi_1)\sin\theta_0 \ . \tag{C.30}$$

Also from the geometry in Figure C.2, the distance r and the angle α are related to the distance r_1 and the angle Ω_1 be means of

$$r\sin\alpha = r_1\sin\Omega_1 \ . \tag{C.31}$$

The differentials $d\phi$ and dz can now be found in terms of $d\alpha$ using (C.26), (C.30), and (C.31) as

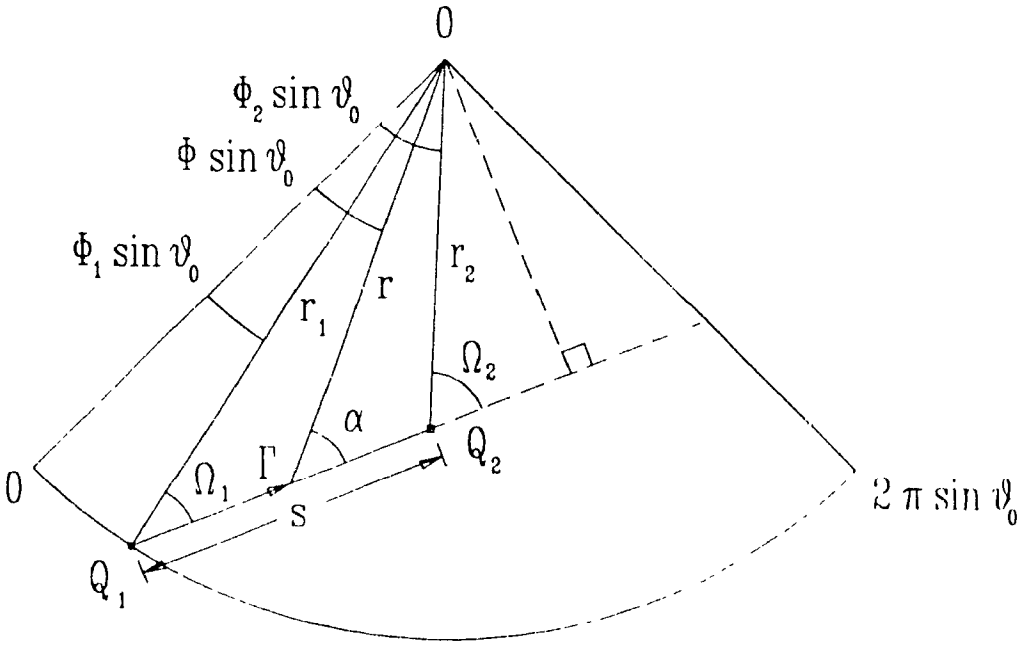

Figure C.2. Geodesic path Γ on a right circular cone developed into a planar pie slice [28]

$$d\phi = \frac{d\alpha}{\sin\theta_0} \tag{C.32}$$

and

$$dz = dr \cos\theta_0$$

$$= \left(\frac{-r_1 \sin\Omega_1 \cos\alpha \, d\alpha}{\sin^2\alpha} \right) \cos\theta_0 \, . \tag{C.33}$$

Substituting (C.31)-(C.33) into (C.29), the differential arc length ds' is found as a function of differential angle $d\alpha$ to be

$$(ds')^2 = (r^2 \cos^2\theta_0) \tan^2\theta_0 \left(\frac{d\alpha}{\sin\theta_0} \right)^2 + \left(\frac{r_1 \sin\Omega_1 \cos\alpha \, d\alpha}{\sin^2\alpha} \right)^2$$

$$= \left(\frac{r_1 \sin\Omega_1}{\sin\alpha} \right)^2 (1 + \cot^2\alpha) (d\alpha)^2 \, ,$$

$$ds' = \frac{r_1 \sin \Omega}{\sin \alpha} d\alpha \quad . \tag{C.34}$$

It should be noted that the absolute value signs are omitted in (C.34) because the value of Ω_1 is always between 0 and π radians so that the sine of angle Ω_1 is always positive